Engineering of fluorescent chemogenetic sensors for biomolecule detection and imaging

Fanny Broch

▶ To cite this version:

Fanny Broch. Engineering of fluorescent chemogenetic sensors for biomolecule detection and imaging. Theoretical and/or physical chemistry. Université Paris sciences et lettres, 2021. English. NNT : 2021UPSLE076 . tel-04368463

HAL Id: tel-04368463
https://theses.hal.science/tel-04368463
Submitted on 1 Jan 2024

PSL UNIVERSITÉ PARIS

THÈSE DE DOCTORAT
DE L'UNIVERSITÉ PSL

Préparée à l'École Normale Supérieure

Engineering of fluorescent chemogenetic sensors for biomolecule detection and imaging

Soutenue par
Fanny BROCH
Le 09 décembre 2021

Dirigée par
Arnaud GAUTIER

Ecole doctorale n° 388
Chimie Physique et Chimie Analytique de Paris Centre

Spécialité
Chimie-Physique

Composition du jury :

Mme. Dr. Claire DÉO European Molecular Biology Laboratory	*Rapporteur*
M. Prof. Arnaud GAUTIER Sorbonne Université	*Directeur de thèse*
Mme. Dr. Florence MAHUTEAU-BETZER Institut Curie	*Présidente du jury*
Mme. Prof Amy PALMER University of Colorado Boulder	*Examinateur*
M. Prof. Pablo RIVERA-FUENTES Ecole Polytechnique Fédérale de Lausanne	*Examinateur*
M. Prof. Michaël RYCKELYNCK Université de Strasbourg	*Rapporteur*

ENS | PSL

SORBONNE UNIVERSITÉ

cnrs

Engineering of fluorescent chemogenetic sensors for biomolecule detection and imaging

préparée par
Fanny BROCH

et dirigée par
Prof. Arnaud GAUTIER

Thèse de doctorat de Chimie-Physique

Acknowledgements

Je voudrais tout d’abord remercier Pr Arnaud Gautier, mon directeur de thèse, de m’avoir fait confiance et de m’avoir encadrée depuis plus de trois ans, mais aussi et surtout pour sa bienveillance, sa patience et son optimisme infaillible. J’ai eu la chance immense d’avoir été encadrée par une personne aussi inspirante tant professionnellement qu’humainement. Merci de nous transmettre ta passion, merci de nous pousser à croire en nous, merci d’avoir mille idées et de toujours vouloir tout tester. Merci également pour ton soutien durant ces trois années riches en évènements. Je peine à trouver les mots pour dire à quel point j’en suis reconnaissante.

Je remercie les membres du jury, Dr Claire Déo, Dr Florence Mahuteau-Betzer, Pr Amy Palmer, Pr Pablo Rivera-Fuentes et Pr Michael Ryckelynck, d’avoir accepté d’évaluer mon travail et d’avoir été présents à ma soutenance de thèse.

Je souhaite remercier toute l’équipe avec laquelle j’ai travaillé au fil des ans. Un immense merci à Hela, d’avoir été ma binôme de thèse et surtout une amie précieuse. Merci d’avoir été là depuis le début de cette aventure, dans les bons moments qui ont été nombreux, mais aussi dans les moments plus difficiles. On a beaucoup ri tous les jours, au laboratoire, en conférence ou dans nos tout petits appartements, on a fui les fantômes de l’ENS, fait et défait des cartons, et je me sens très chanceuse d’avoir pu faire cette thèse avec toi ! Merci également à Louise pour les nombreuses aventures que l’on aura traversées de l’ENS à Jussieu, merci de nous faire rire, de nous faire partager ta passion pour la pâtisserie et ta culture musicale invraisemblable. Je remercie infiniment Marie-Aude pour sa présence depuis le début, pour ses remarques qui n’ont jamais manqué de me faire rire, et pour tout ce qu’elle m’a appris (surtout d’élever les cellules comme des tomates cerises). Un grand merci également à Alison de m’avoir énormément appris, et d’avoir été un exemple de persévérance et de détermination.

Je remercie Lina et Aurélien, non seulement d’avoir participé à différents projets de cette thèse, mais également d’avoir été d’un grand soutien, je vous ai certes encadrés mais vous m’avez aussi énormément appris. Je remercie Sara de son éternelle bienveillance et de nous faire rire chaque jour en anglais mais surtout en français et parfois même en italien. Et évidemment, merci pour les post-its et les goûters. Je remercie également Tiphaine, Amandine, Marie, et Chenge d’avoir fait partie de cette belle expérience durant laquelle j’ai été, c’est certain, très bien entourée !

Je voudrais remercier de tout mon cœur Audrey, Mary et Lucas, d’avoir été ma deuxième famille d’abord dans les laboratoires de l’ENS, puis dans tous les brunchs de Paris, dans la forêt de Bures-sur-Yvette, sur une barque à la Baule ou dans un escape game plein de sable à Lille. Ces trois ans et demi à vos côtés sont remplis de beaux souvenirs et de beaucoup d’amour !

J’ai eu la chance d’avoir commencé cette thèse au laboratoire PASTEUR, des débuts qui ont eux aussi été riches en belles rencontres. Merci en particulier à Emmanuelle et Isabelle pour leur bonne humeur et leurs histoires qui ont animé nos déjeuners**.** Merci à Ludovic Jullien, David, Käthlin, Jordy, Thomas, Raja, Marina, et tous les membres du laboratoire.

Merci également à tous les membres du Laboratoire des BioMolécules, pour leur accueil il y a deux ans de cela et de partager, de près ou de loin, mon quotidien. Un grand merci à Delphine et Françoise pour leur sourire, et sans qui les longues matinées en culture cellulaire auraient été bien moins plaisantes ! Merci à Nicolas pour ta gentillesse et ton humour au quotidien. Un immense merci à Éliane pour son accueil et sa présence rayonnante au quotidien. Merci à Mathieu et Valentin, et merci à Erwan de nous avoir en quelques mois tout appris sur la Bretagne, mais surtout de m'avoir soutenue (et supportée) pendant la rédaction de ce manuscrit.

Un grand merci à l'équipe de l'unité de chimie du Palais de la Découverte, en particulier à Ludovic et Sarah, de m'avoir énormément appris, soutenue, de m'avoir regardée m'émerveiller sans relâche de pouvoir faire une flamme dans de l'air liquide, et de m'avoir si bien accueillie au sein de l'équipe.

Un immense merci à mes amis qui m'accompagnent sur ce chemin, pour certain(e)s depuis presque quinze ans ! De près ou de loin, votre soutien est précieux. Merci Louise et Emma, d'être des amies formidables et d'être toujours là pour moi, que ce soit pour partir à l'aventure ou passer des heures à se raconter nos vies. Merci Jean, d'être un ami aussi attentif et patient (et de porter mes cadeaux d'anniversaire dans ton sac à dos au milieu des montagnes slovènes). Merci Anthony, Malik et Maxime, d'être là depuis tant d'années, merci Antoine pour le sucre impalpable, et merci Nico d'avoir croisé mon chemin et de m'avoir aidée à croire que j'en étais capable.

Merci à ceux qui ont rendu la vie belle durant ces trois années, ceux avec qui j'ai dansé et ceux avec qui j'ai couru, ceux avec qui j'ai partagé de beaux moments et qui m'ont entourée durant cette expérience. Je remercie tout particulièrement Marine pour les fous rires entre deux déboulés et les soirées à refaire le monde, Gaël pour avoir été non seulement un partenaire de danse mais également un voisin et un ami formidable, merci à toute l'équipe de la danse dont Elise, Clément, Sofia et Nathalie, et surtout merci Tiphaine de rayonner à chaque cours que tu donnes, ton énergie est une inspiration extraordinaire. Merci à ceux dont j'ai croisé le chemin à Stockholm et que j'ai retrouvé mon plus grand bonheur à Paris, et je remercie Thomas d'avoir été un repère et un soutien précieux.

Merci à Pr Kai Johnsson et son groupe de m'avoir mise sur la voie de la recherche avec énormément d'enthousiasme et de bienveillance. Merci à Yann et Julien de m'avoir encadrée à mes débuts et d'avoir fait de ces quelques mois passés à vos côtés une expérience inoubliable. Merci également à Helen et Silvia d'avoir été des exemples et de m'avoir inspirée à essayer de faire chaque jour mieux que la veille.

Enfin, je remercie de tout cœur ma famille sans qui rien de tout cela ne serait arrivé. Merci à mes parents pour leur soutien infaillible, leurs encouragements, et de n'avoir jamais cessé de croire en moi. Merci à ma mamie, et merci à mon frère, Romain, d'être des exemples de force et de résilience, de toujours me faire rire et de m'inspirer chaque jour. Je vous remercie mille fois de m'entourer à chaque nouvelle étape.

List of abbreviations

ADP: adenosine-5'-diphosphate
AMP: adenosine-5'-monophosphate
AMPA: α-amino-3-hydroxy-5-methyl-4-isoxazolepropionic acid
ATP: adenosine-5'-triphosphate
BALM: binding-activated localization microscopy
BiFC : bimolecular fluorescence complementation
BON: bacterial OsmY and nodulation
BphP : bacteriophytochrome
BRET: bioluminescence resonance energy transfer
BSA: bovine serum albumin
BV: biliverdin
CALI: Chromophore-assisted light inactivation
CaM: calmodulin
CBCR: cyanobacteriochrome
CFP: cyan fluorescent protein
CLEM: correlative light-electron microscopy
CMV: human cytomegalovirus
CRABPII: cellular retinoic acid binding protein II
CyDye: cyanine dye
DFHBI: 3,5-difluoro-4-hydroxybenzylidene imidazolinone
DIR: dimethylindole red
DMEM: Dulbecco's Modified Eagle Medium
DNA: deoxyribonucleic acid
DPBS: Dulbecco's Phosphate-Buffered Saline
eDHFR: *E*. coli dihydrofolate reductase
EGFP: enhanced green fluorescent protein
E. coli: *Escherichia coli*
ERK2: extracellular signal-regulated kinase 2
FAP: fluorogen activating protein
FAST: Fluorescence Activating absorption Shifting Tag
FbFP: flavin-based fluorescent protein
FKBP: FK506 binding protein
FMN: flavin mononucleotide
FLIM: fluorescence lifetime imaging microscopy
FP: fluorescent protein
FRB: FKBP–rapamycin binding
FRET: Forster resonance energy transfer
FUCCI: fluorescence ubiquitination cell cycle indicator
GABA: γ-aminobutyric acid
GlnK1:
GltI: glutamate/aspartate import solute-binding protein
GFP: green fluorescent protein
GTP: guanosine-5'-triphosphate
HA: hemagglutinin
Hha: *Halorhodospira halophila*
HBR: hydroxybenzylidene rhodanine
hCRPBII: human cellular retinol binding protein II
HEK293: human embryonic kidney
IANBD: *N*,*N*'-Diméthyl-*N*-(iodoacétyl)-*N*'-(7-nitrobenz-2-oxa-1,3-diazol-4-yl)éthylènediamine
IRES: internal ribosome entry site
IFP: infrared fluorescent protein
JF dyes: Janelia Fluor dyes
Kbp: K^+ binding protein
LOV: light, oxygen, voltage
LysM: lysine motif
MAPK: mitogen-activated protein kinases
MBD: methyl-CpG binding domain
MEM: minimum essential media
MEK1: mitogen-activated protein kinase kinase
MG: malachite green
miniSOG: mini Singlet Oxygen Generator
mT2: mTurquoise2
NADPH: nicotinamide adénine dinucléotide phosphate
NIR: near infrared
PALM: photo-activated localization microscopy
PAS-GAF domain: Per-ARNT-Sim repeats cGMP phosphodiesterase/adenylate cyclase/FhlA transcriptional activator domain
PBP: periplasmic binding protein
PBS: phosphate buffered saline
PCR: polymerase chain reaction
PDB: protein data bank
PDGFR: platelet-derived growth factor receptor
PHY: phytochrome
PKA: protein kinase A
PNA: peptide nucleic acid
POI: protein of interest
PPI: protein-protein interaction
PYP: photoactive yellow protein
RESOLFT: reversible saturable optical fluorescence transition
RFP: red fluorescent protein
RNA: ribonucleic acid
ROS: reactive oxygen species
RspA: *Rheinheimera sp. A13L*
SELEX: systematic evolution of ligands by exponential enrichment
SiR: Silicon rhodamine
SOFI: stochastic optical fluctuation imaging
SRRF: super-resolution radial fluctuations
STED: Stimulated emission depletion
STORM: stochastic optical reconstruction microscopy
***S. cerevisiae*:** Saccharomyces cerevisiae
TAC: 2-triazacryptand [2,2,3]-1-(2-methoxyethoxy)benzene
TEFLA: tethered fluorogen assay
TEV: *Tobacco Etch Virus*
TO: thiazole orange
UV: Ultraviolet
YFP: yellow fluorescent protein
YO: oxazole yellow

Contents

CHAPTER IV: DESIGN AND CHARACTERIZATION OF K$^+$-FAST, A POTASSIUM ION SENSOR BASED ON FAST. **103**

CHAPTER V: DESIGN AND CHARACTERIZATION OF ATP-FAST, A MODULAR ADENOSINE-5'-TRIPHOSPHATE SENSOR BASED ON FAST. **125**

CHAPTER VI: IDENTIFICATION AND OPTIMIZATION OF NEW CPFAST AND SPLIT FAST REPORTERS...**165**

Chapter I

General introduction

The 21st century appears to be the era of biotechnology. The human genome has been sequenced,[1] and can now be edited by the revolutionary CRISPR method, awarded in 2020 by the Nobel prize in Chemistry to Jennifer Doudna and Emmanuelle Charpentier.[2] Genetic engineering has played a tremendous role in fundamental research and therapeutic developments, advancing the fields of immunotherapy, cell therapy as well as gene therapy that directly targets defective genes.[3] The past two years have been marked by the unmissable bringing to the front stage of mRNA vaccines, and efforts are now directed towards the translation of this technology to drug development.[4] Interdisciplinary strategies such as the Blue Brain Project, combining neuroscience and computational methods, aim at tackling the impressive challenge of simulating and understanding neurobiology.[5]

These impressive breakthroughs testify of the continuously improving comprehension of human biology. Researchers are indeed able to visualize and study the organism in greater and greater details, supported by the progress of multiple advanced imaging techniques. At the macroscopic scale, methods such as ultrasound, Computed Tomography (CT), Magnetic Resonance Imaging (MRI), and Positron Emission Tomography (PET) are widely used and constantly improving in terms of imaging depth, contrast, and resolution.[6] The frontiers of the imaging field are also being expanded by the emergence of new imaging techniques such as optoacoustic, as well as the development of combined strategies for multimodal imaging.

In parallel, fluorescence microscopy established itself as the golden standard method for studying biological processes at the microscopic level, now even tending towards nanoscopic resolution.

I.1. Fluorescence microscopy

I.1.1 Imaging and fluorescence

Fluorescence was first described in 1852 by Sir George G. Stokes, describing the emission of light from a sample that was subject to light excitation with a shorter wavelength. Upon absorption of a photon followed by vibrational relaxation, a photon is indeed emitted with lower energy (thus longer wavelength), from the lowest excited electronic state to the ground state (S0 ← S1 relaxation). The different possible de-excitation pathways of an absorbed photon are conveniently represented by the Perrin-Jablonski diagram (Figure I-1), including internal conversion, intersystem crossing, phosphorescence, or fluorescence.

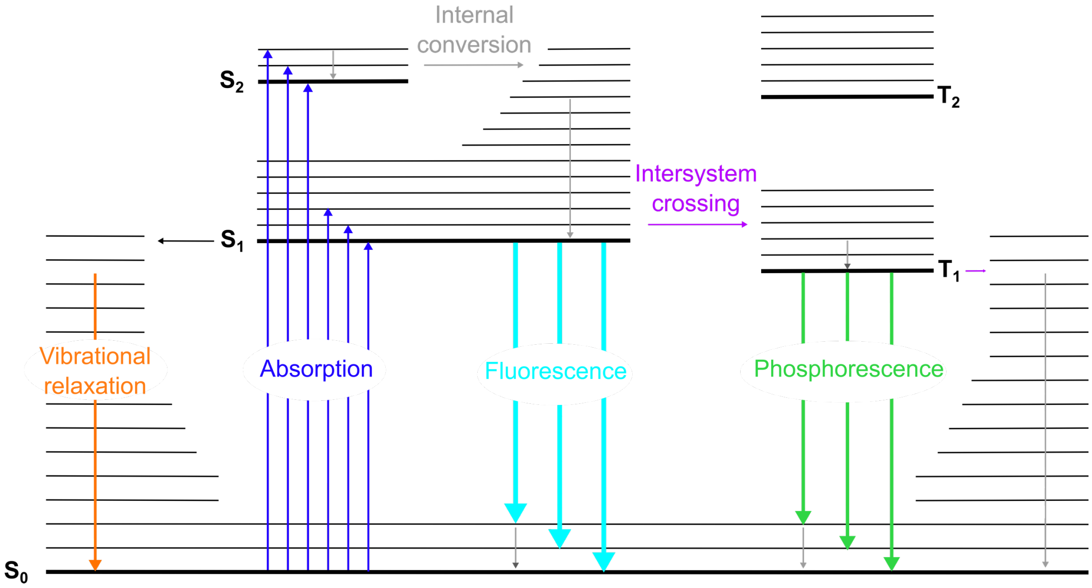

Figure I-1. Perrin-Jablonski diagram. Adapted from Valeur. [65]

Imaging biology by fluorescence microscopy relies on the coupling of an element of interest with a fluorescent reporter, that is either a synthetic fluorophore, generally a small molecule, or a genetically encoded reporter. This second category is mostly composed of fluorescent proteins that benefit from absolute targeting specificity upon cellular genetic modification, and the constantly evolving family of photoactive proteins covers a wide range of spectral properties and imaging applications.[7] Outstanding images obtained from the Brainbow technique illustrate the potential of fluorescence microscopy to provide meaningful insights and understanding of systems as complex as neuronal networks,[8] in two- as well as in threedimensions, as recently described by Livet's research group.[9] Such technical exploits testify of the progress achieved in the field of fluorescence microscopy over the last three decades.

On the one hand, technical developments have been continuously improving spatial and temporal resolution. Two-photon microscopy, using excitation from two photons with longer wavelength (usually in the infrared region) than the emitted light, stands as a significant example of increased imaging depth, better tissue penetration and reduced photobleaching.[10] This method, which provides a high imaging contrast due to low background signal and high-intensity excitation to a restricted focal volume, has rapidly contributed to major advances, notably in the study of neurobiological processes.[11]

Super-resolution microscopy has also tremendously contributed to the field of fluorescence imaging, by overcoming the diffraction barrier that limits lateral resolution to approximately 200 nm in confocal microscopy. It was notably acknowledged as a significant breakthrough by the scientific community in 2014, attributing the Nobel Prize in Chemistry to Eric Betzig, William E. Moerner and Stefan W. Hell for their equal contribution in the development of stimulated-emission-depletion (STED) microscopy.[12] Together with reversible saturable optical fluorescence transition (RESOLFT) microscopy,[13] these methods rely on the use of a depletion laser beam with a zero intensity point at the center of the excitation spot, that de-excites peripheral fluorescent molecules to their ground state. Single-molecule localization microscopy uses a different approach based on photoswitchable fluorescent reporters: either synthetic dyes in the context of stochastic optical reconstruction microscopy (STORM)[14], or genetically encoded proteins for photo-activated localization microscopy (PALM).[15] Fluorescent signals from a sparse subset of reporters, switched on stochastically, are accumulated and fitted to precisely determine the position of each single-molecule. The resulting images reach a spatial resolution down to 20 nm; yet the high number of acquisitions necessary for image reconstruction leads to low time-resolution and irreversible photobleaching. Combining STED to the PALM principle, thus relying on the stochastic switch-on of photoswitchable molecules upon highly targeted excitation, the position of a single molecule could be determined with approximately 2-nm precision and better temporal resolution using MINFLUX (standing for minimal emission fluxes) method.[16]

On the other hand, each progress on the physics end of microscopy had to be followed up by molecular improvements of the fluorescent probes. Indeed, concomitant optimization of the fluorophores has allowed to keep up with the requirements from newly developed techniques, thus constantly pushing the boundaries of fluorescence imaging. In the last two decades, the growing outreach of super-resolution microscopy has notably encouraged the development of various photoswitchable molecules, either synthetic dyes or FPs, that have been thoroughly described in very instructive reviews.[17,18] Accordingly, derivatization of rhodamine motifs have lately yielded several examples of photoactivatable,[19] spontaneously blinking[20,21] or photoregulated fluxional fluorophores.[22]

Beyond information about cellular structures, organization and molecular localizations, fluorescence microscopy provides the opportunity to visualize cellular processes. To this end, fluorescent probes need to be further engineered by coupling them to a sensing domain, in order to generate a biosensor. In the case of genetically encoded reporters, this sensing unit is generally an analyte-specific protein domain, interacting proteins, or the target sequence of a specific enzyme. These sensors rely on the conformational change undergone by a sensing domain upon signal detection, leading to a change in optical properties of the reporter domain. Typically, this can be a change of fluorescence intensity from a single fluorescent protein reporter, or a modified Förster resonance energy transfer (FRET) efficiency between two fluorescent proteins.

As described in more details in chapter II, engineering of fluorescent proteins has yielded to a number of genetically encoded biosensors, allowing imaging of metal ions, small molecules and voltage, that were notably used widely for the study of neurotransmission.[23–25] Keeping up as well with the emerging super-resolution imaging methods, innovative biosensors are also being developed to record cellular activity with high spatial resolution. Measuring fluorescence fluctuations of a single FP by stochastic optical fluctuation imaging (SOFI), that could be modulated by proximity with the photoswitchable Dronpa, FLINC sensors (fluorescence fluctuation increase by contact) were for instance used to probe protein-protein interactions and protein kinase A enzymatic activity.[26] Interestingly, this method could be generalized to the visualization of diverse PPIs, and elegantly illustrated the perspectives offered by the use of new biosensing methods and innovative fluorescent reporters.

I.1.2 Chemogenetic fluorescent reporters and recent advances

The expansion of the palette of hybrid fluorescent reporters attests of the increasing interest in their unique properties, including targeting specificity of a genetically encoded tag coupled to the modularity of a synthetic probe by accessible chemical modification. Recent developments of such chemogenetic systems have been thoroughly described by Benaissa et al. in 2020[27], as well as their diverse applications from imaging to photoactuation and drug delivery. [28, 29] Constant evolution and improvements of microscopy techniques are indeed consistently encouraging the development of adequate fluorescent probes. For instance, a number of near-infrared fluorophores are being functionalized with chemical handles in order to generate ligands for self-labelling tags.[30–32] Intrinsic properties of some hybrid systems could also be exploited, such as UnaG photobleaching by photo-oxidation of bilirubin that proved useful for the development of a blinking probe for single-molecule localization microscopy.[33] Moreover, the use of PYP-tag for imaging protein degradation was an indicative example of the beneficial use of a chemogenetic reporter. Indeed, time-specific covalent labelling with a polarity-sensitive fluorogen allowed one to correlate the decrease of fluorescent signal to degradation of the fusion protein, without being affected by continuous protein expression.[34]

Engineering of chemogenetic probes have been followed by the design of various biosensing systems, that will further be described in the literature review presented in chapter II. The hybrid nature of these reporters has indeed offered new perspectives for innovative biosensing opportunities. Among the most recent developments of biosensors based on covalent self-labelling tags, the use of HaloTag has notably allowed unprecedented targeting of a membrane tension probe, HaloFlipper, to study mechanobiology by confocal microscopy and fluorescence lifetime imaging microscopy (FLIM).[35] Ligand engineering of a cell-impermeant SNAP-tag substrate also enabled to study trafficking of a widely targeted G-protein coupled receptor, glucagon-like peptide-1 receptor (GLP1R).[36] The characterization of environment sensitive color-shifting ligands, showing a significant spectral shift upon spirocyclization, yielded different biosensors when coupled to a Ca^{2+}-sensitive HaloTag fusion or a NADPH-dependent eDHFR mutant.[37] Biosensors could also be generated by combining SNAP-tag to a bioluminescent luciferase. Relying on a similar principle as Snifits design, described in further details in the following chapter, the use of BRET allowed the development of sensors for various small molecule drugs, as well as NADPH and NAD^+, suitable for point-care diagnostic.[38–40]

Challenging biosensing applications have also been recently addressed with non-covalent hybrid reporters such as fluorogen-binding proteins (FAPs). Visualization of cellular apposition has for example been tackled by strategies relying on a heterobivalent ligand, targeting two different FAPs expressed at the membrane of co-cultured cell populations. This so-called tethered fluorogen assay (TEFLA) showed promising results as a strong fluorescence increase was observed from the lower-affinity activated fluorogen at cellular contact regions.[41] A similar strategy was developed to probe transient and long-term contacts between co-cultured cells expressing either a FAP or HaloTag at their membrane.[42] Finally, impressive progress in computer-based structural and functional predictions enabled de novo design of several biosensors based on the coupling of mini-FAPs to different sensing modalities.[43] Fluorescent properties of the fluorogen DFHBI thus could be modulated by pH variations or by the presence of Ca^{2+} , and further modelization even allowed the generation of a reversible PPI reporter based on the complementation of split-mFAPs fragments. This last example demonstrates the countless imaging possibilities now within our grasp, by parallel optimization of computational methods, technical improvements and adequate tool development for fluorescence microscopy.

I.2. Using FAST as a reporter in biosensors

I.2.1. FAST principle

Among chemogenetic reporters subsequently described in chapter II, our group developed in 2016 the Fluorescence Activating and absorption-Shifting Tag FAST, a small protein tag (14 kDa) engineered from the photoactive yellow protein (PYP). Directed evolution on the loop 94-101 of this photoreceptor from *Halorhodospira halophila* indeed yielded a variant that non-covalently binds hydroxybenzylidene-rhodanine (HBR) derivatives. (Figure I-2) Together with the mutation of the reactive cysteine residue C69 to a glycine, the resulting variant non-covalently binds HBR derivatives in a highly dynamic and fully reversible manner.[44] HBR derivatives are fluorogenic small molecules, that undergo a significant absorption red shift and fluorescence increase upon deprotonation and immobilization in the binding cavity of FAST.

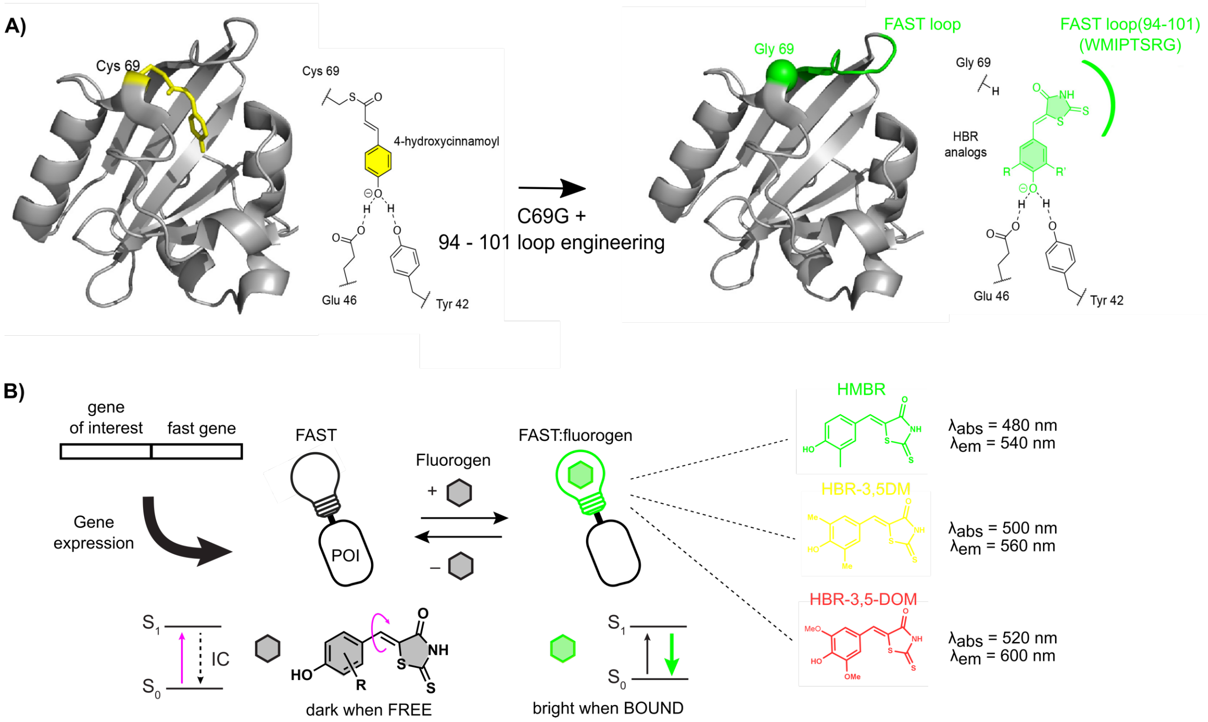

Figure I-2. Engineering of the chemogenetic reporter FAST. A) FAST was engineered by introduction of the mutation C69G and directed evolution of the loop 94-101 from its parent protein PYP (PDB 1NWZ). **B)** FAST non-covalently and selectively binds fluorogenic HBR analogs, including HMBR (green), HBR-3,5-DM (yellow) and HBR-3,5-DOM (red).

These synthetic fluorogens can be functionalized, providing a large diversity of biophysical properties. Substitution of the electron-donating phenol ring notably yielded the spectrally separated HMBR, HBR-3,5-DM and HBR-3,5-DOM (λ_{em} = 540 nm, 560 nm and 600 nm respectively), offering the possibility for multiplexed imaging.[45] Push-pull compounds with extended electron conjugation, as well as GFP-like chromophores derivatives, allowed to further red-shift emission wavelengths of the FAST:fluorogen complexes.[46–48] Moreover, impermeant fluorogens were obtained by conjugating a carboxymethyl group to the rhodanine heterocycle, and enabled to study protein trafficking in both mammalian and bacterial cells.[49–51] Furthermore, stochastic labelling of FAST provided by controlled fluorogen concentration, together with intrinsically fast binding off-rates, made the tag suitable for single molecule localization microscopy[52] and live cell imaging with sub - 100 nm resolution.[53]

In addition to its rapid folding and wide modularity, FAST displays several advantages in regard of imaging application. In fact, fluorogen binding provides instantaneous fluorescence enhancement upon labelling, that is consequently independent from the presence of oxygen and does not require any maturation time. In addition to protein labelling in various cellular localizations and *in vivo* imaging (notably in zebrafish), these advantageous properties have extended the frontiers of fluorescence imaging in multiple contexts. Taking advantage of its functionality in oxygen-restricted environments, FAST was for example used as a reporter to study strictly anaerobic *Clostridium* organisms, either individually or in an orthogonal manner with SNAP-tag and Halotag-expressing species.[54,55] This property has been used for bacterial and yeast screening for metabolic engineering[56,57], and allowed to circumvent heterogeneous oxygen distribution in adherent bacterial populations to study *E. Coli* multispecies biofilm formation.[58,59]

I.2.2. FAST mutational and topological variants

The initial engineering of FAST was then followed by several developments of FAST variants, expanding the spectral properties and imaging possibilities offered by this hybrid reporter (Figure I-3).

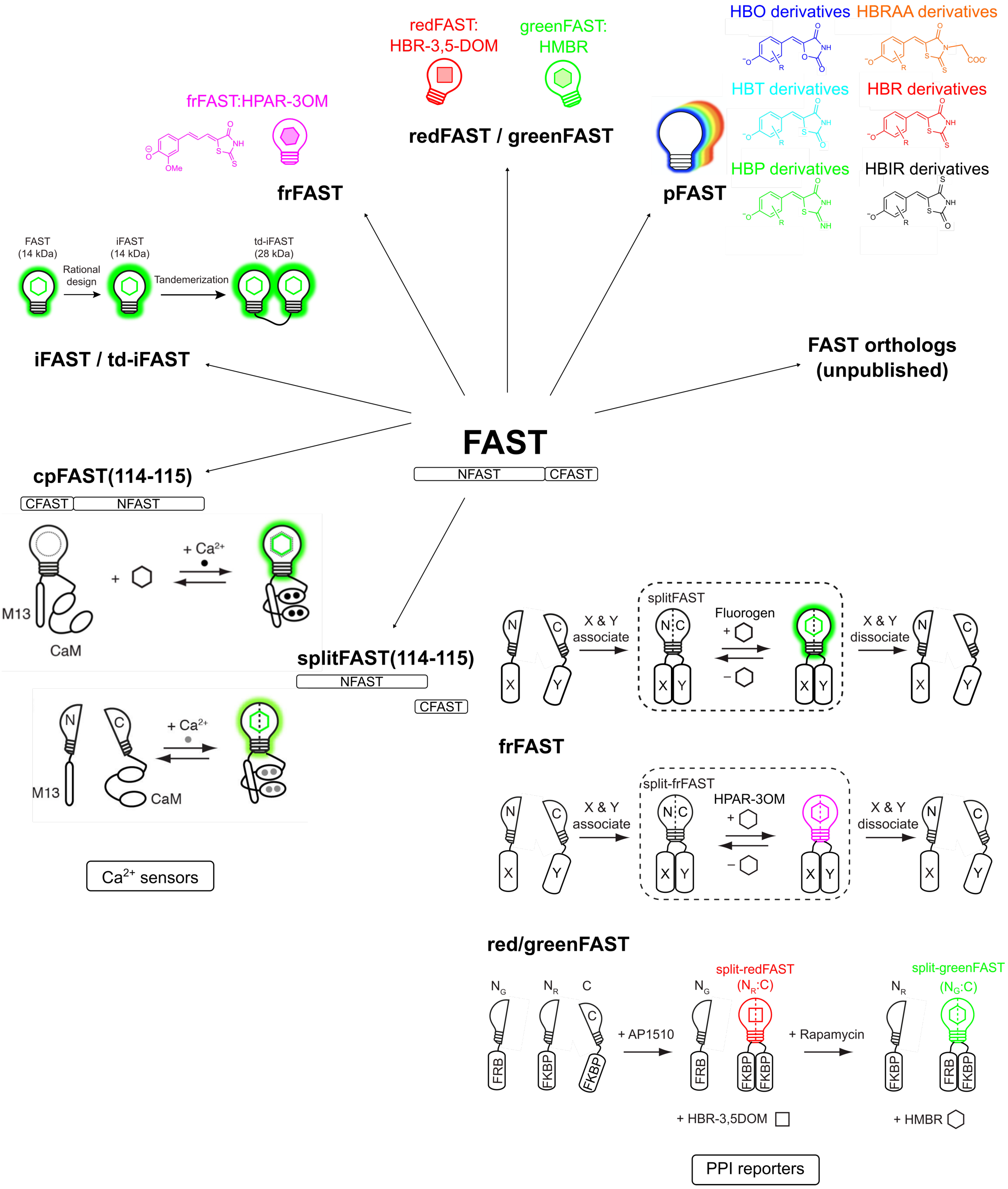

Figure I-3. FAST mutational and topological variants.

Improved brightness was notably achieved with improved FAST (iFAST) by the introduction of the single mutation V107I, and homodimerization of both variants resulted in the tandems td-FAST and td-iFAST, showing 2.8- and 3.8-fold higher brightness than FAST, respectively (Figure I-3).[60] In 2020, combination of molecular engineering, rational design and directed evolution then yielded far-red FAST (frFAST), reaching a red-shifted emission peak at λ_{em} = 670nm.[61] Such absorption/emission properties allowed multicolour imaging in multicellular organisms, in particular internal organs of zebrafish larvae as well as chicken embryos. The orthogonal system comprising greenFAST and redFAST, selectively binding the green fluorogen HMBR and the red fluorogen HBR-3,5-DOM respectively, was described the same year.[62] Live cells co-expressing fusions to the cell cycle regulators Cdt1 and geminin to redFAST and greenFAST, respectively, notably allowed imaging of a FAST-based fluorescence ubiquitination cell cycle indicator (FUCCI) by two-color fluorescence microscopy.

Finally, the most recent efforts in FAST engineering by directed evolution and rational design allowed the identification of the promiscuous tag pFAST, that binds a wide range of fluorogens covering the entire visible spectrum, with improved brightness and affinity.[27] Due to its versatile nature, this chemogenetic tag was suitable for a multitude of imaging protocols in live and fixed mammalian cells, cultured neurons, as well as multicellular organisms. Moreover, pFAST labelling of actin and microtubules in cultured neurons could be notably imaged with impressive resolution by 3D-STED nanoscopy, opening very promising perspectives for super-resolution microscopy applications. Relying on the observation that FAST binding and optical properties can be substantially altered by sequence variability, several ortholog versions of FAST were generated and characterized (Rakotoarison & Tebo et al., manuscript in preparation). To this end, the loop 94-101 was replaced by the mutated fluorogen binding sequence WMIPTSRG in six different PYP orthologs from protobacterial strains, all showing 70-78% sequence homology with the initial prototype from *Halorhodospira halophila* (Hha). Interestingly, all six FAST orthologs are capable of binding the fluorogens HMBR, HBR-3,5-DM and HBR-3,5-DOM with similar or improved brightness and affinity compared to ^{Hha}FAST, and are thus suitable candidates for the design of FAST-related hybrid probes for imaging and biosensing applications.

In the aim of designing a reporter domain for biosensing tools, topological variants of FAST were also engineered. As described in further details in chapter II, a circularly permuted version of FAST was developed by connecting its native termini and creating new ones at position 114-115. Coupling cpFAST(114-115) to the Ca^{2+}-sensitive protein pair calmodulin/M13 notably allowed the generation of an intramolecular Ca^{2+} sensor.[63] Splitting FAST at the same position then allowed the generation of splitFAST(114-115), composed of a large NFAST fragment and a small 11-residues peptide CFAST fragment. Subsequent characterization and optimization of splitFAST as a PPI reporter yielded an intermolecular version of this Ca^{2+} indicator, by fusion of M13 to the NFAST(1-114) fragment, and fusion of calmodulin to CFAST(115-124) (CFAST10).[64] A variety of cellular processes could be visualized as well with splitFAST, and it was demonstrated that splitting other FAST variants resulted in functional PPI reporters. The rapamycin-induced interaction between FKBP and FRB was notably visualized by fusion to either frFAST fragments, yielding a 7-fold fluorescence increase upon complementation, that also proved to be reversible.[61] Interestingly, this splitting strategy could also be applied to the orthogonal system constituted by greenFAST and redFAST. The mutations conferring selectivity to both variants being located in the NFAST fragment, the two split systems shared a common CFAST fragment. This unique property thus allowed the visualization of two consecutive PPIs sharing a common interaction partner, in two-colour confocal microscopy.[62] These diverse applications showed the versatility of the chemogenetic system FAST and the diverse biosensing possibilities offered by such a reporter in the context of biosensors design.

I.3. Aim of the thesis

Encouraged by the demonstrated utility of FAST as a fluorescent chemogenetic reporter in various contexts, and the imaging opportunities envisioned from its unique properties, my PhD project aimed at generalizing and optimizing the use of FAST and its variants for biosensing applications.

The design of an intramolecular FAST-based Ca^{2+} biosensor, coupling cpFAST(114-115) to calmodulin/M13 pair, showed that fluorogen binding to the reporter domain, thus fluorescent signal, can be conditioned by the binding state of the sensing unit. We suggested that this principle could be applied to generalize the design of biosensors from any given recognition domain, given that the latter undergoes a sufficient conformational change upon analyte binding. This hypothesis relies on the suggested allosteric coupling between our chemogenetic fluorescent reporter and an analyte-sensing protein domain. In fact, a fluorogenic biosensor able to bind both a fluorogen and an analyte of interest is involved in the equilibrium described in Figure I-4.

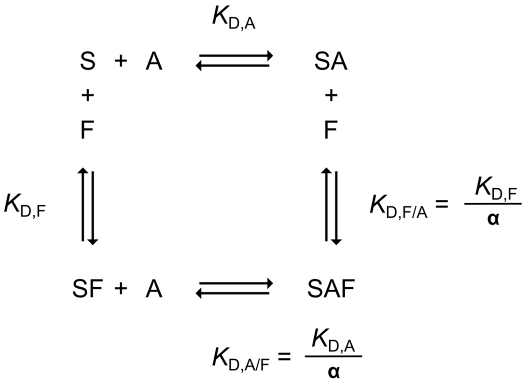

S: sensor, A: analyte, F: fluorogen

α : cooperativity constant:

- **α** = 0 : mutually exclusive binding of A and F
- **α** = 1 : independent binding of A and F
- **α** > 1 : cooperative binding of A and F
- **α** < 1 : anticooperative binding of A and F

$$K_{D,A} = \frac{[S][A]}{[SA]} \quad K_{D,F} = \frac{[S][F]}{[SF]} \quad K_{D,A/F} = \frac{[SF][A]}{[SFA]} \quad K_{D,F/A} = \frac{[SA][F]}{[SFA]}$$

Figure I-4. General scheme describing the binding of two different ligands to two binding sites. Adapted from Velazquez-Campoy[66]

Allostery can be defined as the phenomenon by which the binding of a ligand influences, favorably or unfavorably, the binding of another ligand. First described in oligomeric and symmetric proteins, allosteric proteins can be monomeric proteins in which two binding sites (that can be far apart) are coupled by a macromolecular conformational change induced by the binding of either ligand and having an effect on the binding of the other ligand. Incorporation of a sensing protein domain undergoing a conformational change upon analyte binding into a fluorogen-activating protein such as FAST can thus create analyte-responsive fluorogenic sensors by allostery. In such allosteric sensors, the binding of the analyte can either raise or lower the binding affinity of the fluorogen, leading to positive or negative allosteric modulation of fluorescence. The cooperativity constant $\alpha = K_{D,F} / K_{D,F/A}$ (where $K_{D,F}$ is the binding affinity constant of the fluorogen F in absence of the analyte A, and $K_{D,F/A}$ is the binding affinity constant of the fluorogen F when the analyte A is already bound to the sensor) enables to know if the cooperativity is positive ($\alpha > 1$), or negative ($\alpha < 1$). The case $\alpha = 1$ indicates that the fluorogen and the analyte bind the sensor independently. In allosteric sensors, as the influence between the two ligands is reciprocal, the binding of the fluorogen modifies the binding affinity of the analyte. The binding affinity of the analyte is thus characterized by an apparent dissociation constant $K_{D,app}$ that depends on the fluorogen concentration.

We thus hypothesized that engineering of biosensors based on FAST would allow the visualization and quantification of different types of analytes, such as the metal cation K^+ (chapter IV), or highly biologically relevant small molecules such as glutamate (chapter III) and adenosine-5'-triphosphate (ATP) (chapter V). Relying on previously characterized recognition domains, we aimed at focusing on protein engineering in order to optimize allosteric coupling with the reporter unit, thus generating biosensors with high dynamic range.

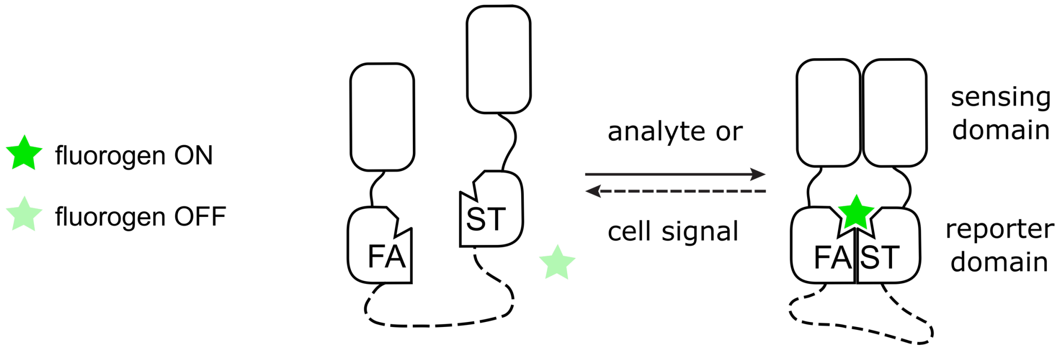

Figure I-5. Principle of FAST-based biosensors. FAST or a FAST variant is coupled to a sensing domain, such as signal detection conditions fluorogen binding to the reporter, thus fluorescence.

In order to expand the chemogenetic reporter toolbox based on FAST, a second objective consisted in exploring its topological variants (chapter VI). Indeed, the identification of a new position for circular permutation and splitting of FAST was considered as a step towards multiplexed imaging with diverse chemogenetic reporters. Screening of various topological variants of FAST was expected to provide new reporter modules suitable for the design of biosensors, either intra- or intermolecular, able to detect and quantify metabolites, follow cellular processes or study protein-protein interactions. Taking advantage of the wide palette of properties offered by the different FAST variants, we expected to develop and optimize reporter units with complementary optical and thermodynamic properties. This objective falls within the scope of recent and growing developments of hybrid biosensing tools, greatly benefitting from the optimization of chemogenetic reporters and taking advantage of their unique features to push the boundaries of fluorescent biosensing.

I.4. References

1. Rood, B. J. E. & Regev, A. The legacy of the Human Genome Project. **373**, 1442–1444 (2021).
2. Jinek, M. *et al.* A Programmable Dual-RNA – Guided. **337**, 816–822 (2012).
3. Bulaklak, K. & Gersbach, C. A. The once and future gene therapy. *Nat. Commun.* **11**, 11–14 (2020).
4. Servick, K. & Hauck, S. mRNA's next challenge: Will it work as a drug? **370**, 1388–1390 (2020).
5. Markram, H. The blue brain project. *Proc. 2006 ACM/IEEE Conf. Supercomput. SC'06* **7**, 153–160 (2006).
6. Kherlopian, A. R. *et al.* A review of imaging techniques for systems biology. *BMC Syst. Biol.* **2**, 1–18 (2008).
7. Rodriguez, E. A. *et al.* The Growing and Glowing Toolbox of Fluorescent and Photoactive Proteins. *Trends Biochem. Sci.* **42**, 111–129 (2017).
8. Livet, J. *et al.* Transgenic strategies for combinatorial expression of fluorescent proteins in the nervous system. *Nature* **450**, 56–62 (2007).
9. Abdeladim, L. *et al.* Multicolor multiscale brain imaging with chromatic multiphoton serial microscopy. *Nat. Commun.* **10**, 1–14 (2019).
10. Denk, W., Strickler, J. & Webb, W. Two-photon laser scanning fluorescence microscopy. *Science* **248**, 73–76 (1990).
11. Svoboda, K. & Yasuda, R. Principles of Two-Photon Excitation Microscopy and Its Applications to Neuroscience. *Neuron* **50**, 823–839 (2006).
12. Hell, S. W. & Wichmann, J. Breaking the diffraction resolution limit by stimulated emission: stimulated-emission-depletion fluorescence microscopy. *Opt. Lett.* **19**, 780 (1994).
13. Klar, T. A., Jakobs, S., Dyba, M., Egner, A. & Hell, S. W. Fluorescence microscopy with diffraction resolution barrier broken by stimulated emission. *Proc. Natl. Acad. Sci. U. S. A.* **97**, 8206–8210 (2000).
14. Rust, M. J., Bates, M. & Zhuang, X. Sub-diffraction-limit imaging by stochastic optical reconstruction microscopy (STORM). *Nat. Methods* **3**, 793–795 (2006).
15. Betzig, E. *et al.* Imaging intracellular fluorescent proteins at nanometer resolution. *Science* **313**, 1642–1645 (2006).
16. Eilers, Y., Ta, H., Gwosch, K. C., Balzarotti, F. & Hell, S. W. MINFLUX monitors rapid molecular jumps with superior spatiotemporal resolution. *Proc. Natl. Acad. Sci. U. S. A.* **115**, 6117–6122 (2018).
17. Jradi, F. M. & Lavis, L. D. Chemistry of Photosensitive Fluorophores for Single-Molecule Localization Microscopy. *ACS Chem. Biol.* **14**, 1077–1090 (2019).
18. Bléger, D. & Hecht, S. Visible-Light-Activated Molecular Switches. *Angew. Chem. Int. Ed.* **54**, 11338–11349 (2015).
19. Frei, M. S. *et al.* Photoactivation of silicon rhodamines via a light-induced protonation. *Nat. Commun.* **10**, (2019).
20. Tachibana, R. *et al.* Design of spontaneously blinking fluorophores for live-cell super-resolution imaging based on quantum-chemical calculations. *Chem. Commun.* **56**, 13173–13176 (2020).
21. Zheng, Q. *et al.* Rational Design of Fluorogenic and Spontaneously Blinking Labels for Super-Resolution Imaging. *ACS Cent. Sci.* **5**, 1602–1613 (2019).
22. Halabi, E. A., Pinotsi, D. & Rivera-Fuentes, P. Photoregulated fluxional fluorophores for live-cell super-resolution microscopy with no apparent photobleaching. *Nat. Commun.* **10**, 1–10 (2019).
23. Leopold, A. V., Shcherbakova, D. M. & Verkhusha, V. V. Fluorescent Biosensors for Neurotransmission and Neuromodulation: Engineering and Applications. *Front. Cell. Neurosci.* **13**, (2019).
24. Pal, A. & Tian, L. Imaging voltage and brain chemistry with genetically encoded sensors

and modulators. *Curr. Opin. Chem. Biol.* **57**, 166–176 (2020).

25. Moeyaert, B. & Dedecker, P. Genetically encoded biosensors based on innovative scaffolds. *Int. J. Biochem. Cell Biol.* **125**, (2020).
26. Mo, G. C. H. *et al.* Genetically encoded biosensors for visualizing live-cell biochemical activity at super-resolution. *Nat. Methods* **14**, 427–434 (2017).
27. Benaissa, H. *et al.* An engineered multifunctional protein tag for advanced fluorescence imaging. *bioRxiv* 2021.01.29.428635 (2021).
28. Gautier, A. & Tebo, A. G. Fluorogenic Protein-Based Strategies for Detection, Actuation, and Sensing. *BioEssays* **40**, 1800118 (2018).
29. Thiel, Z., Nguyen, J. & Rivera-Fuentes, P. Genetically Encoded Activators of Small Molecules for Imaging and Drug Delivery. *Angew. Chem. Int. Ed.* **59**, 7669–7677 (2020).
30. Grimm, J. B. *et al.* A general method to optimize and functionalize red-shifted rhodamine dyes. *Nat. Methods* **17**, 815–821 (2020).
31. Wang, L. *et al.* A general strategy to develop cell permeable and fluorogenic probes for multicolour nanoscopy. *Nat. Chem.* **12**, 165–172 (2020).
32. Bachollet, S. P. J. T., Addi, C., Pietrancosta, N., Mallet, J. M. & Dumat, B. Fluorogenic Protein Probes with Red and Near-Infrared Emission for Genetically Targeted Imaging. *Chem. Eur. J.* **26**, 14467–14473 (2020).
33. Kwon, J. *et al.* Bright ligand-activatable fluorescent protein for high-quality multicolor live-cell super-resolution microscopy. *Nat. Commun.* **11**, 1–11 (2020).
34. Gao, J., Hori, Y., Takeuchi, O. & Kikuchi, K. Live-Cell Imaging of Protein Degradation Utilizing Designed Protein-Tag Mutant and Fluorescent Probe with Turn-Off Switch. *Bioconjug. Chem.* **31**, 577–583 (2020).
35. Strakova, K. *et al.* Haloflippers: A general tool for the fluorescence imaging of precisely localized membrane tension changes in living cells. *ACS Cent. Sci.* **6**, 1376–1385 (2020).
36. Poc, P. *et al.* Interrogating surface: Versus intracellular transmembrane receptor populations using cell-impermeable SNAP-tag substrates. *Chem. Sci.* **11**, 7871–7883 (2020).
37. Wang, L., Hiblot, J., Popp, C., Xue, L. & Johnsson, K. Environmentally Sensitive Color-Shifting Fluorophores for Bioimaging. *Angew. Chem. Int. Ed.* **59**, 21880–21884 (2020).
38. Griss, R. *et al.* Bioluminescent sensor proteins for point-of-care therapeutic drug monitoring. *Nat. Chem. Biol.* **10**, 598–603 (2014).
39. Yu, Q. *et al.* Semisynthetic sensor proteins enable metabolic assays at the point of care. *Science* **361**, 1122–1126 (2018).
40. Yu, Q. *et al.* A biosensor for measuring NAD+ levels at the point of care. *Nat. Metab.* **1**, 1219–1225 (2019).
41. Ackerman, D. S., Vasilev, K. V., Schmidt, B. F., Cohen, L. B. & Jarvik, J. W. Tethered Fluorogen Assay to Visualize Membrane Apposition in Living Cells. *Bioconjug. Chem.* **28**, 1356–1362 (2017).
42. Carpenter, M. A. *et al.* Protein Proximity Observed Using Fluorogen Activating Protein and Dye Activated by Proximal Anchoring (FAP-DAPA) System. *ACS Chem. Biol.* **15**, 2433–2443 (2020).
43. Klima, J. C. *et al.* Incorporation of sensing modalities into de novo designed fluorescence-activating proteins. *Nat. Commun.* **12**, 1–19 (2021).
44. Plamont, M.-A. *et al.* Small fluorescence-activating and absorption-shifting tag for tunable protein imaging in vivo. *Proc. Natl. Acad. Sci.* **113**, 497–502 (2016).
45. Li, C. *et al.* Dynamic multicolor protein labeling in living cells. *Chem. Sci.* **8**, 5598–5605 (2017).
46. Li, C. *et al.* Design and characterization of red fluorogenic push-pull chromophores holding great potential for bioimaging and biosensing. *Org. Biomol. Chem.* **14**, 9253–9261 (2016).
47. Povarova, N. V. *et al.* Red-Shifted Substrates for FAST Fluorogen-Activating Protein Based on the GFP-Like Chromophores. *Chem. Eur. J.* **25**, 9592–9596 (2019).
48. Myasnyanko, I. N. *et al.* Color Tuning of Fluorogens for FAST Fluorogen-Activating

Protein. *Chem. Eur. J.* **27**, 3986–3990 (2021).

49. Li, C. *et al.* Fluorogenic Probing of Membrane Protein Trafficking. *Bioconjug. Chem.* **29**, 1823–1828 (2018).
50. Peron-Cane, C. *et al.* Fluorescent secreted bacterial effectors reveal active intravacuolar proliferation of Listeria monocytogenes in epithelial cells. *PLoS Pathog.* **16**, 1–29 (2020).
51. Chekli, Y. *et al.* Visualizing the dynamics of exported bacterial proteins with the chemogenetic fluorescent reporter FAST. *Sci. Rep.* **10**, 1–14 (2020).
52. Smith, E. M., Gautier, A. & Puchner, E. M. Single-Molecule Localization Microscopy with the Fluorescence-Activating and Absorption-Shifting Tag (FAST) System. *ACS Chem. Biol.* **14**, 1115–1120 (2019).
53. Venkatachalapathy, M., Belapurkar, V., Jose, M., Gautier, A. & Nair, D. Live cell super resolution imaging by radial fluctuations using fluorogen binding tags. *Nanoscale* **11**, 3626–3632 (2019).
54. Streett, H. E., Kalis, K. M. & Papoutsakis, E. T. A Strongly Fluorescing Anaerobic Reporter and Protein-Tagging System for Clostridium Organisms Based on the Fluorescence-Activating and Absorption-Shifting Tag Protein (FAST). *Appl. Environ. Microbiol.* **85**, e00622-19 (2019).
55. Charubin, K., Streett, H. & Papoutsakis, E. T. Development of Strong Anaerobic Fluorescent Reporters for Clostridium acetobutylicum and Clrostridium ljungdahlii Using HaloTag and SNAP-tag Proteins. *Appl. Environ. Microbiol.* **86**, 1–19 (2020).
56. Flaiz, M., Ludwig, G., Bengelsdorf, F. R. & Dürre, P. Production of the biocommodities butanol and acetone from methanol with fluorescent FAST-tagged proteins using metabolically engineered strains of Eubacterium limosum. *Biotechnol. Biofuels* **14**, 1–20 (2021).
57. Lu, Z., Peng, B., Ebert, B. E., Dumsday, G. & Vickers, C. E. Auxin-mediated protein depletion for metabolic engineering in terpene-producing yeast. *Nat. Commun.* **12**, (2021).
58. Monmeyran, A. *et al.* The inducible chemical-genetic fluorescent marker FAST outperforms classical fluorescent proteins in the quantitative reporting of bacterial biofilm dynamics. *Sci. Rep.* **8**, 10336 (2018).
59. Monmeyran, A. *et al.* Four species of bacteria deterministically assemble to form a stable biofilm in a millifluidic channel. *npj Biofilms Microbiomes* **7**, (2021).
60. Tebo, A. G., Pimenta, F. M., Zhang, Y. & Gautier, A. Improved Chemical-Genetic Fluorescent Markers for Live Cell Microscopy. *Biochemistry* **57**, 5648–5653 (2018).
61. Li, C. *et al.* A Far-Red Emitting Fluorescent Chemogenetic Reporter for In Vivo Molecular Imaging. *Angew. Chem. Int. Ed.* **59**, 17917–17923 (2020).
62. Tebo, A. G. *et al.* Orthogonal fluorescent chemogenetic reporters for multicolor imaging. *Nat. Chem. Biol.* **17**, 30–38 (2021).
63. Tebo, A. G. *et al.* Circularly Permuted Fluorogenic Proteins for the Design of Modular Biosensors. *ACS Chem. Biol.* **13**, 2392–2397 (2018).
64. Tebo, A. G. & Gautier, A. A split fluorescent reporter with rapid and reversible complementation. *Nat. Commun.* **10**, 2822 (2019).
65. Valeur, B. & Berberan-Santos, M. N. Molecular Fluorescence: Principles and Applications, 2nd Edition - Wiley. (2012).
66. Velazquez-Campoy, A., Goñi, G., Peregrina, J. R. & Medina, M. Exact analysis of heterotropic interactions in proteins: Characterization of cooperative ligand binding by isothermal titration calorimetry. *Biophys. J.* **91**, 1887–1904 (2006).

Chapter II

Fluorogenic chemogenetic biosensors

This section is based on the following article:

Illuminating Cellular Biochemistry: Fluorogenic Chemogenetic Biosensors for Biological Imaging

ChemPlusChem 85, 1487-1497 (2020)

Fanny Broch and Arnaud Gautier

II.1. Abstract

Cellular activity is defined by the precise spatiotemporal regulation of various components, such as ions, small molecules, or proteins. Studying cell physiology consequently requires the optical recording of these processes, notably by using fluorescent biosensors. The recent development of various fluorogenic systems greatly expanded the palette of reporters to be included in these sensors design. Fluorogenic reporters consist of a protein or RNA tag that can complex either an endogenous or a synthetic fluorogenic dye (so-called fluorogen). The intrinsic nature of these tags, along with the high tunability of their cognate chromophore provide interesting features such as far-red to near-infrared emission, oxygen independence, or unprecedented color versatility. These engineered photoreceptors, self-labelling proteins, or noncovalent aptamers and protein tags were rapidly identified as promising reporters to observe biological events. This Minireview focuses on the new perspectives they offer to design unique and innovative biosensors, thus pushing the boundaries of cellular imaging.

II.2. Introduction

The pioneering discovery of the green fluorescent protein (GFP) and its development into a fluorescent reporter has been a landmark for the investigation of cellular structure and physiology.[1] The subsequent use of genetically encoded probes and their improvements have tremendously widened our understanding of living matter over the last two decades.[2] These fluorescent markers represent powerful and reliable tools for imaging proteins of interest, cellular components or even structures as complex as the neuronal circuits in a brain.[3]

Deciphering complex cellular processes requires synthetic or genetically encoded biosensors able to detect small metabolites, enzyme activity or specific recognition events. Genetically encoded biosensors are commonly designed by coupling a fluorescent reporter together with a sensing unit (e. g. environment-sensitive domain, analyte-binding domain or enzyme substrate domain) that undergoes a conformational change upon input signal. They can generally be categorized in two classes: intensiometric and ratiometric biosensors. Intensiometric sensors consist in a single fluorescent reporter with fluorescence emission properties sensitive to the conformational or environmental change undergone by its coupled sensing unit. Ratiometric biosensors on the other hand consist in a sensing unit conjugated with two fluorophores that form a Förster Resonance Energy Transfer (FRET) pair: upon biological event, a change in the FRET efficiency is observed due to a change in the position and orientation of the two fluorophores.

Genetic encoding allows the targeting of GFP-based biosensors with absolute specificity in various cell types and subcellular localizations. Recent reviews show how the development of such biosensors greatly helped deciphering biological processes, by allowing the observation of various cellular signaling pathways with high spatial and temporal resolution.[4] The performance and reliability of these reporter systems allow their use not only in cells, but also in high-throughput metabolic screenings.[5]

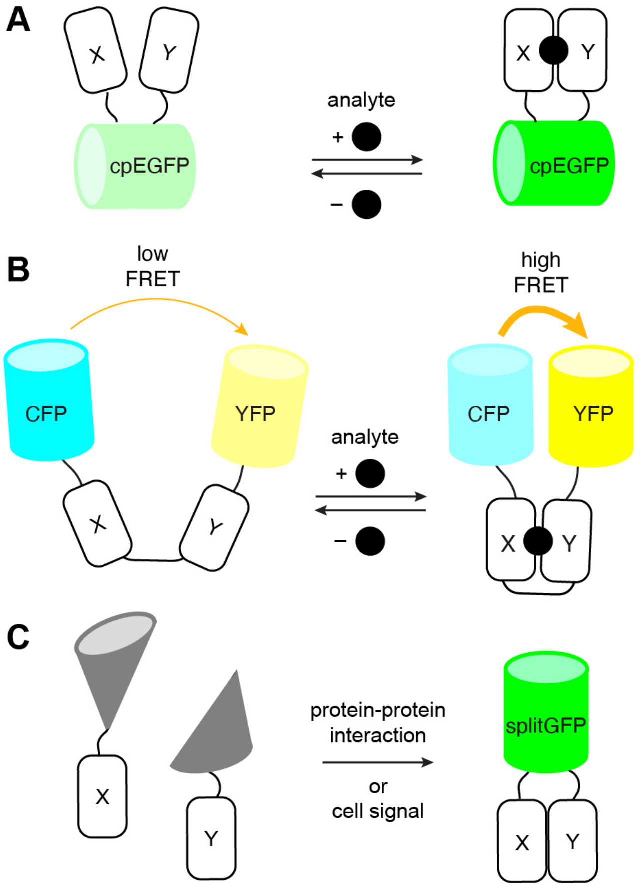

Figure II-1. Genetically encoded intensiometric and ratiometric biosensors. A) General design of intensiometric biosensor based on single fluorescent protein (cpEGFP: circularly permuted enhanced green fluorescent protein). **B)** General design of FRET-based biosensors (CFP: cyan fluorescent protein (FRET donor), YFP: yellow fluorescent protein (FRET acceptor)). **C)** Bimolecular fluorescence complementation (BIFC) assays for the detection of protein-protein interactions or cell signal.

The calcium ion sensor GCaMP nicely illustrates how genetically encoded intensiometric biosensors can be designed by coupling GFP-like fluorescent proteins with analyte recognition domains (Figure II-1A). GCaMP relies on the Ca^{2+}-dependent interaction between calmodulin (CaM) and the peptide M13, linked to each terminus of circularly permuted EGFP: brightness of the fluorescent protein is restored upon the calcium-induced interaction between CaM and M13.[6] Many improved calcium indicators followed, optimizing the sensitivity, reliability, color and brightness.[7,8] Fluorescent proteins have also been essential for the design of ratiometric biosensors, by insertion of a sensing domain between two fluorescent proteins, acting as FRET donor and acceptor. (Figure II-1B). This strategy was illustrated by the early development of Cameleons, a family of Ca^{2+} sensors also based on CaM/M13.[9] Similar designs notably allowed the visualization of kinase activity by inserting a substrate peptide sequence between the FRET pair.[10] Sensing of small molecules such as glutamate was also allowed by insertion of periplasmic binding proteins: these two-domains receptors were particularly useful in the development of the glutamate sensor GluSnFR and its improved versions for neurotransmission imaging.[11,12]

Finally, fluorescent proteins were also elegantly used to design reporters of protein-protein interactions (PPIs). Splitting fluorescent proteins in two complementary fragments allowed the design of bimolecular fluorescence complementation (BiFC) assays for the detection of PPI, relying on the reconstitution of a functional fluorescent reporter when the two fragments are brought in close proximity (Figure II-1C).[13] A subsequent tripartite split-GFP allowed to reach higher in vivo signal-to-noise ratio.[14]

These different systems are well characterized and commonly used to design reliable assays both in vitro and in vivo; yet they present certain limitations that arise from the use of GFP-like fluorescent proteins. The relatively large size of fluorescent proteins can drastically modify folding of the sensing domain, as well as its affinity for its cognate analyte, in a way that is hardly predictable. The observation of dynamic processes can also be impeded by the lag time between event occurrence and actual signal observation, due to the delay necessary for protein folding and chromophore maturation. The latter being dependent on the presence of oxygen, the use of these biosensors is also restricted to aerobic conditions. Finally, regarding split fluorescent proteins, despite their many applications and improvements (particularly in terms of solubility and decreased self-assembly) their reconstitution is irreversible: consequently, they cannot be used for the study of both association and dissociation of two interacting proteins.[15]

The frontiers of biosensing were further pushed with the initial developments of the self-labeling proteins SNAP-tag,[16] HaloTag,[17] and CLIP-tag,[18] which enable the selective anchoring of tunable synthetic probes. In addition to their essential role as labeling tools, chemogenetic sensors can be constructed in situ, taking advantage of the genetically encoded tag to target environment- or cation-sensitive probes with absolute specificity. This way Ca^{2+} transients,[19,20] dynamics of other biologically relevant cations,[21–23] as well as micro-viscosity,[24] could be precisely evaluated at different sub-cellular localizations. Combination of HaloTag with a voltage sensitive rhodopsin also yielded an electrochromic FRET voltage sensor for the imaging of action potentials in various organisms.[25] Moreover, the general design of Snifits,[26,27] where SNAP-tag is labelled with a bifunctional molecule containing both a FRET acceptor and an affinity ligand for the analyte-binding protein, was applied to the imaging of several neurotransmitters[28–30] (Figure II-2). This approach allowed the combination of SNAP-tag with various donors such as a fluorophore conjugated to the orthogonal HaloTag,[31] or even with a bioluminescent luciferase.[32]

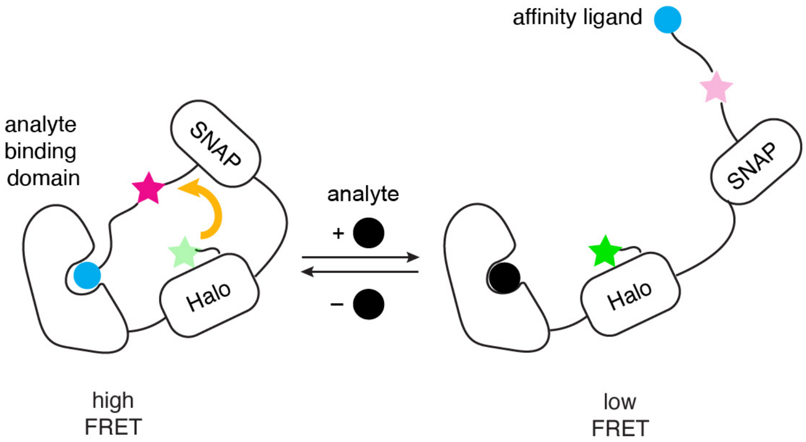

Figure II-2. Schematic illustration of the Snifit biosensors.

Recently, biosensor design has taken a new turn with the development of chemogenetic systems composed of proteins or RNA aptamers that bind and activate the fluorescence of fluorogenic dyes (so-called fluorogens), which are otherwise dark when free (Figures II-3 and II-4). These fluorescent hybrid reporters make use of natural or synthetic fluorogens, each having their own advantages. Natural fluorogens are endogenously present in cells and thus do not need to be delivered (if present at sufficient concentrations). Synthetic fluorogens, on the other hand, can be tuned and equipped with new properties by molecular engineering. Moreover, they need to be exogenously applied, offering new possibilities to create original labeling protocols. The underlying mechanisms, advantages and general applications of these fluorogen-activating systems have been thoroughly described in recent reviews.[33,34] Here we focus on the new opportunities these novel chemogenetic hybrid reporters offer for the design of innovative biosensors enabling to observe and study biological processes in new ways.

II.3. Chemogenetic optical reporters and biosensors based on natural fluorogens

Various chemogenetic optical reporters were designed from chromoproteins that incorporate natural fluorogenic chromophores such as flavin or bilins as prosthetic groups. These chromoproteins are often weakly fluorescent because they evolved to maximize the efficiency of their natural photocycle. Protein engineering allowed to enhance their fluorescence properties by impairing their natural photocycle.

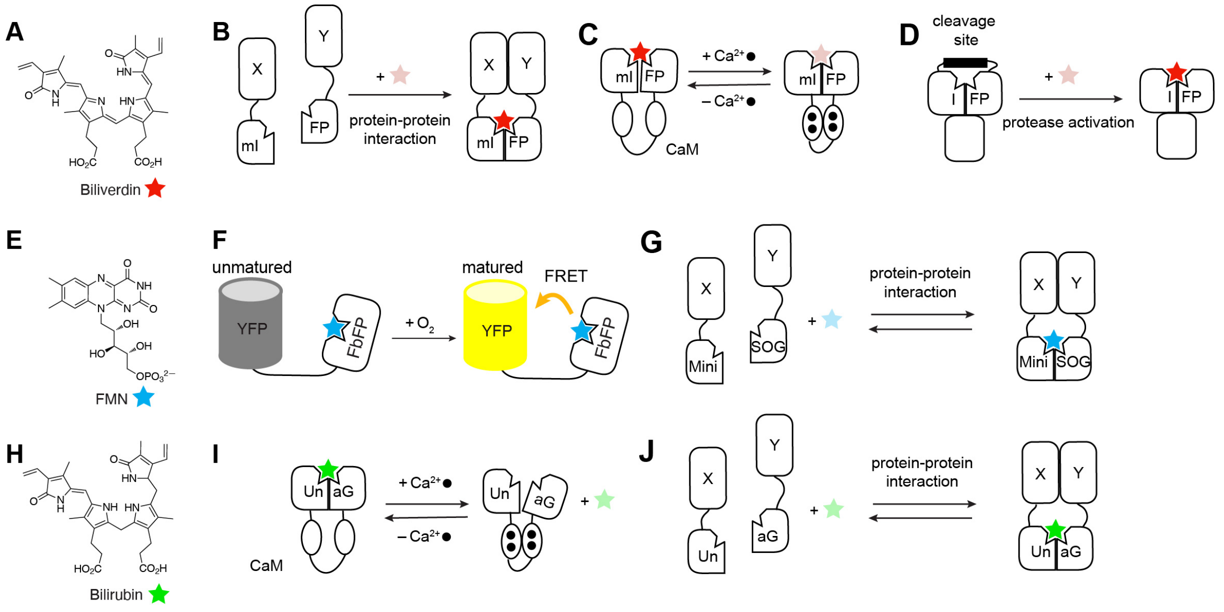

Figure II-3. Fluorescent chemogenetic biosensors based on natural fluorogens. (A) Chemical structure of the endogenous fluorogen biliverdin (BV). **(B)** iSplit: irreversible reconstitution of mIFP upon protein-protein interaction allows covalent BV binding, thus fluorescence activation. **(C)** NIR-GECO1: Conformational change of the calmodulin sensing module upon calcium binding yields fluorescence inactivation of the complexed BV. **(D)** iProtease: release of the biliverdin binding site after protease cleavage allows covalent binding of BV, thus fluorescence activation. **(E)** Chemical structure of the endogenous fluorogen flavin mono-nucleotide FMN. **(F)** FluBO: YFP chromophore maturation, thus FRET efficiency, depends on molecular oxygen levels. **(G)** Split miniSOG: reversible reconstitution assembly upon protein-protein interactions allows non-covalent binding of FMN, and thus fluorescence activation **(H)** Chemical structure of the endogenous fluorogen bilirubin (BR). **(I)** BReleaCa: conformational change of calmodulin upon Ca^{2+} binding reduces UnaG affinity for BR, thus fluorescence intensity. **(J)** uPPI: reversible reconstitution of UnaG upon protein-protein interaction allows non-covalent binding of BR, thus fluorescence activation.

II.3.1. Biliverdin-based optical reporters and biosensors

Far-red and near-infrared fluorescent optical reporters were engineered from bacterial phytochromes. These photoreceptors sense far-red light through photoisomerization of a covalently attached biliverdin (BV) chromophore (Figure II-3A) and function as light driven signal transducers. BV is an endogenous and ubiquitous molecule that is non-fluorescent when free but can fluoresce near-infrared light when immobilized. Near-infrared fluorescent markers are highly desirable for both imaging and biosensing applications. They enable to reduce phototoxicity from excitation light, to dramatically decrease auto-fluorescence from living samples, and to image in deeper tissues because of reduced scattering. Near-infrared fluorescence was however difficult to attain with GFP-like fluorescent proteins: one of the redder one, mNeptune, reaches an emission maximum at 650 nm. The first infrared optical reporter was designed by suppression of the PHY domain of the bacteriophytochrome of Deinococcus radiodurans, and introduction of key mutations in the immediate environment of BV in the remaining PAS-GAF domains to prevent BV photoisomerization and lock it into an emissive conformation.[35] The resulting mutant IFP1.4 displays excitation and emission maxima at 684 and 708 nm, respectively, and allowed imaging both in vitro and in living mice. Improved brightness and photostability were obtained with iRFP (ex/em 690/713 nm), a near-infrared variant similarly evolved from a different bacteriophytochrome (BphP) scaffold, that reached observable brightness level without exogenously applied biliverdin.[36]

These enhanced properties made iRFP a suitable candidate for in vivo studies of PPIs with BiFC. iRFP was split between its PAS and GAF domains, generating two fragments that could be then respectively fused to each interacting partner (Figure II-3B). This infrared split system (iSplit) formed a highly stable and irreversible complex, that enabled visualization of the FKBP-FRB interaction up to 36 hours after rapamycin injection in living mice.[37] The irreversibility of the complementation can allow the integration of transient or low abundant interactions in a cumulative manner, however it prevents imaging of dynamic processes involving dissociation of a protein-protein complex. A reversible split IFP was engineered shortly after, by testing fluorescence brightness and dissociation capacity of fragments from several IFP1.4 splitting sites. The interaction of PKA catalytic and regulatory subunits and their cAMP-induced dissociation could thus be observed in both mammalian cells and yeast.[38]

The above mentioned IFPs inherited a tendency to dimerize at high concentrations, as the BphPs they originate from are multimeric. This dimeric nature may hinder further development of infrared reporters, as it can interfere with the dynamics of the observed process. Consequently, a monomeric mIFP was engineered from a monomeric truncated BphP, only retaining the PAS-GAF domains.[39] A near-infrared Ca^{2+} indicator for optical imaging (NIR-

GECO1) was obtained by insertion of the calcium binding domain calmodulin into mIFP (Figure 3C).[40] The fluorescent properties and Ca^{2+}-dependent response of this biosensor were optimized by random mutagenesis and screening of the connection sites between the different domains. NIR-GECO1 showed an inverse response to Ca^{2+} transients, that could be slightly improved by addition of exogenous biliverdin in cultured neurons. This sensor was shown to be useful in multiplexed imaging experiments, up to four colors (three indicators, together with a FRET indicator and a single-FP sensor). Recently an analogous biosensor was engineered from the small monomeric GAF-FP, which was rationally designed and evolved to be the minimal size biliverdin-binding single domain.[41] Insertion in GAF-FP of the calcium-dependent pair CaM/M13 resulted in the near-infrared Ca^{2+} indicator GAF-CaMP2. Screening of different insertion sites, randomization of two amino-acids linkers at connecting sites, and further mutagenesis of the initial scaffold were necessary to adjust the affinity and the dynamic range of the final design. Contrary to its predecessor this indicator gives a positive response, nevertheless it needs to be fused to the superfolding sfGFP to be correctly expressed in mammalian cells, reaching 1.2-fold larger molecular size than NIR-GECO1. GAF-CaMP2 enabled ratiometric measurement of intracellular Ca^{2+} transients, and allowed their visualization in three different organelles when expressed with two other GFP-based calcium sensors.[42]

Infrared fluorogenic reporters were also used for the monitoring of cell apoptosis. Circular permutation of IFP, connecting the PAS and GAF domains with a motif recognized by a specific protease, displaced the catalytic cysteine away from the biliverdin complexation cavity, thus impeding fluorogen binding. iProtease design consequently relied on the reconstitution of functional IFP after protease cleavage, leading to an observable fluorescence increase (Figure II-3D). This strategy applied to a caspase reporter iCasper, successfully reported apoptosis in neurons, during morphogenesis of Drosophila embryo and during tumorigenesis.[43]

A brighter set of monomeric infrared reporters, miRFPs, were evolved from the PAS-GAF domains of the Rhodopseudomonas palustris Bacteriophytochrome protein RpBphP1, by random mutagenesis and selection of the brightest mutants in mammalian cells, in parallel with screening in bacteria.[44] This way three spectrally distinct miRFP variants were developed, and were then applied to various biosensors. A BiFC system based on their split version (miSplits) successfully reported two different PPIs in the same cell, and was also used as an RNA reporter when fused to two proteins interacting with RNA with high affinity. Interestingly, the smallest NIR FP to date (17 kDa) was recently derived from a biliverdin-binding cyanobacteriochrome (CBCR) scaffold.[45] miRFP670nano was successfully used as a FRET pair donor in fully NIR sensors for different kinases activities, that could be coupled in cell experiments with optogenetic tools. Furthermore, by fusion of distinct miRFPs to two different proteins subject to cell-cycle dependent degradation at opposite phases, a far-red version of the previously reported fluorescence ubiquitination-based cell cycle indicator (FUCCI)[46] was developed and applied for detection of proliferation status of cells in living mice.[44] Following the same strategy, a near-infrared FUCCI was also developed based on the small ultra-red FP (smURFP),[47] an IFP evolved from allophycocyanin α-subunit (Trichodesmium erythraeum) to form a bright covalent complex with biliverdin.

II.3.2. Flavin-based optical reporters and biosensors

One challenge that can remarkably be addressed by engineering fluorogenic systems is the visualization of biological processes under anaerobic conditions. Indeed, the strict oxygen-dependence of GFP-like proteins for their chromophore maturation restricts their use to aerobic environments. This limitation prompted the development of fluorescent reporters that could be applied both in the presence and absence of oxygen.

The light oxygen voltage (LOV) domain of bacterial photoreceptors were modified to generate cyan-green fluorescent reporters that non-covalently bind flavin mononucleotide (FMN) (Figure II-3E). Only retaining the photoactive LOV domain of the receptor, where the reactive cysteine was substituted by a nonreactive alanine, significantly improved the brightness of the complex formed with FMN. The biosynthesis of this natural chromophore does not require oxygen, and contrary to biliverdin-binding IFPs, FMN-binding fluorescent proteins (FbFPs) are not limited by chromophore endogenous supply.[48–50] An hypoxia FRET biosensor (fluorescent protein based biosensor for oxygen, FluBO) rapidly exploited this oxygen independence, by coupling a donor FbFP to the oxygen-sensitive yellow fluorescent protein (YFP) as acceptor.[51] This system offers a direct ratiometric readout of molecular oxygen levels. Indeed, hypoxic conditions prevent maturation of YFP chromophore and most of the fluorescent signal originates from the FbFP, while oxygen supply immediately increases fluorescence from YFP (Figure II-3F). Similarly, the dimeric flavoenzyme lipoamide dehydrogenase was fused to mCherry to obtain a FRET sensor for intracellular NAD^+/NADH ratio.[52] The flavoprotein reduction alters fluorescence from the bound cofactor flavin adenine dinucleotide, altering FRET efficiency, thus offering a ratiometric evaluation of the NAD^+/NADH redox state. This FRET biosensor design could in principle be generalized, although it remains restricted to the limited variety of sufficiently bright flavoenzymes in their oxidized form.

Interestingly, the FbFP variant iLOV[53] showed intrinsic affinity for Cu^{2+} with high specificity in regard of other metal ions. This property allowed the use of iLOV as a reliable Cu^{2+} biosensor: at physiological pH, its fluorescence is reversibly quenched up to 80% upon Cu^{2+} binding, supposedly from coordination of the metal ion to FMN-interacting residues in the binding site.[54]

Another metal cation, Mn^{3+}, could be probed by a flavoprotein mutant in which tyrosine analogues were incorporated.[55]

Interestingly, the role of the LOV cofactor FMN is not limited to fluorogenicity, but also includes photosensitizer properties by generation of reactive oxygen species (ROS) without the need for any exogenous cofactor. These ROS are short-lived and phototoxic, inducing irreversible damage on cellular components. The mini Singlet Oxygen Generator (miniSOG) takes advantage of these characteristics to localize single proteins of interest or cellular structures with high resolution by correlated light and electron microscopy (CLEM). Generation of singlet oxygen $^1O_2$ under blue-light illumination allowed the local polymerization of osmiophilic polymers that can be detected by electron microscopy.[56] Directed evolution yielded an improved miniSOG2 that allowed highly specific cell ablation of single neurons in the Drosophila larvae.[57] This photosensitizer function was also improved by site-directed mutagenesis, resulting in a singlet oxygen photosensitizing protein SOPP3,[58] and used as a genetically encoded antimicrobial agent that proved effective against Gram-positive and negative bacteria.[59] With the aim of using CLEM to study intracellular PPIs, a miniSOG variant with improved solubility was split at a viable circular permutation position (Figure II-3G).[60] This development led to two soluble protein fragments that could efficiently and reversibly reassemble, offering a way to study protein-protein interactions such as the neurotoxic assemblies of α-synuclein by CLEM.

II.3.3. Bilirubin-based optical reporters and biosensors

Hypoxia can also be probed by different sensors based on the UnaG reporter, a natural protein that fluoresces green light when complexing the endogenous bilirubin (Figure II-3H).[61] UnaG shows higher fluorescence quantum yield than FbFP, and was consequently a promising candidate to improve molecular oxygen probes under both aerobic and anaerobic conditions. One strategy consisted in genetically encoding destabilized UnaG with a promoter showing positive hypoxia-specific activity, inducing expression at low oxygen levels.[62] Destabilization allows an efficient protein turnover, resulting in decreasing fluorescence under oxygen supply. Targeted incorporation of cysteines forming a disulfide bridge also allowed to monitor cellular redox state and hypoxia with reduced/oxidized UnaG (roUnaG) in mammalian cells and in bacteria with addition of exogenous bilirubin.[63]

UnaG was elegantly used to design biosensors by conditioning bilirubin unbinding to the recognition of a given analyte. A Ca^{2+}-sensor based on UnaG, BReleaCa,[64] was developed by inserting the Ca^{2+}-binding protein CaM close to the bilirubin binding site (Figure II-3I). The resulting sensor gives an on-off response to Ca^{2+} increase, due to a significantly reduced affinity of UnaG for bilirubin in the Ca^{2+}-bound state of the hybrid protein.

UnaG could also be turned into a split reporter for the visualization of PPI in cells. The well-known rapamycin induced FKBP-FRB interaction was probed as a proof-of-concept using a UnaG-based PPI reporter (uPPI) consisting in a UnaG that was split at a loop site (Figure II-3J).[65] The two co-expressed fragments showed low intrinsic affinity, offering a reliable and reversible signal with low background fluorescence and reduced response time compared to GFP-based PPI reporters. This example demonstrates that it is possible to obtain biosensors with faster dynamics using fluorogen-binding reporters rather than fluorescent proteins, assuming that complexation of a pre-formed fluorophore is more efficient than chromophore maturation.

II.4. Chemogenetic optical reporters and biosensors based on synthetic fluorogens

The recent development of chemogenetic optical reporters based on synthetic fluorogens opened new prospects for the design of optical biosensors. The use of synthetic fluorogens rather than natural ones allows the generation of fluorogenicity through various activation mechanisms, and the tuning of fluorogen properties by molecular engineering.

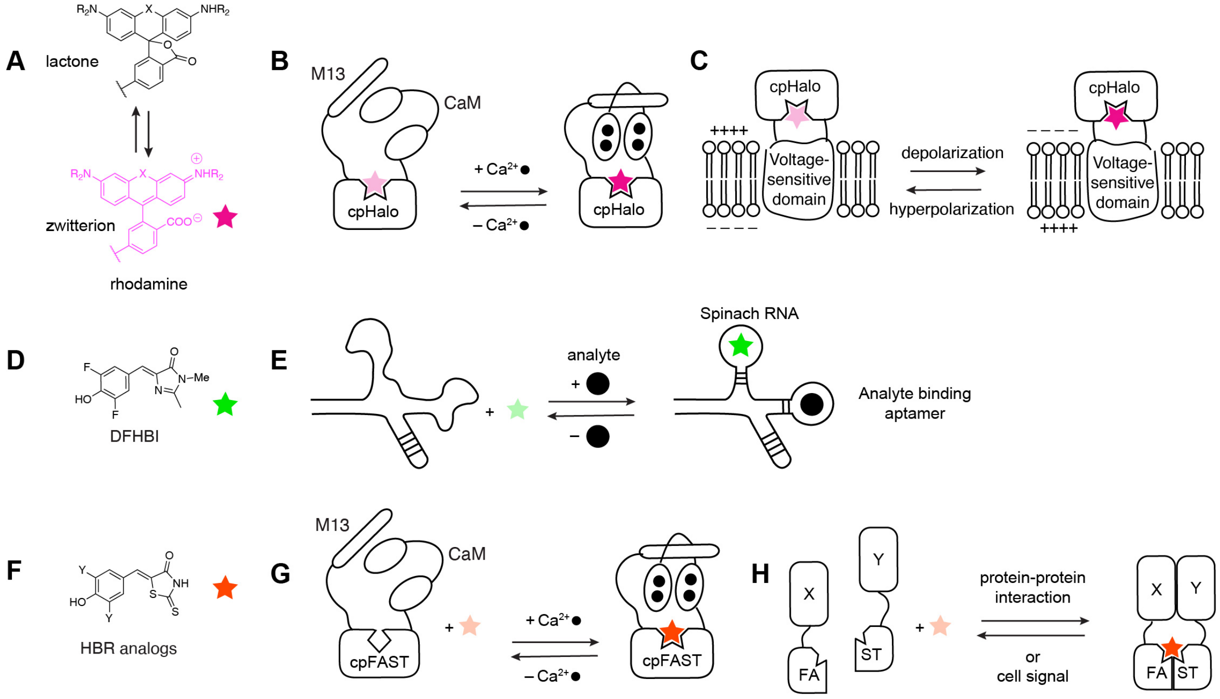

Figure II-4. Fluorescent chemogenetic biosensors based on synthetic fluorogens. (A) Chemical structure of synthetic fluorogenic rhodamines. **(B)** HaloCaMP: upon Ca^{2+} binding, conformational change of the sensing module CaM/M13 yields fluorescence activation of the rhodamine dye covalently linked to a circularly permuted (cp) HaloTag. **(C)** HArcLight: conformational change of a voltage-sensitive domain yields fluorescence activation of the rhodamine dye covalently linked to a circularly permuted HaloTag. **(D)** Chemical structure of the synthetic fluorogen 3,5-difluoro-4-hydroxybenzylidene imidazolinone (DFHBI). **(E)** RNA aptamers: Conformational change of the sensing module upon analyte complexation allows non-covalent binding of DFHBI, thus fluorescence activation. **(F)** Chemical structure of the synthetic fluorogenic HBR analogs. **(G)** FAST-based Ca^{2+} sensor: conformational change of the sensing module CaM/M13 increases affinity for the HBR analog, thus fluorescence intensity. **(H)** split FAST: reversible reconstitution of FAST upon assembly of the sensing module allows non-covalent binding of the HBR analog, thus fluorescence activation.

II.4.1. Covalent fluorogenic labelling

Recent efforts have been undertaken for the development of fluorogenic chromophores able to covalently and orthogonally label the previously mentioned protein tags SNAP-tag,[16] HaloTag[17] and CLIP-tag.[18] Silicon-rhodamine (SiR) derivatives for instance are found in their dark spirolactone form in solution, but in their bright zwitterionic form when bound to a protein tag (Figure II-4A).[66] Highly cell-permeable fluorogenic analogs were newly obtained by replacing the carboxyl group by an electron-poor amide group, in equilibrium with its spirolactam form.[67] Similarly, fluorogenic Janelia Fluor (JF) dyes derived from carbofluorescein and carborhodamine were developed and applied to super-resolution microscopy, as well as single-particle tracking experiments.[68–70] These strategies avoid conjugation of the fluorophore with an intramolecular quencher to create fluorogenecity, and different functionalization allowed the development of cyan to near-infrared fluorogens for multicolor imaging.[71] The cationic aromatic fluorophores “channel dyes” also show large fluorescence increase upon binding to HaloTag, due to cation-π interaction with a tryptophan benzene ring.[72,73]

Self-labeling proteins can be elegantly engineered to obtain fluorogenic hybrid indicators. A destabilized variant of HaloTag prone to aggregation (AgHalo) was notably engineered to report on impaired proteostasis induced by cellular stress.[74,75] AgHalo aggregation was detected using a fluorogenic ligand that fluoresces only when AgHalo forms insoluble aggregates. Fusion of AgHalo to a protein of interest enables the study of its stress-induced aggregation. An orthogonal SNAP-tag based system was developed as an addition to the aggregation tag method (AggTag),[76] allowing the simultaneous detection of two different proteins’ aggregation. Very recently, a circularly permuted (cp)HaloTag version was elegantly included in the design of fluorescent chemogenetic biosensors, combining both protein engineering and fine-tuning of the coupled fluorophore.[77] The fluorescence of JF dyes can be enhanced by increased interactions with surface residues of HaloTag, allowing the creation of highly sensitive indicators through conformational coupling to a sensing domain. Coupling of cpHaloTag with. calcium-binding domain and voltage-sensitive domain allowed the creation of calcium and voltage indicators (Figure II-4B, C), which were successfully used in cultured rat hippocampal neurons using diverse and interchangeable environment-sensitive JF dyes, further illustrating the flexibility of hybrid reporters.

Systems that directly integrate fluorogenicity in their initial design were recently developed. The cellular retinoic acid binding protein II (CRABPII)[78] and the closely related human Cellular Retinol Binding Protein II (hCRPBII)[79] were engineered into red fluorescent reporters by introducing a lysine residue in their binding cavity to allow the formation of an iminium with aldehyde-containing merocyanine dye precursors. Engineering of hCRPBII combined with the use of a julolidine retinal analog further allowed the development of a ratiometric pH sensor.[80] The sensor takes advantage of the sensitivity of the bound chromophore to the electrostatic environment within the binding cavity. The absorption profile changes as a function of the protonation state of a carboxylic side chain in proximity of the bound iminium. Unfortunately, the julolidine retinal analog was not membrane-permeable, preventing cellular evaluation.

The photoactive yellow protein (PYP) was also engineered into a small self-labeling protein tag, taking advantage of its ability to react with hydroxycynamoyl and coumaryl thioester derivatives.[81] Fluorogenic ligands were obtained coupling a fluorescent moiety and a quencher,[82] or using environment-sensitive fluorogens that only display high fluorescence intensity in the low-polar cavity of the protein tag.[83] Engineering of both fluorogens and PYP mutants led to enhanced brightness and labeling kinetics.[84–87] A sensor for methylated-DNA was obtained by fusing a methyl-CpG binding domain (MBD) with PYP. Labeling with an oxazole yellow (YO) ligand that strongly fluoresces upon DNA-binding allowed to track DNA-methylation during mitosis with good signal-to-noise ratio.[88]

Optical reporters relying on covalent tethering of a fluorogen allowed imaging of various biological events. Biosensing was achieved by signal integration, or fluorescence intensity change of a synthetic indicator anchored to a genetically encoded tag. In addition to that, engineering of non-covalent fluorogenic systems greatly expanded the palette of reporters that could be incorporated in the design of biosensors, particularly suitable for monitoring dynamic and reversible processes.

II.4.2. Non-covalent fluorogenic labelling

Among semi-synthetic fluorogenic systems, RNA aptamers are one remarkable alternative to GFP-like FPs, as they can adopt geometrical conformations suitable for small molecules binding. The Spinach RNA aptamer nicely illustrates how short RNA sequences can serve as scaffold to complex synthetic fluorogens such as DFHBI (Figure II-4D) with high specificity and affinities.[89] The use of SELEX (Systematic Evolution of Ligands by EXponential enrichment),[90] targeted mutagenesis as well as directed evolution later yielded several RNA-fluorogen reporters such as Spinach2,[91] Broccoli,[92] Mango,[93] the Peppers series,[94] Riboglow[95] and o-Coral.[96] These systems display high brightness and thermostability, and together with the expanded fluorogen palette including the NIR and cell-permeable SiR,[97,98] they offer a wide range of emission properties for efficient monitoring of RNA dynamics in living cells.[99]

Rational design enabled to make fluorophore binding dependent on the presence of analytes endogenously targeted by RNA structures, notably by riboswitches. In this manner, different riboswitches aptamers showing conformational change upon cyclic dinucleotides binding were inserted in Spinach2, leading to specific sensors for c-di-GMP, c-AMP-GMP and c-di-AMP in bacteria (Figure II-4E).[100,101] Applications of cyclic dinucleotides biosensors were extended to both aerobic and anaerobic contexts by rational mutagenesis.[102] Despite this successful phylogenetic-based optimization, biosensors design for various small-molecule analytes is generally facilitated by high-throughput screening methods. In this way, a theophylline biosensor was developed as proof-of-concept combining a droplet-based microfluidic screening with Next Generation Sequencing.[103]

Recently, biosensors taking advantage of aptamer reporters' nature were developed to track specific RNAs in living cells. The mirror image aptamer L–Mango was used to image micro-RNAs (miRNA): acting as a blocking strand to an achiral peptide nucleic acid (PNA), it is displaced by overexpressed miRNAs and then properly folds to complex and activate its cognate dye.[104] This study shows that L-aptamers are biocompatible and can self-deliver to cells by cholesterol conjugation, opening the way for new RNA-based probes for imaging and biosensing.

Another type of semi-synthetic reporters, fluorogen activating proteins (FAPs) derived from single-chain variable fragments of antibodies, were selected by directed evolution to specifically bind and strongly activate known fluorogens including Malachite Green (MG) or Thiazole Orange (TO). Such fluorophores and their derivatives offer tunable properties such as cell permeability, far-red emission,[105–108] and biocompatible imaging in living cells, yeast[109,110] and bacteria.[111] Control of labelling densities with far-red emitting MG makes it a suitable candidate for super-resolution microscopy, notably for Binding Activated Localization Microscopy (F-BALM)[112] and single particle tracking.[113] A Cy5 analogue conjugated to TO1, showing both cell-exclusion and pH-sensitivity, yielded a FAP-based biosensor able to follow endocytosis and recycling of a surface protein, while indicating pH evolution in vesicles by FRET emission changes.[114] Receptor trafficking visualization with STED microscopy was possible by fusion of the improved pH biosensor TrapHic, based on a Cy3 analogue-MG tandem dye.[115] A similar strategy enabled to follow internalization of the pharmacologically-relevant $GABA_A$ receptor, and its localization along the neuronal endosome-lysosome axis.[110] Membrane-impermeant dyes were also used to probe opening of synaptic fusion pores that ensure neuropeptides transmission.[116] Easy diffusion of the small size MG compared to the larger intracellular FAP favors the formation of the fluorescent protein-dye complex inside the synaptic pore, interestingly taking advantage of both components' inherent properties. A FAP-based assay for membrane apposition also made ingenious use of both genetic targeting of membrane proteins and modularity of the fluorogen, by synthetically connecting MG and dimethylindole red (DIR). A more than 10-fold fluorescence increase from the lower affinity dye MG can be observed at the contact sites between cocultured cells expressing two different FAPs.[117]

FAP-based systems can also act as highly localized photosensitizers with dyes functionalized with heavy atoms, notably by activation of the ROS-generating di-iodinated MG analog.[118] Combined with the different strategies to target such systems to tumor cells,[119] this property shows promising potential for targeted photodamage. Moreover, FAPs biosensors do not only rely on the fluorogen versatility: the protein part itself can be engineered to undergo observable conformational change. This was illustrated by insertion of a peptide cleavage sequence adjacent to a minimal glycosylation site, connecting FAP to a blocking domain, that can only be released and allow dye binding in case of defective O-glycosylation.[120]

A similar but smaller semi-synthetic reporter, the Fluorescence Activating and Absorption-Shifting Tag (FAST), was recently developed.[121] Evolved from the Photoactive Yellow Protein, the cavity of this 14 kDa protein tag can complex fluorogenic compounds derived from the hydroxybenzylidene rhodanine (HBR) family (Figure II-4F) in a highly dynamic and reversible manner. The versatility of HBR derivatives makes FAST a suitable candidate for multicolor imaging in various subcellular compartments.[122,123] Membrane-impermeant fluorogens also allowed visualization and quantification of membrane proteins trafficking.[124] An improved FAST version (iFAST) was obtained by introduction of a single mutation (V107I), and dimerization of this reporter resulted in tandem FAST (td-iFAST) that reached higher brightness values than EGFP and mCherry in vitro.[125] FAST fluorescence being oxygen-independent, it is a reliable reporter for the study of bacterial biofilm formation[126] or in strictly anaerobic conditions such as Clostridium organisms.[127] It was also applied to super-resolution microscopy, taking advantage of the rapid fluorogen exchange for single-particle tracking[128] or sub-diffraction imaging with a conventional microscope using Super-Resolution Radial Fluctuations (SRRF).[129] Interestingly, red-shifted GFP-like fluorogens binding FAST with comparable affinity were recently investigated, and show promising photostability for long-time imaging.[130]

FAST proved useful as reporting domain in the development of a multicolor real-time Ca^{2+} indicator.[131] This strategy relied on the Ca^{2+}-dependent interaction of the sensing module CaM/M13, modifying the reporter affinity for its cognate dye, and consequently the observed brightness (Figure II-4G). Noteworthy, this sensor was developed using a circularly permuted version of FAST (cpFAST). The creation of new termini closer to the fluorogen binding pocket made it more sensitive to the presence of Ca^{2+}. Careful control of fluorogen concentration allowed one to observe 2 to 3-fold fluorescence increase upon Ca^{2+} transients in living cells. FAST also tolerates splitting at its circular permutation site, and reconstitution of the functional tag is rapid and reversible, opening the way to numerous biosensing applications (Figure II-4H). First, split FAST enabled real-time observation of both FKBP/FRB complex formation and dissociation, and this proof-of-concept was then extended to follow MEK1 and ERK2 interaction upon activation of the MAPK signaling pathway. Split FAST was also applied to the design of a caspase activity biosensor to visualize apoptosis, and each split part was fused as well to either CaM or M13 to generate an intermolecular Ca^{2+} biosensor.[132] This modularity shows great potential for further development of FAST-based biosensors with highly tunable properties to investigate cellular processes in various organisms.

II.5. Conclusion & perspectives

The recent and plentiful developments of new fluorogenic reporter systems have opened the way towards new horizons in the field of bioimaging and biosensing. The intrinsic properties of these fluorogenic systems, notably oxygen independence, substantially broaden the range of sensors applications. They also constitute a great addition of bio-orthogonal reporting modules for multiplexed biosensing, applicable to the design of single-reporter indicators, FRET sensors or even BiFC.

Systems binding to endogenous fluorogens offer interesting features notably for deep tissue imaging without the need for delivery. On the other hand, tunable synthetic fluorogens make these systems very valuable for modular multicolor biosensing. They enable to change the reporter emission properties in an easier way than switching fluorescent proteins, that generally requires re-engineering of the entire chimera. Thus, the chromophores color palette expansion has allowed simultaneous observation of various cellular processes.

The improvements of screening methods combined with increasing knowledge of structural characteristics allows the combination of rational design and high-throughput optimization, yielding more performant biosensors in a faster timeline. Engineering of new fluorogenic systems, together with the development of microscopy techniques, allowed unprecedented spatial and temporal resolution. New opportunities for *in vivo* biosensing and super-resolution microscopy are emerging with the expanding availability of fluorogens with adjustable concentrations for the different systems described.

To conclude, the design of biosensors based on fluorogenic reporters represents a great opportunity to observe and study cellular processes in innovative and original ways. The flexibility of their properties allows to overcome most of the usual limitations encountered in the field of fluorescence microscopy. Because of the very promising perspectives they offer for biological imaging, it is a safe bet to say that fluorogenic chemogenetic biosensors will stand as indispensable tools for cell biologists in the coming years.

Notes

The authors declare the following competing financial interest: A.G. is co-founder and hold equity in Twinkle Bioscience/The Twinkle Factory, a company commercializing the FAST technology.

Acknowledgements
This work was supported by the European Research Council (ERC-2016-CoG-724705 FLUOSWITCH).

Keywords: biosensors · chemogenetic reporters · fluorescent labels · fluorescence imaging · proteins

II.6. References

1. Tsien, R. Y. the Green Fluorescent Protein. *Annu. Rev. Biochem.* **67**, 509–544 (1998).
2. Chudakov, D. M., Matz, M. V., Lukyanov, S. & Lukyanov, K. A. Fluorescent Proteins and Their Applications in Imaging Living Cells and Tissues. *Physiol. Rev.* **90**, 1103–1163 (2010).
3. Livet, J. *et al.* Transgenic strategies for combinatorial expression of fluorescent proteins in the nervous system. *Nature* **450**, 56–62 (2007).
4. Greenwald, E. C., Mehta, S. & Zhang, J. Genetically encoded fluorescent biosensors illuminate the spatiotemporal regulation of signaling networks. *Chem. Rev.* **118**, 11707–11794 (2018).
5. Zhao, Y. *et al.* SoNar, a highly responsive NAD+/NADH sensor, allows high-throughput metabolic screening of anti-tumor agents. *Cell Metab.* **21**, 777–789 (2016).
6. Nakai, J., Ohkura, M. & Imoto, K. A high signal-to-noise Ca(2+) probe composed of a single green fluorescent protein. *Nat. Biotechnol.* **19**, 137–141 (2001).
7. Chen, T.-W. *et al.* Ultrasensitive fluorescent proteins for imaging neuronal activity. *Nature* **499**, 295–300 (2013).
8. Yang, Y. *et al.* Improved calcium sensor GCaMP-X overcomes the calcium channel perturbations induced by the calmodulin in GCaMP. *Nat. Commun.* **9**, 1504 (2018).
9. Miyawaki, A. *et al.* Fluorescent indicators for Ca2+ based on green fluorescent proteins and calmodulin. *Nature* **388**, 882–887 (1997).
10. Ting, A. Y., Kain, K. H., Klemke, R. L. & Tsien, R. Y. Genetically encoded fluorescent reporters of protein tyrosine kinase activities in living cells. *Proc. Natl. Acad. Sci. U. S. A.* **98**, 15003–15008 (2001).
11. Tsien, R. Y. Building and breeding molecules to spy on cells and tumors. *FEBS Lett.* **579**, 927–932 (2005).
12. Hires, S. A., Zhu, Y. & Tsien, R. Y. Optical measurement of synaptic glutamate spillover and reuptake by linker optimized glutamate-sensitive fluorescent reporters. *Proc. Natl. Acad. Sci.* **105**, 4411–4416 (2008).
13. Cabantous, S., Terwilliger, T. C. & Waldo, G. S. Protein tagging and detection with engineered self-assembling fragments of green fluorescent protein. *Nat. Biotechnol.* **23**, 102–107 (2005).
14. Cabantous, S. *et al.* A new protein-protein interaction sensor based on tripartite split-GFP association. *Sci. Rep.* **3**, 2854 (2013).
15. Wiens, M. D. & Campbell, R. E. Surveying the landscape of optogenetic methods for detection of protein-protein interactions. *Wiley Interdiscip. Rev.: Syst. Biol. Med.* **10**, (2018).
16. Keppler, A. *et al.* A general method for the covalent labeling of fusion proteins with small molecules in vivo. *Nat. Biotechnol.* **21**, 86–89 (2003).
17. Los, G. V. *et al.* HaloTag: A novel protein labeling technology for cell imaging and protein analysis. *ACS Chem. Biol.* **3**, 373–382 (2008).
18. Gautier, A. *et al.* An Engineered Protein Tag for Multiprotein Labeling in Living Cells. *Chem. Biol.* **15**, 128–136 (2008).
19. Bannwarth, M. *et al.* Indo-1 derivatives for local calcium sensing. *ACS Chem. Biol.* **4**, 179–190 (2009).
20. Deo, C., Sheu, S. H., Seo, J., Clapham, D. E. & Lavis, L. D. Isomeric Tuning Yields Bright and Targetable Red Ca2+ Indicators. *J. Am. Chem. Soc.* **141**, 13734–13738 (2019).
21. Hirata, T. *et al.* Protein-Coupled Fluorescent Probe to Visualize Potassium Ion Transition on Cellular Membranes. *Anal. Chem.* **88**, 2693–2700 (2016).
22. Matsui, Y. *et al.* Visualization of long-term Mg $^{2+}$ dynamics in apoptotic cells using a novel targetable fluorescent probe. *Chem. Sci.* **8**, 8255–8264 (2017).
23. Zastrow, M. L., Huang, Z. & Lippard, S. J. HaloTag-Based Hybrid Targetable and Ratiometric Sensors for Intracellular Zinc. *ACS Chem. Biol.* **15**, 396–406 (2020).
24. Wang, C., Song, X., Chen, L. & Xiao, Y. Specifically and wash-free labeling of SNAP-tag fused proteins with a hybrid sensor to monitor local micro-viscosity. *Biosens. Bioelectron.* **91**, 313–320 (2017).
25. Abdelfattah, A. *et al.* Bright and photostable chemigenetic indicators for extended in vivo voltage imaging. *Science* **365**, 699–704 (2019).
26. Farrants, H., Hiblot, J., Griss, R. & Johnsson, K. Chapter 7 Rational design and

applications of semisynthetic modular biosensors: SNIFITs and LUCIDs. **1596**, 101–117 (2017).
27. Brun, M. A. *et al.* Semisynthesis of fluorescent metabolite sensors on cell surfaces. *J. Am. Chem. Soc.* **133**, 16235–16242 (2011).
28. Brun, M. A. *et al.* A semisynthetic fluorescent sensor protein for glutamate. *J. Am. Chem. Soc.* **134**, 7676–7678 (2012).
29. Masharina, A., Reymond, L., Maurel, D., Umezawa, K. & Johnsson, K. A fluorescent sensor for GABA and synthetic GABAB receptor ligands. *J. Am. Chem. Soc.* **134**, 19026–19034 (2012).
30. Schena, A. & Johnsson, K. Sensing acetylcholine and anticholinesterase compounds. *Angew. Chem. Int. Ed.* **53**, 1302–1305 (2014).
31. Sallin, O. *et al.* Semisynthetic biosensors for mapping cellular concentrations of nicotinamide adenine dinucleotides. *Elife* **7**, e32638 (2018).
32. Yu, Q. *et al.* Semisynthetic sensor proteins enable metabolic assays at the point of care. *Science* **361**, 1122–1126 (2018).
33. Gautier, A. & Tebo, A. G. Fluorogenic Protein-Based Strategies for Detection, Actuation, and Sensing. *BioEssays* **40**, 1800118 (2018).
34. Péresse, T. & Gautier, A. Next-generation fluorogen-based reporters and biosensors for advanced bioimaging. *Int. J. Mol. Sci.* **20**, 6412 (2019).
35. Shu, X. *et al.* Mammalian Expression of Infrared Fluorescent Proteins Engineered from a Bacterial Phytochrome. *Science* **324**, 804–807 (2009).
36. Filonov, G. S. *et al.* Bright and stable near-infrared fluorescent protein for in vivo imaging. *Nat. Biotechnol.* **29**, 757–761 (2011).
37. Filonov, G. S. & Verkhusha, V. V. A near-infrared bifc reporter for in vivo imaging of protein-protein interactions. *Chem. Biol.* **20**, 1078–1086 (2013).
38. Tchekanda, E., Sivanesan, D. & Michnick, S. W. An infrared reporter to detect spatiotemporal dynamics of protein-protein interactions. *Nat. Methods* **11**, 641–644 (2014).
39. Yu, D. *et al.* A naturally monomeric infrared fluorescent protein for protein labeling in vivo. *Nat. Methods* **12**, 763–765 (2015).
40. Qian, Y. *et al.* A genetically encoded near-infrared fluorescent calcium ion indicator. *Nat. Methods* **16**, 171–174 (2019).
41. Rumyantsev, K. A. *et al.* Minimal domain of bacterial phytochrome required for chromophore binding and fluorescence. *Sci. Rep.* **5**, 18348 (2015).
42. Subach, O. M., Barykina, N. V., Anokhin, K. V., Piatkevich, K. D. & Subach, F. V. Near-Infrared Genetically Encoded Positive Calcium Indicator Based on GAF-FP Bacterial Phytochrome. *Int. J. Mol. Sci.* **20**, 3488 (2019).
43. To, T. L. *et al.* Rationally designed fluorogenic protease reporter visualizes spatiotemporal dynamics of apoptosis in vivo. *Proc. Natl. Acad. Sci. U. S. A.* **112**, 3338–3343 (2015).
44. Shcherbakova, D. M. *et al.* Bright monomeric near-infrared fluorescent proteins as tags and biosensors for multiscale imaging. *Nat. Commun.* **7**, 12405 (2016).
45. Oliinyk, O. S., Shemetov, A. A., Pletnev, S., Shcherbakova, D. M. & Verkhusha, V. V. Smallest near-infrared fluorescent protein evolved from cyanobacteriochrome as versatile tag for spectral multiplexing. *Nat. Commun.* **10**, 279 (2019).
46. Sakaue-Sawano, A. *et al.* Visualizing Spatiotemporal Dynamics of Multicellular Cell-Cycle Progression. *Cell* **132**, 487–498 (2008).
47. Rodriguez, E. A. *et al.* A far-red fluorescent protein evolved from a cyanobacterial phycobiliprotein. *Nat. Methods* **13**, 763–769 (2016).
48. Drepper, T. *et al.* Reporter proteins for in vivo fluorescence without oxygen. *Nat. Biotechnol.* **25**, 443–445 (2007).
49. Drepper, T. *et al.* Flavin mononucleotide-based fluorescent reporter proteins outperform green fluorescent protein-like proteins as quantitative in vivo real-time reporters. *Appl. Environ. Microbiol.* **76**, 5990–5994 (2010).
50. Wingen, M. *et al.* The photophysics of LOV-based fluorescent proteins-new tools for cell biology. *Photochem. Photobiol. Sci.* **13**, 875–883 (2014).
51. Potzkei, J. *et al.* Real-time determination of intracellular oxygen in bacteria using a genetically encoded FRET-based biosensor. *BMC Biol.* **10**, 28 (2012).
52. Hudson, D. A., Caplan, J. L. & Thorpe, C. Designing Flavoprotein-GFP Fusion Probes for Analyte-Specific Ratiometric Fluorescence Imaging. *Biochemistry* **57**, 1178–1189 (2018).

53. Chapman, S. *et al.* The photoreversible fluorescent protein iLOV outperforms GFP as a reporter of plant virus infection. *Proc. Natl. Acad. Sci. U. S. A.* **105**, 20038–20043 (2008).
54. Ravikumar, Y., Nadarajan, S. P., Lee, C. S., Rhee, J. K. & Yun, H. A New-Generation Fluorescent-Based Metal Sensor – iLOV Protein. *J. Microbiol. Biotechnol.* **25**, 503–510 (2015).
55. Liu, X. *et al.* Significant expansion of fluorescent protein sensing ability through the genetic incorporation of superior photo-induced electron-transfer quenchers. *J. Am. Chem. Soc.* **136**, 13094–13097 (2014).
56. Shu, X. *et al.* A genetically encoded tag for correlated light and electron microscopy of intact cells, tissues, and organisms. *PLoS Biol.* **9**, 4 (2011).
57. Makhijani, K. *et al.* Precision Optogenetic Tool for Selective Single- and Multiple-Cell Ablation in a Live Animal Model System. *Cell Chem. Biol.* **24**, 110–119 (2017).
58. Westberg, M., Bregnhøj, M., Etzerodt, M. & Ogilby, P. R. No Photon Wasted: An Efficient and Selective Singlet Oxygen Photosensitizing Protein. *J. Phys. Chem.* **121**, 9366–9371 (2017).
59. Hilgers, F. *et al.* Genetically Encoded Photosensitizers as Light-Triggered Antimicrobial Agents. *Int. J. Mol. Sci.* **20**, 4608 (2019).
60. Boassa, D. *et al.* Split-miniSOG for Spatially Detecting Intracellular Protein-Protein Interactions by Correlated Light and Electron Microscopy. *Cell Chem. Biol.* **26**, 1407–1416 (2019).
61. Kumagai, A. *et al.* A bilirubin-inducible fluorescent protein from eel muscle. *Cell* **153**, 1602–1611 (2013).
62. Erapaneedi, R., Belousov, V. V, Schäfers, M. & Kiefer, F. A novel family of fluorescent hypoxia sensors reveal strong heterogeneity in tumor hypoxia at the cellular level. *EMBO J.* **35**, 102–113 (2016).
63. Hu, H. *et al.* Monitoring cellular redox state under hypoxia using a fluorescent sensor based on eel fluorescent protein. *Free Radic. Biol. Med.* **120**, 255–265 (2018).
64. Shitashima, Y., Shimozawa, T., Asahi, T. & Miyawaki, A. A dual-ligand-modulable fluorescent protein based on UnaG and calmodulin. *Biochem. Biophys. Res. Commun.* **496**, 872–879 (2018).
65. To, T. L., Zhang, Q. & Shu, X. Structure-guided design of a reversible fluorogenic reporter of protein-protein interactions. *Protein Sci.* **25**, 748–753 (2016).
66. Lukinavičius, G. *et al.* Fluorogenic Probes for Multicolor Imaging in Living Cells. *J. Am. Chem. Soc.* **138**, 9365–9368 (2016).
67. Wang, L. *et al.* A general strategy to develop cell permeable and fluorogenic probes for multicolour nanoscopy. *Nat. Chem.* **12**, 165–172 (2020).
68. Grimm, J. B. *et al.* Carbofluoresceins and carborhodamines as scaffolds for high-contrast fluorogenic probes. *ACS Chem. Biol.* **8**, 1303–1310 (2013).
69. Grimm, J. B. *et al.* Bright photoactivatable fluorophores for single-molecule imaging. *Nat. Methods* **13**, 985–988 (2016).
70. Zheng, Q. *et al.* Rational Design of Fluorogenic and Spontaneously Blinking Labels for Super-Resolution Imaging. *ACS Cent. Sci.* **5**, 1602–1613 (2019).
71. Lukinavičius, G. *et al.* A near-infrared fluorophore for live-cell super-resolution microscopy of cellular proteins. *Nat. Chem.* **5**, 132–139 (2013).
72. Clark, S. A., Singh, V., Vega Mendoza, D., Margolin, W. & Kool, E. T. Light-Up ‘channel Dyes’ for Haloalkane-Based Protein Labeling in Vitro and in Bacterial Cells. *Bioconjug. Chem.* **27**, 2839–2843 (2016).
73. Liu, Y. *et al.* The Cation−π Interaction Enables a Halo-Tag Fluorogenic Probe for Fast No-Wash Live Cell Imaging and Gel-Free Protein Quantification. *Biochemistry* **56**, 1585–1595 (2017).
74. Liu, Y. *et al.* AgHalo: A Facile Fluorogenic Sensor to Detect Drug-Induced Proteome Stress. *Angew. Chem. Int. Ed.* **56**, 8672–8676 (2017).
75. Liu, Y. *et al.* A HaloTag-Based Multicolor Fluorogenic Sensor Visualizes and Quantifies Proteome Stress in Live Cells Using Solvatochromic and Molecular Rotor-Based Fluorophores. *Biochemistry* **57**, 4663–4674 (2018).
76. Jung, K. H., Kim, S. F., Liu, Y. & Zhang, X. A Fluorogenic AggTag Method Based on Halo- and SNAP-Tags to Simultaneously Detect Aggregation of Two Proteins in Live Cells. *ChemBioChem* **20**, 1078–1087 (2019).
77. Deo, C. *et al.* Bright and tunable far-red chemigenetic indicators. *bioRxiv* 2020.01.08.898783 (2020). doi:10.1101/2020.01.08.898783
78. Yapici, I. *et al.* "Turn-on " protein fluorescence: In situ formation of cyanine dyes. *J. Am.*

Chem. Soc. **137**, 1073–1080 (2014).

79. Wang, W. *et al.* Tuning the Electronic Absorption of Protein-Embedded All-trans-retinal. *Science* **338**, 1340–1344 (2012).
80. Berbasova, T. *et al.* A Genetically Encoded Ratiometric pH Probe: Wavelength Regulation-Inspired Design of pH Indicators. *ChemBioChem* **19**, 1288–1295 (2018).
81. Hori, Y., Ueno, H., Mizukami, S. & Kikuchi, K. Photoactive yellow protein-based protein labeling system with turn-on fluorescence intensity. *J. Am. Chem. Soc.* **131**, 16610–16611 (2009).
82. Hori, Y., Nakaki, K., Sato, M., Mizukami, S. & Kikuchi, K. Development of protein-labeling probes with a redesigned fluorogenic switch based on intramolecular association for no-wash live-cell imaging. *Angew. Chem. Int. Ed.* **51**, 5611–5614 (2012).
83. Hori, Y. *et al.* Development of fluorogenic probes for quick No-Wash live-cell imaging of intracellular proteins. *J. Am. Chem. Soc.* **135**, 12360–12365 (2013).
84. Hori, Y., Hirayama, S., Sato, M. & Kikuchi, K. Redesign of a Fluorogenic Labeling System to Improve Surface Charge, Brightness, and Binding Kinetics for Imaging the Functional Localization of Bromodomains. *Angew. Chem. Int. Ed.* **54**, 14368–14371 (2015).
85. Hirayama, S., Hori, Y., Benedek, Z., Suzuki, T. & Kikuchi, K. Fluorogenic probes reveal a role of GLUT4 N-glycosylation in intracellular trafficking. *Nat. Chem. Biol.* **12**, 853–859 (2016).
86. Kamikawa, Y. *et al.* Design of a protein tag and fluorogenic probe with modular structure for live-cell imaging of intracellular proteins. *Chem. Sci.* **7**, 308–314 (2016).
87. Gao, J. *et al.* Development of fluorogenic probes for rapid, high-contrast imaging of transient nuclear localization of sirtuin 3. *Chembiochem* **21**, 656–662 (2019).
88. Hori, Y. *et al.* Synthetic-Molecule/Protein Hybrid Probe with Fluorogenic Switch for Live-Cell Imaging of DNA Methylation. *J. Am. Chem. Soc.* **140**, 1686–1690 (2018).
89. Paige, J. S., Wu, K. Y. & Jaffrey, S. R. RNA Mimics of Green Fluorescent Protein. *Science* **333**, 642–646 (2011).
90. Tuerk, C. & Gold, L. Systematic evolution of ligands by exponential enrichment: RNA ligands to bacteriophage T4 DNA polymerase. *Science* **249**, 505–510 (1990).
91. Strack, R. L., Disney, M. D. & Jaffrey, S. R. A superfolding Spinach2 reveals the dynamic nature of trinucleotide repeat-containing RNA. *Nat. Methods* **10**, 1219–1224 (2013).
92. Filonov, G. S., Moon, J. D., Svensen, N. & Jaffrey, S. R. Broccoli: Rapid selection of an RNA mimic of green fluorescent protein by fluorescence-based selection and directed evolution. *J. Am. Chem. Soc.* **136**, 16299–16308 (2014).
93. Trachman, R. J. *et al.* Structure and functional reselection of the Mango-III fluorogenic RNA aptamer. *Nat. Chem. Biol.* **15**, 472–479 (2019).
94. Chen, X. *et al.* Visualizing RNA dynamics in live cells with bright and stable fluorescent RNAs. *Nat. Biotechnol.* **37**, 1287–1293 (2019).
95. Braselmann, E. *et al.* A multicolor riboswitch-based platform for imaging of RNA in live mammalian cells. *Nat. Chem. Biol.* **14**, 964–971 (2018).
96. Bouhedda, F. *et al.* A dimerization-based fluorogenic dye-aptamer module for RNA imaging in live cells. *Nat. Chem. Biol.* **16**, 69–76 (2019).
97. Song, W., Strack, R. L., Svensen, N. & Jaffrey, S. R. Plug-and-play fluorophores extend the spectral properties of spinach. *J. Am. Chem. Soc.* **136**, 1198–1201 (2014).
98. Wirth, R., Gao, P., Nienhaus, G. U., Sunbul, M. & Jäschke, A. SiRA: A Silicon Rhodamine-Binding Aptamer for Live-Cell Super-Resolution RNA Imaging. *J. Am. Chem. Soc.* **141**, 7562–7571 (2019).
99. Truong, L. & Ferré-D'Amaré, A. R. From fluorescent proteins to fluorogenic RNAs: Tools for imaging cellular macromolecules. *Protein Sci.* **28**, 1374–1386 (2019).
100. Kellenberger, C. A., Chen, C., Whiteley, A. T., Portnoy, D. A. & Hammond, M. C. RNA-Based Fluorescent Biosensors for Live Cell Imaging of Second Messenger Cyclic di-AMP. *J. Am. Chem. Soc.* **137**, 6432–6435 (2015).
101. Kellenberger, C. A., Wilson, S. C., Sales-Lee, J. & Hammond, M. C. RNA-Based Fluorescent Biosensors for Live Cell Imaging of Second Messenger Cyclic di-GMP and cyclic AMP-GMP. *J. Am. Chem. Soc.* **135**, 4906–4909 (2013).
102. Wang, X. C., Wilson, S. C. & Hammond, M. C. Next-generation RNA-based fluorescent biosensors enable anaerobic detection of cyclic di-GMP. *Nucleic Acids Res.* **44**, e139 (2016).
103. Autour, A., Bouhedda, F., Cubi, R. & Ryckelynck, M. Optimization of fluorogenic RNA-based biosensors using droplet-based microfluidic ultrahigh-throughput screening.

Methods **161**, 46–53 (2019).
104. Zhong, W. & Sczepanski, J. T. A Mirror Image Fluorogenic Aptamer Sensor for Live-Cell Imaging of MicroRNAs. *ACS Sensors* **4**, 566–570 (2019).
105. Szent-Gyorgyi, C. *et al.* Fluorogen-activating single-chain antibodies for imaging cell surface proteins. *Nat. Biotechnol.* **26**, 235–240 (2008).
106. Szent-Gyorgyi, C. *et al.* Malachite green mediates homodimerization of antibody VL domains to form a fluorescent ternary complex with singular symmetric interfaces. *J. Mol. Biol.* **425**, 4595–4613 (2014).
107. Yates, B. P., Peck, M. A. & Berget, P. B. Directed Evolution of a Fluorogen-Activating Single Chain Antibody for Function and Enhanced Brightness in the Cytoplasm. *Mol. Biotechnol.* **54**, 829–841 (2013).
108. Telmer, C. A. *et al.* Rapid, Specific, No-wash, Far-red Fluorogen Activation in Subcellular Compartments by Targeted Fluorogen Activating Proteins. *ACS Chem. Biol.* **10**, 1239–1246 (2015).
109. Fitzpatrick, J. A. J. *et al.* STED nanoscopy in living cells using fluorogen activating proteins. *Bioconjug. Chem.* **20**, 1843–1847 (2009).
110. Lorenz-Guertin, J. M. *et al.* A versatile optical tool for studying synaptic GABAA receptor trafficking. *J. Cell Sci.* **130**, 3933–3945 (2017).
111. Saurabh, S., Perez, A. M., Comerci, C. J., Shapiro, L. & Moerner, W. E. Super-resolution Imaging of Live Bacteria Cells Using a Genetically Directed, Highly Photostable Fluoromodule. *J. Am. Chem. Soc.* **138**, 10398–10401 (2016).
112. Yan, Q. *et al.* Localization microscopy using noncovalent fluorogen activation by genetically encoded FAPs. *Chemphyschem* **15**, 687–695 (2014).
113. Schwartz, S. L. *et al.* Fluorogen-activating proteins provide tunable labeling densities for tracking FcεRI independent of IgE. *ACS Chem. Biol.* **10**, 539–546 (2015).
114. Grover, A. *et al.* Genetically encoded pH sensor for tracking surface proteins through endocytosis. *Angew. Chem. Int. Ed.* **51**, 4838–4842 (2012).
115. Perkins, L. A. *et al.* Genetically Targeted Ratiometric and Activated pH Indicator Complexes (TRApHIC) for Receptor Trafficking. *Biochemistry* **57**, 861–871 (2018).
116. Bulgari, D. *et al.* Activity-evoked and spontaneous opening of synaptic fusion pores. *Proc. Natl. Acad. Sci.* **34**, 17039–17044 (2019).
117. Ackerman, D. S., Vasilev, K. V., Schmidt, B. F., Cohen, L. B. & Jarvik, J. W. Tethered Fluorogen Assay to Visualize Membrane Apposition in Living Cells. *Bioconjug. Chem.* **28**, 1356–1362 (2017).
118. He, J. *et al.* A genetically targetable near-infrared photosensitizer. *Nat. Methods* **13**, 263–268 (2016).
119. Wang, Y. *et al.* Affibody-Targeted Fluorogen Activating Protein for in vivo Tumor Imaging. *Physiol. Behav.* **176**, 139–148 (2017).
120. Bachert, C. & Linstedt, A. D. A sensor of protein O-glycosylation based on sequential processing in the Golgi apparatus. *Traffic* **14**, 47–56 (2013).
121. Plamont, M.-A. *et al.* Small fluorescence-activating and absorption-shifting tag for tunable protein imaging in vivo. *Proc. Natl. Acad. Sci.* **113**, 497–502 (2016).
122. Li, C. *et al.* Design and characterization of red fluorogenic push-pull chromophores holding great potential for bioimaging and biosensing. *Org. Biomol. Chem.* **14**, 9253–9261 (2016).
123. Li, C. *et al.* Dynamic multicolor protein labeling in living cells. *Chem. Sci.* **8**, 5598–5605 (2017).
124. Li, C. *et al.* Fluorogenic Probing of Membrane Protein Trafficking. *Bioconjug. Chem.* **29**, 1823–1828 (2018).
125. Tebo, A. G., Pimenta, F. M., Zhang, Y. & Gautier, A. Improved Chemical-Genetic Fluorescent Markers for Live Cell Microscopy. *Biochemistry* **57**, 5648–5653 (2018).
126. Monmeyran, A. *et al.* The inducible chemical-genetic fluorescent marker FAST outperforms classical fluorescent proteins in the quantitative reporting of bacterial biofilm dynamics. *Sci. Rep.* **8**, 10336 (2018).
127. Streett, H. E., Kalis, K. M. & Papoutsakis, E. T. A Strongly Fluorescing Anaerobic Reporter and Protein-Tagging System for Clostridium Organisms Based on the Fluorescence-Activating and Absorption-Shifting Tag Protein (FAST). *Appl. Environ. Microbiol.* **85**, e00622-19 (2019).
128. Venkatachalapathy, M., Belapurkar, V., Jose, M., Gautier, A. & Nair, D. Live cell super resolution imaging by radial fluctuations using fluorogen binding tags. *Nanoscale* **11**, 3626–3632 (2019).

129. Smith, E. M., Gautier, A. & Puchner, E. M. Single-Molecule Localization Microscopy with the Fluorescence-Activating and Absorption-Shifting Tag (FAST) System. *ACS Chem. Biol.* **14**, 1115–1120 (2019).
130. Povarova, N. V. *et al.* Red-Shifted Substrates for FAST Fluorogen-Activating Protein Based on the GFP-Like Chromophores. *Chem. Eur. J.* **25**, 9592–9596 (2019).
131. Tebo, A. G. *et al.* Circularly Permuted Fluorogenic Proteins for the Design of Modular Biosensors. *ACS Chem. Biol.* **13**, 2392–2397 (2018).
132. Tebo, A. G. & Gautier, A. A split fluorescent reporter with rapid and reversible complementation. *Nat. Commun.* **10**, 2822 (2019).

Chapter III

Design and characterization of Glu-FAST, a glutamate sensor based on FAST.

III.1. Introduction

Our first development of a FAST-based fluorogenic chemogenetic biosensor targeted the visualization of glutamate, a ubiquitous small molecule of high relevance both intra- and extracellularly. In addition to its amino acid nature implying an involvement in metabolic processes, glutamate is mostly known and studied for its role in cell signalling.[1,2] It is indeed the most important excitatory neurotransmitter in the central nervous system, and was also recently found to be involved in signalling between other cell types. Interestingly, while cytosolic glutamate reaches concentrations in the millimolar range, synaptic glutamate levels have been estimated around micromolar concentrations upon release evoked by action potentials. These glutamate transients are nevertheless involved in the activation of a number of post-synaptic receptors, either ionotropic (thus inducing the opening of the associated ion channel), or metabolotropic (activating metabolic pathways through second messengers). This crucial role has made glutamate a target of choice for the study of glutamate homeostasis in neurological diseases, including for instance Parkinson's and Alzheimer's diseases as well as epilepsy.[3]

Because of its significant biological relevance, the design of biosensors for glutamate has been considered a valuable addition to the fluorescence imaging toolbox. The identification and characterization of the glutamate/aspartate import solute-binding protein GltI (also known as YBEJ), has provided a very promising sensing domain for such developments. Indeed, GltI belongs to the large family of *E. coli* periplasmic binding proteins (PBPs), that selectively bind a wide range of small molecules including glucose and maltose, but also dipeptides or metal ions such as Fe(III).[4] The two domains of PBPs are connected by a hinge region and display an analyte-binding site at their interface: they consequently undergo a relatively large conformational change upon ligand binding. This structural difference between the analyte-bound and -free conformation has allowed the generation of an intensiometric biosensors collection by covalently coupling an environment-sensitive synthetic fluorophore[5], as well as a family of ratiometric biosensors family by insertion of PBPs between fluorescent proteins forming a FRET-pair.[6]

The exploration of PBPs properties thus gave rise to the first fully protein-based glutamate sensor, FLIPE, consisting in the insertion of GltI between the enhanced cyan FP (ECFP) and Venus, a yellow FP (YFP) variant.[7] This first example showed a modest yet encouraging ratio change upon analyte-binding. Moreover, its affinity for glutamate could be adjusted by site-directed mutagenesis of GltI and allowed the visualization of stimulated glutamate release when expressed at the membrane of glutamatergic neurons. Following developments of genetically encoded glutamate biosensors were then largely based on the same recognition protein domain GltI. Relying on a similar design, several FRET sensors were indeed described starting with the development of GluSnFR, first introduced in 2005,[8] and the further description and characterization of its optimized version SuperGluSnFR in 2008.[9] In fact, truncation of 8 and 5 residues at the N and C termini, respectively, yielded a dramatic improvement of the ratio change reaching ΔR_{max} = 44% *in vitro*. SuperGluSnFR allowed the visualization of glutamate transients evoked by action potentials in cultured neurons.

A different design strategy relying on the variation of the fluorescent signal from a single FP enabled the generation of intensiometric glutamate biosensors. Insertion of the circularly permuted enhanced GFP (cpGFP) after the residue 253 of GltI yielded iGluSnFR, a single-wavelength sensor able to indicate synaptic release of glutamate in neurons and astrocytes.[10] Coupling between the interdomain hinge region and the fluorescent reporter was enhanced by optimization of linkers, and screening individual mutants in clarified lysate allowed to identify the best variant GltI253.L1LV/L2NP that reached ΔF/F = 4.5 upon addition of glutamate *in vitro*. Subsequent site-directed mutagenesis of the sensing unit allowed to generate variants of this biosensor covering a wide range of affinities for glutamate. High-frequency bursts at glutamatergic synapses could notably be visualized with $iGlu_f$ and $iGlu_u$, low affinity biosensors providing very high temporal resolution.[11] The optical and thermodynamic properties of such biosensors could also be modified by protein engineering of the reporter domain. SF-iGluSnFR, a variant with higher stability and recombinant bacterial expression levels, was notably engineered by replacement of the cpGFP by the circularly permuted superfolder GFP.[12] Blue, cyan and yellow variants were also generated by introduction of chromophore mutations and subsequent re-engineering of linkers in the case of SF-Azurite-iGluSnFR and SF-mTurquoise2-iGluSnFR. Red-shifting of the biosensor could also be obtained by introduction of 3-aminotyrosine (aY), a genetically encoded non-canonical residue into the GFP chromophore region (at position 66).[13] The possibility of multiplexed imaging was exemplified by the simultaneous visualization of Ca^{2+} and glutamate release in mouse neurons using the green fluorescent sensor GECO1 and the red-emitting aY-iGluSnFR. An alternative strategy consisting in replacing GFP by the red-emitting circularly permuted RFP led to an interesting topological study for re-engineering the resulting R-iGluSnFR sensor.[14] In addition to linkers screening required from fluorescent protein switching, this study demonstrated the possible circular permutation of the glutamate-binding protein GltI, that could thus be inserted into the fluorescent protein while retaining the same connectivity between the reporter and the sensing unit.

While genetically encoded glutamate sensors have been extensively described and improved over time, fewer imaging tools relied on hybrid strategies. Introduction of reactive cysteine into the ligand-binding domain of α-amino-3-hydroxy-5-methyl-4-isoxazolepropionic acid (AMPA) receptor GluR2, or into GltI, allowed the covalent coupling of environment-sensitive synthetic probes Oregon green and IANBD, respectively.[15,16] Despite thorough *in vitro* characterization, notably determining a 2.9-fold fluorescence increase upon glutamate addition, the use of the latter has not yet been demonstrated in neurons.

The general design of Snifit biosensors, previously described in chapter II, was applied to glutamate relying on the kainate receptor subunit iGluR5, another type of glutamate-binding ionotropic receptor.[17] Snifit-iGluR5 is, to the best of our knowledge, the only glutamate sensing approach based on a chemogenetic reporter unit. Demonstrated possibilities offered by such reporters for innovative imaging applications encouraged us to explore the design of a glutamate biosensor based on the fluorogenic reporter FAST. While the principle of Snifit sensors relies on ligand displacement to generate a change of optical signal, we suggested that direct binding of the synthetic fluorogen in the pocket of FAST should allow modulation of the fluorescent signal by allosteric coupling with the glutamate-binding domain.

III.2. Study of the glutamate biosensor topologies

III.2.1. Influence of the connectivity

Based on the previously described designs of genetically encoded fluorescent biosensors for glutamate, the Glutamate/aspartate import solute-binding protein (GltI) was selected as a promising sensing domain in the design of FAST-based glutamate indicators. A recent study by Wu et al.[18] demonstrated that the iGluSnFR sensor design tolerated the replacement of its reporter domain by another fluorescent protein variant, and that its properties could further be modified by changing the connectivity between the different constituents. In particular, the successful circular permutation between R-iGluSnFR and R^{ncp}-iGluSnFR not only allowed to improve by 10-fold the affinity for glutamate, it also demonstrated the possibility to incorporate a circularly permuted version of GltI as analyte-binding domain.

As previously discussed, cpFAST and splitFAST already proved useful as reporter module for biosensing applications. Transposing these observations to the design of glutamate biosensors based on FAST, four different entities could be considered: GltI or cpGltI as sensing domain, FAST or cpFAST as reporter domain. These “building blocks” could be connected in different ways, giving rise to eight possible sensor topologies: on the one hand, inserting FAST or cpFAST in either of the sensing units, and on the other hand, inserting GltI or cpGltI in either of the reporter units (Figure III-1). The eight proteins were expressed in bacteria and purified for subsequent in vitro characterization.

It should be noted that the sequence of the sensing domain GltI varied with the topology, based on insights from the aforementioned studies. Glu-FAST-1, Glu-FAST-2 and their circularly permuted versions, cpGlu-FAST-1 and cpGlu-FAST-2, include the sensing domain of the initial iGluSnFR design, GltI(5-279)[10]. In the case of Glu-FAST-3, Glu-FAST-4 and their cp version, two mutations were introduced at each connecting site with the reporter domain (P252L, P253V, K254N, L255P), as described in the development of R^{ncp}-iGluSnFR. Finally, to obtain cpGlu-FAST-3 and cpGlu-FAST-4, the native termini of the sensing domain were connected by a 37 residues linker to obtain cpGltI.

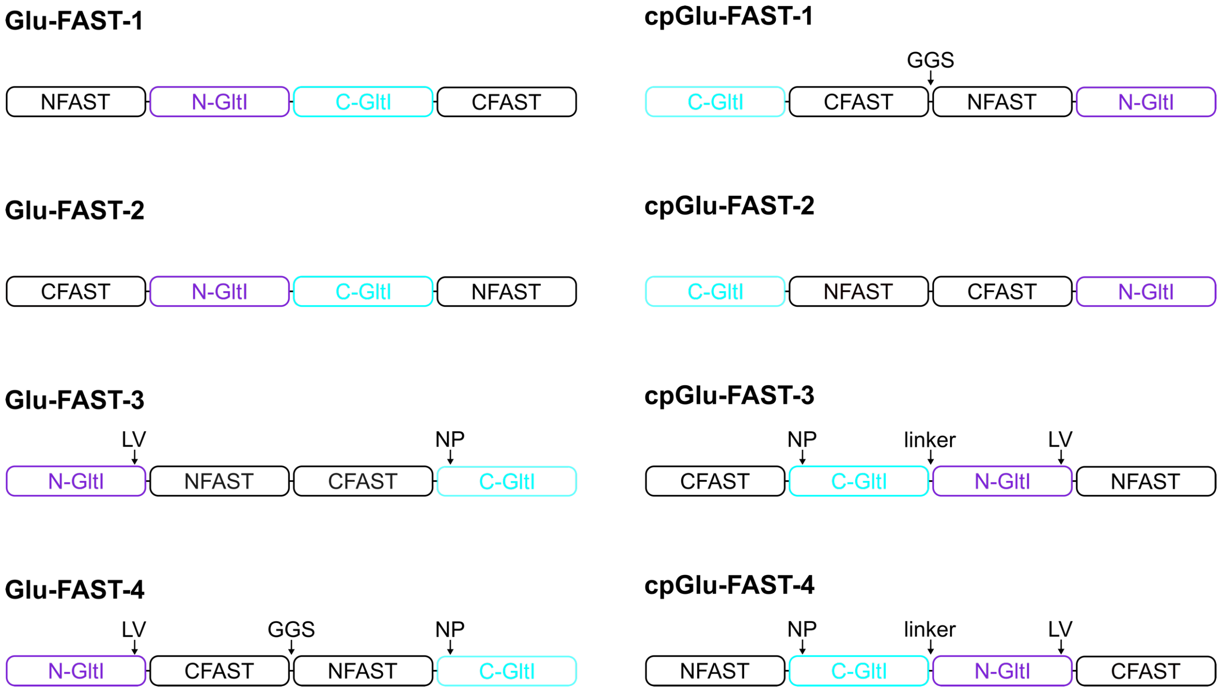

Figure III-1. Eight topologies result from the coupling of FAST/cpFAST with the Glutamate/aspartate import solute-binding protein (GltI).

For fluorescence to be conditioned by the presence of the analyte, the affinity of FAST for its cognate fluorogen should be modified upon glutamate binding. Thus, HMBR dissociation constants were measured for all constructs in the absence and in the presence of a saturating concentration of glutamate ([glutamate]$_{sat}$ = 5 mM) (Figure III-2). A control experiment measuring the influence of glutamate on the affinity of FAST for HMBR allowed us to verify that the reporter itself was not sensitive to the analyte. We observed that all topologies showed reasonable fluorogen affinity, ranging from 0.1 to 1.7 µM, indicating that FAST or cpFAST remain functional upon coupling with the glutamate binding domain GltI. A trend could be drawn from these results, underlining different behaviours depending on the use of FAST or cpFAST as a reporter domain:

- The topologies including FAST in its native (cpGlu-FAST-2 and Glu-FAST-3) or split form (Glu-FAST 1 and cpGlu-FAST-4) showed no or weak glutamate dependence, resulting in similar fluorogen binding affinities in both analyte-bound and analyte-free sensor conformations. Moreover, the K_D values of these topologies were very close to FAST. These results suggested that FAST was folding properly in these topologies, leading to its functional reconstitution.

- The topologies including cpFAST in its native (cpGlu-FAST-1 and Glu-FAST-4) or split form (Glu-FAST-2 and cpGlu-FAST-3, respectively) showed variable dependence to the presence of glutamate, in agreement with cpFAST having a higher conformational sensitivity. Fluorogen affinity increased upon analyte addition, attesting of a positive cooperative coupling between the reporter and the sensing unit. In this case, the circular permutation of the reporter presumably lowered the affinities for HMBR in absence of glutamate, allowing a larger variation of affinity upon glutamate binding.

Glu-FAST-2 and Glu-FAST-4 topologies showed promising dependence on glutamate: indeed, around a 2-fold affinity increase for HMBR was observed upon glutamate addition. The affinity range was higher in the Glu-FAST-4 sensor version, giving an interesting indication that reporter insertion in the sensing domain allows its efficient reconstitution, resulting in binding properties very close to cpFAST. However, Glu-FAST-2 showed a slightly higher glutamate dependence. Moreover, this topology displayed favourable features regarding the aim of this project: a biosensor design based on the native sensing domain avoids effort and time-costly protein engineering steps. For instance, the determination of a suitable insertion position of the fluorescent reporter in the sensing domain (as in Glu-FAST-3 or Glu-FAST-4 topologies), or the development of a functional circularly permuted sensing domain (as in cpGlu-FAST-1 or cpGlu-FAST-3 topologies) could impede the generalization of our biosensor design to other analytes.

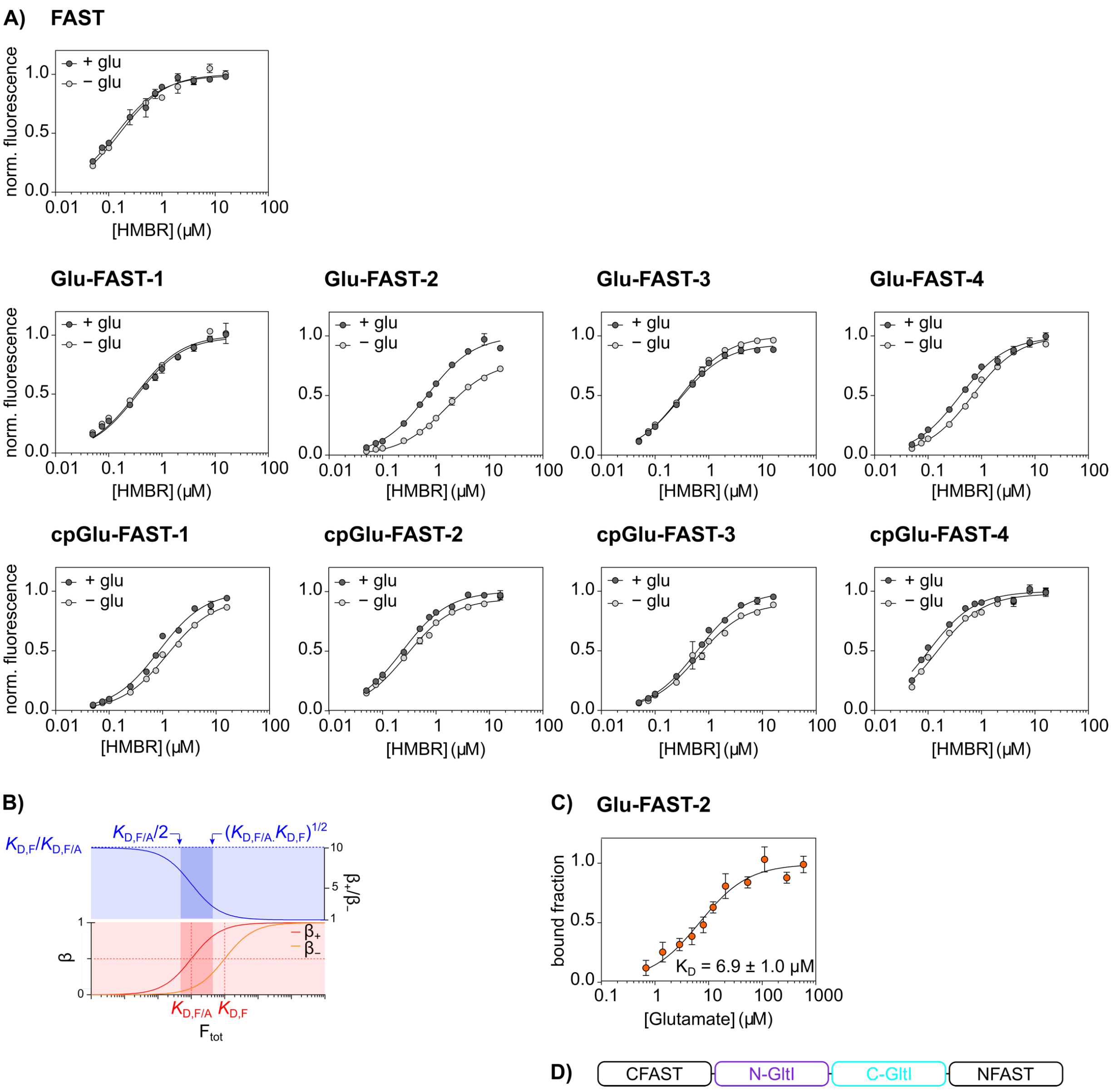

Figure III-2. Characterization of the FAST-based glutamate biosensor topologies. A) HMBR titration curves of FAST and the eight topologies of FAST-based glutamate biosensors, in absence (light grey) or in presence of 5 mM glutamate (dark grey) in pH 7.4 HEPES buffer (50 mM) containing NaCl (150 mM). The least-squares fit (line) gave the thermodynamic dissociation constant $K_{D,HMBR}$ and $K_{D,HMBR/glu}$ provided in Table III-1. The sensor concentration was fixed at 0.1 µM. **B)** Simulated fluorogen binding curves in the presence and absence of analyte (with $K_{D,F}$ = 10 $K_{D,F/A}$). β_+ and β_- are the fluorogen bound fractions in presence and absence of the analyte, respectively. Choosing the concentration of fluorogen between $K_{D,F/A}/2$ and $(K_{D,F/A}.K_{D,F})^{1/2}$ (contrasted rectangles) is a good compromise to obtain both good dynamic range and satisfactory detection sensitivity. Adapted from Tebo et al.[19] **C)** Glutamate titration curve of Glu-FAST-2 in the presence of 1 µM HMBR. Data represent the mean ± sem (n = 3). The least-squares fit (line) gave the thermodynamic dissociation constant $K_{D,glu\ app}$. The sensor concentration was fixed at 0.1 µM. **D)** Topology of the selected biosensor Glu-FAST-2.

Table III-1. Characterization of the FAST-based glutamate biosensor topologies. For each sensor is given the dissociation constant of the fluorogen in absence of glutamate ($K_{D,HMBR}$), in presence of 5 mM of glutamate ($K_{D,HMBR/glu}$), and the cooperativity constant α, calculated as the ratio of the dissociation constant in absence of glutamate and in presence of glutamate ($K_{D,HMBR}/K_{D,HMBR/glu}$).

Sensor	$K_{D,HMBR}$ (μM)	$K_{D,HMBR/glu}$ (μM)	α
FAST	0.14 ± 0.01	0.16 ± 0.01	1.1
Glu-FAST-1	0.33 ± 0.04	0.34 ± 0.03	1.0
cpGlu-FAST-1	1.2 ± 0.08	0.86 ± 0.08	1.4
Glu-FAST-2	1.5 ± 0.05	0.68 ± 0.05	2.2
cpGlu-FAST-2	0.28 ± 0.02	0.24 ± 0.01	1.2
Glu-FAST-3	0.31 ± 0.01	0.28 ± 0.02	1.1
cpGlu-FAST-3	0.63 ± 0.06	0.61 ± 0.03	1.0
Glu-FAST-4	0.68 ± 0.04	0.40 ± 0.02	1.7
cpGlu-FAST-4	0.14 ± 0.01	0.10 ± 0.01	1.4

Consequently, Glu-FAST-2 was selected as the most promising version for further characterization and optimization, as it could in principle be transposed to other sensors by switching the analyte recognition domain. To determine the glutamate affinity of Glu-FAST-2, we measured fluorescence in presence of 1 μM HMBR and various glutamate concentrations. Note that the concentration of HMBR was chosen equal to $(K_{D,HMBR}.K_{D,HMBR/glu})^{1/2}$. As it was previously described, this concentration is a good compromise to have both a good dynamic range and an acceptable fluorescence signal. Glutamate titration with Glu-FAST-2 showed a 1.8-fold fluorescence increase upon addition of the analyte. Fitting of the glutamate titration curve yielded an apparent dissociation constant $K_{D,glu\ app}$ = 6.9 ± 1.0 μM. This affinity was expected to be too high for the detection of intracellular glutamate concentrations, estimated in the millimolar range, but could nevertheless be useful for extracellular measurement. Further optimization would however be required to improve the dynamic range, in order to provide a reliable increase of the fluorescent signal upon analyte-binding.

III.2.2. Evaluation of alternative circularly permutated FAST variants

In the course of this thesis, two viable circular permutation positions of FAST, cpFAST(24-25) and cpFAST(98-99), were identified and characterized, and will be more thoroughly described in chapter VI of this manuscript. While cpFAST(98-99) showed proper folding and interaction between its NFAST and CFAST fragments, yielding good affinities for HMBR, the weak affinity between cpFAST(24-25) fragments resulted in a protein tag with poor folding and low affinity for the fluorogen. Despite their very different properties and behaviours, they were both considered interesting candidates to be used as reporter domains in biosensors based on FAST. Indeed, cpFAST(98-99) characteristics were similar to cpFAST(114-115) and were thus expected to provide comparable biosensing opportunities. In the case of cpFAST(24-25), low affinity between the two fragments was suggested to yield biosensors with very low background fluorescence, assuming that the reporter complementation could be coerced by conformational strain from the coupled sensing domain.

The aforementioned topological study underlined the critical influence of the sensing domain insertion position. For exhaustive assessment of the behaviour change upon such modifications, we decided to insert GltI in both cpFAST(24-25) and cpFAST(98-99), and their non-circularly permuted versions, respectively at the position 24-25 and 98-99, yielding Glu-FAST(24-25)-2, Glu-FAST(98-99)-2, Glu-FAST(24-25)-1 and Glu-FAST(98-99)-1, respectively. The HMBR affinity dependence on the presence of glutamate was thus determined for these four designs (Figure III-3).

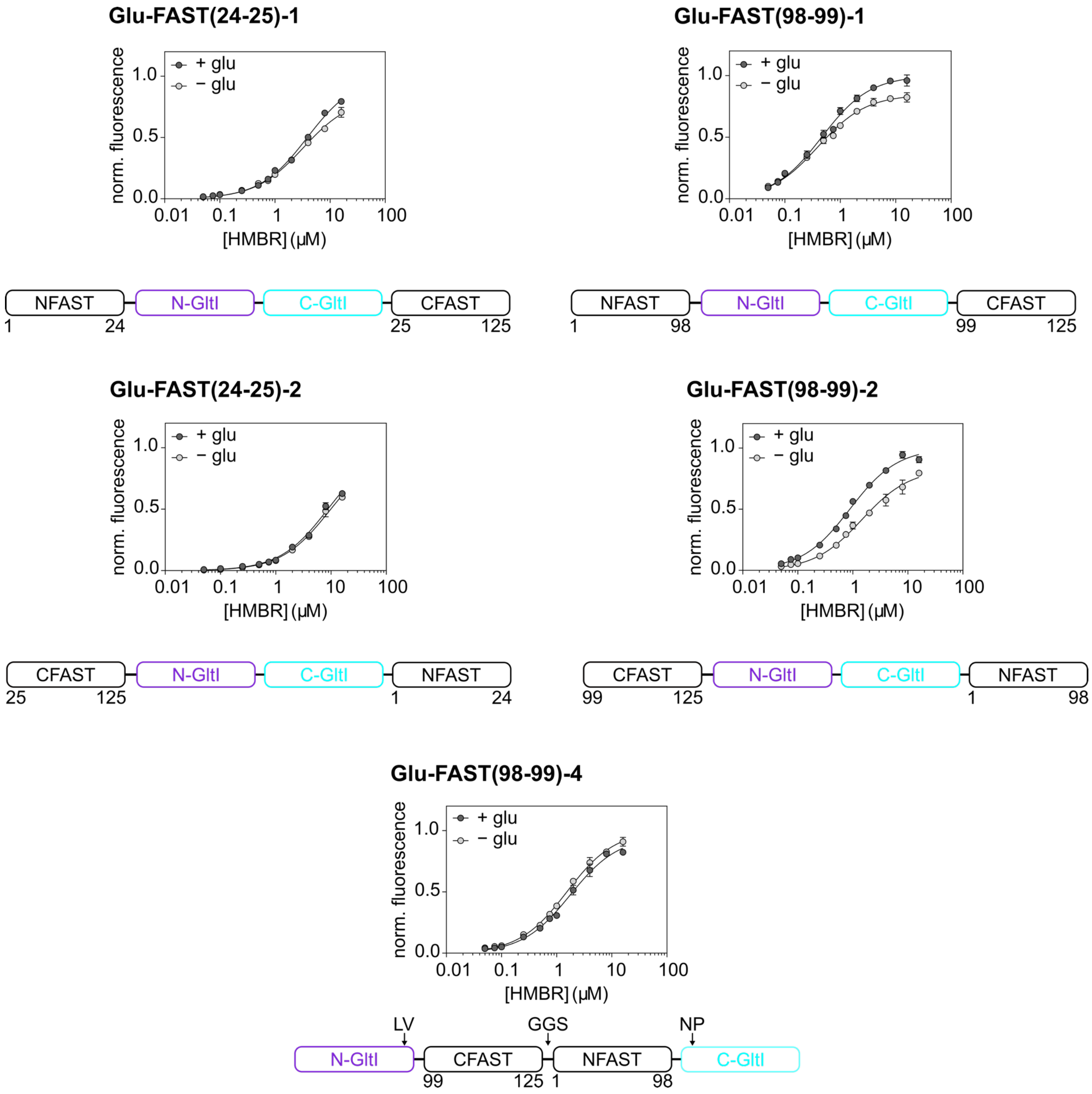

Figure III-3. Characterization of the glutamate biosensors based on circular permutations of FAST. HMBR titration curves of glutamate sensors variants based on cpFAST(24-25) and cpFAST(98-99), in absence (light grey) or in presence of 5 mM glutamate (dark grey) in pH 7.4 HEPES buffer (50 mM) containing NaCl (150 mM). Data represent the mean ± sem (n = 3). The least-squares fit (line) gave the thermodynamic dissociation constant $K_{D,HMBR}$ and $K_{D,HMBR/glu}$ provided in Table III-2. The sensor concentration was fixed at 0.1 µM.

Table III-2. Characterization of the glutamate biosensors based on circular permutations of FAST. For each sensor is given the dissociation constant of the fluorogen in absence of glutamate ($K_{\mathrm{D,HMBR}}$), in presence of 5 mM of glutamate ($K_{\mathrm{D,HMBR/glu}}$), and the cooperativity constant α, calculated as the ratio of the dissociation constant in absence of glutamate and in presence of glutamate ($K_{\mathrm{D,HMBR}}/K_{\mathrm{D,HMBR/glu}}$).

Sensor	$K_{\mathrm{D,HMBR}}$ (µM)	$K_{\mathrm{D,HMBR/glu}}$ (µM)	α
Glu-FAST(24-25)-1	3.3 ± 0.2	3.9 ± 0.3	1.2
Glu-FAST(24-25)-2	9.3 ± 1.3	8.7 ± 1.3	1.1
Glu-FAST(98-99)-1	0.40 ± 0.02	0.46 ± 0.03	1.2
Glu-FAST(98-99)-2	1.5 ± 0.1	0.88 ± 0.06	1.7
Glu-FAST(98-99)-4	1.5 ± 0.1	1.7 ± 0.1	0.8

Firstly, no glutamate dependence was observed from insertion of GltI in FAST at position 24-25 or cpFAST(24-25) (respectively Glu-FAST(24-25)-1 and Glu-FAST(24-25)-2). Indeed, the reporter domain showed low affinity for the fluorogen, and did not appear to reconstitute in the analyte-bound conformation of the biosensor. The coupling did not appear strong enough to force the intramolecular interaction between FAST fragments upon additional conformational strain provided by glutamate binding. Thus, consistently with the low affinity observed between the fragments NFAST(1-24) and CFAST(25-125) (further discussed in chapter VI), fluorescence seemed to arise only from the binding of HMBR to the CFAST(25-125) fragment. The tag reconstitution could also be hampered by NFAST(1-24) being completely unfolded, making its restructuration energetically unfavourable.

On the other hand, insertion of GltI in cpFAST(98-99) or FAST at position 98-99 yielded biosensors that behave in a similar way as insertion in cpFAST(114-115) or in FAST at position 114-115. Indeed, low glutamate dependence was observed from insertion of the sensing domain in FAST at position 98-99 (Glu-FAST(98-99)-1). The reporter in this topology retained very high affinity for the fluorogen, indicating that the interaction between the two fragments led to proper folding of the tag. However, positive cooperative allosteric coupling was observed from the sensor resulting from the insertion of GltI in cpFAST(98-99) (Glu-FAST(98-99)-2). Showing properties similar to Glu-FAST-2, the affinity of Glu-FAST(98-99)-2 for HMBR increased by 1.7-fold upon glutamate binding.

Encouraged by the results obtained with cpFAST(98-99), we also tested whether the insertion of cpFAST(98-99) in the sensing domain could yield a functional glutamate biosensor Glu-FAST(98-99)-4. Yet this topology resulted in a sensor weakly dependent on the analyte, and rather low affinity for HMBR. This may be explained by the termini of this circular permutation being located in close proximity to the fluorogen binding pocket, in the loop that was originally evolved from PYP to non-covalently bind HBR derivatives. This position is thus expected to be directly involved in the fluorogen binding. Consequently, conformational strain caused by insertion into GltI might prevent efficient reconstitution of the fluorogen binding site. Thus, the impaired conformation of the reporter domain in Glu-FAST(98-99)-4 yielded low fluorogen affinities in both open and closed biosensor conformations.

Nevertheless, the promising properties of cpFAST(98-99) did not allow improvement in the biosensor performance compared to Glu-FAST-2 based on cpFAST(114-115). This study showed us however that cpFAST(98-99) could be an additional reporter available for the development of fluorogenic biosensors, offering further design opportunities (see chapter VI).

III.3. Optimization of the selected glutamate biosensor design

III.3.1. Sensing module optimization

GltI truncations

Although functional, Glu-FAST-2 displayed a rather weak positive allosteric coupling between the sensing and the reporter domains, that appeared to prevent the biosensor from showing a high dynamic range. One optimization strategy then consisted in increasing the rigidity of the connecting regions to increase the sensitivity of the reporter to the conformational change undergone by the sensing domain upon glutamate binding. The crystal structure of the sensing domain GltI indicated spatially close and relatively flexible native termini regions. We suggested that truncation of these weakly structured residues could reduce unspecific interactions between the flanking reporter fragments, thus improving the signal-to-noise ratio of the biosensor. Analogous screening of truncated GltI versions in the development of SuperGluSnFR allowed the dramatic improvement of the sensor performance, by modulating the distance and orientation between the two FRET partners.[9]

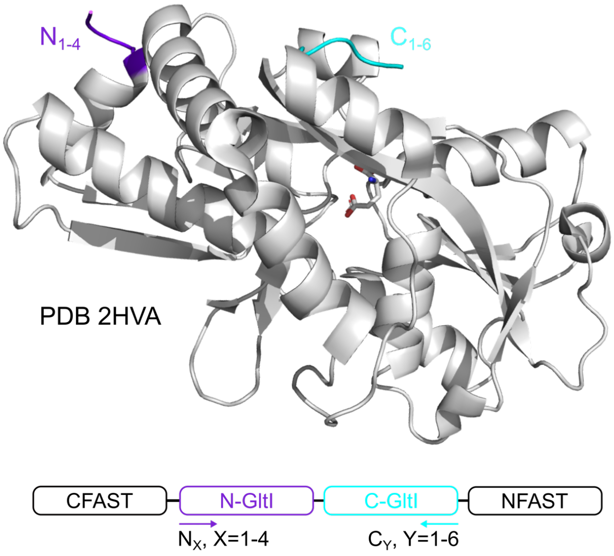

Figure III-4. Truncation of the sensing domain GltI. A library of 35 glutamate sensors with the Glu-FAST-2 topology was generated from truncation of 0 to 4 and 0 to 6 residues at the N- and C-terminus of GltI, respectively (represented in purple and cyan, respectively).

The flexible terminal sequences of GltI consist in four residues at the N-terminus (AAGS) and six residues at the C-terminus (NDKALK). The combination of all possible truncation lengths gave rise to 35 GltI N_xC_y variants that were inserted in cpFAST(114-115), with the insertion of GltI N_0C_0 being Glu-FAST-2 (Figure III-4). The glutamate dependence of the resulting biosensors (Glu-FAST-2-GltI(N_xC_y)) was measured and compared to the insertion of full-length GltI in the reporter domain (Figure III-5).

This first characterization allowed to identify potential candidates of biosensors with improved features. They needed to show a comparable or higher dependence to glutamate than Glu-FAST-2 ($\alpha \geq 2.2$), while retaining reasonable fluorescence intensity and affinity for the fluorogen in the analyte-bound conformation of the sensor. In this regard, two constructs seemed to have interesting characteristics: Glu-FAST-2-GltI(N_0C_2) and Glu-FAST-2-GltI(N_1C_0). No linear response was observed from increasing the number of truncated residues, nevertheless some trend could be drawn from this screening. Depending on the combination, biosensors with less than 6 truncated residues appeared to enable reconstitution of the reporter to some extent in the glutamate-bound and/or -free conformation, with variable glutamate dependence. However, truncation of more than 6 residues, especially for GltI-N_4C_X, led to low affinity for HMBR as well as dramatically decreased apparent brightness. This observation indicated a limit in the number of truncated residues, above which the distance between GltI termini did not allow proper interaction between the two reporter fragments, leading to improper immobilization of the fluorogen, thus low brightness. Further characterization showed that GltI truncations had no effect on the biosensors affinity for glutamate, that remained around 5 μM. Despite a slightly higher positive cooperativity, Glu-FAST-2-GltI(N_0C_2) and Glu-FAST-2-GltI(N_1C_0) did not show a significantly improved dynamic range, suggesting that a more significant increase of the cooperativity constant α would be required to observe a valuable improvement of the biosensor performance.

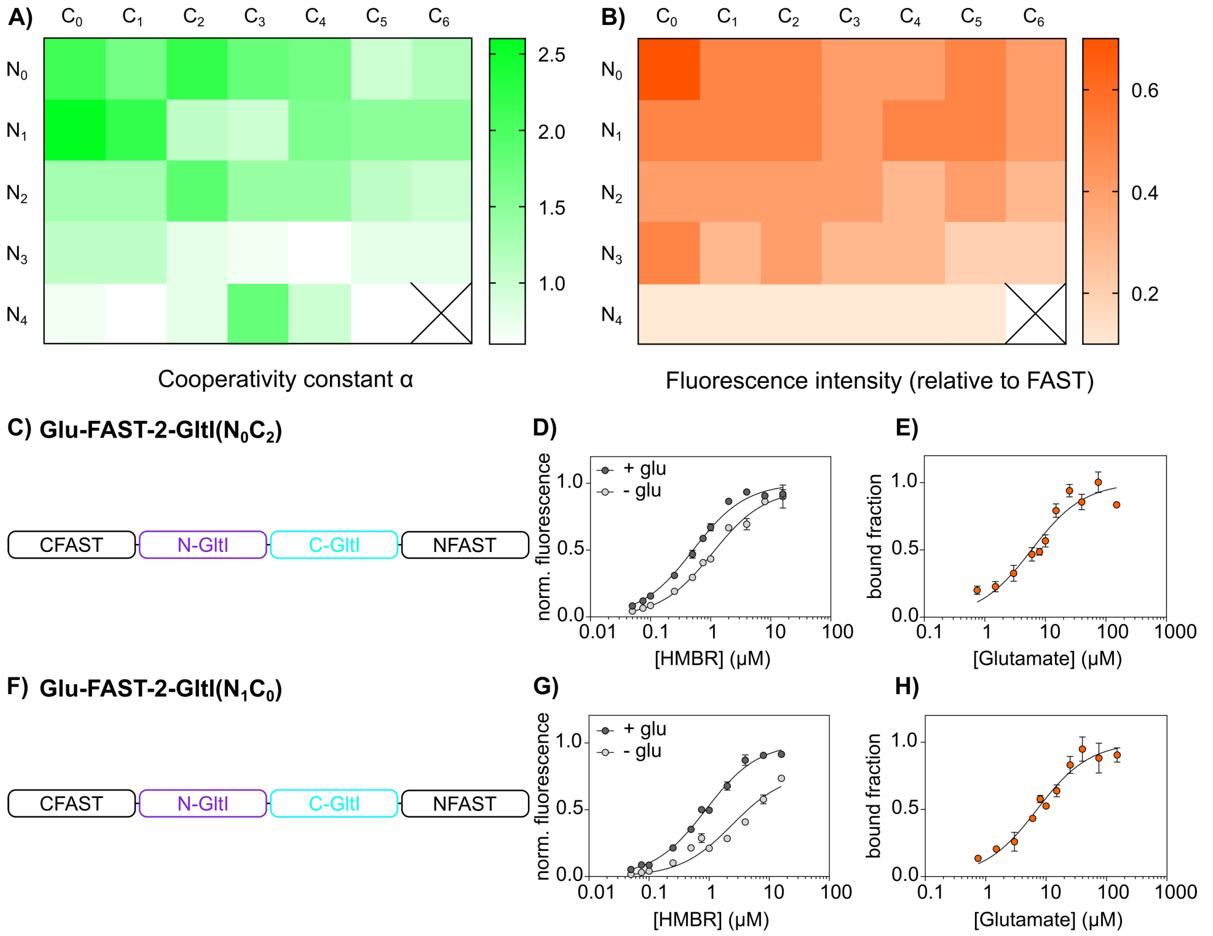

Figure III-5. Characterization of GltI truncations in Glu-FAST-2. A) Cooperativity constant depicted in pseudo-color from the lowest (white) to the highest (bright green). **B)** Relative brightness compared to FAST, depicted in pseudo-color from the lowest (white) to the highest (bright orange). **C) & F)** Topologies of the selected biosensors Glu-FAST-2-GltI(N_0C_2) and Glu-FAST-2-GltI(N_1C_0), respectively. **D) & G)** HMBR titration curves of Glu-FAST-2-GltI(N_0C_2) and Glu-FAST-2-GltI(N_1C_0), respectively, in absence (light grey) or in presence of 5 mM glutamate (dark grey) in pH 7.4 HEPES buffer (50 mM) containing NaCl (150 mM). The least-squares fit (line) gave the thermodynamic dissociation constant $K_{D,HMBR}$ and $K_{D,HMBR/glu}$ provided in Table III-3. **E) & H)** Glutamate titration curve of Glu-FAST-2-GltI(N_0C_2) and Glu-FAST-2-GltI(N_1C_0), respectively, in the presence of 1 µM HMBR. Data represent the mean ± sem (n = 3). The least-squares fit (line) gave the apparent thermodynamic dissociation constant $K_{D,glu\ app}$ provided in Table III-3. The sensor concentration was fixed at 0.1 µM.

Table III-3. Characterization of GltI truncations in Glu-FAST-2. For each sensor is given the dissociation constant of the fluorogen in absence of glutamate ($K_{D,HMBR}$), in presence of 5 mM of glutamate ($K_{D,HMBR/glu}$), and the cooperativity constant α, calculated as the ratio of the dissociation constant in absence of glutamate and in presence of glutamate ($K_{D,HMBR}/K_{D,HMBR/glu}$). The apparent dissociation constant of glutamate is also given with the associated fluorescence intensity increase observed upon glutamate addition (F_{max}/F_{min}).

Sensor	$K_{D,HMBR}$ (µM)	$K_{D,HMBR/glu}$ (µM)	α	$K_{D,glu\ app}$ (µM)	F_{max}/F_{min}
Glu-FAST-2-GltI(N_0C_2)	1.1 ± 0.1	0.51 ± 0.09	2.2	5.9 ± 1.4	1.9
Glu-FAST-2-GltI(N_1C_0)	2.4 ± 0.6	0.88 ± 0.07	2.7	7.1 ± 1.2	1.9

GltI truncations did not yield sufficient rigidity to prevent FAST fragments self-assembly while allowing optimal reporter conformation in the glutamate-bound biosensor form. While this strategy was successful in the optimization of the FRET sensor SuperGluSnFR, our results suggested that reconstitution of FAST is less sensitive than FRET efficiency to modifications of distance and orientation of the sensing domain termini. Optimization of the Glu-FAST biosensor by rational design should thus focus on efficiently preventing unspecific interactions between the reporter fragments, and ensure efficient complementation upon interaction of the sensor with glutamate.

III.3.2. Reporter module optimization

FAST orthologs

Modification of the sensing domain termini regions showed inconclusive results: consequently, efforts were then directed towards rational design of the reporter domain itself. As will be described in further details in chapter VI of this manuscript, different ortholog versions of the originally developed FAST from *Halorodhospira halophila* ($^{(\mathrm{Hha})}$FAST) were previously generated and characterized. The resulting $^{\mathrm{HboL}}$FAST, $^{\mathrm{HspG}}$FAST, $^{\mathrm{RspA}}$FAST, $^{\mathrm{Ilo}}$FAST, $^{\mathrm{TsiA}}$FAST, and $^{\mathrm{Rsa}}$FAST displayed various brightness and fluorogen binding properties. Ongoing research about the split versions of these orthologs demonstrated that interaction between NFAST and CFAST fragments strongly depend on the ortholog sequence. Indeed, when used as reporter for protein-protein interactions, very different behaviours were observed in terms of complementation efficiency when brought in close proximity, as well as self-assembly. Such differences were expected to be transposed in the context of biosensors design.

It was first decided to generate and characterize the circularly permuted versions of these orthologs, cp$^{\mathrm{Ortholog}}$FAST(114-115), in order to assess their functionality and fluorogen binding properties. However, setbacks were encountered at the production step, attributed to low stability and possible tendency to aggregate. We observed poor bacterial overexpression of cp$^{\mathrm{TsiA}}$FAST and cp$^{\mathrm{Rsa}}$FAST, and encountered purification difficulties for cp$^{\mathrm{HspG}}$FAST and cp$^{\mathrm{RspA}}$FAST. Only cp$^{\mathrm{HboL}}$FAST and cp$^{\mathrm{Ilo}}$FAST could thus be isolated and characterized. HMBR titration showed that both reporters were functional, and the results were consistent with previous comparisons of FAST and cpFAST, showing around a 6-fold affinity loss for the fluorogen upon circular permutation.

Table III-4. Characterization of circular permutation of $^{\mathrm{Ortholog}}$FAST variants. For each ortholog is given the dissociation constant of the fluorogen HMBR for the native protein $^{\mathrm{Ortholog}}$FAST and its circularly permuted version cp$^{\mathrm{Ortholog}}$FAST.

Ortholog	$^{\mathrm{Ortholog}}$FAST $K_{\mathrm{D,HMBR}}$ (µM)	cp$^{\mathrm{Ortholog}}$FAST $K_{\mathrm{D,HMBR}}$ (µM)
$^{(\mathrm{Hha})}$FAST	0.13	0.99 ± 0.11
$^{\mathrm{HboL}}$FAST	0.08	0.44 ± 0.03
$^{\mathrm{Ilo}}$FAST	0.23	1.3 ± 0.2

This conserved tendency interestingly provided a small affinity range between the different circularly permuted orthologs, that could have an influence on the cooperativity of glutamate binding in their corresponding biosensor. This observation, in addition to the expected differences of complementation properties between $^{\mathrm{Ortholog}}$NFAST and $^{\mathrm{Ortholog}}$CFAST fragments, both motivated an attempt to insert the sensing domain GltI in these cp$^{\mathrm{HboL}}$FAST and cp$^{\mathrm{Ilo}}$FAST. Fluorogen binding of the resulting biosensors Glu-$^{\mathrm{HboL}}$FAST-2 and Glu-$^{\mathrm{Ilo}}$FAST-2 was evaluated and showed the functional reconstitution of the reporter domain in the glutamate-bound form. The observed behaviour of both generated sensors were consistent with the respective split ortholog FAST versions used as a reporter. Indeed, split FAST and split $^{\mathrm{HboL}}$FAST properties appeared comparable when characterized as reporters of the FKBP-FRB interaction (Rakotoarison & Tebo et al., manuscript in preparation). Moreover, the same characterization showed that split $^{\mathrm{Ilo}}$FAST displayed lower specific complementation and self-assembly, suggesting lower affinity between $^{\mathrm{Ilo}}$FAST fragments that was confirmed when using this ortholog version as a reporter in our glutamate biosensor. However, despite $K_{\mathrm{D,HMBR/glu}}$ values comparable to the circularly permuted $^{\mathrm{Ortholog}}$FAST versions, both sensors provided similar cooperativity constants α to Glu-FAST-2. This modest inter-domain interaction did not yield to any change in the biosensors affinity for glutamate, nor allowed any dynamic range improvement between the analyte-bound and -free conformations.

Table III-5. Characterization of glutamate biosensors based on $^{\mathrm{Ortholog}}$FAST variants. For each sensor is given the dissociation constant of the fluorogen in absence of glutamate ($K_{\mathrm{D,HMBR}}$), in presence of 5 mM of glutamate ($K_{\mathrm{D,HMBR/glu}}$), and the cooperativity constant α, calculated as the ratio of the dissociation constant in absence of glutamate and in presence of glutamate ($K_{\mathrm{D,HMBR}}/K_{\mathrm{D,HMBR/glu}}$). The dissociation constant of glutamate are also given with the associated fluorescence intensity increase observed upon glutamate addition ($F_{\mathrm{max}}/F_{\mathrm{min}}$).

Sensor	$K_{\mathrm{D,HMBR}}$ (µM)	$K_{\mathrm{D,HMBR/glu}}$ (µM)	α	$K_{\mathrm{D,glu\ app}}$ (µM)	$F_{\mathrm{max}}/F_{\mathrm{min}}$
Glu-$^{\mathrm{HboL}}$FAST-2	1.3 ± 0.1	0.53 ± 0.03	2.4	6.4 ± 1.8	1.7
Glu-$^{\mathrm{Ilo}}$FAST-2	2.7 ± 0.2	1.2 ± 0.1	2.3	10 ± 2.6	1.8

Although the use of FAST orthologs as reporter domains did not allow to optimize our glutamate sensor, this study tended to confirm the previously suggested weak allosteric coupling of this design. Improving the α constant would then rely on a substantially lower self-assembly, while retaining high specific complementation between reporter fragments. The behavioural consistency between the use of $^{\text{Ortholog}}$FAST as protein-protein interaction reporters and their insertion in biosensors is nevertheless promising for the general objective of fluorogenic sensor design. In fact, $^{\text{RspA}}$FAST and $^{\text{TsiA}}$FAST were notably characterized by very low unspecific interaction between their split fragments, thus showing potential to substantially improve the dynamic range of such biosensors.

FAST truncations

Other strategies to decrease self-assembly of the reporter domain then focused on truncations of the reporter fragments termini. It was previously demonstrated that deleting a single residue at the C-terminus of CFAST decreased the fragment apparent affinity for NFAST in both cpFAST(114-115) and its split version.[20] Indeed, the use of CFAST10 (= CFAST(115-124)) allowed a significant improvement of the dynamic range in different sensors and PPI reporter designs. Thus, we assumed that applying a similar strategy to our glutamate sensor design would also lead to decreased unspecific reporter assembly.

In the PPI reporter designs based on splitFAST, CFAST10 was fused to the POI or sensing domain at its N-terminus; while in Glu-FAST-2 sensor topology the glutamate sensing domain is connected at the C-terminus of CFAST. A different response upon truncation of CFAST was consequently expected, and removal of a single residue was tested at both termini of the fragment (yielding CFAST(116-125) and CFAST(115-124)). Each truncation indeed affected differently the resulting sensors (Figure III-6). Glu-FAST-2-CFAST(115-124) showed significantly lower HMBR affinity in both glutamate-bound and -free conformations. While this effect was expected to some extent from reduced fragments affinity, it might also result from shifting by one residue the CFAST fragment towards GltI, thus decreasing its availability to interact with NFAST. It should be noted that CFAST10 fusion at the N-ter of calmodulin led to the successful development of a Ca^{2+} sensor based on splitFAST10; however, this intermolecular design might provide more flexibility, thus better complementation of the reporter. On the other hand, the reporter affinity for HMBR upon glutamate-induced complementation of CFAST(116-125) was comparable to CFAST11. Moreover, removal of Gly115 did not affect the biosensor affinity for glutamate, and appeared to slightly decrease the fragments affinity, moderately improving the fluorescence dynamic range.

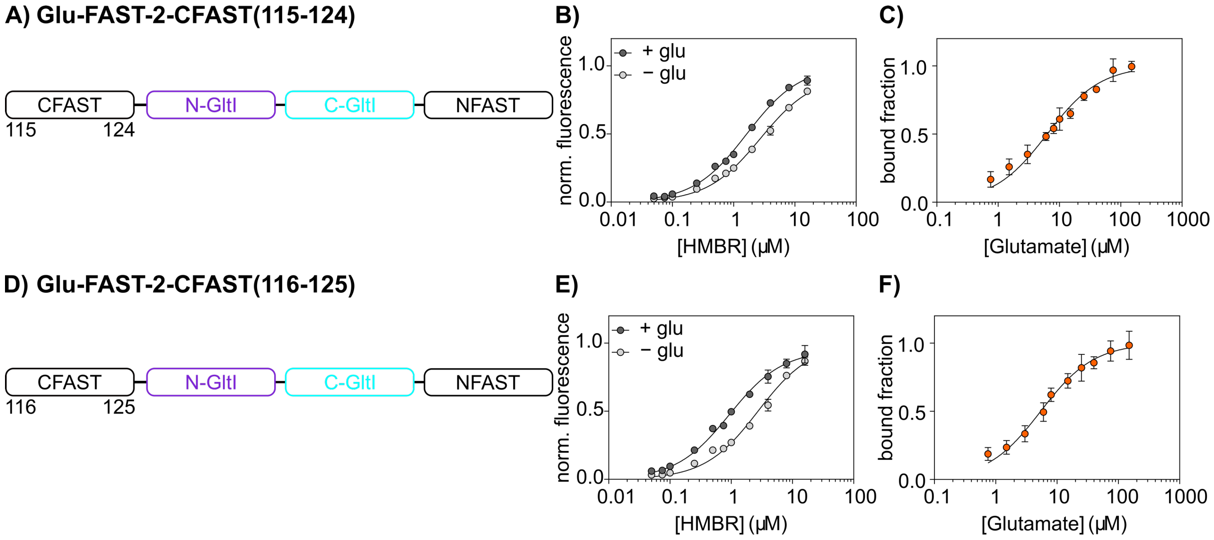

Figure III-6. Characterization of CFAST truncations in Glu-FAST-2. A) & D) Topologies of the biosensors Glu-FAST-2-CFAST(115-124) and Glu-FAST-2-CFAST(116-125), respectively. **B) & E)** HMBR titration curves of Glu-FAST-2-CFAST(115-124) and Glu-FAST-2-CFAST(116-125), respectively, in absence (light grey) or in presence of 5mM glutamate (dark grey) in pH 7.4 HEPES buffer (50 mM) containing NaCl (150 mM). **C) & F)** Glutamate titration curve of Glu-FAST-2-CFAST(115-124) and Glu-FAST-2-CFAST(116-125), respectively in the presence of 1 µM HMBR. Data represent the mean ± sem (n = 3). The least-squares fit (line) gave the thermodynamic dissociation constant $K_{\mathrm{D,HMBR}}$ and $K_{\mathrm{D,HMBR/glu}}$ and the apparent dissociation constant $K_{\mathrm{D,glu\ app}}$ provided in Table III-6. The sensor concentration was fixed at 0.1 µM.

Table III-6. Characterization of CFAST truncations in Glu-FAST-2. For each sensor is given the dissociation constant of the fluorogen in absence of glutamate ($K_{\mathrm{D,HMBR}}$), in presence of 5 mM of glutamate ($K_{\mathrm{D,HMBR/glu}}$), and the cooperativity constant α, calculated as the ratio of the dissociation constant in absence of glutamate and in presence of glutamate ($K_{\mathrm{D,HMBR}}/K_{\mathrm{D,HMBR/glu}}$). The dissociation constant of glutamate is also given with the associated fluorescence intensity increase observed upon glutamate addition ($F_{\mathrm{max}}/F_{\mathrm{min}}$).

Sensor	$K_{\mathrm{D,HMBR}}$ **(µM)**	$K_{\mathrm{D,HMBR/glu}}$ **(µM)**	**α**	$K_{\mathrm{D,glu\ app}}$ **(µM)**	$F_{\mathrm{max}}/F_{\mathrm{min}}$
Glu-FAST-2-CFAST(115-124)	2.8 ± 0.2	1.7 ± 0.1	1.6	6.3 ± 0.9	1.7
Glu-FAST-2-CFAST(116-125)	2.7 ± 0.3	0.93 ± 0.06	2.9	5.4 ± 0.4	2.4

Next we tested whether FAST fragments affinity could be further decreased by truncation of NFAST. As deletion at the connecting sites seemed to unfavourably shift the fragments, thus hampering their interaction, the C-terminus residue of NFAST (Ser114) was removed. Modest improvement of the cooperativity constant α was obtained upon insertion of the resulting fragment NFAST(1-113) in the Glu-FAST-2 topology. However, this deletion also came with a lower fluorogen affinity of the biosensor in closed conformation. The effect of NFAST(1-113) combined with CFAST(116-125) was also evaluated, and a similar affinity loss for HMBR was observed. In neither case was the dynamic range noticeably improved upon glutamate addition. These results confirmed that a significant HMBR affinity difference is required between the glutamate-bound and -free conformation, in order to substantially improve our FAST-based biosensor. Consequently, NFAST truncation did not yield a satisfying increase of the sensor performance.

Table III-7. Characterization of NFAST truncations in Glu-FAST-2 and Glu-FAST-2-CFAST(116-125). For each sensor is given the dissociation constant of the fluorogen in absence of glutamate ($K_{D,HMBR}$), in presence of 5 mM of glutamate ($K_{D,HMBR/glu}$), and the cooperativity constant α, calculated as the ratio of the dissociation constant in absence of glutamate and in presence of glutamate ($K_{D,HMBR}/K_{D,HMBR/glu}$). The dissociation constant of glutamate is also given with the associated fluorescence intensity increase observed upon glutamate addition (F_{max}/F_{min}).

Sensor	**$K_{D,HMBR}$ (μM)**	**$K_{D,HMBR/glu}$ (μM)**	**α**	**$K_{D,glu\ app}$ (μM)**	**F_{max}/F_{min}**
Glu-FAST-2-NFAST(1-113)	2.7 ± 0.5	1.1 ± 0.1	2.5	4.0 ± 0.9	2.0
Glu-FAST-2-NFAST(1-113)-CFAST(116-125)	2.6 ± 0.3	1.2 ± 0.2	2.2	7.8 ± 2.0	2.0

To conclude, it was observed that modifications of the reporter domain indeed have an influence on Glu-FAST sensor fluorescent properties. However, a balance needs to be found between decreasing the fragments affinity, thus lowering their unspecific interaction, without adverse affinity loss of the reconstituted reporter for the fluorogen. In this regard, the CFAST(116-125) was identified as a promising element for the optimization of the FAST-based biosensors.

III.3.3. Linkers optimization

GG linkers

In addition to protein engineering of the constituent domains, insertion and optimization of inter-domain linkers are usually a crucial step in the development of fluorescent biosensors. Indeed, by modifying the length and flexibility of the connecting sequences between the different domains, the affected orientation and interaction of the coupled reporter can yield to a substantial change of its fluorescent properties. It was observed that the Glu-FAST-2 topology allowed the reconstitution of a functional cpFAST reporter upon interaction of the sensor with glutamate, with $K_{D,HMBR/glu}$ = 0.7 μM. Yet, previous characterization showed that cpFAST(114-115) could reach fluorogen dissociation constant close to native FAST (cpFAST(114-115)7 indeed diplayed $K_{D,HMBR}$ = 0.16 μM) when weakly constrained by a long and flexible 18-residues GGS linker.[19] This tends to indicate that the analyte-bound state of the sensor did not provide optimal folding of the reporter domain.

Consequently, we tested whether additional flexibility at the insertion point of GltI into cpFAST(114-115) could increase accessibility of each reporter fragment, thus yielding a more efficient complementation in the presence of glutamate. Two glycine residues were thus inserted at one or both connecting sites between the sensing and the reporter domains (Figure III-7). These short flexible linkers were expected to improve the affinity of the reconstituted cpFAST for the fluorogen, without losing the allosteric coupling with GltI.

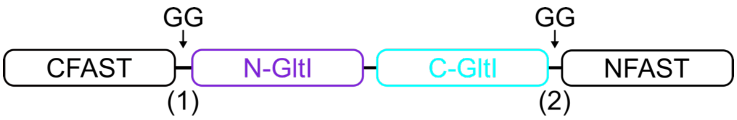

Figure III-7. Position of GG linkers insertions in Glu-FAST-2.

Table III-8. Characterization of GG linkers insertions in Glu-FAST-2. For each sensor is given the dissociation constant of the fluorogen in absence of glutamate ($K_{D,HMBR}$), in presence of 5 mM of glutamate ($K_{D,HMBR/glu}$), and the cooperativity constant α, calculated as the ratio of the dissociation constant in absence of glutamate and in presence of glutamate ($K_{D,HMBR}/K_{D,HMBR/glu}$). The dissociation constant of glutamate is also given with the associated fluorescence intensity increase observed upon glutamate addition (F_{max}/F_{min}).

Sensor	$K_{D,HMBR}$ (µM)	$K_{D,HMBR/glu}$ (µM)	α	$K_{D,glu\ app}$ (µM)	F_{max}/F_{min}
Glu-FAST-2-GG(1)	0.90 ± 0.01	0.53 ± 0.03	1.7	5.5 ± 1.4	1.6
Glu-FAST-2-GG(2)	1.3 ± 0.09	0.90 ± 0.06	1.4	6.1 ± 1.0	1.9
Glu-FAST-2-GG(1+2)	0.86 ± 0.05	0.48 ± 0.02	1.8	5.3 ± 1.0	1.7

We observed that insertion of these GG linkers had a weak effect on the glutamate dependence of the biosensors. Increased flexibility seemed to improve accessibility of FAST fragments in both the analyte-bound and -free states of the sensor. The observed self-assembly was thus too high for the biosensors to show any improved properties.

Moreover, the affinity of the sensors for glutamate did not seem to be altered by either single or double linker insertion. Consistently with the weak allosteric coupling observed from this design, and previous conclusions from the development of fluorescent biosensors with analogous topology,[9] modifications of the native N- and C- termini of GltI did not perturb glutamate binding to the sensing domain. As expected, the fluorescence intensity ratios between the two states were not improved either by any GG linker insertion as unspecific reporter complementation slightly increased background fluorescence as well. Consequently, it was concluded that our FAST-based glutamate sensing system would not be improved by adding flexibility between the different domains.

PP linkers

Instead of inserting flexible linkers, we next tested the insertion of rigid linkers. To increase structural rigidity between the reporter and the sensing domain, we inserted proline residues, characterized by their conformationally strained nature. Two-proline spacers were thus inserted at one or both insertion positions of the sensing domain into the reporter (Figure III-8).

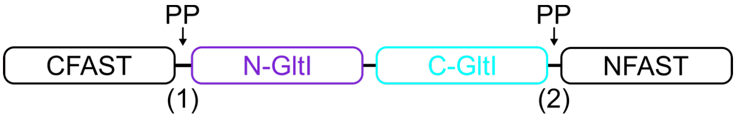

Figure III-8. Position of PP linkers insertions in Glu-FAST-2.

Table III-9. Characterization of PP linkers insertions in Glu-FAST-2. For each sensor is given the dissociation constant of the fluorogen in absence of glutamate ($K_{D,HMBR}$), in presence of 5 mM of glutamate ($K_{D,HMBR/glu}$), and the cooperativity constant α, calculated as the ratio of the dissociation constant in absence of glutamate and in presence of glutamate ($K_{D,HMBR}/K_{D,HMBR/glu}$). The dissociation constant of glutamate with Glu-FAST-2-PP(1+2) is also given with the associated fluorescence intensity increase observed upon glutamate addition (F_{max}/F_{min}).

Sensor	$K_{D,HMBR}$ (μM)	$K_{D,HMBR/glu}$ (μM)	α	$K_{D,glu\ app}$ (μM)	F_{max}/F_{min}
Glu-FAST-2-PP(1)	2.1 ± 0.1	1.0 ± 0.1	2.1	-	-
Glu-FAST-2-PP(2)	2.7 ± 0.2	1.3 ± 0.1	2.1	-	-
Glu-FAST-2-PP(1+2)	3.9 ± 0.2	1.3 ± 0.1	3.0	5.7 ± 1.4	1.9

Unspecific interactions between reporter fragments indeed seemed hampered by insertion of PP linkers in Glu-FAST-2. Despite the affinity loss for HMBR in the glutamate-bound form of the biosensor as well, the observed α constant generally appeared to be improved by additional strain. Noticeable increase of this ratio was observed upon insertion of two prolines at each connecting site (Glu-FAST-2-PP(1+2) : α = 3.0). It should however be noted that these proline insertions did not affect the sensor properties in an additive manner. These first observations encouraged us to study such insertions in the promising sensor variants previously identified.

III.3.4. Design and characterization of an optimized glutamate biosensor

Proline linkers at different positions were thus combined with CFAST(116-125). A similar tendency towards impeded unspecific complementation of the reporter was observed, that might be supported not only by additional rigidity but also increased distance between cpFAST fragments. Certain combinations also showed hampered complementation of the reporter in the glutamate-bound conformation of the sensor. Nevertheless, combination of CFAST(116-125) with insertion of one PP linker at either connection site showed promising glutamate-dependence of the fluorogen affinity. In particular, significant improvement was measured from Glu-FAST-2-CFAST(116-125)-PP(2) (α = 4.3), namely Glu-FAST-2.1, mostly provided by the low fluorogen affinity in the open sensor conformation (Figure III-9).

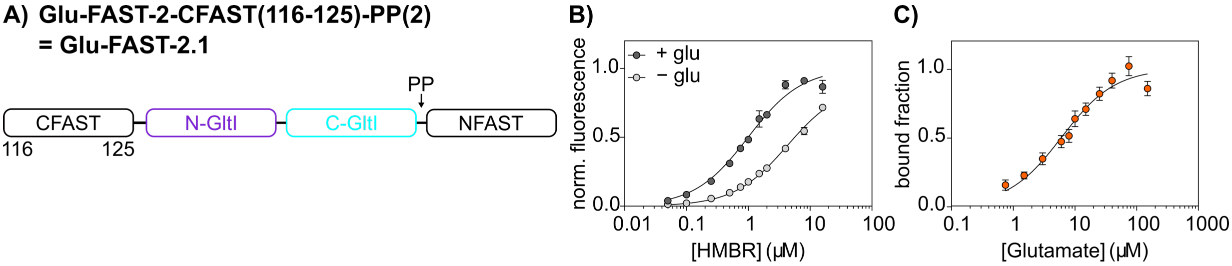

Figure III-9. Characterization of Glu-FAST-2.1. A) Topology of the selected biosensors Glu-FAST-2-CFAST(116-125)-PP(2), namely Glu-FAST-2.1. **B)** HMBR titration curve of Glu-FAST-2.1 in absence (light grey) or in presence of 5 mM glutamate (dark grey) in pH 7.4 HEPES buffer (50 mM) containing NaCl (150 mM). **C)** Glutamate titration curve of Glu-FAST-2.1 in the presence of 1 µM HMBR. Data represent the mean ± sem (n = 3). The least-squares fit (line) gave the thermodynamic dissociation constant $K_{\mathrm{D,HMBR}}$ and $K_{\mathrm{D,HMBR/glu}}$ and the apparent dissociation constant $K_{D,\mathrm{glu\ app}}$ provided in Table III-10. The sensor concentration was fixed at 0.1 µM.

Table III-10. Characterization of PP linkers insertions in Glu-FAST-2-CFAST10. For each sensor is given the dissociation constant of the fluorogen in absence of glutamate ($K_{D,HMBR}$), in presence of 5 mM of glutamate ($K_{D,HMBR/glu}$), and the cooperativity constant α, calculated as the ratio of the dissociation constant in absence of glutamate and in presence of glutamate ($K_{D,HMBR}/K_{D,HMBR/glu}$). The dissociation constant of glutamate is also given with the associated fluorescence intensity increase observed upon glutamate addition (F_{max}/F_{min}).

Sensor	$K_{D,HMBR}$ (µM)	$K_{D,HMBR/glu}$ (µM)	α	$K_{D,glu\ app}$ (µM)	F_{max}/F_{min}
Glu-FAST-2-CFAST(116-125)-PP(1)	4.2 ± 0.2	1.7 ± 0.1	2.5	4.1 ± 0.4	1.8
Glu-FAST-2-CFAST(116-125)-PP(2)	4.3 ± 0.3	1.0 ± 0.1	4.3	6.1 ± 1.0	2.5
Glu-FAST-2-CFAST(116-125)-PP(1+2)	2.4 ± 0.2	1.3 ± 0.1	1.8	-	-

Glutamate titration was performed with the most promising sensor variants identified. As previously observed, modification of the connecting sites does not seem to affect the biosensors affinity for glutamate, with dissociation constants remaining close to 5 µM. The largest dynamic range improvement expectedly arose from Glu-FAST-2.1. Thus, a 2.5-fold fluorescence increase was observed in the presence of glutamate, confirming that a significant enhancement of the cooperativity constant α is required to improve the dynamic range of our Glu-FAST biosensor.

III.3.5. Characterization in mammalian cells

The successive optimization steps of the Glu-FAST-2 topology, leading to Glu-FAST-2.1, was expected to yield a biosensor providing a reliable signal in cell observations by fluorescence microscopy. As glutamate concentration changes are mainly related to intercellular signalling, especially in neurons, we tested as a preliminary experiment whether our glutamate biosensors could be expressed at the cell surface (Figure III-10). We first fused our biosensor at the C-terminal of a platelet-derived growth factor receptor (PDGFR) transmembrane peptide. Imaging by confocal microscopy showed a strong fluorescent signal that mostly localized in the endoplasmic reticulum, suggesting that Glu-FAST-2 was successfully expressed, but that conformational or aggregation issues prevented entire completion of the secretion to the plasma membrane. The hemagglutinin (HA) tag was removed by PCR amplification from the originally used pDisplay plasmid, as it was previously shown to interact with the expressed protein during the development of the surface-displayed iGluSnFR biosensor[21]. This however did not permit successful surface-expression of neither Glu-FAST-2 and Glu-FAST-2.1. Cytosolic expression of our fluorogenic glutamate biosensor was nevertheless possible: however, intracellular glutamate concentration in the millimolar range substantially exceeds the analyte affinity of our biosensor. Further protein engineering of the sensing domain in particular would have been necessary to adjust the affinity range of the biosensor.

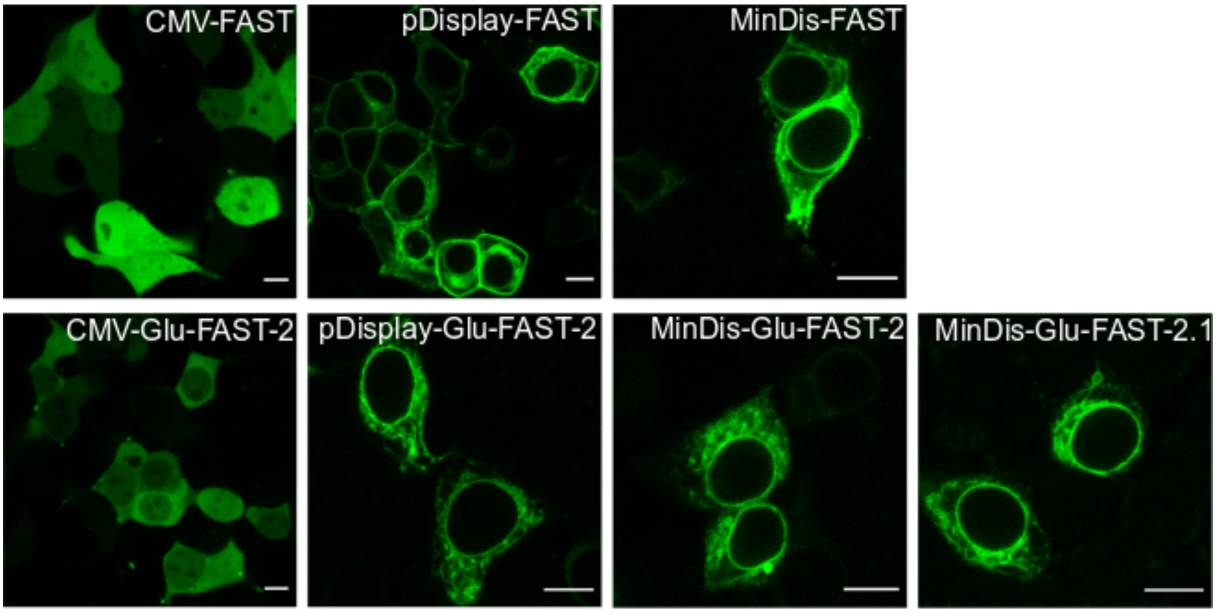

Figure III-10. Confocal micrographs of live HEK293T cells expressing FAST and Glu-FAST-2, or expressing FAST, Glu-FAST-2 and Glu-FAST-2.1 in a pDisplay plasmid (extracellular membrane targeting) or its truncated version pCMV(MinDis). [HMBR] = 5 µM, scale bar 10 µm.

III.4. Discussion

The development of a glutamate biosensor based on the coupling between FAST and a single-protein sensing unit GltI illustrated the possibility to modulate fluorogen binding to the reporter domain by analyte binding to the sensing domain. The first step of our study demonstrated the importance of a preliminary screening of the possible topologies offered by such design, that highly determined the ability of the different protein chimeras to act as glutamate-sensing tools. A convenient insertion of GltI between the fragments of cpFAST(114-115) yielded Glu-FAST-2, a biosensor showing positive cooperative coupling between glutamate and fluorogen binding. The affinity for glutamate in the micromolar range displayed by Glu-FAST-2 was previously demonstrated to be suitable for imaging neuronal transmission (SuperGluSnFR $K_{D,glu}$ = 2.5 μM, R-iGluSnFR $K_{D,glu}$ =11 ± 2 μM),[9,22] but is presumably too high for imaging cytosolic glutamate or synaptic glutamate release with fast kinetics. Interestingly, substantial affinity decrease was already obtained by mutating the sensing domain: mutations E25D or S72T in GltI notably enabled the design of the fast and ultrafast ($iGlu_f$ and $iGlu_u$) sensor variants of iGluSnFR, respectively, providing better time-resolved imaging. Tuning the biosensor affinity for glutamate thus appears feasible by site-directed mutagenesis of GltI and could be envisioned to adjust Glu-FAST-2 properties.

However, the exploration of different strategies to improve the modest dynamic range of Glu-FAST-2 was undertaken first. Despite an unsuccessful attempt to replace FAST by one of its ortholog versions, optimization of the reporter domain was still considered desirable towards the general aim of designing fluorogenic allosteric biosensors. The effect of residue deletions at the termini of FAST fragments was evaluated, encouraged by the previously described improvement of cpFAST and splitFAST properties when using CFAST10 (= CFAST(115-124)) instead of CFAST11 (= CFAST(115-125)).[20,23] While analogous deletion of residue 125 did not prove useful in the context of Glu-FAST-2, supposedly due to different connectivity between the sensing and the reporter domains, the dynamic range of our glutamate sensor was increased by deletion of residue Gly115.

Previous developments of both ratiometric and intensiometric sensors based on GltI underlined the necessity to optimize interdomain connecting regions, either by deletion of flexible residues at the termini of the sensing domain, or by addition and screening of short linkers. In the case of Glu-FAST-2, we tested the insertion of flexible linkers to improve the cooperativity constant α by decreasing $K_{D,HMBR/glu}$ value, assuming that it would provide a better reporter domain complementation upon analyte-binding to the sensor. However, increased accessibility of FAST fragments failed at increasing the reporter affinity for the fluorogen in the biosensor closed-conformation: on the opposite it favoured cpFAST self-assembly, thus yielded a higher background signal. An antagonist attempt to add strain at the connecting sites by removing up to ten termini residues to the sensing domain GltI yielded unpredictable and inconclusive results. Nevertheless, an optimized glutamate sensor version Glu-FAST-2.1 was obtained by insertion of a two-proline linker between GltI and NFAST, combined with truncation of Gly115 in the CFAST fragment.

It should be noted that a significant improvement of the cooperativity constant (from $\alpha = 2.2$ in the case of Glu-FAST-2 to $\alpha = 4.3$ in the case of Glu-FAST-2.1) was necessary to obtain moderate improvement of the dynamic range (from 1.8 to 2.5-fold fluorescence increase upon addition of glutamate). These results suggested a moderate allosteric coupling between cpFAST and GltI. Folding of the reporter in the analyte-bound conformation provided reasonable fluorogen binding constants, that could nonetheless be improved by insertion of flexible GG linkers, providing better accessibility of the fragments. Improving α mainly relied on hampering reconstitution of cpFAST in the open conformation of the sensor. Further optimization of the linkers to enhance and combine both tendencies would certainly be required to further improve the properties of Glu-FAST-2 biosensor.

Difficulties encountered to properly target Glu-FAST-2 and Glu-FAST-2.1 at the cellular membrane appeared to be the main limitation of our approach. Such biosensors with micromolar affinities for glutamate were indeed mainly envisioned to be suitable for imaging glutamatergic signalling, thus extracellular transients. It was suggested that conformational or aggregation issues hampered proper completion of the secretory pathway: several strategies can be considered to overcome this limitation. For instance, coupling a FAST variant with improved folding and solubility (such as pFAST) to the sensing unit GltI could possibly facilitate proper membrane-expression of the resulting biosensor. Moreover, insertion of the reporter in the sensing module instead of flanking the latter with FAST fragments might prevent the exposure of hydrophobic patches that appeared to yield improper folding of the tag. Indeed, HEK cells transfected with a pDisplay plasmid encoding for the sensor topology Glu-FAST-4 appeared to show fluorescent signal at the cellular membrane in preliminary microscopy experiments (data not shown). Confirmation of such observations would then require re-engineering of the different components of the sensor in order to design an optimized FAST-based sensor for imaging extracellular glutamate levels.

III.5. Material & methods

General

Synthetic oligonucleotides used for cloning were purchased from Integrated DNA Technology. PCR reactions were performed with Q5 polymerase (New England Biolabs) in the buffer provided. PCR products were purified using QIAquick PCR purification kit (Qiagen). Isothermal assemblies (Gibson assembly) were performed using homemade mix prepared according to previously described protocols (modified from the original described protocol).[24] Gibson products were purified using MinElute PCR purification kit (Qiagen). Gibson products were transformed in DH10 E. coli. Small-scale isolation of plasmid DNA was done using QIAprep miniprep kit (Qiagen) from 3 mL of overnight culture supplemented with appropriate antibiotics. Large-scale isolation of plasmid DNA was done using the QIAprep maxiprep kit (Qiagen) from 150 mL of overnight culture supplemented with appropriate antibiotics. All plasmid sequences were confirmed by Sanger sequencing with appropriate sequencing primers (GATC Biotech). The preparation of HMBR, HBR-3,5DOM and HBR-3,5DM was previously described.[25,26]

Protein expression and purification

Expression vectors of the glutamate biosensors with an N-terminal His-tag under the control of a T7 promoter were transformed in Rosetta(DE3)pLysS *Escherichia coli* competent cells. Bacterial cells were grown at 37 °C in Lysogeny Broth (LB) supplemented with chloramphenicol (34 µg/mL) and kanamycin (50 µg/mL) until OD_{600nm} = 0.6. Expression was induced overnight at 16°C by the addition of isopropyl β-D-1-thiogalactopyranoside (IPTG) (c_f = 1 mM). Cells were harvested by centrifugation (4000 × *g* for 20 min at 4°C) and stored at -30°C. The cell pellets were resuspended in lysis buffer (TES 1x: trisaminomethane (Tris) 200 mM, EDTA 0.65 mM and sucrose 0.5 M, protease inhibitor PMSF 1 mM, DNase, MgCl2 5 mM) and kept on ice for 1h, followed by resuspension in TES 0.25x to induce lysis by osmotic choc. Cellular fragments were removed by centrifugation (9200 × *g* for 1h at 4°C). The supernatant was incubated overnight at 4°C by gentle agitation with Ni-NTA agarose beads in Tris (50 mM), NaCl (150 mM) buffer with 20 mM imidazole. The beads were then washed sequentially with 10 volumes of Tris (50 mM), NaCl (150 mM) buffer with 20 mM imidazole, then with 5 volumes of Tris buffer complemented with 40mM imidazole, and the proteins were eluted with 3 volumes of Tris buffer with 0.5 M imidazole. The buffer was afterwards exchanged with HEPES buffer (HEPES 50 mM, NaCl 150 mM pH 8) using PD-10 or PD-MidiTrap G-25 desalting columns (GE Healthcare). Purity of the proteins was evaluated using SDS-PAGE electrophoresis stained with Coomassie blue.

Thermodynamic analysis

Determination of the thermodynamic constants by titration experiments were performed with a Spark 10M plate reader (Tecan) in HEPES buffer (HEPES 50 mM, NaCl 150 mM, pH 7.4). Normalized fluorescence intensity was plotted as a function of fluorogen concentration and fitted in GraphPad Prism 7 to a one-site specific binding model.

Mammalian cell culture

HEK 293T cells (ATCC CRL-3216) were cultured in Dulbecco's modified Eagle's medium (DMEM) supplemented with phenol red, Glutamax I, and 10% (vol/vol) fetal calf serum, at 37 °C in a 5% CO2 atmosphere. HeLa cells (ATCC CCL-2) were cultured in modified Eagle's medium (MEM) supplemented with phenol red, 1× non-essential amino acids, 1× sodium pyruvate, and 10% (vol/vol) fetal calf serum at 37 °C in a 5% CO2 atmosphere. For imaging, cells were seeded in µDish IBIDI (Biovalley) coated with poly-L-lysine. Cells were transiently transfected with the plasmids allowing the mammalian expression of the sensors under the control of a CMV promoter, using Genejuice (Merck) according to the manufacturer's protocol for 24 h prior to imaging.

Fluorescence microscopy

Confocal micrographs of mammalian cells were acquired on a Zeiss LSM 710 Laser Scanning Microscope equipped with a Plan Apochromat 63×/1.4 NA oil immersion objective and on a Leica TCS SP5 confocal laser scanning microscope equipped with a 63×/ 1.4 NA oil immersion objective. Live cells were washed twice with DPBS (Dulbecco's Phosphate-Buffered Saline), immediately prior to imaging. DMEM media (without serum and phenol red) containing the fluorogens at the indicated concentration was added to the cells. The cells were imaged directly without washing. ZEN and Leica LAS AF software were used to collect the data. The images were analyzed with Fiji (Image J).

Sequences

Protein sequence of FAST:
EHVAFGSEDIENTLAKMDDGQLDGLAFGAIQLDGDGNILQYNAAEGDITGRDPKQVIGKNFF
KDVAPGTDSPEFYGKFKEGVASGNLNTMFEWMIPTSRGPTKVKVHMKKALSGDSYWVFVK
RV

Protein sequence of cpFAST2:
GDSYWVFVKRV**GGS**EHVAFGSEDIENTLAKMDDGQLDGLAFGAIQLDGDGNILQYNAAEG
DITGRDPKQVIGKNFFKDVAPGTDSPEFYGKFKEGVASGNLNTMFEWMIPTSRGPTKVKVH
MKKALS

Protein sequence of GltI:
AAGSTLDKIAKNGVIVVGHRESSVPFSYYDNQQKVVGYSQDYSNAIVEAVKKKLNKPDLQVK
LIPITSQNRIPLLQNGTFDFECGSTTNNVERQKQAAFSDTIFVVGTRLLTKKGGDIKDFANLKD

KAVVVTSGTTSEVLLNKLNEEQKMNMRIISAKDHGDSFRTLESGRAVAFMMDDVLLAGERAKAKKPDNWEIVGKPQSQEAYGCMLRKDDPQFKKLMDDTIAQVQTSGEAEKWFDKWFKNPIPPKNLNMNFELSDEMKALFKEPNDKALK

Protein sequence of cpGltI:
KNLNMNFELSDEMKALFKEPNDKALK**GGSHHHHHHGMASMTGGQQMGRDLYDDDDKDPGSSGS**AAGSTLDKIAKNGVIVVGHRESSVPFSYYDNQQKVVGYSQDYSNAIVEAVKKKLNKPDLQVKLIPITSQNRIPLLQNGTFDFECGSTTNNVERQKQAAFSDTIFVVGTRLLTKKGGDIKDFANLKDKAVVVTSGTTSEVLLNKLNEEQKMNMRIISAKDHGDSFRTLESGRAVAFMMDDVLLAGERAKAKKPDNWEIVGKPQSQEAYGCMLRKDDPQFKKLMDDTIAQVQTSGEAEKWFDKWFKNPIPP

Protein sequence of Glu-FAST-1:
EHVAFGSEDIENTLAKMDDGQLDGLAFGAIQLDGDGNILQYNAAEGDITGRDPKQVIGKNFFKDVAPGTDSPEFYGKFKEGVASGNLNTMFEWMIPTSRGPTKVKVHMKKALSAAGSTLDKIAKNGVIVVGHRESSVPFSYYDNQQKVVGYSQDYSNAIVEAVKKKLNKPDLQVKLIPITSQNRIPLLQNGTFDFECGSTTNNVERQKQAAFSDTIFVVGTRLLTKKGGDIKDFANLKDKAVVVTSGTTSEVLLNKLNEEQKMNMRIISAKDHGDSFRTLESGRAVAFMMDDVLLAGERAKAKKPDNWEIVGKPQSQEAYGCMLRKDDPQFKKLMDDTIAQVQTSGEAEKWFDKWFKNPIPPKNLNMNFELSDEMKALFKEPNDKALKGDSYWVFVKRV

Protein sequence of cpGlu-FAST-1:
KNLNMNFELSDEMKALFKEPNDKALKGDSYWVFVKRV**GGS**EHVAFGSEDIENTLAKMDDGQLDGLAFGAIQLDGDGNILQYNAAEGDITGRDPKQVIGKNFFKDVAPGTDSPEFYGKFKEGVASGNLNTMFEWMIPTSRGPTKVKVHMKKALSAAGSTLDKIAKNGVIVVGHRESSVPFSYYDNQQKVVGYSQDYSNAIVEAVKKKLNKPDLQVKLIPITSQNRIPLLQNGTFDFECGSTTNNVERQKQAAFSDTIFVVGTRLLTKKGGDIKDFANLKDKAVVVTSGTTSEVLLNKLNEEQKMNMRIISAKDHGDSFRTLESGRAVAFMMDDVLLAGERAKAKKPDNWEIVGKPQSQEAYGCMLRKDDPQFKKLMDDTIAQVQTSGEAEKWFDKWFKNPIPP

Protein sequence of Glu-FAST-2:
GDSYWVFVKRVAAGSTLDKIAKNGVIVVGHRESSVPFSYYDNQQKVVGYSQDYSNAIVEAVKKKLNKPDLQVKLIPITSQNRIPLLQNGTFDFECGSTTNNVERQKQAAFSDTIFVVGTRLLTKKGGDIKDFANLKDKAVVVTSGTTSEVLLNKLNEEQKMNMRIISAKDHGDSFRTLESGRAVAFMMDDVLLAGERAKAKKPDNWEIVGKPQSQEAYGCMLRKDDPQFKKLMDDTIAQVQTSGEAEKWFDKWFKNPIPPKNLNMNFELSDEMKALFKEPNDKALKEHVAFGSEDIENTLAKMDDGQLDGLAFGAIQLDGDGNILQYNAAEGDITGRDPKQVIGKNFFKDVAPGTDSPEFYGKFKEGVASGNLNTMFEWMIPTSRGPTKVKVHMKKALS

Protein sequence of cpGlu-FAST-2:
KNLNMNFELSDEMKALFKEPNDKALKEHVAFGSEDIENTLAKMDDGQLDGLAFGAIQLDGDGNILQYNAAEGDITGRDPKQVIGKNFFKDVAPGTDSPEFYGKFKEGVASGNLNTMFEWMIPTSRGPTKVKVHMKKALSGDSYWVFVKRVAAGSTLDKIAKNGVIVVGHRESSVPFSYYDNQQKVVGYSQDYSNAIVEAVKKKLNKPDLQVKLIPITSQNRIPLLQNGTFDFECGSTTNNVERQKQAAFSDTIFVVGTRLLTKKGGDIKDFANLKDKAVVVTSGTTSEVLLNKLNEEQKMNMRIISAKDHGDSFRTLESGRAVAFMMDDVLLAGERAKAKKPDNWEIVGKPQSQEAYGCMLRKDDPQFKKLMDDTIAQVQTSGEAEKWFDKWFKNPIPP

Protein sequence of Glu-FAST-3:
AAGSTLDKIAKNGVIVVGHRESSVPFSYYDNQQKVVGYSQDYSNAIVEAVKKKLNKPDLQVKLIPITSQNRIPLLQNGTFDFECGSTTNNVERQKQAAFSDTIFVVGTRLLTKKGGDIKDFANLKDKAVVVTSGTTSEVLLNKLNEEQKMNMRIISAKDHGDSFRTLESGRAVAFMMDDVLLAGERAKAKKPDNWEIVGKPQSQEAYGCMLRKDDPQFKKLMDDTIAQVQTSGEAEKWFDKWFKNPI**LV**EHVAFGSEDIENTLAKMDDGQLDGLAFGAIQLDGDGNILQYNAAEGDITGRDPKQVIGKNF

FKDVAPGTDSPEFYGKFKEGVASGNLNTMFEWMIPTSRGPTKVKVHMKKALSGDSYWVFVKRV**NP**LNMNFELSDEMKALFKEPNDKALK

Protein sequence of cpGlu-FAST-3:
GDSYWVFVKRV**NP**LNMNFELSDEMKALFKEPNDKALK**GGSHHHHHHGMASMTGGQQMGRDLYDDDDKDPGSSGS**AAGSTLDKIAKNGVIVVGHRESSVPFSYYDNQQKVVGYSQDYSNAIVEAVKKKLNKPDLQVKLIPITSQNRIPLLQNGTFDFECGSTTNNVERQKQAAFSDTIFVVGTRLLTKKGGDIKDFANLKDKAVVVTSGTTSEVLLNKLNEEQKMNMRIISAKDHGDSFRTLESGRAVAFMMDDVLLAGERAKAKKPDNWEIVGKPQSQEAYGCMLRKDDPQFKKLMDDTIAQVQTSGEAEKWFDKWFKNPI**LV**EHVAFGSEDIENTLAKMDDGQLDGLAFGAIQLDGDGNILQYNAAEGDITGRDPKQVIGKNFFKDVAPGTDSPEFYGKFKEGVASGNLNTMFEWMIPTSRGPTKVKVHMKKALS

Protein sequence of Glu-FAST-4:
AAGSTLDKIAKNGVIVVGHRESSVPFSYYDNQQKVVGYSQDYSNAIVEAVKKKLNKPDLQVKLIPITSQNRIPLLQNGTFDFECGSTTNNVERQKQAAFSDTIFVVGTRLLTKKGGDIKDFANLKDKAVVVTSGTTSEVLLNKLNEEQKMNMRIISAKDHGDSFRTLESGRAVAFMMDDVLLAGERAKAKKPDNWEIVGKPQSQEAYGCMLRKDDPQFKKLMDDTIAQVQTSGEAEKWFDKWFKNPI**LV**GDSYWVFVKRV**GGS**EHVAFGSEDIENTLAKMDDGQLDGLAFGAIQLDGDGNILQYNAAEGDITGRDPKQVIGKNFFKDVAPGTDSPEFYGKFKEGVASGNLNTMFEWMIPTSRGPTKVKVHMKKALS**NP**LNMNFELSDEMKALFKEPNDKALK

Protein sequence of cpGlu-FAST-4:
EHVAFGSEDIENTLAKMDDGQLDGLAFGAIQLDGDGNILQYNAAEGDITGRDPKQVIGKNFFKDVAPGTDSPEFYGKFKEGVASGNLNTMFEWMIPTSRGPTKVKVHMKKALS**NP**LNMNFELSDEMKALFKEPNDKALK**GGSHHHHHHGMASMTGGQQMGRDLYDDDDKDPGSSGS**AAGSTLDKIAKNGVIVVGHRESSVPFSYYDNQQKVVGYSQDYSNAIVEAVKKKLNKPDLQVKLIPITSQNRIPLLQNGTFDFECGSTTNNVERQKQAAFSDTIFVVGTRLLTKKGGDIKDFANLKDKAVVVTSGTTSEVLLNKLNEEQKMNMRIISAKDHGDSFRTLESGRAVAFMMDDVLLAGERAKAKKPDNWEIVGKPQSQEAYGCMLRKDDPQFKKLMDDTIAQVQTSGEAEKWFDKWFKNPI**LV**GDSYWVFVKRV

Protein sequence of Glu2.1:
DSYWVFVKRVAAGSTLDKIAKNGVIVVGHRESSVPFSYYDNQQKVVGYSQDYSNAIVEAVKKKLNKPDLQVKLIPITSQNRIPLLQNGTFDFECGSTTNNVERQKQAAFSDTIFVVGTRLLTKKGGDIKDFANLKDKAVVVTSGTTSEVLLNKLNEEQKMNMRIISAKDHGDSFRTLESGRAVAFMMDDVLLAGERAKAKKPDNWEIVGKPQSQEAYGCMLRKDDPQFKKLMDDTIAQVQTSGEAEKWFDKWFKNPIPPKNLNMNFELSDEMKALFKEPNDKALK**PP**EHVAFGSEDIENTLAKMDDGQLDGLAFGAIQLDGDGNILQYNAAEGDITGRDPKQVIGKNFFKDVAPGTDSPEFYGKFKEGVASGNLNTMFEWMIPTSRGPTKVKVHMKKALS

Protein sequence of cpFAST(25-24)2:
GLAFGAIQLDGDGNILQYNAAEGDITGRDPKQVIGKNFFKDVAPGTDSPEFYGKFKEGVASGNLNTMFEWMIPTSRGPTKVKIHMKKALSGDSYWVFVKRV**GGS**EHVAFGSEDIENTLAKMDDGQLD

Protein sequence of cpFAST(99-98)2:
MSRGPTKVKIHMKKALSGDSYWVFVKRV**GGS**EHVAFGSEDIENTLAKMDDGQLDGLAFGAIQLDGDGNILQYNAAEGDITGRDPKQVIGKNFFKDVAPGTDSPEFYGKFKEGVASGNLNTMFEWMIPT

Molecular cloning

Unless specified otherwise, designations NFAST and CFAST stand for FAST(1-114) and FAST(115-125), respectively.

The plasmid pAG445, encoding pET28new-His-Glu-FAST-1, was constructed by Gibson assembly from the plasmid pAG399 encoding pET28new-His-FAST. The fragment coding for NFAST was amplified by PCR using the primers ag630/kanF. The fragment coding for CFAST was amplified using the primers ag629/kanR. The insert coding for GltI was amplified from pAG402 encoding pET28new-His-GltI using the primers ag631/ag632. The three fragments were then assembled by Gibson assembly.

The plasmid pAG446, encoding pET28new-His-cpGlu-FAST-1, was constructed by Gibson assembly from the plasmid pAG403 encoding pET28new-His-cpGltI. The fragment coding for CGltI was amplified by PCR using the primers ag632/kanF. The fragment coding for NGltI was amplified using the primers ag631/kanR. The insert coding for cpFAST2 was amplified from pAG400 encoding pET28new-His-cpFAST2 using the primers ag629/ag630. The three fragments were then assembled by Gibson assembly.

The plasmid pAG447, encoding pET28new-His-Glu-FAST-2, was constructed by Gibson assembly from the plasmid pAG400 encoding pET28new-His-cpFAST2. The fragment coding for CFAST was amplified by PCR using the primers ag634/kanF. The fragment coding for NFAST was amplified using the primers ag633/kanR. The insert coding for GltI was amplified from pAG402 encoding pET28new-His-GltI using the primers ag635/ag636. The three fragments were then assembled by Gibson assembly.

The plasmid pAG448, encoding pET28new-His-cpGlu-FAST-2, was constructed by Gibson assembly from the plasmid pAG403 encoding pET28new-His-cpGltI. The fragment coding for CGltI was amplified by PCR using the primers ag636/kanF. The fragment coding for NGltI was amplified using the primers ag635/kanR. The insert coding for FAST was amplified from pAG399 encoding pET28new-His-FAST using the primers ag633/ag634. The three fragments were then assembled by Gibson assembly.

The plasmid pAG449, encoding pET28new-His-Glu-FAST-3, was constructed by Gibson assembly from the plasmid pAG402 encoding pET28new-His-GltI. The fragment coding for NGltI was amplified by PCR in two fragments, using the primers ag607/ag638 and ag579/kanF. The fragment coding for CGltI was amplified using the primers ag637/kanR. The insert coding for FAST was amplified from pAG399 encoding pET28new-His-FAST using the primers ag639/ag640. The four fragments were then assembled by Gibson assembly.

The plasmid pAG450, encoding pET28new-His-cpGlu-FAST-3, was constructed by Gibson assembly from the plasmid pAG400 encoding pET28new-His-cpFAST2. The fragment coding for CFAST was amplified by PCR using the primers ag640/kanF. The fragment coding for NFAST was amplified using the primers ag639/kanR. The insert coding for cpGltI was amplified from pAG403 encoding pET28new-His-cpGltI using the primers ag637/ag638. The three fragments were then assembled by Gibson assembly.

The plasmid pAG451, encoding pET28new-His-Glu-FAST-4, was constructed by Gibson assembly from the plasmid pAG402 encoding pET28new-His-GltI. The fragment coding for NGltI was amplified by PCR in two fragments, using the primers ag607/ag642 and ag579/kanF. The fragment coding for CGltI was amplified using the primers ag641/kanR. The insert coding for cpFAST2 was amplified from pAG400 encoding pET28new-His-cpFAST2 using the primers ag643/ag644. The four fragments were then assembled by Gibson assembly.

The plasmid pAG452, encoding pET28new-His-cpGlu-FAST-4, was constructed by Gibson assembly from the plasmid pAG399 encoding pET28new-His-FAST. The fragment coding for NFAST was amplified by PCR using the primers ag644/kanF. The fragment coding for CFAST was amplified using the primers ag643/kanR. The insert coding for cpGltI was amplified from pAG403 encoding pET28new-His-cpGltI using the primers ag641/ag642. The three fragments were then assembled by Gibson assembly.

The plasmid pAG508, encoding pET28new-His-Glu-FAST(24-25)-2, was constructed by Gibson assembly from the plasmid pAG399 encoding pET28new-His-FAST. The pET28new backbone was amplified by PCR using the primers ag578/kanR and ag579/kanF. The fragment coding for CFAST(25-125) was amplified by PCR using the primers ag634/ag727. The fragment coding for NFAST(1-114) was amplified using the primers ag633/ag728. The fragment coding for GltI was amplified using the primers ag680/ag681. The five fragments were then assembled by Gibson assembly.

The plasmid pAG509, encoding pET28new-His-Glu-FAST(98-99)-2, was constructed by Gibson assembly from the plasmid pAG399 encoding pET28new-His-FAST. The pET28new backbone was amplified by PCR using the primers ag578/kanR and ag579/kanF. The fragment coding for CFAST(99-125) was amplified by PCR using the primers ag634/ag729. The fragment coding for NFAST(1-98) was amplified using the primers ag633/ag730. The fragment coding for GltI was amplified using the primers ag680/ag681. The five fragments were then assembled by Gibson assembly.

The plasmid pAG510, encoding pET28new-His-Glu-FAST(24-25)-1, was constructed by Gibson assembly from the plasmid pAG399 encoding pET28new-His-FAST. The fragment coding for NFAST(1-24) was amplified by PCR using the primers ag734/kanF. The fragment coding for CFAST(25-125) was amplified using the primers ag733/kanR. The fragment coding for GltI was amplified using the primers ag680/ag681. The three fragments were then assembled by Gibson assembly.

The plasmid pAG511, encoding pET28new-His-Glu-FAST(98-99)-1, was constructed by Gibson assembly from the plasmid pAG399 encoding pET28new-His-FAST. The fragment coding for NFAST(1-98) was amplified by PCR using the primers ag736/kanF. The fragment coding for CFAST(99-125) was amplified using the primers ag735/kanR. The fragment coding for GltI was amplified using the primers ag680/ag681. The three fragments were then assembled by Gibson assembly.

The plasmid pAG602, encoding pET28new-His-Glu-FAST(24-25)-4, was constructed by Gibson assembly from the plasmid pAG449. The fragment coding for NGltI was amplified by PCR using the primers ag844/kanF. The fragment coding for CGltI was amplified using the primers ag843/kanR. The insert coding for cpFAST(99-98) was amplified from pAG481 encoding pET28new-His-CFAST(99-125)-GGS-NFAST(1-98) using the primers ag845/ag846. The three fragments were then assembled by Gibson assembly.

The plasmid pAG515, encoding pET28new-His-Glu-FAST-2-GltI(N_0C_1), was constructed by Gibson assembly from the plasmid pAG450. The fragment coding for CFAST was amplified by PCR using the primers ag634/kanF. The fragment coding for NFAST was amplified using the primers ag704/kanR. The insert coding for GltI(N_0C_1) was amplified from pAG445 using the primers ag680/ag806. The three fragments were then assembled by Gibson assembly.

Similarly, the plasmids pAG516-520, encoding pET28new-His-Glu-FAST-2-GltI(N_0C_x), was constructed by Gibson assembly from the plasmid pAG450. The fragment coding for CFASTwas amplified by PCR using the primers ag634/kanF. The fragment coding for NFAST was amplified using the primers ag704/kanR. The inserts coding for GltI(N_0C_x) were amplified from pAG445 using the primers ag680/ag807, ag680/ag808, ag680/ag809, ag680/ag810 and ag680/ag811 respectively. The three fragments were then assembled by Gibson assembly.

The plasmid pAG521, encoding pET28new-His-Glu-FAST-2-GltI(N_1C_0), was constructed by Gibson assembly from the plasmid pAG450. The fragment coding for CFAST was amplified by PCR using the primers ag705/kanF. The fragment coding for NFAST was amplified using the primers ag633/kanR. The insert coding for GltI(N1C0) was amplified from pAG445 using the primers ag681/ag812. The three fragments were then assembled by Gibson assembly.

Similarly, the plasmids pAG522-527, encoding pET28new-His-Glu-FAST-2-GltI(N_1C_x), was constructed by Gibson assembly from the plasmid pAG450. The fragment coding for CFAST was amplified by PCR using the primers ag705/kanF. The fragment coding for NFAST was amplified using the primers ag704/kanR. The inserts coding for GltI(N_1C_x) were amplified from pAG445 using the primers ag806/ag812, ag807/ag812, ag808/ag812, ag809/ag812, ag810/ag812 and ag811/ag812 respectively. The three fragments were then assembled by Gibson assembly.

The plasmid pAG528, encoding pET28new-His-Glu-FAST-2-GltI(N_2C_0), was constructed by Gibson assembly from the plasmid pAG450. The fragment coding for CFAST was amplified by PCR using the primers ag705/kanF. The fragment coding for NFAST was amplified using the primers ag633/kanR. The insert coding for GltI(N_2C_0) was amplified from pAG445 using the primers ag681/ag813. The three fragments were then assembled by Gibson assembly.

Similarly, the plasmids pAG529-534, encoding pET28new-His-Glu-FAST-2-GltI(N_2C_x), was constructed by Gibson assembly from the plasmid pAG450. The fragment coding for CFAST was amplified by PCR using the primers ag705/kanF. The fragment coding for NFAST was amplified using the primers ag704/kanR. The inserts coding for GltI(N_2C_x) were amplified from pAG445 using the primers ag806/ag813, ag807/ag813, ag808/ag813, ag809/ag813, ag810/ag813 and ag811/ag813 respectively. The three fragments were then assembled by Gibson assembly.

The plasmid pAG535, encoding pET28new-His-Glu-FAST-2-GltI(N_3C_0), was constructed by Gibson assembly from the plasmid pAG450. The fragment coding for CFAST was amplified by PCR using the primers ag705/kanF. The fragment coding for NFAST was amplified using the primers ag633/kanR. The insert coding for GltI(N_3C_0) was amplified from pAG445 using the primers ag681/ag814. The three fragments were then assembled by Gibson assembly.

Similarly, the plasmids pAG536-541, encoding pET28new-His-Glu-FAST-2-GltI(N_3C_x), was constructed by Gibson assembly from the plasmid pAG450. The fragment coding for CFAST was amplified by PCR using the primers ag705/kanF. The fragment coding for NFAST was amplified using the primers ag704/kanR. The inserts coding for GltI(N_3C_x) were amplified from pAG445 using the primers ag806/ag814, ag807/ag814, ag808/ag814, ag809/ag814, ag810/ag814 and ag811/ag814 respectively. The three fragments were then assembled by Gibson assembly.

The plasmid pAG542, encoding pET28new-His-Glu-FAST-2-GltI(N_4C_0), was constructed by Gibson assembly from the plasmid pAG450. The fragment coding for CFAST was amplified by PCR using the primers ag705/kanF. The fragment coding for NFAST was amplified using the primers ag633/kanR. The insert coding for GltI(N_4C_0) was amplified from pAG445 using the primers ag681/ag815. The three fragments were then assembled by Gibson assembly.

Similarly, the plasmids pAG543-548, encoding pET28new-His-Glu-FAST-2-GltI(N_4C_x), was constructed by Gibson assembly from the plasmid pAG450. The fragment coding for CFAST was amplified by PCR using the primers ag705/kanF. The fragment coding for NFAST was amplified using the primers ag704/kanR. The inserts coding for GltI(N_4C_x) were amplified from pAG445 using the primers ag806/ag815, ag807/ag815, ag808/ag815, ag809/ag815, ag810/ag815 and ag811/ag815 respectively. The three fragments were then assembled by Gibson assembly.

The plasmid pAG697, encoding pET28new-His-cp^{HboL}FAST(114-115), was constructed by Gibson assembly from the plasmid pAG586 encoding pET28a-His-TEV-^{HboL}FAST-V107I. The pET28new backbone was amplified by PCR using the primers ag578/kanF, and the primer ag960 containing the sequence coding for GGS-^{HboL}CFAST, with the primer kanR. The insert was amplified using the primers ag958/ag959. The three fragments were then assembled by Gibson assembly.

Similarly, the plasmid pAG700, encoding pET28new-His-cp$^{\mathrm{Ilo}}$FAST(114-115), was constructed by Gibson assembly from the plasmid pAG589 encoding pET28a-His-TEV-$^{\mathrm{Ilo}}$FAST-V107I. The pET28new backbone was amplified by PCR using the primers ag578/kanF, and the primer ag967 containing the sequence coding for GGS-$^{\mathrm{Ilo}}$CFAST, with the primer kanR. The insert was amplified using the primers ag965/ag966. The three fragments were then assembled by Gibson assembly.

The plasmid pAG707, encoding pET28new-His-Glu-$^{\mathrm{HboL}}$FAST-2 was constructed by Gibson assembly from the plasmid pAG697. The fragment coding for $^{\mathrm{HboL}}$CFAST was amplified by PCR using the primers ag980/kanF. The fragment coding for $^{\mathrm{HboL}}$NFAST was amplified using the primers ag984/kanR. The insert was amplified from pAG445 using the primers ag680/ag681. The three fragments were then assembled by Gibson assembly.

Similarly, the plasmid pAG711, encoding pET28new-His-Glu-$^{\mathrm{Ilo}}$FAST-2 was constructed by Gibson assembly from the plasmid pAG700. The fragment coding for $^{\mathrm{Ilo}}$CFAST was amplified by PCR using the primers ag981/kanF. The fragment coding for $^{\mathrm{Ilo}}$NFAST was amplified using the primers ag984/kanR. The insert was amplified from pAG445 using the primers ag680/ag681. The three fragments were then assembled by Gibson assembly.

The plasmid pAG513, encoding pET28new-His-Glu-FAST-2-CFAST(116-125), was constructed by Gibson assembly from the plasmid pAG447. The pET28new backbone was amplified by PCR using the primers ag579/kanF. The fragment coding for CFAST(116-125)-GltI-NFAST was amplified using the primers ag804/kanR. The two fragments were then assembled by Gibson assembly.

The plasmid pAG514, encoding pET28new-His-Glu-FAST-2-CFAST(115-124), was constructed by Gibson assembly from the plasmid pAG447. The fragment coding for CFAST(115-124) was amplified by PCR using the primers ag805/kanF. The fragment coding for GltI-NFAST was amplified using the primers ag680/kanR. The two fragments were then assembled by Gibson assembly.

The plasmid pAG627, encoding pET28new-His-Glu-FAST-2-NFAST(1-113), was constructed by Gibson assembly from the plasmid pAG447. The pET28new backbone was amplified by PCR using the primers ag578/kanR. The fragment coding for CFAST was amplified using the primers ag634/kanF. The insert coding for GltI-NFAST(1-113) was amplified by PCR using the primers ag635/ag908. The three fragments were then assembled by Gibson assembly.

The plasmid pAG628, encoding pET28new-His-Glu-FAST-2-NFAST(1-113)-CFAST(116-125), was constructed by Gibson assembly from the plasmid pAG513. The pET28new backbone was amplified by PCR using the primers ag578/kanR and ag579/kanF. The insert coding for CFAST(116-125)-GltI-NFAST(1-113) was amplified by PCR using the primers ag804/ag908. The three fragments were then assembled by Gibson assembly.

The plasmid pAG487, encoding pET28new-His-Glu-FAST-2-GG(1), was constructed by Gibson assembly from the plasmid pAG447. The fragment coding for CFAST was amplified by PCR using the primers ag705/kanF. The fragment coding for GltI-NFAST was amplified using the primer ag708 containing the sequence coding for GG linker, with the primer kanR. The two fragments were then assembled by Gibson assembly.

The plasmid pAG488, encoding pET28new-His-Glu-FAST-2-GG(2), was constructed by Gibson assembly from the plasmid pAG447. The fragment coding for CFAST-GltI was amplified by PCR using the primer ag709 containing the sequence coding for linker GG with the primer kanF. The fragment coding for NFAST was amplified using the primers ag704/kanR. The two fragments were then assembled by Gibson assembly.

The plasmid pAG489, encoding pET28new-His-Glu-FAST-2-GG(1+2), was constructed by Gibson assembly from the plasmid pAG447. The fragment coding for CFAST was amplified by PCR using the primers ag705/kanF. The fragment coding for NFAST was amplified using the primers ag704/kanR. The insert coding for GltI was amplified using the primers ag708/ag709 containing the sequence coding for linkers GG. The three fragments were then assembled by Gibson assembly.

The plasmid pAG630, encoding pET28new-His-Glu-FAST-2-PP(1), was constructed by Gibson assembly from the plasmid pAG447. The fragment coding for CFAST was amplified by PCR using the primers ag705/kanF. The fragment coding for GltI-NFAST was amplified using the primer ag909 containing the sequence coding for PP linker, with the primer kanR. The two fragments were then assembled by Gibson assembly.

Similarly, the plasmid pAG631, encoding pET28new-His-Glu-FAST-2-CFAST10-PP(1)was constructed by Gibson assembly from the plasmids pAG513. The fragment coding for CFAST(116-125) was amplified by PCR using the primers ag705/kanF. The fragment coding for GltI-NFAST was amplified using the primers ag909/kanR. The two fragments were then assembled by Gibson assembly.

The plasmid pAG633, encoding pET28new-His-Glu-FAST-2-PP(2), was constructed by Gibson assembly from the plasmid pAG447. The fragment coding for CFAST-GltI was amplified by PCR using the primer ag910 containing the sequence coding for linker PP with the primer kanF. The fragment coding for NFAST was amplified using the primers ag704/kanR. The two fragments were then assembled by Gibson assembly.

Similarly, the plasmid pAG634, encoding pET28new-His-Glu-FAST-2-CFAST10-PP(2) (pET28new-His-Glu-FAST-2.1), was constructed by Gibson assembly from the plasmids pAG513. The fragment coding for CFAST(116-125)-GltI was amplified by PCR using the primers ag910/kanF. The fragment coding for NFAST was amplified using the primers ag704/kanR. The two fragments were then assembled by Gibson assembly.

The plasmid pAG636, encoding pET28new-His-Glu-FAST-2-PP(1+2), was constructed by Gibson assembly from the plasmid pAG447. The fragment coding for CFAST was amplified by PCR using the primers ag705/kanF. The fragment coding for NFAST was amplified using the primers ag704/kanR. The insert coding for GltI was amplified using the primers ag909/ag910 containing the sequence coding for linkers PP. The three fragments were then assembled by Gibson assembly.

Similarly, the plasmids pAG637, encoding pET28new-His-Glu-FAST-2-CFAST10-PP(1+2), was constructed by Gibson assembly from the plasmids pAG513. The fragment coding for CFAST(116-125) was amplified by PCR using the primers ag705/kanF. The fragment coding for NFAST was amplified using the primers ag704/kanR. The insert coding for GltI was amplified with the primers ag909/ag910. The three fragments were then assembled by Gibson assembly.

The plasmid pAG676, encoding CMV-Glu-FAST-2-myc, was constructed by Gibson assembly from the plasmid pAG447. The CMV backbone was amplified by PCR using primers ag358/ag313 and ag348/ag314. The insert coding for CFAST-GltI-NFAST was amplified by PCR using the primers ag231/596. The three fragments were then assembled by Gibson assembly.

The plasmid pAG621, encoding pDisplay-Glu-FAST-2, was constructed by Gibson assembly from the plasmid pAG447. The pDisplay backbone was amplified by PCR using the primers ag313/ag571 and ag314/ag572. The insert coding for CFAST-GltI-NFAST was amplified by PCR using the primers ag852/ag853. The three fragments were then assembled by Gibson assembly.

The plasmid pAG737, encoding pCMV(MinDis)-Glu-FAST-2, was constructed by Gibson assembly from the plasmid pAG621. The pDisplay backbone was amplified by PCR using the primers ag1064/ag314 and ag571/ag313. The insert was amplified from the plasmid pAG447 using the primers ag1065/853. The three fragments were then assembled by Gibson assembly.

Similarly, the plasmid pAG738 and pAG821, encoding pCMV(MinDis)-Glu-FAST-2.1 and pCMV(MinDis)-FAST, respectively, was constructed by Gibson assembly from the plasmid pAG621. The pDisplay backbone was amplified by PCR using the primers ag1064/ag314 and ag571/ag313. The insert was amplified from the plasmid pAG634 or pAG104, using the primers ag1066/853 or ag574/1206, respectively. The three fragments were then assembled by Gibson assembly.

Plasmid	**From**	**Primers**
pAG399	pAG104 + pET28new	ag601,602, 578, 579, 580, 581
pAG400	pAG120 + pET28new	ag603,604, 578, 579, 580, 581
pAG402	synthetic gene + pET28new	ag607, 608, 578, 579
pAG403	synthetic gene + pET28new	ag609, 610, 611, 612, 578, 579
pAG445	pAG399 + pAG402	ag629, 630, 631, 632, kanF, kanR
pAG446	pAG403 + pAG400	ag629, 630, 631, 632, kanF, kanR
pAG447	pAG400 + pAG402	ag633, 634, 635, 636, kanF, kanR
pAG448	pAG403 + pAG399	ag633, 634, 635, 636, kanF, kanR
pAG449	pAG402 + pAG399	ag637, 638, 639, 640, kanF, kanR
pAG450	pAG400 + pAG403	ag637, 638, 639, 640, kanF, kanR
pAG451	pAG402 + pAG400	ag641, 642, 643, 644, kanF, kanR
pAG452	pAG399 + pAG403	ag641, 642, 643, 644, kanF, kanR
pAG487	pAG447	ag705, 708, 709, kanF, kanR
pAG488	pAG447	ag704, 706, 707, kanF, kanR
pAG489	pAG447	ag704, 706, 707, kanF, kanR
pAG508	pAG399 + pAG402 + pAG445	ag579, 578, 633, 634, 680, 681, 727, 728, kanF, kanR
pAG509	pAG399 + pAG402 + pAG445	ag578, 579, 633, 634, 680, 681, 729, 730, kanF, kanR
pAG510	pAG399+pAG402	ag733, 734, 680, 681, kanF, kanR
pAG511	pAG399+pAG403	ag735, 736, 680, 681, kanF, kanR
pAG513	pAG447	ag579, 804, kanF, kanR
pAG514	pAG447	ag680, 805, kanF, kanR
pAG515	pAG450 + pAG445	ag680, 806, 704, 705, kanF, kanR
pAG516	pAG450 + pAG445	ag680, 807, 704, 705, kanF, kanR
pAG517	pAG450 + pAG445	ag680, 808, 704, 705, kanF, kanR
pAG518	pAG450 + pAG445	ag680, 809, 704, 705, kanF, kanR
pAG519	pAG450 + pAG445	ag680, 810, 704, 705, kanF, kanR
pAG520	pAG450 + pAG445	ag680, 811, 704, 705, kanF, kanR
pAG521	pAG450 + pAG445	ag812, 681, 704, 705, kanF, kanR
pAG522	pAG450 + pAG445	ag812, 806, 704, 705, kanF, kanR
pAG523	pAG450 + pAG445	ag812, 807, 704, 705, kanF, kanR
pAG524	pAG450 + pAG445	ag812, 808, 704, 705, kanF, kanR
pAG525	pAG450 + pAG445	ag812, 809, 704, 705, kanF, kanR

pAG526	pAG450 + pAG445	ag812, 810, 704, 705, kanF, kanR
pAG527	pAG450 + pAG445	ag812, 811, 704, 705, kanF, kanR
pAG528	pAG450 + pAG445	ag813, 681, 704, 705, kanF, kanR
pAG529	pAG450 + pAG445	ag813, 806, 704, 705, kanF, kanR
pAG530	pAG450 + pAG445	ag813, 807, 704, 705, kanF, kanR
pAG531	pAG450 + pAG445	ag813, 808, 704, 705, kanF, kanR
pAG532	pAG450 + pAG445	ag813, 809, 704, 705, kanF, kanR
pAG533	pAG450 + pAG445	ag813, 810, 704, 705, kanF, kanR
pAG534	pAG450 + pAG445	ag813, 811, 704, 705, kanF, kanR
pAG535	pAG450 + pAG445	ag814, 681, 704, 705, kanF, kanR
pAG536	pAG450 + pAG445	ag814, 806, 704, 705, kanF, kanR
pAG537	pAG450 + pAG445	ag814, 807, 704, 705, kanF, kanR
pAG538	pAG450 + pAG445	ag814, 808, 704, 705, kanF, kanR
pAG539	pAG450 + pAG445	ag814, 809, 704, 705, kanF, kanR
pAG540	pAG450 + pAG445	ag814, 810, 704, 705, kanF, kanR
pAG541	pAG450 + pAG445	ag814, 811, 704, 705, kanF, kanR
pAG542	pAG450 + pAG445	ag815, 681, 704, 705, kanF, kanR
pAG543	pAG450 + pAG445	ag815, 806, 704, 705, kanF, kanR
pAG544	pAG450 + pAG445	ag815, 807, 704, 705, kanF, kanR
pAG545	pAG450 +pAG445	ag815, 808, 704, 705, kanF, kanR
pAG546	pAG450 + pAG445	ag815, 809, 704, 705, kanF, kanR
pAG547	pAG450 + pAG445	ag815, 810, 704, 705, kanF, kanR
pAG548	pAG450 + pAG445	ag815, 811, 704, 705, kanF, kanR
pAG602	pAG449 + pAG481	ag843, 844, 845, 846, kanF, kanR
pAG621	pAG211 + pAG447	ag313, 314, 571, 572, 852, 853
pAG627	pAG447	ag578, 908, kanF, kanR
pAG628	pAG513	ag578, 908, kanF, kanR
pAG630	pAG447	ag705, 909, kanF, kanR
pAG631	pAG513	ag705, 909, kanF, kanR
pAG633	pAG447	ag704, 910, kanF, kanR
pAG634	pAG513	ag704, 910, kanF, kanR
pAG636	pAG447	ag704, 705, 909, 910, kanF, kanR
pAG637	pAG513	ag704, 705, 909, 910, kanF, kanR
pAG676	pAG398 + pAG447	ag231, 313, 314, 358, 596, 848
pAG737	pAG621 + pAG447	ag313, 314, 571, 853, 1064, 1065
pAG738	pAG621 + pAG634	ag313, 314, 571, 853, 1064, 1066
pAG821	pAG621 + pAG104	ag313, 314, 571, 574, 1064, 1206

Primer	Sequence
kanf	gcatcaaccaaaccgttattcattcgtg
kanr	cacgaatgaataacggtttggttgatgc
ag231	gaaataagcttttgttcggatccggaaagggctttcttcatgtg
ag313	ctcaccttgctcctgccgagaaagtatcca
ag314	tggatactttctcggcaggagcaaggtgag
ag358	ggtggcagatctgagtccggtag
ag571	gtcgacgaacaaaaactcatctcag
ag572	agatctggccggctgggcc
ag578	taatgactcgagcaccaccaccacc
ag579	catgctagccatatggctgccg
ag580	gcctagagcaagacgtttcccgttgaatatg
ag581	attcaacgggaaacgtcttgctctaggc
ag596	ctaccggactcagatctgccaccatgggtgacagctattgggtctttg
ag601	ggcagccatatggctagcatggagcatgttgcctttgg
ag602	ggtggtggtgctcgagtcattacacccgtttcacaaagaccc
ag603	ggcagccatatggctagcatgggtgacagctattgggtc
ag604	ggtggtggtgctcgagtcattaggaaagggctttcttcatgtg
ag607	ggcagccatatggctagcatggcagcgggcagtactctg
ag608	ggtggtggtgctcgagtcattatttcagtgccttgtcattcggttc
ag609	cagcggcagcgcagcgggcagtactctg
ag610	ggtggtggtgctcgagtcattacggcggaattggatttttgaacc
ag611	ggcagccatatggctagcatgaaaaacctgaacatgaatttcgaactg
ag612	tgcccgctgcgctgccgctgctgcc
ag629	cgaatgacaaggcactgaaaggtgacagctattgggtctttg
ag630	tccagagtactgcccgctgcggaaagggctttcttcatgtgc
ag631	acatgaagaaagccctttccgcagcgggcagtactc
ag632	aagacccaatagctgtcacctttcagtgccttgtcattcgg
ag633	cgaatgacaaggcactgaaagagcatgttgcctttggc
ag634	tccagagtactgcccgctgccacccgtttcacaaagaccc
ag635	gggtctttgtgaaacgggtggcagcgggcagtactc
ag636	ctgccaaaggcaacatgctctttcagtgccttgtcattcgg
ag637	ttgtgaaacgggtgaacccgctgaacatgaatttcgaactgtcag
ag638	aaggcaacatgctccaccagaattggatttttgaaccacttatcaaacc
ag639	tcaaaaatccaattctggtggagcatgttgcctttggc
ag640	aaattcatgttcagcgggttcacccgtttcacaaagaccc
ag641	agaaagccctttccaacccgctgaacatgaatttcgaactgtcag
ag642	caatagctgtcacccaccagaattggatttttgaaccacttatcaaacc
ag643	gttcaaaaatccaattctggtgggtgacagctattgggtctttg
ag644	gaaattcatgttcagcgggttggaaagggctttcttcatgtgc
ag680	gcagcgggcagtactc
ag681	tttcagtgccttgtcattcgg
ag704	gagcatgttgcctttggc
ag705	cacccgtttcacaaagaccc
ag706	ctgccaaaggcaacatgctcctcttccggaatacgcaacac
ag707	gggtctttgtgaaacgggtgatgggtctgttcaattttgtgaaag

ag708	gtctttgtgaaacgggtgggtggtgcagcgggcagtactc
ag709	gccaaaggcaacatgctcgccgcctttcagtgccttgtcattcgg
ag727	ggcagccatatggctagcatggggttggcctttggcgcaattc
ag728	ggtggtggtgctcgagtcattaatccagttgtccgtcgtccattttgg
ag729	ggcagccatatggctagcatgagcaggggaccaaccaag
ag730	ggtggtggtgctcgagtcattatgtcggtatcatccattcgaacatgg
ag733	ccgaatgacaaggcactgaaagggttggcctttggcgc
ag734	ccagagtactgcccgctgcatccagttgtccgtcgtcc
ag735	ccgaatgacaaggcactgaaaagcaggggaccaaccaagg
ag736	ccagagtactgcccgctgctgtcggtatcatccattcgaac
ag804	gcagccatatggctagcatggacagctattgggtctttgtgaaac
ag805	tccagagtactgcccgctgcccgtttcacaaagacccaatagc
ag806	ctgccaaaggcaacatgctccagtgccttgtcattcggttc
ag807	ctgccaaaggcaacatgctctgccttgtcattcggttctttg
ag808	ctgccaaaggcaacatgctccttgtcattcggttctttgaacag
ag809	ctgccaaaggcaacatgctcgtcattcggttctttgaacagtgc
ag810	ctgccaaaggcaacatgctcattcggttctttgaacagtgctttc
ag811	ctgccaaaggcaacatgctccggttctttgaacagtgctttc
ag812	gggtctttgtgaaacgggtggcgggcagtactctggac
ag813	gggtctttgtgaaacgggtgggcagtactctggacaaaatcg
ag814	gggtctttgtgaaacgggtgagtactctggacaaaatcgcc
ag815	gggtctttgtgaaacgggtgactctggacaaaatcgccaaaaac
ag843	aacccgctgaacatgaatttcg
ag844	caccagaattggattttgaaccac
ag845	gtggttcaaaaatccaattctggtgagcagaggcccaaccaag
ag846	gaaattcatgttcagcgggttagtaggaatcatccattcaaacattgtattaagattgc
ag848	ggatccgaacaaaagcttatttctgaagag
ag852	ggggcccagccggccagatctatgggtgacagctattgggtc
ag853	gatgagtttttgttcgtcgacggaaagggctttcttcatgtgc
ag908	tggtggtgctcgagtcattaaagggctttcttcatgtgcacc
ag909	ctttgtgaaacgggtgccaccagcagcgggcagtactctg
ag910	caaaggcaacatgctctggtggtttcagtgccttgtcattcgg
ag1064	agatctgtcaccagtggaacctg
ag1065	gttccactggtgacagatctggtgacagctattgggtctttg
ag1066	gttccactggtgacagatctgacagctattgggtctttgtgaaac
ag1206	gttccactggtgacagatctatggagcatgttgcctttgg

III.6. References

1. Nedergaard, M., Takano, T. & Hansen, A. J. Beyond the role of glutamate as a neurotransmitter. *Nat. Rev. Neurosci.* **3**, 748–755 (2002).
2. Gundlach, J., Commichau, F. M. & Stülke, J. Perspective of ions and messengers: an intricate link between potassium, glutamate, and cyclic di-AMP. *Curr. Genet.* **64**, 191–195 (2018).
3. Platt, S. R. The role of glutamate in central nervous system health and disease - A review. *Vet. J.* **173**, 278–286 (2007).
4. Dwyer, M. A. & Hellinga, H. W. Periplasmic binding proteins: A versatile superfamily for protein engineering. *Curr. Opin. Struct. Biol.* **14**, 495–504 (2004).
5. De Lorimier, R. M. *et al.* Construction of a fluorescent biosensor family. *Protein Sci.* **11**, 2655–2675 (2002).
6. Deuschle, K. *et al.* Construction and optimization of a family of genetically encoded metabolite sensors by semirational protein engineering. *Protein Sci.* **14**, 2304–2314 (2005).
7. Okumoto, S. *et al.* Detection of glutamate release from neurons by genetically encoded surface-displayed FRET nanosensors. *Proc. Natl. Acad. Sci.* **102**, 8740–8745 (2005).
8. Tsien, R. Y. Building and breeding molecules to spy on cells and tumors. *FEBS Lett.* **579**, 927–932 (2005).
9. Hires, S. A., Zhu, Y. & Tsien, R. Y. Optical measurement of synaptic glutamate spillover and reuptake by linker optimized glutamate-sensitive fluorescent reporters. *Proc. Natl. Acad. Sci.* **105**, 4411–4416 (2008).
10. Marvin, J. S. *et al.* An optimized fluorescent probe for visualizing glutamate neurotransmission. *Nat. Methods* **10**, 162–170 (2013).
11. Helassa, N. *et al.* Ultrafast glutamate sensors resolve high-frequency release at Schaffer collateral synapses. *Proc. Natl. Acad. Sci.* 1–6 (2018).
12. Marvin, J. S. *et al.* Stability, affinity, and chromatic variants of the glutamate sensor iGluSnFR. *Nat. Methods* **15**, 936–939 (2018).
13. Zhang, S. & Ai, H. W. A general strategy to red-shift green fluorescent protein based biosensors. *Nat. Chem. Biol.* **16**, 1434–1439 (2020).
14. Campbell, R. E. *et al.* Genetically Encoded Glutamate Indicators with Altered Color and Topology. *ACS Chem. Biol.* **13**, 1832–1837 (2018).
15. Namiki, S., Sakamoto, H., Iinuma, S., Iino, M. & Hirose, K. Optical glutamate sensor for spatiotemporal analysis of synaptic transmission. *Eur. J. Neurosci.* **25**, 2249–2259 (2007).
16. Coates, C., Kerruth, S., Helassa, N. & Török, K. Kinetic Mechanisms of Fast Glutamate Sensing by Fluorescent Protein Probes. *Biophys. J.* 117–127 (2019).
17. Brun, M. A. *et al.* A semisynthetic fluorescent sensor protein for glutamate. *J. Am. Chem. Soc.* **134**, 7676–7678 (2012).
18. Wu, J. *et al.* Genetically Encoded Glutamate Indicators with Altered Color and Topology. *ACS Chem. Biol.* acschembio.7b01085 (2018). doi:10.1021/acschembio.7b01085
19. Tebo, A. G. *et al.* Circularly Permuted Fluorogenic Proteins for the Design of Modular Biosensors. *ACS Chem. Biol.* **13**, 2392–2397 (2018).
20. Tebo, A. G. & Gautier, A. A split fluorescent reporter with rapid and reversible complementation. *Nat. Commun.* **10**, 2822 (2019).
21. Marvin, J. S. *et al.* An optimized fluorescent probe for visualizing glutamate neurotransmission. *Nat. Methods* **10**, 162–170 (2013).
22. Wu, J. *et al.* Genetically Encoded Glutamate Indicators with Altered Color and Topology. *ACS Chem. Biol.* **13**, 1832–1837 (2018).
23. Tebo, A. G. *et al.* Circularly Permuted Fluorogenic Proteins for the Design of Modular Biosensors. *ACS Chem. Biol.* **13**, 2392–2397 (2018).
24. Gibson, D. G. *et al.* Enzymatic assembly of DNA molecules up to several hundred

kilobases. *Nat. Methods* **6**, 343–5 (2009).
25. Plamont, M.-A. *et al.* Small fluorescence-activating and absorption-shifting tag for tunable protein imaging in vivo. *Proc. Natl. Acad. Sci.* **113**, 497–502 (2016).
26. Li, C. *et al.* Dynamic multicolor protein labeling in living cells. *Chem. Sci.* **8**, 5598–5605 (2017).

Chapter IV

Design and characterization of K$^+$-FAST, a potassium ion sensor based on FAST.

IV.1. Introduction

The next step into the engineering of fluorogenic biosensors based on the chemogenetic reporter FAST focused on the development of a hybrid system able to detect the potassium metal cation K$^+$, in the aim of demonstrating that our design is applicable to different types of analyte. K$^+$ is the most abundant intracellular metal ion that plays an essential role in cellular ion homeostasis, and is involved in a number of cellular processes acting as a co-factor for proteins and enzymes.[1] Its functions also include maintaining membrane potentials of organelles and excitable cells, that is particularly important for neurotransmission, as it is involved in neuron membrane depolarization triggered by action potentials.

Despite many improvements of synthetic fluorescent indicators, mostly based on the derivatization of a crown ether ionophore motif, small molecule K$^+$ biosensors struggle to meet the requirements of selective targeting, low affinity to image high ionic concentrations, and high selectivity, in particular over sodium ion Na$^+$.[2–4] Description of a fluorescent sensor based on the K$^+$-selective chelator TAC (2-triazacryptand [2,2,3]-1-(2-methoxyethoxy)benzene),[5] followed by the synthesis of variants with various emission properties, yielded another family of synthetic extracellular K$^+$ indicators with low pH sensitivity and higher selectivity.[6,7]

The development of hybrid fluorescent sensors has allowed to overcome certain limitations encountered by synthetic probes. Indeed, functionalizing the TAC chelator with a chloroalkane, separated from the cryptand motif by a cell-impermeant PEG linker, allowed targeting of the sensing moiety to the genetically encoded HaloTag, expressed at the cell membrane.[8] Furthermore, interesting selectivity was reached with another hybrid strategy based on metal recognition by nucleic acid binding moieties. FRET biosensors were thus generated by conjugating two synthetic fluorophores at the termini of DNA G-quadruplex motifs,[9,10] while a single-wavelength readout could notably be obtained from an RNA aptamer Broccoli chimera forming a tripartite complex with K$^+$ and the fluorophore DFHBI.[11]

The development of genetically encoded K$^+$ biosensors was initiated surprisingly late, due to the lack of a suitable recognition domain. Nevertheless, Ashraf et al. identified and described in 2016 the potassium (K$^+$) binding protein Kbp (also known as YgaU) from *E. coli*.[12] This two-domain protein, composed of a bacterial OsmY and nodulation (BON) domain and a lysine motif (LysM), undergoes a significant structural change from an "open" conformation to a more compact, globular one when bound to potassium. The design of intensiometric and ratiometric sensors rapidly took advantage of these properties. Two analogous FRET sensors, GEPII (Genetically Encoded Potassium Ion Indicator)[13] and KIRIN1 (K$^+$ Ion Ratiometric INdicator)[14], were consecutively designed by flanking the Kbp sensing unit with optimized CFP/YFP variants FRET pairs. In both cases, the thermodynamic and optical properties could be modulated by protein engineering, demonstrating the assets offered by genetically encoded biosensors. On the one hand, modification of the sensing unit allowed to significantly decrease the affinity of GEPIIs for K^+, either by site-directed mutagenesis or by insertion of various linkers between the BON and Lys domains, thus covering an affinity range from 0.42 to 30 mM for K^+. On the other hand, switching fluorescent proteins to the Clover green fluorescent protein (GFP) and the mRuby2 red fluorescent protein (RFP) pair yielded KIRIN-GR (KIRIN1 with GFP and RFP), a red-shifted FRET sensor for K^+ visualization.

Moreover, a different strategy consisting in the insertion of Kbp into the enhanced green fluorescent protein (EGFP) at position 144 yielded GINKO1, that binds K^+ with relatively high affinity ($K_{D,K+} = 0.42 \pm 0.03$ mM). This single-FP K^+ biosensor displayed a 2.5-fold fluorescence emission increase, as well as a 3.5-fold increase in the excitation ratio (F_{500nm}/F_{400nm}), making the optical readout both intensiometric and ratiometric. These different biosensor designs were able to probe K^+ in bacterial media, human plasma sample, and in different cell types including neurons.

The recent expansion of the fluorescent toolbox for K^+ imaging, significantly enriched by the development of FRET and single-FP genetically encoded sensors, has demonstrated the great advantage of relying on a protein recognition module for metal ions, both in terms of selectivity and modularity of its thermodynamic properties. We consequently suggested that coupling our chemogenetic reporter FAST to such sensing domain, undergoing a large conformational change upon analyte-binding, would provide allosteric modulation of the fluorescent properties displayed by the resulting hybrid K^+ biosensor.

IV.2. Study of the potassium biosensor topologies

Following the same principle as previously described in chapter III of this manuscript, the first step of designing a potassium ion (K^+) sensor based on FAST consisted in a topological study (Figure IV-1). As demonstrated by the existing genetically encoded biosensors GEPIIs[13], KIRIN1 and GINKO1[14], the sensing domain Kbp could be flanked at each termini by a reporter domain. Kbp was thus inserted in FAST at position 114-115, or in cpFAST(114-115), yielding K^+-FAST-1 and K^+-FAST-2, respectively. Structural observation of Kbp indicated that the termini of the sensing domain were spatially distant, which was suggested to possibly hamper proper interaction between FAST fragments. Short flexible two-glycine linkers were consequently added at both insertion sites, and were expected to facilitate proper folding of the reporter. Moreover, we suggested that the reporter units FAST and cpFAST could be inserted between the BON and Lys domains at position S96, yielding K^+-FAST-3 and K^+-FAST-4, respectively. No circularly permutation of Kbp has been reported to be functional; consequently, the circularly permuted versions of the four described topologies were not generated.

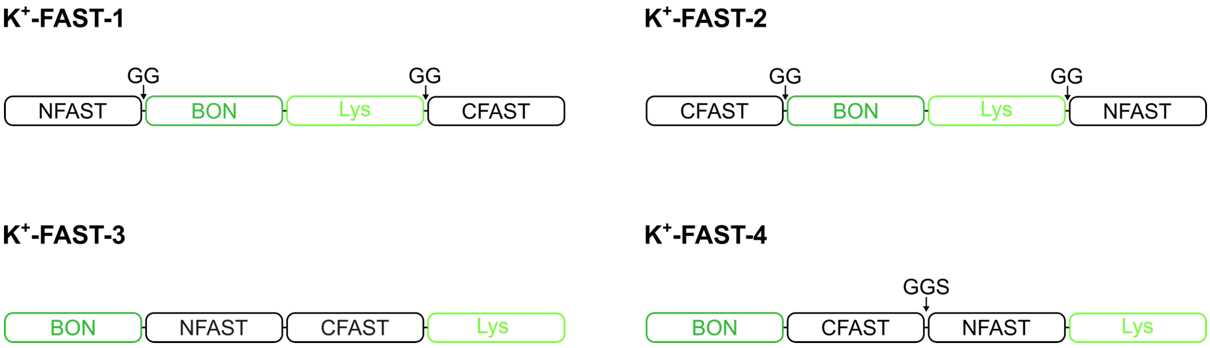

Figure IV-1. Four topologies result from the coupling of FAST/cpFAST with the K^+-binding protein (Kbp).

We first verified that addition of K^+ did not affect the reporter FAST itself, and determined then whether the fluorogen binding properties of each topology were dependent on the presence of K^+ (Figure IV-2). As previously reported in the development of the single FP biosensor GINKO1[14], splitting the sensing unit to insert a reporter between the BON and Lys domains appeared to annihilate the K^+-binding property of Kbp. Topologies K^+-FAST-3 and K^+-FAST-4 indeed showed very weak dependence on the presence of the analyte. The insertion of Kbp in FAST and the insertion of FAST in Kbp, respectively K$^+$-FAST-1 and K$^+$-FAST-3, seemed to allow proper folding of the reporter as they displayed very high binding affinities for HMBR, in both analyte-bound and -free conformations ($K_{D,HMBR}$ = 0.21 ± 0.03 μM and $K_{D,HMBR/K+}$ = 0.34 ± 0.03 μM for K$^+$-FAST-1, and $K_{D,HMBR}$ = 0.26 ± 0.02 μM and $K_{D,HMBR/K+}$ = 0.21 ± 0.02 μM for K$^+$-FAST-3). The insertion of cpFAST in Kbp, K$^+$-FAST-4, displayed on the contrary very low fluorogen binding affinities, suggesting that proper folding is hampered by fusion of the sensing domain close to the fluorogen binding region ($K_{D,HMBR}$ = 2.4 ± 0.1 μM and $K_{D,HMBR/K+}$ = 3.1 ± 0.1 μM). A promising topology was however identified, K$^+$-FAST-2, where the insertion of Kbp in cpFAST led to a biosensor displaying a reasonable positive cooperative coupling between the reporter and the sensing unit ($K_{D,HMBR}$ = 0.44 ± 0.02 μM and $K_{D,HMBR/K+}$ = 0.19 ± 0.01 μM, yielding α = 2.3).

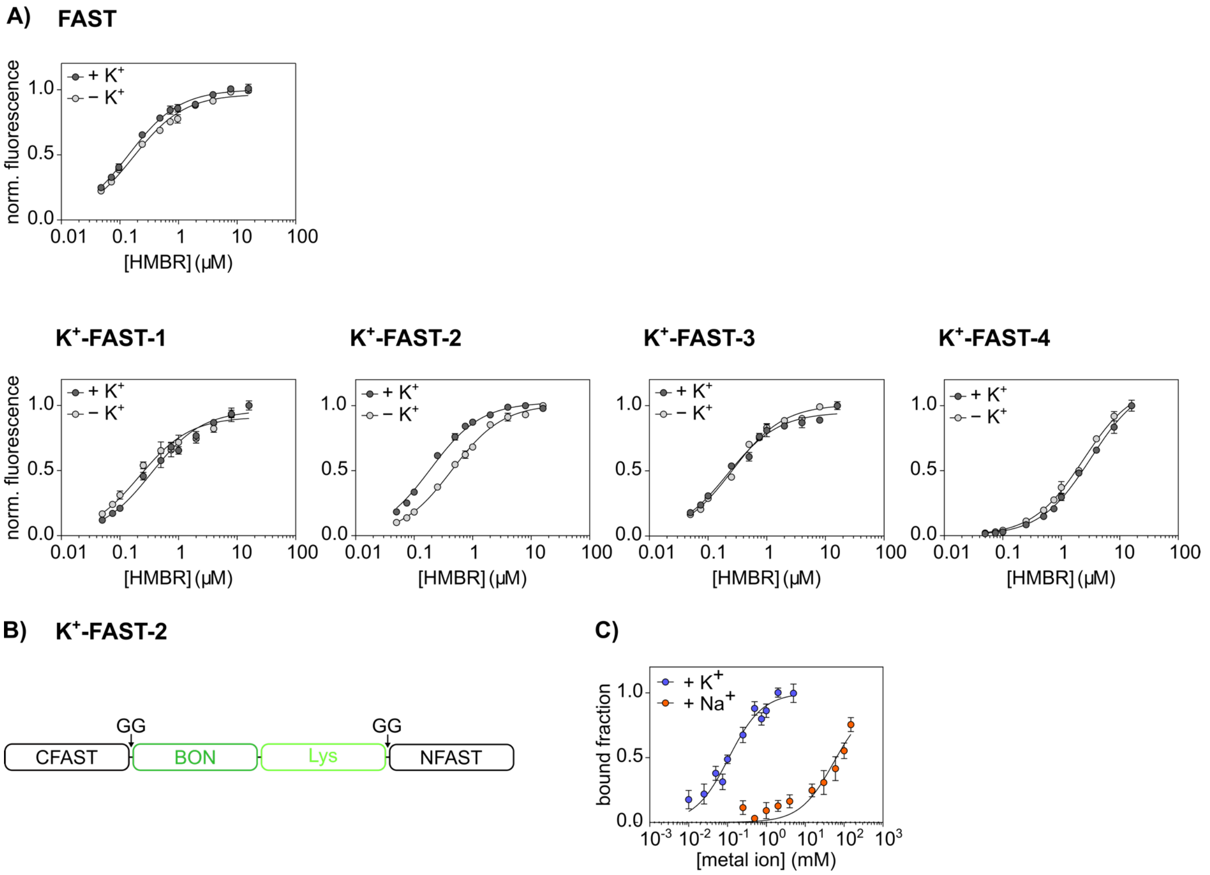

Figure IV-2. Characterization of the FAST-based K$^+$ biosensor topologies. A) HMBR titration curves of FAST and the four topologies of FAST-based K$^+$ biosensors, in absence (light grey) or in presence of 10 mM K$^+$ (dark grey) in pH 7.4 HEPES buffer (50 mM) containing $MgCl_2$ (75 mM). **B)** Topology of the selected biosensor topology K$^+$-FAST-2. **C)** K$^+$ and Na$^+$ titration curve of K$^+$-FAST-2 in the presence of 0.1 μM HMBR. Data represent the mean ± sem (n = 3). The least-squares fit (line) gave the thermodynamic dissociation constant $K_{D,HMBR}$ and $K_{D,HMBR/K+}$ and the apparent dissociation constant $K_{D,K+\ app}$ provided in Table IV-1. The sensor concentration was fixed at 0.1 μM.

Table IV-1. Characterization of the FAST-based K$^+$ biosensor topologies. For each sensor is given the dissociation constant of the fluorogen in absence of K$^+$ ($K_{D,HMBR}$), in presence of 10 mM of K$^+$ ($K_{D,HMBR/K+}$), and the cooperativity constant α, calculated as the ratio of the dissociation constant in absence of K$^+$ and in presence of K$^+$ ($K_{D,HMBR}/K_{D,HMBR/K+}$). The apparent dissociation constant of K$^+$ at [HMBR] = 0.1 µM with K$^+$-FAST-2 is also given with the associated fluorescence intensity increase observed upon K$^+$ addition (F_{max}/F_{min}).

Sensor	$K_{D,HMBR}$ (µM)	$K_{D,HMBR/K+}$ (µM)	α	$K_{D,K+\ app}$ (mM)	F_{max}/F_{min}
FAST	0.15 ± 0.01	0.17 ± 0.01	0.9	-	-
K$^+$-FAST-1	0.21 ± 0.03	0.34 ± 0.03	0.6	-	-
K$^+$-FAST-2	0.44 ± 0.02	0.19 ± 0.01	2.3	0.14 ± 0.02	1.9
K$^+$-FAST-3	0.26 ± 0.02	0.21 ± 0.02	1.2	-	-
K$^+$-FAST-4	2.4 ± 0.1	3.1 ± 0.1	0.8	-	-

K$^+$-FAST-2 was consequently selected for further characterization as it displayed the most promising properties for fluorescent detection of K$^+$. Subsequent titration of K$^+$ showed a 1.9-fold fluorescence increase upon addition of the analyte, and allowed to determine the apparent dissociation constant for K$^+$ binding $K_{D,K+\ app}$ = 0.14 ± 0.02 mM at [HMBR] = 0.1 µM. This value was surprisingly low, indicating an affinity for K$^+$ very close to the native Kbp domain, previously determined by isothermal titration calorimetry.[12]

Selectivity was identified as a common concern in the development of metal ions sensors in general, thus needed to be addressed in the development of our FAST-based K$^+$ biosensor. Na$^+$ was consequently titrated as well with K$^+$-FAST-2, allowing to determine that our biosensor displayed a non-negligible apparent affinity for Na$^+$ ions ($K_{D,Na+\ app}$ ~ 50 mM). Although achieving high selectivity, with a 350-fold higher affinity for K$^+$ over Na$^+$, these binding properties were predicted to hamper any biological applications of our biosensor. In fact, physiological Na$^+$ concentrations would usually coincide with the detection range of K$^+$-FAST-2, making our biosensor too sensitive for any use in physiological conditions.

IV.3. Optimization of the selected K^+ biosensor design

IV.3.1. Modulating K^+-FAST affinity by engineering the sensing domain

A significant affinity decrease was desirable in order to detect potassium ions in physiological conditions with our K^+-FAST-2 sensor. Several mutations in the sensing unit Kbp were previously reported to disfavour K^+ binding; yet the most drastic affinity decrease was obtained by insertion of a 15-residues flexible linker between the BON and Lys domains. This $(GGGGS)_3$ sequence was thus inserted in the sensing domain of K^+-FAST-2, yielding K^+-FAST-5 (Figure IV-3). The resulting biosensor remained functional: proper folding of FAST provided fluorogen dissociation constants comparable to K^+-FAST-2 ($K_{D,HMBR}$ = 0.42 ± 0.03 μM and $K_{D,HMBR/K+}$ = 0.23 ± 0.02 μM), and the conserved positive cooperative coupling between the reporter and the sensing unit provided a 1.9-fold fluorescence increase upon K^+ addition. Titration indeed indicated a significant 8-fold affinity loss for the analyte ($K_{D,K+\ app}$ = 1.1 ± 0.3 mM at [HMBR] = 0.1 μM). The concomitant affinity decrease for Na^+ ions, confirmed by the absence of any fluorescent signal at Na^+ concentrations up to 350 mM, conferred K^+-FAST-5 suitable properties for application in physiological conditions. Nevertheless, the properties of this biosensor were expected to be further improved, notably in terms of dynamic range, in order to enhance the reliability of the fluorescent signal.

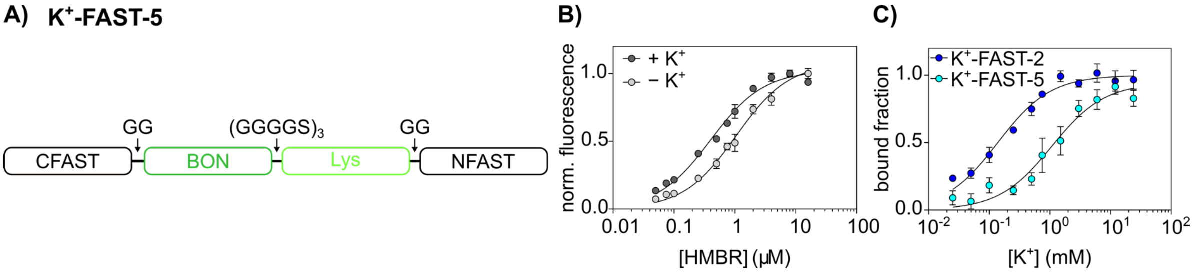

Figure IV-3. Characterization of K^+-FAST-5. A) Topology of K^+-FAST-5. **B)** HMBR titration curve of K^+-FAST-5 in absence (light grey) or in presence of 100 mM K^+ (dark grey) in pH 7.4 HEPES buffer (50 mM) containing $MgCl_2$ (75 mM). **C)** K^+ titration curve of K^+-FAST-5 in the presence of 0.1 μM HMBR. Data represent the mean ± sem (n = 3). The least-squares fit (line) gave the thermodynamic dissociation constant $K_{D,HMBR}$ and $K_{D,HMBR/K+}$ and the apparent dissociation constant $K_{D,K+\ app}$ provided in Table IV-2. The sensor concentration was fixed at 0.1 μM.

Table IV-2. Characterization of K^+-FAST-5. The dissociation constant of the fluorogen is given in absence of K^+ ($K_{D,HMBR}$), in presence of 100 mM of K^+ ($K_{D,HMBR/K+}$), and the cooperativity constant α, calculated as the ratio of the dissociation constant in absence of K^+ and in presence of K^+ ($K_{D,HMBR}/K_{D,HMBR/K+}$). The apparent dissociation constant of K^+ at [HMBR] = 0.1 µM is also given with the associated fluorescence intensity increase observed upon K^+ addition (F_{max}/F_{min}).

Sensor	**$K_{D,HMBR}$ (µM)**	**$K_{D,HMBR/K+}$ (µM)**	**α**	**$K_{D,K+ app}$ (mM)**	**F_{max}/F_{min}**
K^+-FAST-5	0.42 ± 0.03	0.23 ± 0.02	1.8	1.1 ± 0.3	1.9

IV.3.2. Exploring the effect of linkers on the dynamic range of K^+-FAST-5

Optimization of Glu-FAST-2, previously described in chapter III, provided several insights about the parameters influencing the dynamic range of a FAST-based biosensor. In this regard, increasing rigidity of the insertion regions was first considered as a possible source of improvement. However, the first strategy consisting in deleting the GG linkers between Kpb and FAST fragments led to purification issues during recombinant expression of the biosensors in *E. coli*. We then followed a second strategy to decrease flexibility of the connecting sites, by replacing either one or both two-glycine linkers by short rigid two-proline linkers in K^+-FAST-5 (Figure IV-4). The fluorogen binding affinity in both analyte-bound and -free conformations of the resulting biosensors were affected in an equivalent manner. This concomitant affinity decrease resulted in comparable cooperativity constants, however the additional rigidity of these systems appeared to hinder proper folding of the reporter in the presence of K^+, compared to the initial K^+-FAST-5 sensor. K^+ titration with the most promising candidates K^+-FAST-5-PP(1), showing the highest $\alpha = 2.0$ (from $K_{D,HMBR} = 0.73 \pm 0.06$ µM and $K_{D,HMBR/K+} = 0.37 \pm 0.03$ µM), did not provide any dynamic range improvement. Indeed, increasing the dissociation constant $K_{D,HMBR/K+}$ yielded a lower fluorescence intensity than K^+-FAST-5 at equivalent fluorogen concentration ([HMBR] = 0.1 µM). On the contrary, increasing fluorogen concentration up to 0.3 µM significantly increased the background fluorescence in the absence of K^+. Consequently, we concluded that linkers optimization by rational design would not provide any substantial improvement of our FAST-based K^+-biosensor.

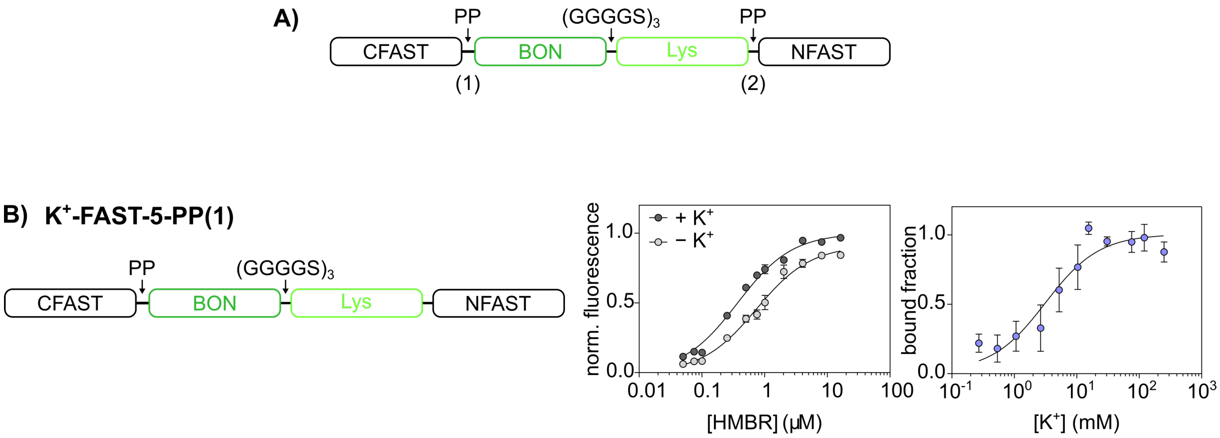

Figure IV-4. Characterization of PP-linkers insertion in K$^+$-FAST-5. A) Position of linker's insertion in K$^+$-FAST-5 topology. **B)** Topology of K$^+$-FAST-5-PP(1). **C)** HMBR titration curve of K$^+$-FAST-5-PP(1) in absence (light grey) or in presence of 100 mM K$^+$ (dark grey) in pH 7.4 HEPES buffer (50 mM) containing $MgCl_2$ (75 mM). **D)** K$^+$ titration curve of K$^+$-FAST-5-PP(1) in the presence of 0.1 µM HMBR. Data represent the mean ± sem (n = 3). The least-squares fit (line) gave the thermodynamic dissociation constant $K_{D,HMBR}$ and $K_{D,HMBR/K+}$ and the apparent dissociation constant $K_{D,K+ app}$ provided in Table IV-3.

Table IV-3. Characterization of PP-linkers insertion in K$^+$-FAST-5. For each sensor is given the dissociation constant of the fluorogen in absence of K$^+$ ($K_{D,HMBR}$), in presence of 100 mM of K$^+$ ($K_{D,HMBR/K+}$), and the cooperativity constant α, calculated as the ratio of the dissociation constant in absence of K$^+$ and in presence of K$^+$ ($K_{D,HMBR}/K_{D,HMBR/K+}$). The apparent dissociation constant of K$^+$ at [HMBR] = 0.1 µM with K$^+$-FAST-5-PP(1) is also given with the associated fluorescence intensity increase observed upon K$^+$ addition (F_{max}/F_{min}).

Sensor	$K_{D,HMBR}$ (µM)	$K_{D,HMBR/K+}$ (µM)	α	$K_{D,K+ app}$ (mM)	F_{max}/F_{min}
K$^+$-FAST-5-PP(1)	0.73 ± 0.06	0.37 ± 0.03	2.0	3.0 ± 0.85	1.5
K$^+$-FAST-5- PP(2)	0.69 ± 0.05	0.50 ± 0.03	1.4	-	-
K$^+$-FAST-5-PP(1+2)	0.63 ± 0.06	0.36 ± 0.02	1.8	-	-

IV.3.3. Optimizing K$^+$-FAST-5 dynamic range by engineering the reporter domain

More efforts were consequently focused towards optimization of the reporter domain. In fact, decreasing the affinity between FAST fragments was shown to help reducing unspecific reconstitution of a functional reporter. Using the truncated fragment CFAST(116-125) proved useful to this end, as demonstrated by the optimized version of our FAST-based glutamate sensor, Glu-FAST-2.1. This strategy was thus applied to K$^+$-FAST-5, and truncation of the residue Gly115 in CFAST yielded an optimized version of the biosensor, K$^+$-FAST-5.1 (Figure IV-5). The latter displayed an improved cooperativity constant (α = 2.5) as a result of the reduced unspecific fluorogen binding in the analyte-free biosensor conformation ($K_{\mathrm{D,HMBR}}$ = 1.0 ± 0.1 µM). Titration of K$^+$ with K$^+$-FAST-5.1 allowed to determine that the apparent affinity of the biosensor for K$^+$ remained in the millimolar range ($K_{\mathrm{D,K+\ app}}$ = 2.2 ± 0.4 mM at [HMBR] = 0.1 µM), and showed a 2.2-fold fluorescence increase upon addition of the analyte. The affinity loss for K$^+$ coincides with a lower affinity of the biosensor for the fluorogen in both analyte-bound and -free conformations, in agreement with a positive cooperative coupling between the sensing and the reporter units.

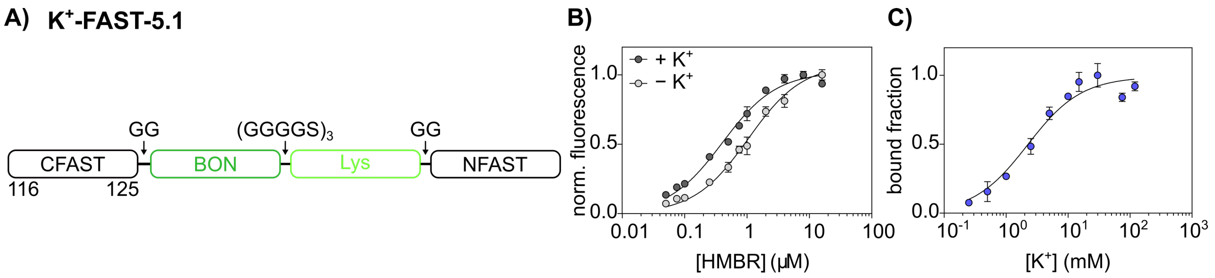

Figure IV-5. Characterization of K$^+$-FAST-5.1. A) Topology of K$^+$-FAST-5-CFAST(116-125), namely K$^+$-FAST-5. **B)** HMBR titration curve of K$^+$-FAST-5.1 in absence (light grey) or in presence of 100 mM K$^+$ (dark grey) in pH 7.4 HEPES buffer (50 mM) containing $MgCl_2$ (75 mM). **C)** K$^+$ titration curve of K$^+$-FAST-5.1 in the presence of 0.1 µM HMBR. Data represent the mean ± sem (n = 3). The least-squares fit (line) gave the thermodynamic dissociation constant $K_{\mathrm{D,HMBR}}$ and $K_{\mathrm{D,HMBR/K+}}$ and the apparent dissociation constant $K_{\mathrm{D,K+\ app}}$ provided in Table IV-4. The sensor concentration was fixed at 0.1 µM.

Table IV-4. Characterization of K$^+$-FAST-5.1. The dissociation constant of the fluorogen is given in absence of K$^+$ ($K_{D,HMBR}$), in presence of 100 mM of K$^+$ ($K_{D,HMBR/K+}$), and the cooperativity constant α, calculated as the ratio of the dissociation constant in absence of K$^+$ and in presence of K$^+$ ($K_{D,HMBR}/K_{D,HMBR/K+}$). The apparent dissociation constant of K$^+$ at [HMBR] = 0.1 µM is also given with the associated fluorescence intensity increase observed upon K$^+$ addition (F_{max}/F_{min}).

Sensor	$K_{D,HMBR}$ (µM)	$K_{D,HMBR/K+}$ (µM)	α	$K_{D,K+ app}$ (mM)	F_{max}/F_{min}
K$^+$-FAST-5.1	1.0 ± 0.1	0.40 ± 0.04	2.5	2.2 ± 0.4	2.2

IV.3.4. Characterization in mammalian cells

Following the successive optimization steps that allowed the generation of a FAST-based biosensor with a compatible affinity for K$^+$ in physiological conditions, suitable selectivity and improved dynamic range, we evaluated its use for cell imaging by fluorescence microscopy. The initially envisioned application for our biosensor implied imaging of signalling processes, as K$^+$ ions are notably important for membrane depolarization in neurotransmission. Unfortunately, attempts to target K$^+$-FAST-5 to the cellular membrane by fusion to a platelet-derived growth factor receptor (PDGFR) sequence were inconclusive (Figure IV-6). In fact, as observed with our aforementioned FAST-based glutamate biosensor, conformational issues seemingly led to aggregation in the endoplasmic reticulum of cells transfected with either the pDisplay-K$^+$-FAST-5 or its HA-tag truncated version pCMV(MinDis)-K$^+$-FAST-5 plasmids. Nonetheless, the biosensor could successfully be expressed in the cytosol, although the affinity of K$^+$-FAST-5 remained significantly too high for any quantification of potassium ion cytosolic levels. Indeed, estimated intracellular K$^+$ concentrations around 200 mM: additional optimization steps would consequently be required to generate a suitable FAST-based K$^+$ biosensor for cellular imaging.

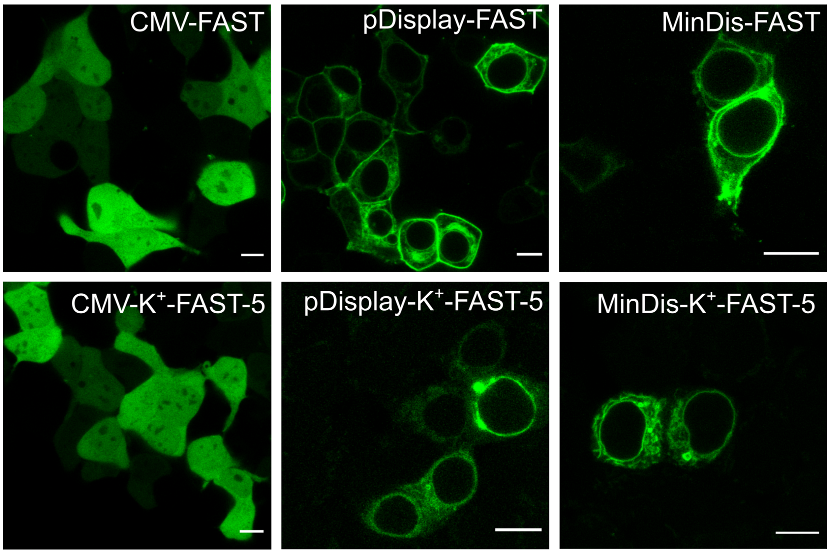

Figure IV-6. Confocal micrographs of live HEK293T cells expressing FAST and K$^+$-FAST-5, or expressing FAST and K$^+$-FAST-5 in a pDisplay plasmid (extracellular membrane targeting) or its truncated version pCMV(MinDis). [HMBR] = 5 µM, scale bar 10 µm.

IV.4. Discussion

The development of a chemogenetic sensor for potassium cations K^+ based on FAST was expected to be a valuable addition to the fluorescent detection toolbox, that was only recently expanded by genetically encoded indicators following the characterization of the K^+ binding protein Kbp. A preliminary topological study confirmed to be very valuable to identify the most promising connectivity between the reporter and the sensing module. Insertion of Kbp in cpFAST(114-115) showed an encouraging positive cooperative coupling (α = 2.3): this topology was similar to Glu-FAST-2 described in chapter II, thus displayed equivalent advantages for the general conception of biosensors. Flanking FAST fragments at the termini of a native protein sensing domain is indeed convenient in the aim of identifying a general design for analyte sensing with a hybrid reporter. Nevertheless, K^+-FAST-2 needed optimization to be suitable for the envisioned analyte detection application, notably in terms of affinity and dynamic range. In fact, proper folding of FAST did not appear dramatically affected by the conformational change undergone by Kbp from the apo- to the K^+-bound form, as the reporter showed very high affinity for the fluorogen in both conformations. The affinity of K^+-FAST-2 for K^+ was surprisingly high as well and approached the binding constant of native Kbp,[12] indicating that the sensing domain was not affected by fusion to the reporter FAST. Kbp also appeared to retain high selectivity for K^+ over Na^+, as titration with K^+-FAST-2 evaluated a 350-fold lower affinity for Na^+.

The affinity of our FAST-based K^+ sensor was adjusted by protein engineering of the sensing domain Kbp. In fact, insertion of a 15-residues linker $(GGGGS)_3$ between the BON and Lys domains significantly decreased the apparent affinity of the resulting sensor K^+-FAST-5 down to the millimolar range, that displayed as well a 1.9-fold fluorescence increase upon K^+ addition. Maintaining a very high selectivity for K^+ over Na^+, no fluorescent response was observed from K^+-FAST-5 upon addition of Na^+ up to 350 mM, a crucial property for the sensor to be suitable for application in biological conditions. Optimizing the allosteric coupling between FAST and Kbp was expected to enhance the dynamic range of K^+-FAST-5. Considering the similar behavior of Glu-FAST-2 and K^+-FAST-5, optimization of our K^+ biosensor was largely based on the previous conclusions withdrawn from the development of the FAST-based glutamate biosensor. Although increasing rigidity of the system by replacement of two-glycine by two-proline linkers was inconclusive, deletion of the residue Gly115 in the CFAST fragment appeared to decrease the affinity between FAST fragments, thus yielded to an improved 2.2-fold fluorescence increase upon K^+ addition. The modest dynamic range and cooperativity constants obtained with our hybrid K^+ sensors, despite the previously demonstrated significant structural change of Kbp upon K^+ binding, tend to speak in favour of optimizing the connecting regions between the sensing and the reporter modules. Further engineering of the reporter fragments with lower self-assembly might improve our sensor's properties; nevertheless, screening of linkers appears to be necessary in addition to rational design strategies.

K^+-FAST-5 was correctly expressed in the cytosol, although fully saturated by the very high intracellular K^+ concentrations. Additional protein engineering of the sensing unit Kbp, notably by site-directed mutagenesis that proved successful in the optimization of GEPIIs, could be envisioned to generate a FAST-based K^+ indicator suitable for intracellular applications. Unfortunately, observations from cells transfected with membrane-targeted K^+ sensors were similar to the results obtained with the FAST-based glutamate sensors described in chapter III. Indeed, fluorescent signal arising only from the endoplasmic reticulum suggested the improper folding of the sensor in this case as well, supporting the hypothesis of aggregation related to FAST fragments. Switching to a topology arising from cpFAST insertion in the sensing module might improve trafficking; nevertheless, re-engineering of the sensor would then be necessary.

Despite these setbacks, this chapter confirmed the hypothesis that FAST can be allosterically coupled to sensing modules to generate biosensors for different types of analytes, including small molecules and metal ions.

IV.5. Material & methods

General

Methods used for this project have been described in chapter III of this manuscript.

Protein expression and purification

Expression vectors of the glutamate biosensors with an N-terminal His-tag under the control of a T7 promoter were transformed in BL21 *Escherichia coli* competent cells. Bacterial cells were grown at 37 °C in Lysogeny Broth (LB) supplemented with kanamycin (50 µg/mL) until OD_{600nm} = 0.6. Subsequent production and purification steps have been described in chapter III of this manuscript. The buffer was afterwards exchanged with HEPES buffer (HEPES 50 mM, $MgCl_2$ 75 mM pH 8) using PD-10 or PD-MidiTrap G-25 desalting columns (GE Healthcare). Purity of the proteins was evaluated using SDS-PAGE electrophoresis stained with Coomassie blue.

Thermodynamic analysis

Determination of the thermodynamic constants by titration experiments were performed with a Spark 10M plate reader (Tecan) in HEPES buffer (HEPES 50 mM, $MgCl_2$ 75 mM, pH 7.4). Normalized fluorescence intensity was plotted as a function of fluorogen concentration and fitted in GraphPad Prism 7 to a one-site specific binding model.

Mammalian cell culture & fluorescence microscopy

Methods used for this project have been described in chapter III of this manuscript.

Sequences

Protein sequence of FAST:
EHVAFGSEDIENTLAKMDDGQLDGLAFGAIQLDGDGNILQYNAAEGDITGRDPKQVIGKNFFKDVAPGTDSPEFYGKFKEGVASGNLNTMFEWMIPTSRGPTKVKVHMKKALSGDSYWVFVKRV

Protein sequence of cpFAST2:
GDSYWVFVKRV**GGS**EHVAFGSEDIENTLAKMDDGQLDGLAFGAIQLDGDGNILQYNAAEGDITGRDPKQVIGKNFFKDVAPGTDSPEFYGKFKEGVASGNLNTMFEWMIPTSRGPTKVKVHMKKALS

Protein sequence of Kbp:
MGLFNFVKDAGEKLWDAVTGQHDKDDQAKKVQEHLNKTGIPDADKVNIQIADGKATVTGDGLSQEAKEKILVAVGNISGIASVDDQVKTATPATASQFYTVKSGDTLSAISKQVYGNANLYNKIFEANKPMLKSPDKIYPGQVLRIPEE

Protein sequence of K$^+$-FAST-1:
EHVAFGSEDIENTLAKMDDGQLDGLAFGAIQLDGDGNILQYNAAEGDITGRDPKQVIGKNFFKDVAPGTDSPEFYGKFKEGVASGNLNTMFEWMIPTSRGPTKVKVHMKKALS**GG**MGLFNFVKDAGEKLWDAVTGQHDKDDQAKKVQEHLNKTGIPDADKVNIQIADGKATVTGDGLSQEAKEKILVAVGNISGIASVDDQVKTATPATASQFYTVKSGDTLSAISKQVYGNANLYNKIFEANKPMLKSPDKIYPGQVLRIPEE**GG**GDSYWVFVKRV

Protein sequence of K$^+$-FAST-2:
GDSYWVFVKRV**GG**MGLFNFVKDAGEKLWDAVTGQHDKDDQAKKVQEHLNKTGIPDADKVNIQIADGKATVTGDGLSQEAKEKILVAVGNISGIASVDDQVKTATPATASQFYTVKSGDTLSAISKQVYGNANLYNKIFEANKPMLKSPDKIYPGQVLRIPEE**GG**EHVAFGSEDIENTLAKMDDGQLDGLAFGAIQLDGDGNILQYNAAEGDITGRDPKQVIGKNFFKDVAPGTDSPEFYGKFKEGVASGNLNTMFEWMIPTSRGPTKVKVHMKKALS

Protein sequence of K$^+$-FAST-3:
MGLFNFVKDAGEKLWDAVTGQHDKDDQAKKVQEHLNKTGIPDADKVNIQIADGKATVTGDGLSQEAKEKILVAVGNISGIASVDDQVKTATPATEHVAFGSEDIENTLAKMDDGQLDGLAFGAIQLDGDGNILQYNAAEGDITGRDPKQVIGKNFFKDVAPGTDSPEFYGKFKEGVASGNLNTMFEWMIPTSRGPTKVKVHMKKALSGDSYWVFVKRVASQFYTVKSGDTLSAISKQVYGNANLYNKIFEANKPMLKSPDKIYPGQVLRIPEE

Protein sequence of K$^+$-FAST-4:
MGLFNFVKDAGEKLWDAVTGQHDKDDQAKKVQEHLNKTGIPDADKVNIQIADGKATVTGDGLSQEAKEKILVAVGNISGIASVDDQVKTATPATGDSYWVFVKRV**GGS**EHVAFGSEDIENTLAKMDDGQLDGLAFGAIQLDGDGNILQYNAAEGDITGRDPKQVIGKNFFKDVAPGTDSPEFYGKFKEGVASGNLNTMFEWMIPTSRGPTKVKVHMKKALSASQFYTVKSGDTLSAISKQVYGNANLYNKIFEANKPMLKSPDKIYPGQVLRIPEE

Protein sequence of K$^+$-FAST-5:
GDSYWVFVKRV**GG**MGLFNFVKDAGEKLWDAVTGQHDKDDQAKKVQEHLNKTGIPDADKVNIQIADGKATVTGDGLSQEAKEKILVAVGNISGIASVDDQVKTATPATAS**GGGGSGGGGSGGGGS**QFYTVKSGDTLSAISKQVYGNANLYNKIFEANKPMLKSPDKIYPGQVLRIPEE**GG**EHVAFGSEDIENTLAKMDDGQLDGLAFGAIQLDGDGNILQYNAAEGDITGRDPKQVIGKNFFKDVAPGTDSPEFYGKFKEGVASGNLNTMFEWMIPTSRGPTKVKVHMKKALS

Protein sequence of K-FAST-5.1:
DSYWVFVKRV**GG**MGLFNFVKDAGEKLWDAVTGQHDKDDQAKKVQEHLNKTGIPDADKVNIQIADGKATVTGDGLSQEAKEKILVAVGNISGIASVDDQVKTATPATAS**GGGGSGGGGSGGGGS**QFYTVKSGDTLSAISKQVYGNANLYNKIFEANKPMLKSPDKIYPGQVLRIPEE**GG**EHVAFGSEDIENTLAKMDDGQLDGLAFGAIQLDGDGNILQYNAAEGDITGRDPKQVIGKNFFKDVAPGTDSPEFYGKFKEGVASGNLNTMFEWMIPTSRGPTKVKVHMKKALS

Molecular cloning

Unless specified otherwise, designations NFAST and CFAST stand for FAST(1-114) and FAST(115-125), respectively.

The plasmid pAG441, encoding pET28new-His-K$^+$-FAST-1, was constructed by Gibson assembly from the plasmid pAG399 encoding pET28new-His-FAST. The fragment coding for NFAST was amplified by PCR using the primers ag614/kanF. The fragment coding for CFAST was amplified using the primers ag613/kanR. The insert coding for Kbp was amplified from pAG401 encoding pET28new-His-Kbp using the primers ag615/ag616. The three fragments were then assembled by Gibson assembly.

The plasmid pAG442, encoding pET28new-His-K$^+$-FAST-2, was constructed by Gibson assembly from the plasmid pAG400 encoding pET28new-His-cpFAST2. The fragment coding for CFAST was amplified by PCR using the primers ag618/kanF. The fragment coding for NFAST was amplified using the primers ag617/kanR. The insert coding for Kbp was amplified from pAG401 encoding pET28new-His-Kbp using the primers ag619/ag620. The three fragments were then assembled by Gibson assembly.

The plasmid pAG443, encoding pET28new-His-K$^+$-FAST-3, was constructed by Gibson assembly from the plasmid pAG401 encoding pET28new-His-Kbp. The fragment coding for BON was amplified by PCR using the primers ag622/kanF. The fragment coding for Lys was amplified using the primers ag621/kanR. The insert coding for FAST was amplified from pAG399 encoding pET28new-His-FAST using the primers ag623/ag624. The three fragments were then assembled by Gibson assembly.

The plasmid pAG444, encoding pET28new-His-K$^+$-FAST-4, was constructed by Gibson assembly from the plasmid pAG401 encoding pET28new-His-Kbp. The fragment coding for BON was amplified by PCR using the primers ag626/kanF. The fragment coding for Lys was amplified using the primers ag625/kanR. The insert coding for cpFAST2 was amplified from pAG400 encoding pET28new-His-cpFAST2 using the primers ag627/ag628. The three fragments were then assembled by Gibson assembly.

The plasmid pAG512, encoding pET28new-His-K$^+$-FAST-5, was constructed by Gibson assembly from the plasmid pAG442. The fragment coding for CFAST-GG-BON was amplified by PCR using the primer ag732 containing the sequence coding for linker (GGGGS)$_3$, with the primer kanF. The fragment coding for Lys-GG-NFAST was amplified using the primer ag731 containing the complementary sequence coding for linker (GGGGS)$_3$, with the primer kanR. The two fragments were then assembled by Gibson assembly.

The plasmid pAG623, encoding pDisplay-K$^+$-FAST-5, was constructed by Gibson assembly from the plasmid pAG512. The pDisplay backbone was amplified by PCR using the primers ag313/ag571 and ag314/ag572. The insert coding for K$^+$-FAST-5 was amplified by PCR using the primers ag906/ag907. The three fragments were then assembled by Gibson assembly.

The plasmid pAG625, encoding pET28new-His-K$^+$-FAST-5.1, was constructed by Gibson assembly from the plasmid pAG512. The pET28new backbone was amplified by PCR using the primers ag579/kanF. The insert coding for CFAST(116-125)- GG-Kbp(GGGGS)$_3$-GG-NFAST was amplified by PCR using the primers ag804/kanR. The two fragments were then assembled by Gibson assembly.

The plasmid pAG677, encoding CMV-CFAST-K$^+$-FAST-5-myc, was constructed by Gibson assembly from the plasmid pAG512. The CMV backbone was amplified by PCR using primers ag358/ag313 and ag348/ag314. The insert coding for K$^+$-FAST-5 was amplified by PCR using the primers ag231/596. The three fragments were then assembled by Gibson assembly

The plasmid pAG739, encoding pCMV(MinDis)-K$^+$-FAST-5, was constructed by Gibson assembly from the plasmid pAG512. The pCMV(MinDis) backbone was amplified by PCR using primers ag571/ag313 and ag853/ag314. The insert coding for K$^+$-FAST-5 was amplified by PCR using the primers ag1064/1065. The three fragments were then assembled by Gibson assembly.

Plasmid	**From**	**Primers**
pAG399	pAG104 + pET28new	ag578, 579, 580, 581, 601, 602
pAG400	pAG120 + pET28new	ag578, 579, 580, 581, 603, 604
pAG401	synthetic gene + pET28new	ag578, 579, 605, 606
pAG441	pAG399 + pAG401	ag613, 614, 615, 616, kanF, kanR
pAG442	pAG400 + pAG401	ag617, 618, 619, 620, kanF, kanR
pAG443	pAG401 + pAG399	ag621, 622, 623, 624, kanF, kanR
pAG444	pAG401 + pAG400	ag625, 626, 627, 628, kanF, kanR
pAG512	pAG442	ag731, 732, kanF, kanR
pAG623	pAG211 + pAG512	ag313, 314, 571, 572, 906, 907
pAG625	pAG512	ag579, 804, kanF, kanR
pAG677	pAG398 + pAG512	ag231, 313, 314, 358, 596, 848
pAG739	pAG621 + pAG512	ag313, 314, 571, 853, 1064, 1065

Primer	**Sequence**
kanf	gcatcaaccaaaccgttattcattcgtg
kanr	cacgaatgaataacggtttggttgatgc
ag231	gaaataagcttttgttcggatccggaaagggctttcttcatgtg
ag313	ctcaccttgctcctgccgagaaagtatcca
ag314	tggatactttctcggcaggagcaaggtgag
ag358	ggtggcagatctgagtccggtag
ag571	gtcgacgaacaaaaactcatctcag
ag572	agatctggccggctgggcc
ag578	taatgactcgagcaccaccaccacc
ag579	catgctagccatatggctgccg
ag580	gcctagagcaagacgtttcccgttgaatatg
ag581	attcaacgggaaacgtcttgctctaggc
ag596	ctaccggactcagatctgccaccatgggtgacagctattgggtctttg
ag601	ggcagccatatggctagcatggagcatgttgcctttgg
ag602	ggtggtggtgctcgagtcattacacccgtttcacaaagaccc
ag603	ggcagccatatggctagcatgggtgacagctattgggtc
ag604	ggtggtggtgctcgagtcattaggaaagggctttcttcatgtg
ag605	ggcagccatatggctagcatgatgggtctgttcaattttgtgaaagatg
ag606	ggtggtggtgctcgagtcattactactcttccggaatacgcaac
ag613	gtattccggaagagggcggcggtgacagctattgggtctttg
ag614	ttgaacagacccataccaccggaaagggctttcttcatgtgc
ag615	agaaagccctttccggtggtatgggtctgttcaattttgtgaaag
ag616	caatagctgtcaccgccgccctcttccggaatacgcaacac
ag617	gtattccggaagagggcggcgagcatgttgcctttggc
ag618	ttgaacagacccataccacccacccgtttcacaaagaccc
ag619	ttgtgaaacgggtgggtggtatgggtctgttcaattttgtgaaag
ag620	aaggcaacatgctcgccgccctcttccggaatacgcaacac
ag621	gggtctttgtgaaacgggtggccagccagttttataccgttaag
ag622	ctgccaaaggcaacatgctcagtggctggtgtcgcc
ag623	gaaaacggcgacaccagccactgagcatgttgcctttggcag
ag624	acggtataaaactggctggccacccgtttcacaaagaccc
ag625	acatgaagaaagccctttccgccagccagttttataccgttaag
ag626	aagacccaatagctgtcaccagtggctggtgtcgc
ag627	gaaaacggcgacaccagccactggtgacagctattgggtctttg
ag628	acggtataaaactggctggcggaaagggctttcttcatgtgc
ag731	ggcggaggcggaagcggcggaggcggatccggcggaggcggaagccagttttataccgttaagtctggc
ag732	gcttccgcctccgccggatccgcctccgccgcttccgcctccgccgctggcagtggctggtgtc
ag804	gcagccatatggctagcatggacagctattgggtctttgtgaaac
ag848	ggatccgaacaaaagcttatttctgaagag
ag853	gatgagtttttgttcgtcgacggaaagggctttcttcatgtgc
ag906	ggggcccagccggccagatctatgggtgacagctattgggtc
ag907	gatgagtttttgttcgtcgacggaaagggctttcttcatgtgc
ag1064	agatctgtcaccagtggaacctg
ag1065	gttccactggtgacagatctggtgacagctattgggtctttg

IV.6. References

1. Depaoli, M. R. *et al.* Live cell imaging of signaling and metabolic activities. *Pharmacol. Ther.* **202**, 98–119 (2019).
2. Jezek, P., Mahdi, F. & Garlid, K. D. Reconstitution of the beef heart and rat liver mitochondrial K+/H+ (Na+/H+) antiporter. Quantitation of K+ transport with the novel fluorescent probe, PBFI. *J. Biol. Chem.* **265**, 10522–10526 (1990).
3. Rimmele, T. S. & Chatton, J. Y. A novel optical intracellular imaging approach for potassium dynamics in astrocytes. *PLoS One* **9**, 1–9 (2014).
4. Wang, Z., Detomasi, T. C. & Chang, C. J. A dual-fluorophore sensor approach for ratiometric fluorescence imaging of potassium in living cells. *Chem. Sci.* **12**, 1720–1729 (2021).
5. He, H., Mortellaro, M. A., Leiner, M. J. P., Fraatz, R. J. & Tusa, J. K. A Fluorescent Sensor with High Selectivity and Sensitivity for Potassium in Water. *J. Am. Chem. Soc.* **125**, 1468–1469 (2003).
6. Padmawar, P., Yao, X., Bloch, O., Manley, G. T. & Verkman, A. S. K+ waves in brain cortex visualized using a long-wavelength K+-sensing fluorescent indicator. *Nat. Methods* **2**, 825–827 (2005).
7. Namkung, W., Padmawar, P., Mills, A. D. & Verkman, A. S. Cell-Based Fluorescence Screen for K+ Channels and Transporters Using an Extracellular Triazacryptand-Based K+ Sensor. *J. Am. Chem. Soc.* **25**, 7794–7795 (2008).
8. Hirata, T. *et al.* Protein-Coupled Fluorescent Probe to Visualize Potassium Ion Transition on Cellular Membranes. *Anal. Chem.* **88**, 2693–2700 (2016).
9. He, F., Tang, Y., Wang, S., Li, Y. & Zhu, D. Fluorescent amplifying recognition for DNA G-quadruplex folding with a cationic conjugated polymer: A platform for homogeneous potassium detection. *J. Am. Chem. Soc.* **127**, 12343–12346 (2005).
10. Nagatoishi, S., Nojima, T., Juskowiak, B. & Takenaka, S. A Pyrene-Labeled G-Quadruplex Oligonucleotide as a Fluorescent Probe for Potassium Ion Detection in Biological Applications. *Angew. Chemie* **117**, 5195–5198 (2005).
11. Savage, J. C., Shinde, P., Yao, Y., Davare, M. A. & Shinde, U. A Broccoli aptamer chimera yields a fluorescent K+sensor spanning physiological concentrations. *Chem. Commun.* **57**, 1344–1347 (2021).
12. Ashraf, K. U. *et al.* The Potassium Binding Protein Kbp Is a Cytoplasmic Potassium Sensor. *Structure* **24**, 741–749 (2016).
13. Bischof, H. *et al.* Novel genetically encoded fluorescent probes enable real-Time detection of potassium in vitro and in vivo. *Nat. Commun.* **8**, 1–11 (2017).
14. Shen, Y. *et al.* Genetically encoded fluorescent indicators for imaging intracellular potassium ion concentration. *Commun. Biol.* **2**, 18 (2019).

Chapter V

Design and characterization of ATP-FAST, a modular adenosine-5’-triphosphate sensor based on FAST.

V.1. Introduction

Encouraged by the possibility to allosterically couple fluorogen binding to FAST with analyte binding to a sensing module, we shifted our focus towards the development of a biosensor for adenosine-5'-triphosphate (ATP), another highly biologically relevant small molecule.

ATP is a ubiquitous biomolecule known to be highly implicated in cell metabolism. Mainly produced in mitochondria by several pathways including cellular respiration, ketosis or oxidative phosphorylation, ATP is subsequently metabolised by a number of cellular processes that rely on ATP-dependent reactions. Intracellularly, ATP is notably involved in the synthesis and degradation of metabolites, membrane transport by regulation of ion channels, or complex processes such as exocytosis. ATP also plays a significant role in extracellular processes such as purinergic signalling, and its role as a neurotransmitter is being studied, especially in astrocytes.[1,2]

Optical monitoring of ATP levels was first based on the enzymatic reaction of firefly luciferase chimeras. Indeed, the conversion of luciferin to oxyluciferin by the luciferase enzyme consumes ATP in stoichiometric amount, while emitting a proportional amount of chemiluminescent signal. Luciferase-based ATP detection has been broadly used since then, and is considered as a reliable technique. The ubiquity of ATP in all living organisms has notably been exploited for the bioluminescent evaluation of bacterial contamination and propagation in rapid and high-throughput assays.[3] This detection method was also widely implemented for microscopy imaging of cytosolic ATP levels, as well as ATP distribution at the mitochondrial and cellular membranes, from live cells to whole organisms.[4] However, the oxygen-dependent luciferase reaction restricts its application to aerobic environments, and can also be hampered by the limited supply of endogenous luciferin. Moreover, relatively low bioluminescence intensities require long acquisitions, thus low time-resolution.

The first strategy used to study ATP based on fluorescence from a genetically encoded biosensor relied on the coupling of a circularly permuted GFP with the regulatory protein GlnK1 from *Methanococcus jannaschii* as a sensing module, yielding the single-wavelength sensor Perceval.[5] GlnK1 binds ATP and ADP with different affinities; competition between both metabolites thus modulated the sensing domain conformation, and the resulting fluorescence variations allowed the indirect measurement of intracellular ATP/ADP ratios. An improved variant PercevalHR, developed by site-directed mutagenesis, notably enabled visualization of the cellular energy balance in cultured neurons and astrocytes.[6] Direct fluorescent detection of ATP was enabled by the identification of the highly selective ε subunit of bacterial F_OF_1-ATP synthase, a small protein domain composed of one N-terminal β-barrel domain and two C-terminal α-helices. This binding domain undergoes a significant conformational change from a flexible extended structure to a compact form upon ATP complexation, as the two helices fold into a hairpin.[7] Interestingly, homologous ε subunits have been isolated from two different bacterial strains, either the mesophilic *Bacillus subtilis*[8] or the thermophilic *Bacillus sp.* PS3.[9] While the two domains display a high sequence homology, and mutations are mainly located on residues that do not directly interact with ATP, *B.* PS3 ε binds ATP with much higher affinity than *B. subtilis* ε. These properties suggested that the ε subunit of bacterial F_OF_1-ATP synthase was a promising sensing module for the development of fluorescent biosensors with various optical and thermodynamic properties.

Insertion of either ε subunit between a cyan fluorescent protein mseCFP and a mVenus variant yielded the FRET biosensor series Ateams, including the low-affinity sensor AT1.03 based on *B. subtilis* ε (*in vitro* $K_{D,ATP}$ = 3.3 mM at 37 °C) and the high-affinity sensor AT3.10 based on *B.* PS3 ε (*in vitro* $K_{D,ATP}$ = 7.4 µM at 37 °C).[10] Further optimization of the sensing module by site-directed mutagenesis yielded AT1.03NL, an ATeam variant suitable for detection at lower temperatures, that allowed the study of ATP distribution in whole organisms *D. melanogaster* and *C. elegans*.[11] Targeting at subcellular localization enabled the visualization of ATP variations in the endoplasmic reticulum with ERAT4.01[12], as well as extracellular ATP transients using ecAT3.10.[13] However, despite the advantages provided by these ratiometric biosensors, these strategies encountered limitations notably related with differences of maturation time between the two fluorescent proteins.

In the aim of studying the metabolic state distribution of a bacterial cells population, the single-FP biosensors QUEEN (quantitative evaluator of cellular energy) were generated by insertion of the circularly permuted enhanced green fluorescent protein (cpEGFP) into sensing domains with varying affinities for ATP.[14] The QUEEN series thus covered a wide range of affinities for ATP, relying on the sensing module *B*. PS3 ε, a modified version of *B.*PS3 ε containing the C-terminal helix sequence from *B. subtilis* ε, or a mutated version of full length *B. subtilis* ε, that displayed $K_{D,ATP}$ = 7 µM, $K_{D,ATP}$ = 2 mM or was insensitive to ATP, respectively. Interestingly, QUEEN sensors provided a ratiometric measurement of ATP levels from an increasing excitation ratio λ_{ex}400/ λ_{ex}494. Furthermore, the great interest in correlating variations of ATP levels with various cellular processes encouraged the development of intensiometric ATP biosensors, in order to facilitate multiplexed imaging. A similar strategy relied on the insertion of a blue fluorescent protein variant, the Citrine fluorescent protein and mApple into the low-affinity domain *B. subtilis* ε, yielding the MaLion series of blue-, green- and red-emitting ATP biosensors. MaLions notably allowed the simultaneous visualization of nuclear, mitochondrial and cytoplasmic ATP levels in HeLa cells.[15] Finally, the recent design of iATPSnFR using the circularly permuted superfolding GFP variant (cpSFGFP) enabled proper membrane expression and detection of ATP release from neurons and astrocytes with high affinity.[16] Ratiometric measurement of ATP levels were possible by N-terminal fusion of the red fluorescent protein mRuby, as the latter showed constant fluorescence intensity while the sensor retained a two-fold green fluorescence increase upon ATP binding.

The vast interest in quantifying ATP variations during metabolic studies in a wide variety of contexts (either intra- or extracellularly, in bacterial cells, mammalian cells, or even whole organisms), thus encouraged the development of innovative biosensing tools. We envisioned that the advantages displayed by hybrid reporters would be beneficial to the design of ATP sensors. The use of FAST was anticipated to overcome limitations such as oxygen-dependence or maturation time of classical fluorescent proteins, and was consequently considered a promising reporter module for the development of a modular chemogenetic ATP biosensor.[1]

---

[1] A Master's thesis project has been performed in the course of this study by Lina El Hajji, who helped performing the experiments and data analysis for the identification and characterization of ATP-FAST-1.

V.2. Study of the ATP biosensor topologies

Inspired from the previously described ATP indicators, and with the aim of designing an analogous ATP biosensor based on FAST, we needed to identify a suitable sensing unit that would provide a significant effect on the coupled reporter properties upon analyte binding. Consequently, we decided to base our first developments on the high-affinity ATP recognition domain, namely the ε-subunit of F_OF_1-ATP synthase from the thermophilic *Bacillus* PS3 (*B*. PS3 ε), for coupling to the reporter unit. Four different topologies were considered: the sensing unit *B*. PS3 ε was either flanked with FAST fragments, or the reporter domain was inserted in *B*. PS3 ε at position 107-110, that was previously identified as a possible split position.[14,16] Insertion of *B*. PS3 ε in FAST or cpFAST thus yielded ATP-FAST-1 and ATP-FAST-2, respectively, while insertion of FAST or cpFAST in *B*.PS3 ε yielded ATP-FAST-3 and ATP-FAST-4, respectively. All four His-tagged sensors were expressed in bacteria, and purified by affinity chromatography. Note that we obtained protein fractions with high yield and purity, despite some visible aggregation at high protein concentrations that intensified over subsequent freezing and thawing cycles.

Before characterization of ATP-FAST sensors properties, we verified that the reporter domain FAST itself was not affected by the presence of ATP: HMBR titration with FAST was indeed independent on the presence or the absence of ATP. Subsequent titration experiments with the four biosensor topologies allowed us to demonstrate that the presence of ATP modulated the affinity for the HMBR fluorogen, although in different proportions for the four systems. Furthermore, the binding of the fluorogen and ATP operated in a negatively cooperative manner, i.e. the binding of one hampered that of the other (Figure V-1). The topologies ATP-FAST-3 and ATP-FAST-4 in which FAST or cpFAST are inserted within *B*. PS3 ε both showed rather low dependence to the presence of ATP, although ATP sensing was previously described from the single-wavelength sensors QUEEN[14] and iATPSnFR[16] that adopted similar design. Engineering of the connecting regions by insertion and/or optimization of linkers would probably be required to obtain a FAST-based ATP sensor with suitable properties. More interestingly, we observed that the two topologies consisting in the insertion of *B.* PS3 ε within FAST or cpFAST (ATP-FAST-1 and ATP-FAST-2, respectively) showed a much larger dependence on the presence of ATP. A strong negative allosteric modulation was observed: $K_{D,HMBR}$ was considerably smaller for the analyte-free sensor than its analyte-bound form ($K_{D,HMBR/ATP}$), giving cooperativity constants $\alpha_{ATP\text{-}FAST\text{-}1} \sim 0.01$ and $\alpha_{ATP\text{-}FAST\text{-}2} \sim 0.04$.

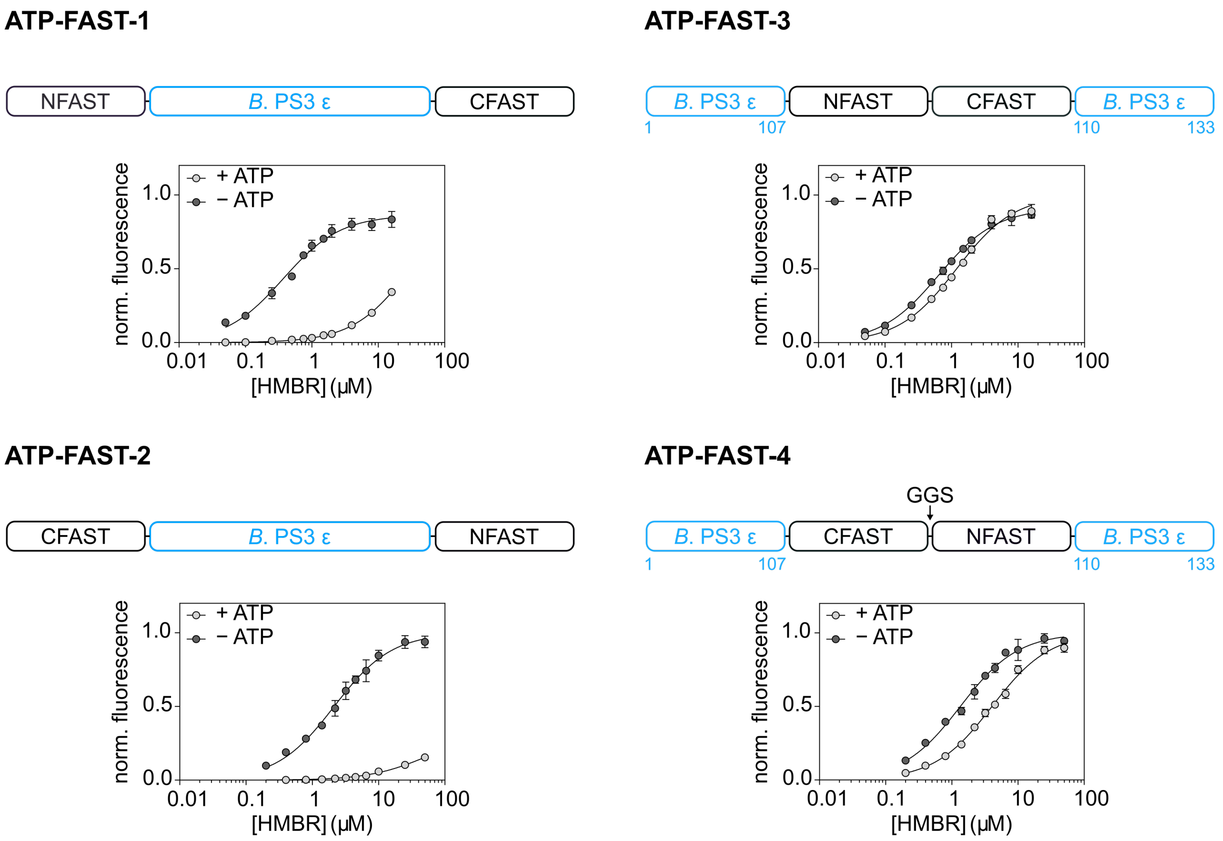

Figure V-1. Characterization of the FAST-based ATP biosensors topologies. HMBR titration curves of the four topologies of FAST-based ATP biosensors, in absence (light grey) or in presence of 5 mM ATP (dark grey) in pH 7.4 HEPES buffer (50 mM) containing $MgCl_2$ (75 mM). Data represent the mean ± sem (n = 3). The least-squares fit (line) gave the thermodynamic dissociation constants $K_{D,HMBR}$ and $K_{D,HMBR/ATP}$ provided in Table V-1. The sensor concentration was fixed at 0.1 µM.

Table V-1. Characterization of the FAST-based ATP biosensors topologies. For each sensor is given the dissociation constant of the fluorogen in absence of ATP ($K_{D,HMBR}$), in presence of 5 mM of ATP ($K_{D,HMBR/ATP}$), and the cooperativity constant α, calculated as the ratio of the dissociation constant in absence of ATP and in presence of ATP ($K_{D,HMBR/ATP}/K_{D,HMBR}$).

Sensor	$K_{D,HMBR}$ (µM)	$K_{D,HMBR/ATP}$ (µM)	α
ATP-FAST-1	0.37 ± 0.03	~ 31	~ 0.01
ATP-FAST-2	2.1 ± 0.1	~ 52	~ 0.04
ATP-FAST-3	0.64 ± 0.02	1.2 ± 0.1	0.5
ATP-FAST-4	1.3 ± 0.1	4.0 ± 0.2	0.3

As ATP-FAST-1 and ATP-FAST-2 showed a strong allosteric coupling on ATP, we next investigated their affinity for ATP. ATP titration at constant fluorogen concentration such that [HMBR] = $K_{\mathrm{D,HMBR}}$ yielded a 3.8-fold and a 2.4-fold fluorescence decrease upon ATP binding, respectively (Figure V-2). In agreement with a strong negative allosteric modulation, ATP-FAST-2 showed a very low apparent dissociation constant for ATP in the micromolar range ($K_{\mathrm{D,ATP\ app}}$ = 2.5 ± 0.4 µM at [HMBR] = 2.1 µM) resulting from the moderate affinity of cpFAST for its cognate fluorogen. Displaying higher affinity for the fluorogen in both analyte-bound and -free state of the sensor, ATP-FAST-1 showed a nearly 40-fold lower apparent affinity for ATP ($K_{\mathrm{D,ATP\ app}}$ = 110 ± 21 µM at [HMBR] = 0.4 µM). ATP concentrations in biological conditions being generally situated in the low millimolar range, ATP-FAST-1 was envisioned to be more suitable for detection in a biological context, and was consequently selected for further characterization and optimization.

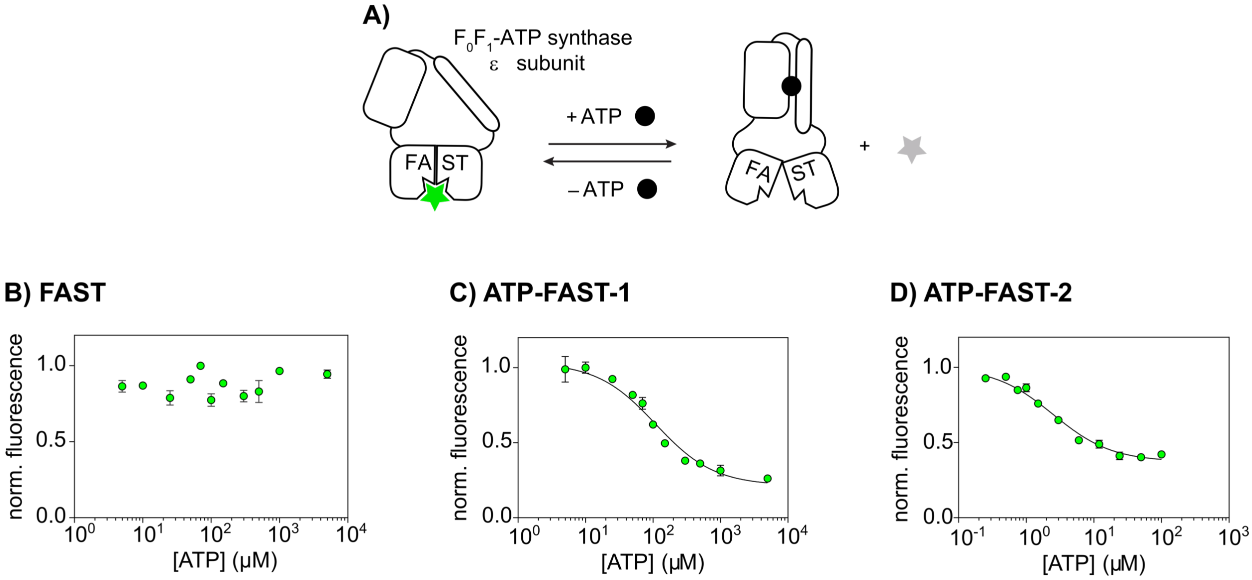

Figure V-2. ATP affinity of ATP-FAST-1 and ATP-FAST-2. A) Schematic representation of ATP-FAST-2. **B-D)** ATP titration curve of FAST, ATP-FAST-1 and ATP-FAST-2, respectively, in the presence of [HMBR] = $K_{D,HMBR}$ in pH 7.4 HEPES buffer (50 mM) containing $MgCl_2$ (75 mM). Data represent the mean ± sem (n = 3). The least-squares fit (line) gave the apparent thermodynamic dissociation constants $K_{D,ATP\ app}$ provided in Table V-2. The sensor concentration was fixed at 0.1 μM.

Table V-2. ATP affinity of ATP-FAST-1 and ATP-FAST-2. For each sensor is given the apparent dissociation constant for ATP with the associated fluorescence intensity decrease observed upon ATP addition (F_{max}/F_{min}).

Sensor	[fluorogen] = $K_{D,HMBR}$ (μM)	$K_{D,ATP\ app}$ (μM)	F_{max}/F_{min}
ATP-FAST-1	0.4	110 ± 21	3.8
ATP-FAST-2	2.1	2.5 ± 0.4	2.4

We then titrated ATP with ATP-FAST-1 at different biologically relevant pH values, ranging from 6.8 to 8.0. Interestingly, at constant HMBR concentration ([HMBR] = 0.4 μM), neither the affinity for ATP nor the dynamic range of the biosensor were affected by pH variations (Figure V-3). This was a valuable observation considering that ATP depletion is sometimes correlated with pH fluctuations in cellular compartments (as observed for example in mitochondria during glycolysis inhibition[17]). Moreover, selectivity of ATP-FAST-1 was evaluated by measuring the biosensor response to the addition of ATP nucleotide analogs GTP, ADP, AMP, adenosine and dATP. No fluorescence decrease could be observed upon addition of 1.2 mM of each compound (such as [analog] > 10 $K_{\mathrm{D,ATP\ app}}$), suggesting that ATP-FAST-1 displayed a high selectivity for ATP and would reliably provide an analyte-specific signal.

Finally, specificity of the biosensor response to ATP was verified by the generation of an ATP-insensitive version. Indeed, two Arg residues (R122 and R126) were previously identified as substantially involved in ATP binding by direct contact, and mutation of these positions drastically influenced the affinity of *B.* PS3 ε for ATP.[9] An ATP-insensitive version of ATeams was thus engineered by the introduction of the mutations R122K/R126K in the sensing domain, yielding AT1.03$^{\mathrm{R122K/R126K}}$ that did not respond to ATP concentrations up to 10 mM.[10] Following the same strategy, the mutations R122K/R126K were also introduced in the sensing unit of ATP-FAST-1. The resulting ATP-FAST-1-R122K/R126K displayed very high affinity for HMBR that was not affected by the presence of ATP ($K_{\mathrm{D,HMBR}}$ = $K_{\mathrm{D,HMBR/ATP}}$ = 0.06 ± 0.01 μM), and subsequent titration confirmed that no fluorescence decrease was observed upon addition of ATP up to 5 mM.

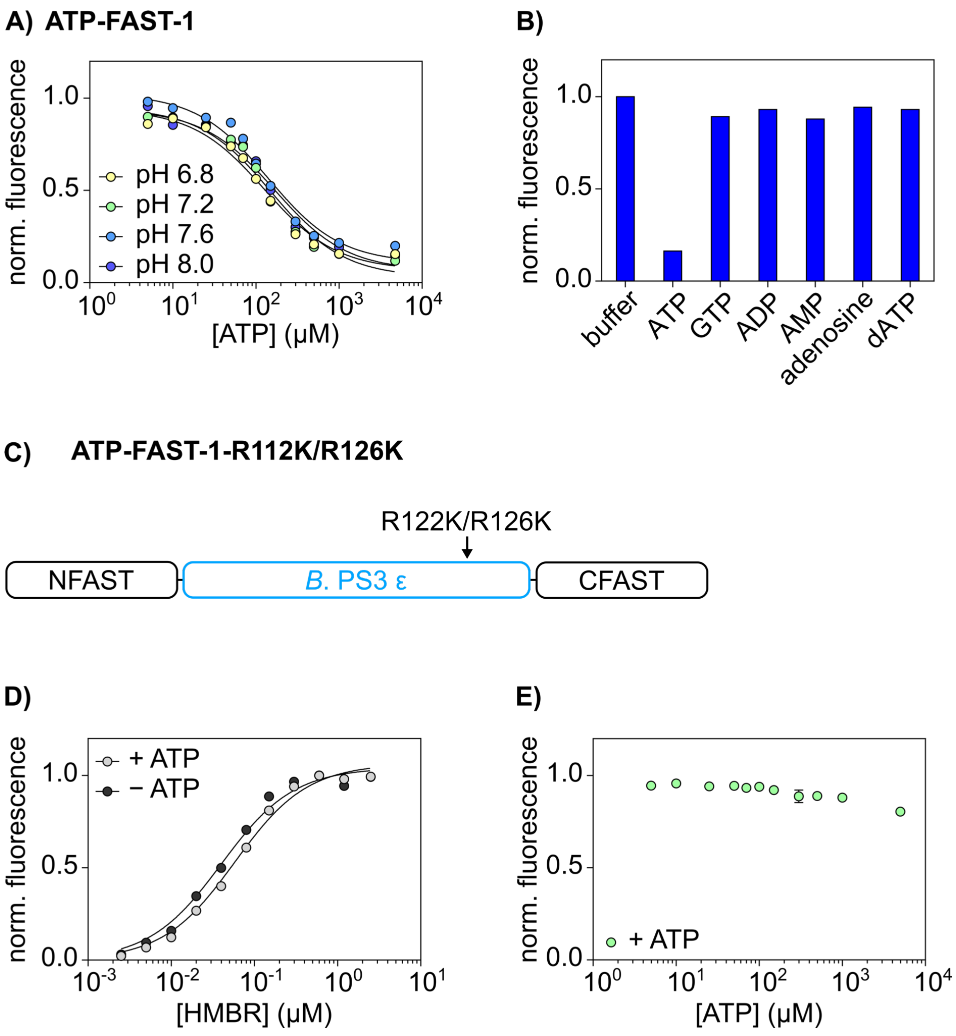

Figure V-3. Characterization of ATP-FAST-1. A) ATP titration curves of ATP-FAST-1 at pH 6.8, 7.2, 7.6 and 8.0 in pH 7.4 HEPES buffer (50 mM) containing MgCl$_2$ (75 mM). Data represent the mean ± sem (n = 3). **B)** Normalized fluorescence intensity upon addition of ATP and analogs at concentration = 10$K_{D,ATP}$ = 1.2 mM in the presence of 0.4 μM HMBR. **C)** Topology of the insensitive sensor ATP-FAST-1-R112K/R126K. **D)** HMBR titration curves of ATP-FAST-1-R112K/R126K, in absence (light grey) or in presence of 5mM ATP (dark grey) in pH 7.4 HEPES buffer (50 mM) containing MgCl$_2$ (75 mM). Data represent the mean ± sem (n = 3). **E)** ATP titration of ATP-FAST-1-R112K/R126K, in the presence of [HMBR] = $K_{D,HMBR}$ in pH 7.4 HEPES buffer (50 mM) containing MgCl$_2$ (75 mM). Data represent the mean ± sem (n = 3). The sensor concentration was fixed at 0.1 μM.

V.3. Characterization of ATP-FAST-1, a highly modular ATP biosensor

V.3.1. Modularity provided by the fluorogen

The hybrid nature of our sensors based on the semi-synthetic reporter FAST provided a high modularity that relied on several parameters. A useful feature provided by a chemogenetic reporter domain is the control of the synthetic fluorophore concentration, that was predicted to affect ATP-FAST-1 biosensing properties. In fact, the theoretical background describing such two-ligand binding sites suggests that the fluorophore concentration is a parameter influencing the biosensor affinity for its cognate analyte (see chapter I - page 24). In the case of ATP-FAST-1, a significant correlation between the fluorogen concentration and ATP binding was expected from the very strong negative allosteric coupling between the reporter and the sensing domain. Titration of ATP was consequently performed at different HMBR concentrations of interest ($c = K_{\mathrm{D,HMBR}}/2$, $K_{\mathrm{D,HMBR}}$ and $(K_{\mathrm{D,HMBR}}.K_{\mathrm{D,HMBR/ATP}})^{1/2}$), that frame the fluorogen concentration range providing a good compromise between dynamic range and detection limit (Figure V-4, complete description of the model by Tebo et al, 2018).[18] Increasing HMBR concentration substantially decreased the biosensor affinity for ATP. Note that a lower dynamic range was observed at higher fluorogen concentrations as predicted by the theoretical model. These results suggested that affinity for ATP could be modulated to a certain extend by varying the concentration of fluorogen.

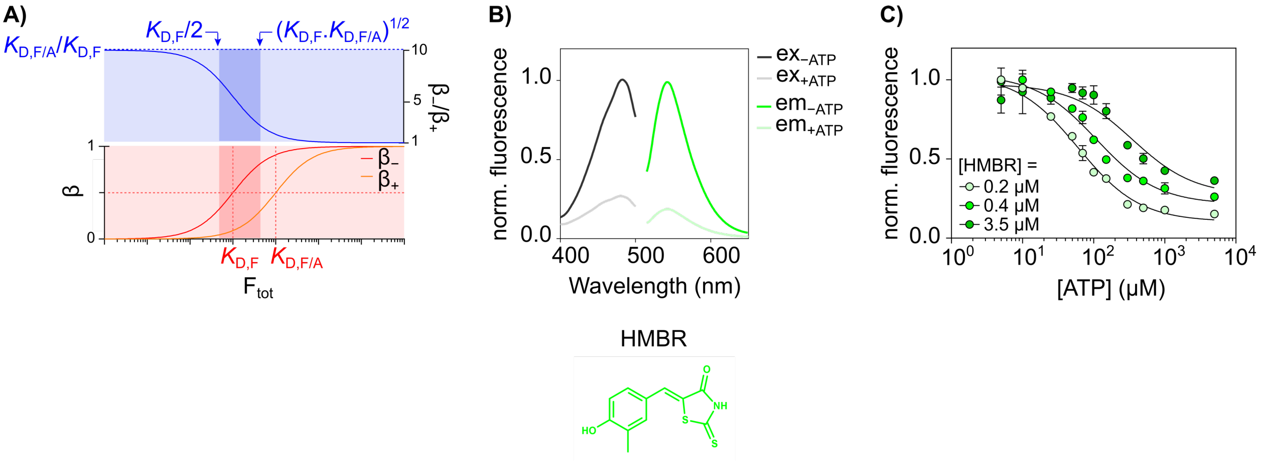

Figure V-4. Modularity provided by varying the fluorogen concentration with ATP-FAST-1. A) Simulated fluorogen binding curves in the presence and absence of analyte (with $K_{D,F/A}$ = 10 $K_{D,F}$). β_+ and β_- are the fluorogen bound fractions in presence and absence of the analyte, respectively. Choosing the concentration of fluorogen between $K_{D,F}/2$ and $(K_{D,F}.K_{D,F/A})^{1/2}$ (contrasted rectangles) is a good compromise to obtain both good dynamic range and satisfactory detection sensitivity. Adapted from Tebo et al.[18] **B)** Excitation and emission spectra of ATP-FAST-1 in the absence and in the presence of 5 mM ATP. The concentration of HMBR was 1 μM. Sensor concentration was fixed at 0.1 μM **C)** ATP titration curves of ATP-FAST-1 in presence of 0.2, 0.4 or 0.5 μM HMBR, in pH 7.4 HEPES buffer (50 mM) containing $MgCl_2$ (75 mM). Data represent the mean ± sem (n = 3). The least-squares fit (line) gave the apparent thermodynamic dissociation constant $K_{D,ATP\ app}$ provided in Table V-3.

Table V-3. Modularity provided by varying the fluorogen concentration with ATP-FAST-1. The apparent dissociation constant for ATP is given with the associated fluorescence intensity decrease observed upon ATP addition (F_{max}/F_{min}).

c	**[HMBR] (μM)**	**$K_{D,ATP\ app}$ (μM)**	**F_{max}/F_{min}**
$K_{D,HMBR}/2$	0.2	61 ± 8.7	6.6
$K_{D,HMBR/ATP}$	0.4	110 ± 21	3.8
$(K_{D,HMBR}.K_{D,HMBR/ATP})^{1/2}$	3.5	350 ± 130	2.7

Another useful feature for the sensor modularity arose from the reporter protein tag domain that could bind a wide range of fluorogens with variable properties. This remarkable feature notably offered the possibility to modify ATP-FAST-1 fluorescence properties by simply changing the synthetic fluorogen bound to the protein tag, without the need for any protein re-engineering. Therefore it was demonstrated that using the HBR derivatives HBR-3,5-DM or HBR-3,5-DOM allowed ATP titration with our FAST-based biosensor with a red-shifted fluorescence readout (λ_{ex} = 500 nm/ λ_{em} = 560 nm and λ_{ex} = 520 nm / λ_{em} = 600 nm, respectively) (Figure V-5). In addition to their shifted spectral features, the binding properties of these two fluorogens were also variable: indeed FAST:HMBR and FAST:HBR-3,5-DM complexes display lower dissociation constants than FAST:HBR-3,5-DOM ($K_{D,HMBR}$ = 0.13 μM, $K_{D,HBR\text{-}3,5DM}$ = 0.08 μM and $K_{D,HBR\text{-}3,5DOM}$ = 0.97 μM).[19] Accordingly, ATP-FAST-1 affinities for HBR-3,5-DM and HBR-3,5-DOM in the analyte-bound and free conformation of the sensor differed from the values obtained with HMBR. Despite higher cooperativity constants ($\alpha_{ATP\text{-}FAST\text{-}1,HBR\text{-}3,5\text{-}DM}$ = 0.21 and $\alpha_{ATP\text{-}FAST\text{-}1,HBR\text{-}3,5\text{-}DOM}$ = 0.07, respectively), indicating a lower coupling between the reporter and the sensing unit when switching fluorogens, titration with HBR-3,5-DM and HBR-3,5-DOM provided a significant 4.7 and 6.5-fold fluorescence decrease upon ATP addition, respectively (Table V-4).

Moreover, as a consequence of the strong allosteric coupling, the ATP dissociation constant of our biosensor was dependent on the fluorogen nature at fixed concentration ([fluorogen] = 1 μM). Indeed, ATP-FAST-1 binds ATP with a higher affinity in presence of HBR-3,5-DOM ($K_{D,ATP\ app}$ = 80 ± 14 μM) than in presence of HMBR or HBR-3,5-DM ($K_{D,ATP\ app}$ = 230 ± 55 μM and $K_{D,ATP\ app}$ = 190 ± 33 μM, respectively), in agreement with a negative allosteric modulation. This modularity was considered a considerable advantage as it provided a suitable sensor for multiplexed experiments, without the need for protein re-engineering. More important modifications of our FAST-based ATP biosensor thermodynamic properties would nevertheless require altering different parameters, such as the protein domains intrinsic properties.

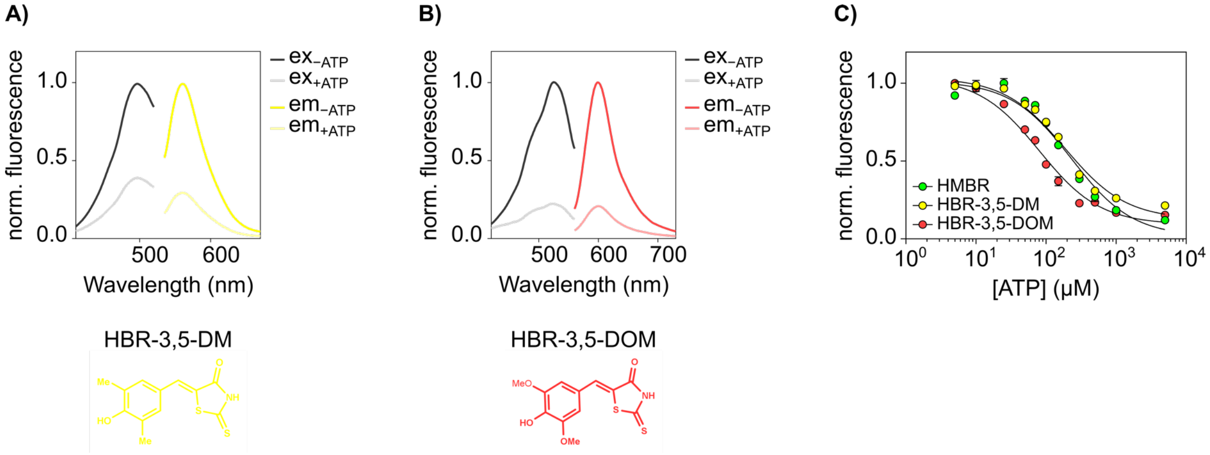

Figure V-5. Modularity provided by varying the fluorogen with ATP-FAST-1. A & B) Excitation and emission spectra of ATP-FAST-1 in the absence and in the presence of 5 mM ATP. The concentration of fluorogen was 1 μM. Sensor concentration was fixed at 0.1 μM. **C)** ATP titration curves of ATP-FAST-1 in presence of 1 μM HMBR (green), HBR-3,5-DM (yellow) and HBR-3,5-DOM (red), in pH 7.4 HEPES buffer (50 mM) containing $MgCl_2$ (75 mM). Data represent the mean ± sem (n = 3). The least-squares fit (line) gave the apparent thermodynamic dissociation constant $K_{D,ATP}$ provided in Table V-4. The sensor concentration was fixed at 0.1 μM.

Table V-4. Modularity provided by varying the fluorogen with ATP-FAST-1. The dissociation constants of the fluorogen in absence of ATP ($K_{D,HMBR}$), in presence of 5 mM of ATP ($K_{D,HMBR/ATP}$), and the cooperativity constant α, calculated as the ratio of the dissociation constant in absence of ATP and in presence of ATP ($K_{D,HMBR}/K_{D,HMBR/ATP}$). The apparent dissociation constant for ATP at 1 μM fluorogen is also given with the associated fluorescence intensity decrease observed upon ATP addition (F_{max}/F_{min}).

Fluorogen	$K_{D,fluorogen}$ (μM)	$K_{D,fluorogen/ATP}$ (μM)	α	$K_{D,ATP\ app}$ (μM)	F_{max}/F_{min}
HMBR	0.37 ± 0.03	~ 31 ± 2.2	~ 0.01	230 ± 55	8.3
HBR-3,5-DM	0.20 ± 0.03	0.94 ± 0.13	0.21	190 ± 33	4.7
HBR-3,5-DOM	0.74 ± 0.08	11 ± 1.2	0.07	80 ± 14	6.5

V.3.2. Modularity from protein engineering

A high-affinity reporter yields a low-affinity ATP biosensor.

The chemogenetic nature of the FAST-based biosensors allowed to take advantage of the modularity provided by protein engineering as well. With the aim of designing an ATP-FAST-1 analog biosensor with lower ATP affinity, thus more suitable to detect changes in intracellular ATP levels, different protein engineering strategies were considered. The first strategy consisted in replacing the sensing domain *B.* PS3 ε by the orthologous domain from mesophilic *B. subtilis*. The latter was indeed demonstrated to selectively bind ATP with an affinity in the millimolar range. ATP-FAST-1-*B.subtilis* and ATP-FAST-2-*B.subtilis* were thus generated by inserting the corresponding sensing domain in FAST or cpFAST, respectively. However, bacterial recombinant expression of these biosensors resulted in low yields and purity, compromising the reliability of the preliminary characterization.

Consequently, efforts were directed towards engineering of the reporter domain. The strong allosteric coupling between the reporter and the sensing unit suggested that the use of a reporter domain with higher fluorogen affinity would lead to a biosensor with lower affinity for ATP. Several versions of FAST have been engineered in the past few years. The most recent one, pFAST, developed by combining directed evolution and rational design, is notably characterized by its ability to bind a very wide palette of fluorogens covering the visible spectrum from 470 to 615 nm.[20] In particular, pFAST binds the aforementioned fluorogens HMBR, HBR-3,5-DM and HBR-3,5-DOM with much higher affinities than FAST, while providing comparable brightness (Figure V-6A,B).

First, we observed a constant fluorescent signal from pFAST upon addition of increasing ATP concentrations up to 30 mM, confirming that the reporter domain was insensitive to the presence of the analyte. Thus, we inserted the sensing domain F_OF_1-ATP synthase ε-subunit in pFAST at position 114-115 and in cp-pFAST(114-115), yielding ATP-pFAST-1 and ATP-pFAST-2, respectively (Figure V-6D-H). Both pFAST-based sensors displayed very high affinity for HMBR in the absence of ATP ($K_{D,HMBR} = 5.1 \pm 0.6$ nM for ATP-pFAST-1 and $K_{D,HMBR} = 10 \pm 0.9$ nM for ATP-pFAST-2). However, ATP-pFAST-1 was characterized by a much lower cooperativity constant than ATP-pFAST-2 ($\alpha_{ATP\text{-}pFAST\text{-}1} \sim 0.01$ vs $\alpha_{ATP\text{-}pFAST\text{-}2} = 0.26$). Moreover ATP detection with ATP-pFAST-2 was anticipated to be challenging, as this biosensor displayed affinities for the fluorogen in the low nanomolar range in both the analyte-bound and -free conformation. A good compromise between a reliable dynamic range and a sufficient fluorescence detection level was consequently hard to reach.

ATP-pFAST-1 was selected as a most promising topology for the design of a low-affinity ATP sensor. Indeed, tighter binding of the reporter unit pFAST to the fluorogen compared to FAST resulted in a dramatic increase of the ATP dissociation constant, in agreement with a negative allosteric modulation: ATP titration with ATP-pFAST-1 yielded a 7.8-fold affinity decrease compared to its FAST-based homolog ATP-FAST-1 ($K_{D,ATP\ app}$ = 730 ± 64 µM vs $K_{D,ATP\ app}$ = 93 ± 7.9 µM respectively, at [HMBR] = 0.1 µM).

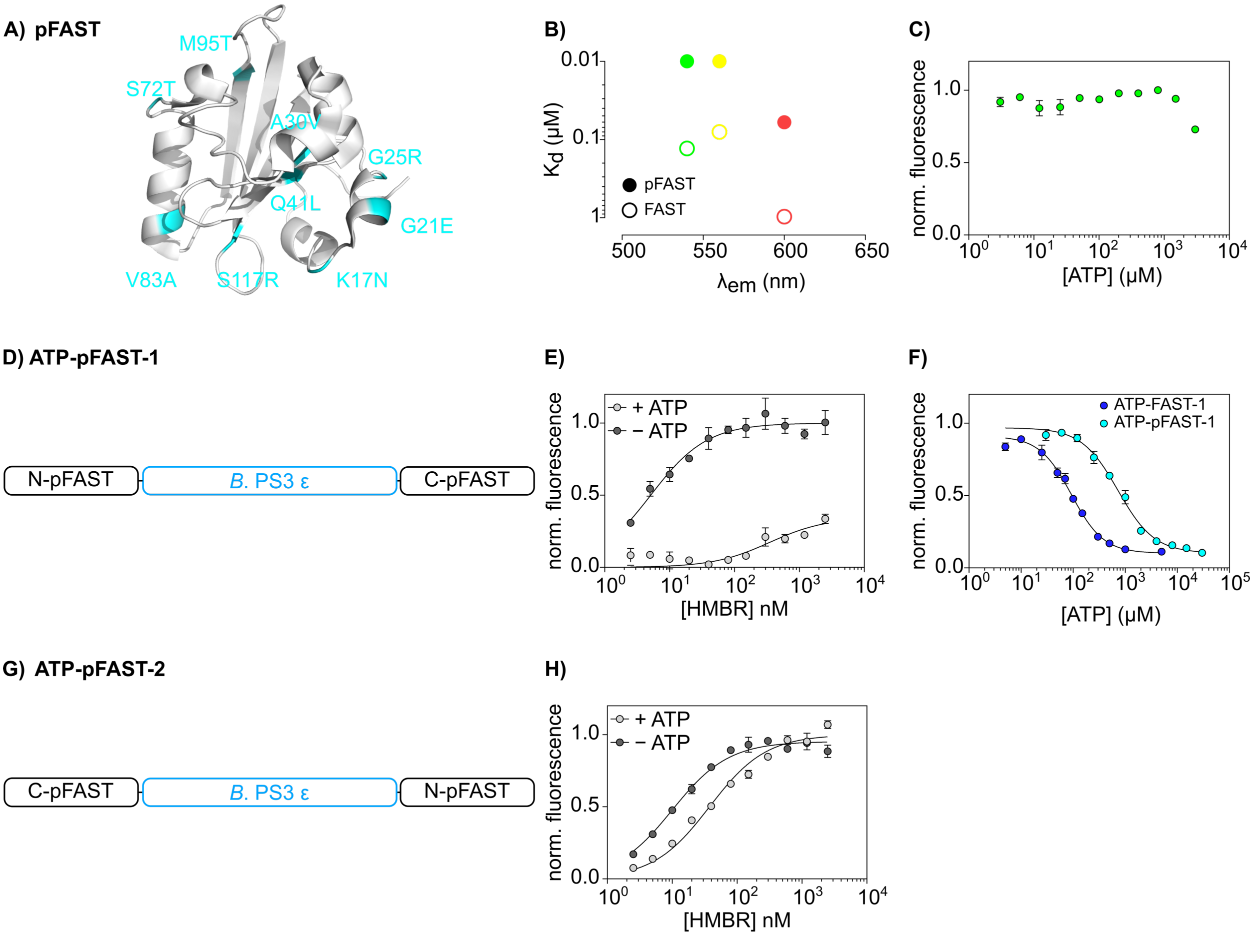

Figure V-6. Generation of a low-affinity sensor ATP-pFAST-1. A) pFAST mutations are shown in cyan on the crystal structure of PYP (PDB 1NWZ), the parent protein of FAST. **B)** Dissociation constants of the fluorogens HMBR (in green), HBR-3,5-DM (in yellow) and HBR-3,5-DOM (red) previously determined with FAST[26] and pFAST[20]. **C)** ATP titration curve of pFAST in the presence of 0.1 µM HMBR in pH 7.4 HEPES buffer (50 mM) containing $MgCl_2$ (75 mM). Data represent the mean ± sem (n = 3). The sensor concentration was fixed at 0.1 µM. **D & G)** Topologies of ATP-pFAST-1 and ATP-pFAST-2, respectively. **E & H)** HMBR titration curves of ATP-pFAST-1 and ATP-pFAST-2, respectively, in absence (light grey) or in presence of 30 mM ATP (dark grey) in pH 7.4 HEPES buffer (50 mM) containing $MgCl_2$ (75 mM). Data represent the mean ± sem (n = 3). The sensor concentration was fixed at 10 nM. **F)** ATP titration curves of ATP-FAST-1 (blue) and ATP-pFAST-1 (cyan) in the presence of 0.1 M HMBR in pH 7.4 HEPES buffer (50 mM) containing $MgCl_2$ (75 mM). Data represent the mean ± sem (n = 3). The least-squares fit (line) gave the thermodynamic dissociation constant $K_{D,HMBR}$ and $K_{D,HMBR/ATP}$ and the apparent dissociation constant $K_{D,ATP\ app}$ provided in Table V-5. The sensor concentration was fixed at 0.1 µM.

Table V-5. Characterization of ATP-pFAST-1 and ATP-pFAST-2. For each sensor is given the dissociation constant of the fluorogen in absence of ATP ($K_{D,HMBR}$), in presence of 30 mM of ATP ($K_{D,HMBR/ATP}$), and the cooperativity constant α, calculated as the ratio of the dissociation constant in absence of ATP and in presence of ATP ($K_{D,HMBR}/K_{D,HMBR/ATP}$). The apparent dissociation constant for ATP is also given with the associated fluorescence intensity decrease observed upon ATP addition (F_{max}/F_{min}).

Sensor	$K_{D,HMBR}$ (nM)	$K_{D,HMBR/ATP}$ (nM)	α	$K_{D,ATP\ app}$ (µM)	F_{max}/F_{min}
ATP-pFAST-1	5.1 ± 0.6	~ 350	~ 0.01	730 ± 64	9.5
ATP-pFAST-2	10.0 ± 0.9	38 ± 4.7	~ 0.26	nd	nd

The chemogenetic reporter unit pFAST also conferred to ATP-pFAST-1 biosensor a high modularity, notably by tuning the different fluorogen-related properties. Indeed, in a similar manner as ATP-FAST-1, switching between fluorogens with different spectral properties yielded a biosensor with easily-tunable color (Figure V-7). A significant fluorescence increase upon ATP depletion was observed with both HBR-3,5-DM and HBR-3,5-DOM fluorogens, reaching similar dynamic ranges as its FAST-based biosensor homolog. Following comparable trends as ATP-FAST-1, and in agreement with the binding properties of the reporter domain pFAST, ATP-pFAST-1 showed a higher apparent affinity for ATP in presence of HBR-3,5-DOM than in presence of HMBR and HBR-3,5-DM at the same concentration. Moreover, the apparent binding constant of ATP to ATP-pFAST-1 could also be modulated by tuning the fluorogen concentration: affinities for ATP in the millimolar range could for instance be obtained with ATP-pFAST-1 in the presence of increasing concentrations of HMBR and HBR-3,5-DM ($K_{D,ATP\ app}$ = 2.6 ± 0.6 mM with [HMBR] = 1 µM and $K_{D,ATP\ app}$ = 1.9 ± 0.4 mM with [HBR-3,5-DM] = 1 µM). Consequently, ATP-pFAST-1 appeared suitable for the reliable quantification of ATP in biological samples.

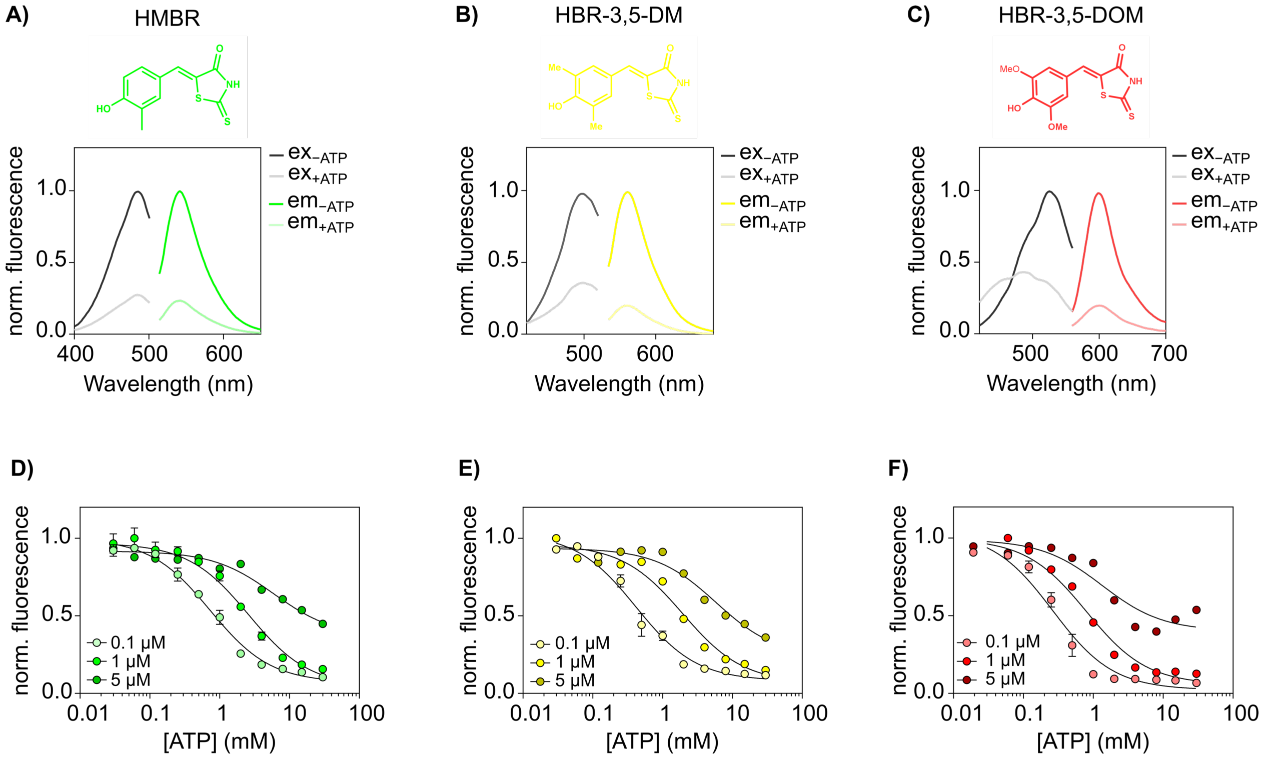

Figure V-7. Modularity provided by varying the fluorogen with ATP-pFAST-1. A-C) Excitation and emission spectra of ATP-pFAST-1 in the absence and in the presence of 30 mM ATP. The concentration of fluorogen was 1 µM. Sensor concentration was fixed at 0.1 µM. **D-F)** ATP titration curves of ATP-pFAST-1 in presence of 0.1, 1 or 5 µM HMBR, HBR-3,5-DM and HBR-3,5-DOM respectively, in pH 7.4 HEPES buffer (50 mM) containing $MgCl_2$ (75 mM). Data represent the mean ± sem (n = 3). The least-squares fit (line) gave the thermodynamic dissociation constant $K_{D,ATP\ app}$ provided in Table V-6. The sensor concentration was fixed at 0.1 µM.

Table V-6 Modularity provided by varying the fluorogen with ATP-pFAST-1. The apparent dissociation constant for ATP is given for each fluorogen with the associated fluorescence intensity decrease observed upon ATP addition (F_{max}/F_{min}).

Fluorogen	[fluorogen] (μM)	$K_{D,ATP\ app}$ (mM)	F_{max}/F_{min}
HMBR	0.1	0.73 ± 0.09	9.5
	1	2.6 ± 0.6	6.4
	5	5.9 ± 2.3	2.5
HBR-3,5-DM	0.1	0.42 ± 0.07	8.5
	1	1.9 ± 0.4	6.6
	5	5.8 ± 2.2	4.0
HBR-3,5-DOM	0.1	0.26 ± 0.06	15
	1	0.80 ± 0.17	7.9
	5	1.3 ± 0.7	2.5

We also performed a complementary characterization with the low-affinity biosensor ATP-pFAST-1 (Figure V-8A). ATP titration with ATP-pFAST-1 at different pH between 6.8 and 8.0 indicated that the affinity of the biosensor for the analyte was not affected by pH variations. However, a significantly lower dynamic range was obtained at pH 6.8, resulting from a higher background fluorescence at saturating ATP concentrations.

No fluorescence decrease was observed upon addition of 7 mM of the ATP analogs GTP, ADP, AMP, adenosine and dATP (such as [analog] = 10$K_{D,ATP}$ at [HMBR] = 0.1 μM) (Figure V-8B), thereby confirming the high selectivity of ATP-pFAST-1 towards ATP. Finally, insertion of the mutations R122K/R126K in the sensing domain of ATP-pFAST-1 yielded an ATP-insensitive biosensor (Figure V-8C,D). The fluorescent signal from ATP-pFAST-1-R122K/R126K did not provide any response upon addition of ATP up to 30 mM, thus verifying the specificity of our pFAST-based ATP biosensor.

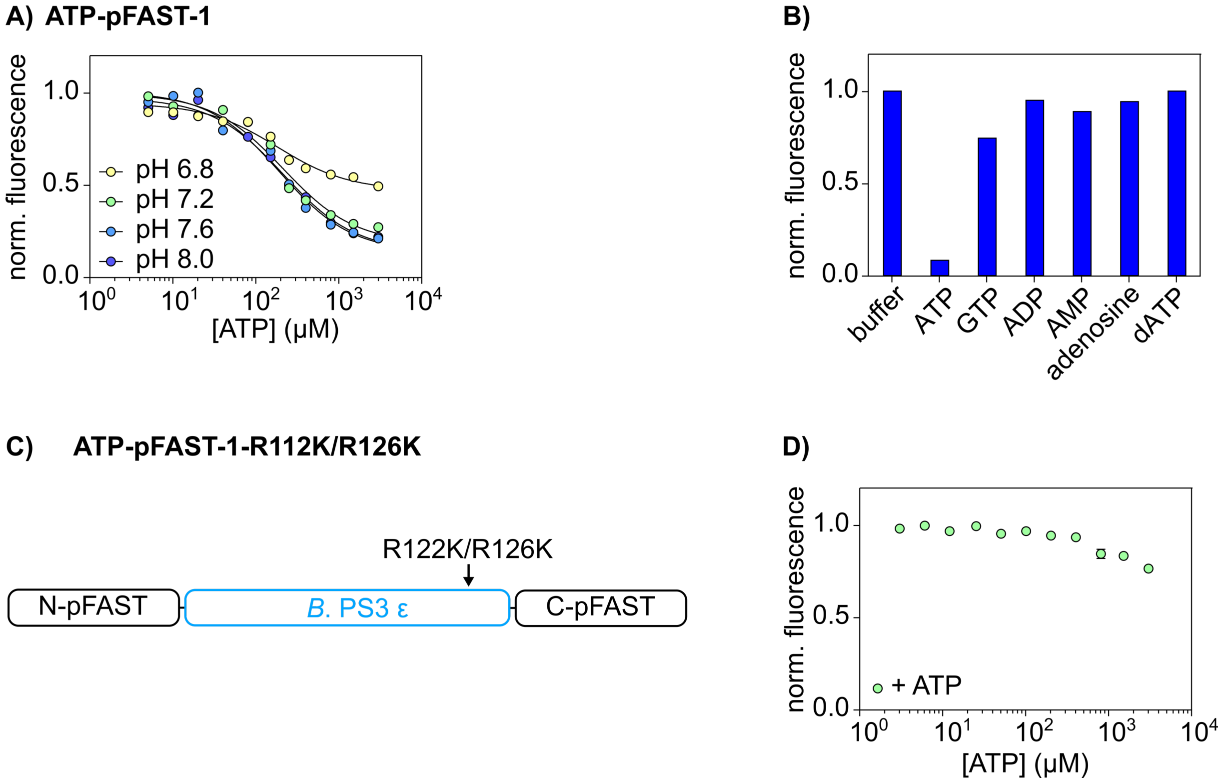

Figure V-8. Characterization of ATP-pFAST-1. A) ATP titration curves of ATP-pFAST-1 at pH 6.8, 7.2, 7.6 and 8.0 in HEPES buffer (50 mM) containing $MgCl_2$ (75 mM). Data represent the mean ± sem (n = 3). The least-squares fit (line) gave the apparent thermodynamic dissociation constant $K_{\mathrm{D,ATP\ app}}$ provided in Table V-7. **B)** Normalized fluorescence intensity upon addition of ATP and analogs at concentration = $10K_{\mathrm{D,ATP}}$ = 7 mM in the presence of 0.1 µM HMBR **C)** Topology of the insensitive sensor ATP-pFAST-1-R112K/R126K. **D)** ATP titration curve of ATP-pFAST-1-R112K/R126K in presence of 1 µM HMBR, in pH 7.4 HEPES buffer (50 mM) containing $MgCl_2$ (75 mM). Data represent the mean ± sem (n = 3). The sensor concentration was fixed at 0.1 µM.

Table V-7. Characterization of pH sensitivity of ATP-pFAST-1. The apparent dissociation constants for ATP are given with the associated fluorescence intensity decrease observed upon ATP addition ($F_{\mathrm{max}}/F_{\mathrm{min}}$).

pH	$K_{\mathrm{D,ATP\ app}}$ (mM)	$F_{\mathrm{max}}/F_{\mathrm{min}}$
6.8	1.8 ± 0.5	2.0
7.2	2.1 ± 0.5	5.5
7.6	1.9 ± 0.4	7.6
8.0	2.1 ± 0.4	7.1

Fusion of the fluorescent protein mCherry yields a ratiometric biosensor

Protein engineering of the genetically encoded part of our chemogenetic system also provided the opportunity to fuse the red-emitting fluorescent protein mCherry at the N-terminus of both ATP-FAST-1 and ATP-pFAST-1 (Figure V-9). Very high yields were obtained from bacterial recombinant expression of these fusions, with good purity and significantly lower aggregation. The resulting biosensors, when used with a compatible fluorogen such as the green-emitting HMBR, enabled ratiometric titration of ATP. The respective affinities of both sensors were not affected by the N-terminal fusion of the fluorescent protein ($K_{\mathrm{D,ATP\ app}}$ = 94 ± 25 µM for mCherry-ATP-FAST-1 and $K_{\mathrm{D,\ ATP\ app}}$ = 1.1 ± 0.2 mM for mCherry-ATP-pFAST-1 at [HMBR] = 1 µM), and the fluorescent signal from HMBR could be normalized by the constant fluorescence intensity of mCherry, that remained unaffected by ATP addition when using the adequate excitation wavelength λ_{ex} = 555 nm.

Acquiring the complete emission spectra from excitation λ_{ex} = 470 nm of mCherry-ATP-FAST-1 and mCherry-ATP-pFAST-1 led to the observation of a local emission maxima at λ_{em}= 610nm, corresponding to a FRET signal resulting from the energy transfer between HMBR as a donor and mCherry as an acceptor. Consistently with the N-terminal fusion of mCherry to the N(p)FAST fragment of the reporter domain, FRET efficiency appeared to be weakly affected by ATP binding. Indeed, distance and orientation between the two fluorophores were not modified upon analyte-induced conformational change of the biosensor. Nevertheless, this energy transfer did not significantly impact HMBR fluorescence intensity, and ATP titration with mCherry-ATP-FAST-1 and mCherry-ATP-pFAST-1 both yielded a large fluorescence decrease in presence of 1 µM HMBR (8.8- and 10-fold, respectively).

The possibility to obtain ratiometric measurements of ATP levels was thus considered a valuable feature as it was envisioned to facilitate studies in biological samples and cells, rendering measurements independent on the biosensor concentration. Moreover, our FAST-based ATP sensors being switched off at saturating ATP concentrations, they were envisioned to be conveniently localized by observation of the red fluorescent signal from mCherry.

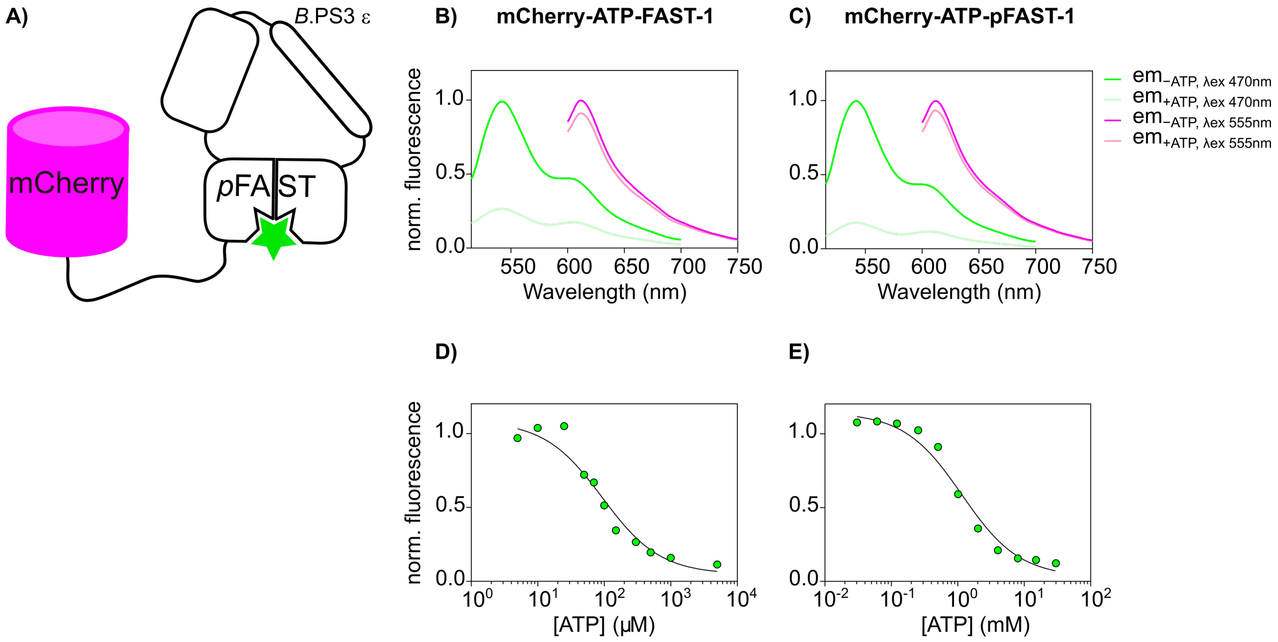

Figure V-9. Characterization of mCherry-ATP-FAST-1 and mCherry-ATP-pFAST-1. A) Topology of the ratiometric biosensor mCherry-ATP-(p)FAST-1. **B & C)** Emission spectra of mCherry-ATP-FAST-1 and mCherry-ATP-pFAST-1, respectively, at λ_{ex} = 470 nm (green) and λ_{ex} = 555 nm (magenta), in the absence and in the presence of 30 mM ATP. The concentration of fluorogen was 1 µM. The sensor concentration was fixed at 0.1 µM. **D & E)** ATP titration curve of mCherry-ATP-FAST-1 and mCherry-ATP-pFAST-1 respectively, in pH 7.4 HEPES buffer (50 mM) containing $MgCl_2$ (75 mM). Data represent the mean ± sem (n = 3). The least-squares fit (line) gave the apparent thermodynamic dissociation constant $K_{D,ATP\ app}$ provided in Table V-8. The sensor concentration was fixed at 0.1 µM.

Table V-8. Characterization of mCherry-ATP-FAST-1 and mCherry-ATP-pFAST-1. The apparent dissociation constants for ATP are given with the associated normalized fluorescence intensity decrease observed upon ATP addition (F_{max}/F_{min}) at 1 µM HMBR.

Sensor	$K_{D,ATP\ app}$	F_{max}/F_{min}
mCherry-ATP-FAST-1	94 ± 25 µM	8.8
mCherry-ATP-pFAST-1	1.1 ± 0.2 mM	10

V.3.3. Applications

Evaluation of ATP-FAST-1 and ATP-pFAST-1 in cells

ATP being involved in a number of various cellular processes, we were interested in evaluating ATP levels at different localizations across the cell (Figure V-10). Both ATP-FAST-1 and ATP-pFAST-1 were successfully expressed in the cytosol, the nucleus (using a nuclear localization signal at the C-terminus of the sensor) and the endoplasmic reticulum (by N-terminal fusion of an ER targeting sequence and the C-terminal fusion of an ER retention sequence) of transfected HeLa cells. Mitochondrial ATP levels were also considered of substantial interest: however, HeLa cells transfected with ATP-FAST-1 fused to the mitochondrial targeting sequence from the subunit VII of human cytochrome c oxidase (mito-ATP-FAST-1) failed to provide a selective localization. We attempted to replace this sequence with one or two successive MTS from the subunit IV of cytochrome c oxidase IV of *S*. cerevisae: the transfected HeLa cells showed sparse fluorescent dots, that were difficult to reliably identify. Considering the relatively high ATP levels in mitochondria, we suggested that part of the biosensor was potentially in the ATP-bound state, thus very weakly fluorescent and hardly observable.

Finally, attempts to express ATP-FAST-1 and ATP-pFAST-1 at the plasma membrane, using the pDisplay plasmid or its hemagglutinin (HA)-tag truncated version pCMV(MinDis), were unsuccessful. We could only detect fluorescent signal from the endoplasmic reticulum, suggesting dysfunctional protein trafficking as previously observed with Glu-FAST and K^+-FAST sensors.

Finally, cytosolic expression in HeLa cells of both ratiometric sensors mCherry-ATP-FAST-1 and mCherry-ATP-pFAST-1, and their ATP-insensitive versions CMV-mCherry-ATP-FAST-1-R122K/R126K and CMV-mCherry-ATP-pFAST-1-R122K/R126K were successful and showed colocalization of the signals from mCherry in the red channel, and from bound HMBR in the green channel. Observations by confocal fluorescence microscopy are thus currently being performed in order to characterize the functionality of our ratiometric FAST-based ATP biosensors in transfected HeLa cells, as well as their ability to detect ATP depletion upon inhibition of glycolysis and oxidative phosphorylation.

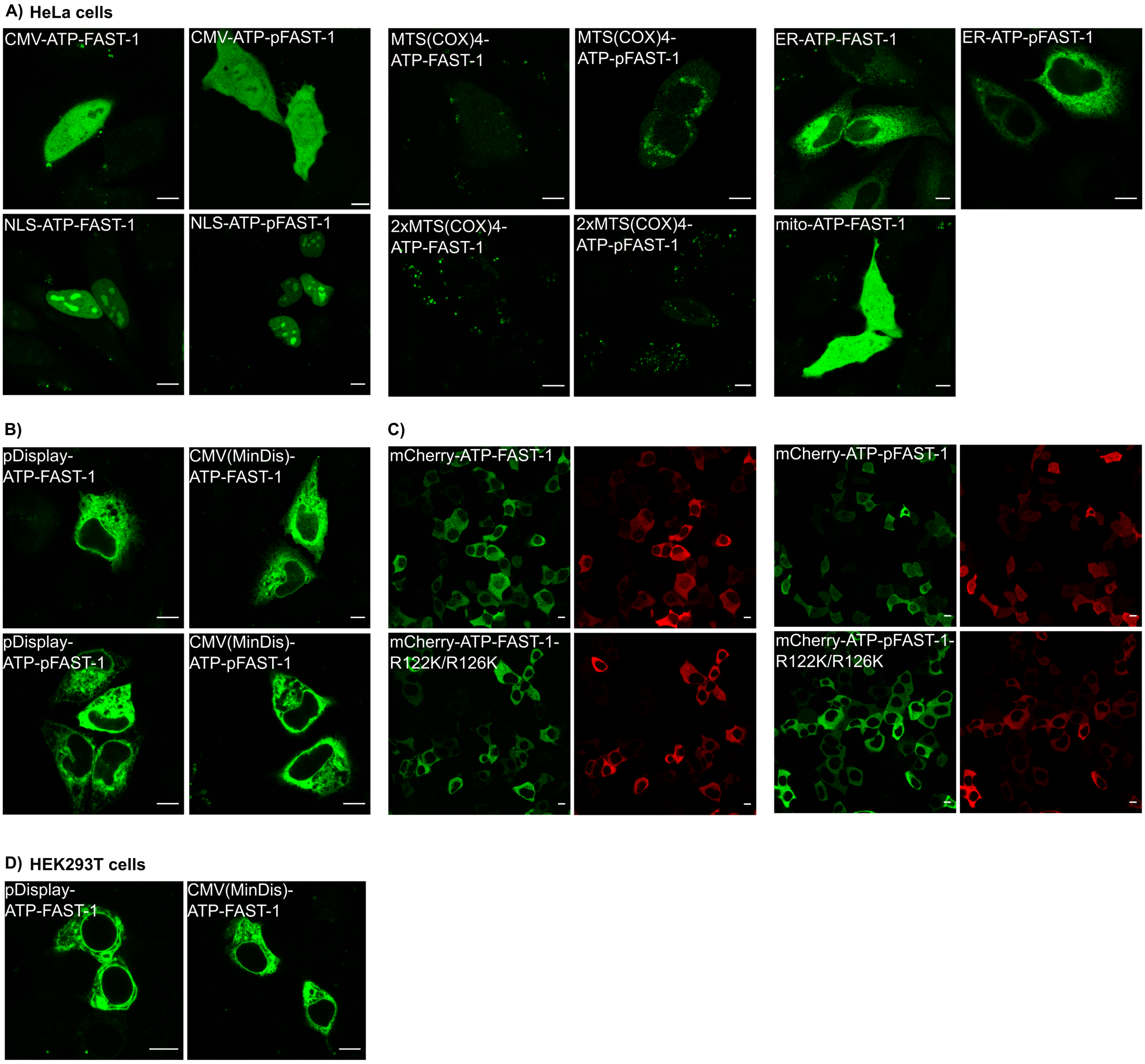

Figure V-10. Confocal micrographs of A) live HeLa cells expressing ATP-FAST-1, or ATP-pFAST-1 fused to a nuclear localization sequence (NLS), an endoplasmic reticulum targeting and retention sequence (ER), a MTS from the subunit VIII of human cytochrome c oxidase (mito) and one or two MTS from the subunit IV of cytochrome c oxidase IV of *S*. cerevisae (MTS(COX)4). **B)** live Hela cells expressing ATP-(p)FAST-1 in a pDisplay plasmid (extracellular membrane targeting) or its truncated version pCMV(MinDis)**. C)** live HeLa cells expressing mCherry-ATP-(p)FAST-1, or mCherry-ATP-(p)FAST-1-R122K/R126K **D)** live HEK cells expressing ATP*p*FAST-1 in a pDisplay or pCMV(MinDis) plasmid. [HMBR] = 5 μM, scale bar 10 μm.

Using mCherry-ATP-FAST-1 for in vitro quantification of metabolites

The accessible production of the biosensors from bacterial recombinant expression, with high yields and purity levels, made mCherry-ATP-FAST-1 and mCherry-ATP-pFAST-1 suitable candidates for *in vitro* measurements. Luminescent enzymatic assays, in which the metabolite is quantified through optical detection of a generic cofactor converted or formed stoichiometrically upon enzymatic conversion of the target metabolite with a specific enzyme have been recently developed for monitoring metabolites at the point of care thus facilitating the diagnostic and monitoring of many diseases.[21,22] We consequently envisioned to quantify metabolites in biological samples with our chemogenetic ATP biosensors. Various metabolites can be depleted by an ATP-dependent enzymatic reaction, and were thus thought to be quantifiable by measuring the correlated fluorescence increase upon ATP depletion. As a proof-of-concept, this principle was applied to the quantification of glucose, that is involved in a two-steps enzymatic reaction with a hexokinase first, and subsequently with glucose-6-phosphate dehydrogenase (G6PDH). This reaction leads to the stoichiometric consumption of ATP and production of NADH. Therefore, quantification of ATP consumption enables to indirectly measure the initial concentration of glucose. Several glucose solutions, including various concentrations within blood glucose concentration range, were evaluated by the fluorescent signal increase of mCherry-ATP-FAST-1 upon ATP depletion, at a fixed fluorogen concentration [HMBR] = 1 μM. The obtained initial and final intensity values were correlated to ATP concentrations using a calibration curve obtained from ATP titration in equivalent conditions, thus the measured ΔF allowed the quantification of ATP depleted by the enzymatic reaction.

In parallel, the A_{340nm} increase resulting from NADH production was evaluated in each sample (Glucose (HK) Assay Kit, Sigma-Aldrich). Comparison of both methods showed that fluorescence readout from our ATP biosensor with [HMBR] = 1 μM could accurately determine glucose concentrations ranging from 1.9 to 5.5 mM, theoretically fitting in the blood glucose concentration range or a 2-fold dilution of blood samples. The calibration curve allowed the identification of a plateau approaching higher glucose concentrations, determined by kinetic factors when reaching low ATP concentration in solution, and the intrinsic biosensor affinity ruling the initial ATP concentration in our quantification method. Nevertheless, this calibration curve can be adjusted to the desired concentration range by modulating one of the aforementioned protein-related or fluorogen-related parameters, here again demonstrating the advantage of a chemogenetic ATP biosensor.

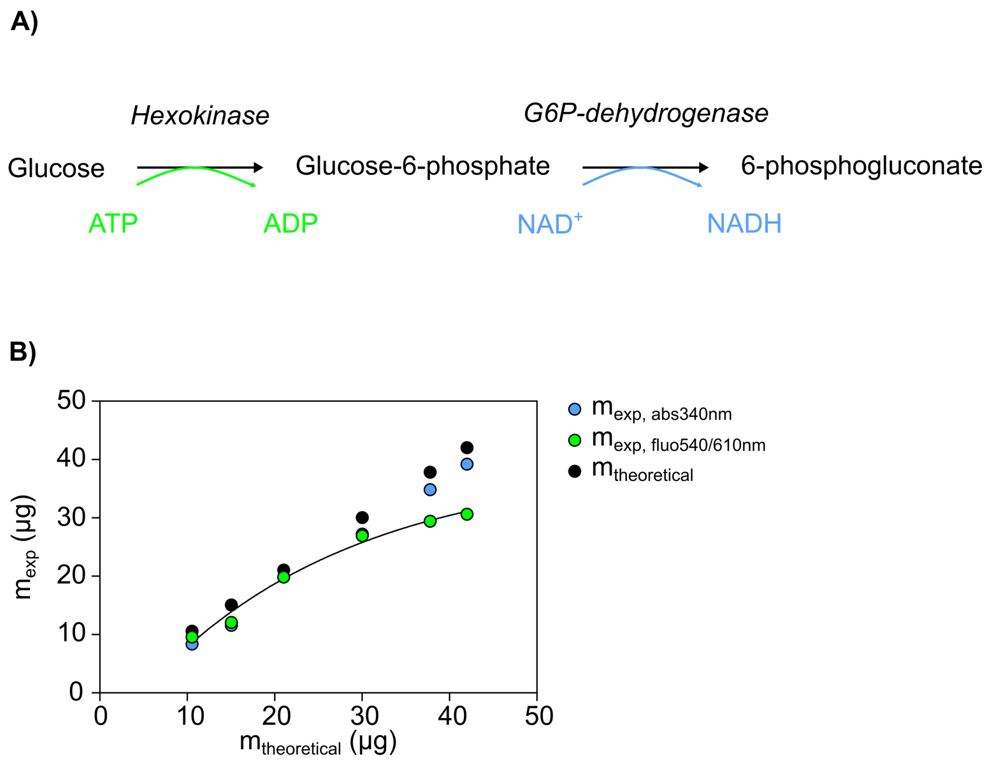

Figure V-11. A) In the first step of glycolysis, glucose is phosphorylated by a hexokinase to form glucose 6-phosphate (G6P), consuming one ATP molecule. G6P is then converted to 6-phosphogluconate by G6PDH, producing one molecule of NADH. **B)** Quantification of a theoretical mass of glucose (black) using the evolution of A_{340} (Glucose (HK) Assay Kit, Sigma-Aldrich) or our ATP-FAST-1 sensor assay in the presence of 1 µM HMBR (green). The concentration of the sensor was fixed 0.1 µM.

V.4. Discussion

ATP is a ubiquitous biomolecule involved in a large variety of biological processes: ATP sensing is consequently considered of significant importance to biological studies. Although several synthetic or genetically encoded biosensors for ATP were developed, no ATP sensing based on a chemogenetic system has been reported yet, to the best of our knowledge.

In this project aiming at the design of an ATP sensor based on the chemogenetic reporter FAST, we identified ATP-FAST-1, a biosensor with very promising properties, that revealed a large allosteric coupling between the reporter and the sensing unit of the sensor. This important inter-domain dependence interestingly allowed to fully take advantage of the hybrid nature of the reporter unit. Indeed, we were able to generate a highly modular biosensor, by tuning different parameters. On the one hand, optical properties of our FAST-based ATP sensor were modulated by the nature of the fluorogen. On the other hand, thermodynamic properties could be controlled by a number of parameters, such as fluorogen binding properties, protein engineering of the sensing domain, or modification of the reporter domain, notably switching between different FAST topological or mutational variants. This study describes the effect of changing the fluorogens between HMBR, HBR-3,5-DM and HBR-3,5-DOM; or replacing FAST by its recently developed variant pFAST. It would then be interesting to explore the multiple possibilities offered by other fluorogens (such as impermeant fluorogens,[23] or fluorophores covering the whole visible spectrum binding pFAST)[20], and different FAST variants (notably frFAST),[24] thus expanding the range of ATP biosensing opportunities.

We also demonstrated again the importance of preliminary topological studies. Indeed, varying connectivity between the different sensor components drastically changed the behaviour of the resulting sensors. The simple permutation between FAST fragments around the sensing domain notably yielded a very high affinity ATP biosensor, ATP-FAST-2. The ability to detect very low ATP concentrations in the micromolar range enables to envision biosensing applications of extracellular ATP, notably in the context of purinergic signalling.

The generation of ratiometric FAST-based ATP sensors provided promising perspectives as well. Indeed, N-terminal fusion of mCherry appeared to increase the yield and the solubility of biosensors obtained from bacterial recombinant expression: these improved properties might also be useful in mammalian cells, notably for membrane targeting that has been unsuccessful so far. Moreover, a relatively low FRET signal could be observed from mCherry upon excitation of HMBR bound to ATP-(p)FAST-1. Although energy transfer could probably be annihilated by introducing a longer and more rigid linker between mCherry and the fluorescent reporter, this FRET signal might be useful in the perspective of generating FAST-based FRET sensors. The

ATP-dependence of FRET efficiency could for instance be improved by fusing mCherry to CFAST instead of NFAST, thereby increasing the effect of conformational changes between the two fluorophores. Moreover, other designs of innovative biosensors could be considered relying on this energy transfer between HMBR and a fluorophore in its vicinity: coupling a FAST-based sensor to a bioluminescent reporter might for instance yield a BRET sensor with high dynamic range.

Still, the normalized single-wavelength readout from ATP-FAST-1 offered a significant fluorescence increase upon ATP depletion that was then independent on the biosensor concentration. This feature, in addition to the high adaptability of our system to varying experimental requirements, was foreseen to be interesting for the visualization of cellular and *in vivo* ATP levels. mCherry-ATP-FAST-1 already allowed the *in vitro* optical quantification of glucose with higher or comparable dynamic range than the existing assays based on a direct fluorescent output from glucose biosensors[25]. Furthermore, the possibility to generalize this quantification method to any metabolite that can be depleted through an ATP-dependent enzymatic reaction represents a considerable advantage of our system. This principle could be generalized to a wide variety of assays, such as the screening of kinase activity, or the development of point-of-care assays for the quantification of biomarkers.

V.5. Material and methods

General

Methods used for this project have been described in chapter III of this manuscript.

Determination of glucose concentrations

Glucose samples were prepared in HEPES buffer (50 mM) containing $MgCl_2$ (75 mM) and were either evaluated with the Glucose (HK) Assay Kit (Sigma-Aldrich) or with our home-made assay containing 1 u of enzyme mix HK-G6P (Sigma-Aldrich), 0.1 µM purified sensor mCherry-ATP-FAST-1 and 1 µM HMBR in HEPES buffer (50 mM) containing $MgCl_2$ (75 mM). After a 30min incubation at 25°C, absorbance was measured with a biophotometer (Eppendorf) and fluorescence was measured Spark 10M plate reader (Tecan).

Sequences

Protein sequence of FAST:
EHVAFGSEDIENTLAKMDDGQLDGLAFGAIQLDGDGNILQYNAAEGDITGRDPKQVIGKNFFKDVAPGTDSPEFYGKFKEGVASGNLNTMFEWMIPTSRGPTKVKVHMKKALSGDSYWVFVKRV

Protein sequence of cpFAST2:
GDSYWVFVKRV**GGS**EHVAFGSEDIENTLAKMDDGQLDGLAFGAIQLDGDGNILQYNAAEGDITGRDPKQVIGKNFFKDVAPGTDSPEFYGKFKEGVASGNLNTMFEWMIPTSRGPTKVKVHMKKALS

Protein sequence of F_OF_1-ATP synthase ε-subunit:
KTIHVSVVTPDGPVYEDDVEMVSVKAKSGELGILPGHIPLKAPLEISAARLKKGGKTQYIAVSGGNLEVRPDKVTIYAQAAERAEDIDVLRAKAAKERAERRLQSQQDDIDFKRAELALKRAMNRLSVAEMK

Protein sequence of ATP-FAST-1:
EHVAFGSEDIENTLAKMDDGQLDGLAFGAIQLDGDGNILQYNAAEGDITGRDPKQVIGKNFFKDVAPGTDSPEFYGKFKEGVASGNLNTMFEWMIPTSRGPTKVKVHMKKALSKTIHVSVVTPDGPVYEDDVEMVSVKAKSGELGILPGHIPLKAPLEISAARLKKGGKTQYIAVSGGNLEVRPDKVTIYAQAAERAEDIDVLRAKAAKERAERRLQSQQDDIDFKRAELALKRAMNRLSVAEMKGDSYWVFVKRV

Protein sequence of ATP-FAST-2:
GDSYWVFVKRVKTIHVSVVTPDGPVYEDDVEMVSVKAKSGELGILPGHIPLKAPLEISAARLKKGGKTQYIAVSGGNLEVRPDKVTIYAQAAERAEDIDVLRAKAAKERAERRLQSQQDDIDFKRAELALKRAMNRLSVAEMKEHVAFGSEDIENTLAKMDDGQLDGLAFGAIQLDGDGNILQYNAAEGDITGRDPKQVIGKNFFKDVAPGTDSPEFYGKFKEGVASGNLNTMFEWMIPTSRGPTKVKVHMKKALS

Protein sequence of ATP-FAST-3:
KTIHVSVVTPDGPVYEDDVEMVSVKAKSGELGILPGHIPLKAPLEISAARLKKGGKTQYIAVSGGNLEVRPDKVTIYAQAAERAEDIDVLRAKAAKERAERRLQSQQEHVAFGSEDIENTLAKMDDGQLDGLAFGAIQLDGDGNILQYNAAEGDITGRDPKQVIGKNFFKDVAPGTDSPEFYGKFKEGVASGNLNTMFEWMIPTSRGPTKVKVHMKKALSGDSYWVFVKRVIDFKRAELALKRAMNRLSVAEMK

Protein sequence of ATP-FAST-4:
KTIHVSVVTPDGPVYEDDVEMVSVKAKSGELGILPGHIPLKAPLEISAARLKKGGKTQYIAVSGGNLEVRPDKVTIYAQAAERAEDIDVLRAKAAKERAERRLQSQQGDSYWVFVKRV**GGS**EHVAFGSEDIENTLAKMDDGQLDGLAFGAIQLDGDGNILQYNAAEGDITGRDPKQVIGKNFFKDVAPGTDSPEFYGKFKEGVASGNLNTMFEWMIPTSRGPTKVKVHMKKALSIDFKRAELALKRAMNRLSVAEMK

Protein sequence of ATP-pFAST-1:
EHVAFGSEDIENTLANMDDEQLDRLAFGVIQLDGDGNILLYNAAEGDITGRDPKQVIGKNFFKDVAPGTDTPEFYGKFKEGAASGNLNTMFEWTIPTSRGPTKVKVHLKKALSKTIHVSVVTPDGPVYEDDVEMVSVKAKSGELGILPGHIPLKAPLEISAARLKKGGKTQYIAVSGGNLEVRPDKVTIYAQAAERAEDIDVLRAKAAKERAERRLQSQQDDIDFKRAELALKRAMNRLSVAEMKGDRYWVFVKRV

Protein sequence of mCherry-ATP-FAST-1:
MASVSKGEEDNMAIIKEFMRFKVHMEGSVNGHEFEIEGEGEGRPYEGTQTAKLKVTKGGPLPFAWDILSPQFMYGSKAYVKHPADIPDYLKLSFPEGFKWERVMNFEDGGVVTVTQDSSLQDGEFIYKVKLRGTNFPSDGPVMQKKTMGWEASSERMYPEDGALKGEIKQRLKLKDGGHYDAEVKTTYKAKKPVQLPGAYNVNIKLDITSHNEDYTIVEQYERAEGRHSTGGMDELYK**SGGGGSGGGGS**EHVAFGSEDIENTLANMDDEQLDRLAFGVIQLDGDGNILLYNAAEGDITGRDPKQVIGKNFFKDVAPGTDTPEFYGKFKEGAASGNLNTMFEWTIPTSRGPTKVKVHLKKALSKTIHVSVVTPDGPVYEDDVEMVSVKAKSGELGILPGHIPLKAPLEISAARLKKGGKTQYIAVSGGNLEVRPDKVTIYAQAAERAEDIDVLRAKAAKERAERRLQSQQDDIDFKRAELALKRAMNRLSVAEMKGDRYWVFVKRV

Protein sequence of mCherry-ATP-pFAST-1:
MASVSKGEEDNMAIIKEFMRFKVHMEGSVNGHEFEIEGEGEGRPYEGTQTAKLKVTKGGPLPFAWDILSPQFMYGSKAYVKHPADIPDYLKLSFPEGFKWERVMNFEDGGVVTVTQDSSLQDGEFIYKVKLRGTNFPSDGPVMQKKTMGWEASSERMYPEDGALKGEIKQRLKLKDGGHYDAEVKTTYKAKKPVQLPGAYNVNIKLDITSHNEDYTIVEQYERAEGRHSTGGMDELYK**SGGGGSGGGGS**EHVAFGSEDIENTLANMDDEQLDRLAFGVIQLDGDGNILLYNAAEGDITGRDPKQVIGKNFFKDVAPGTDTPEFYGKFKEGAASGNLNTMFEWTIPTSRGPTKVKVHLKKALSKTIHVSVVTPDGPVYEDDVEMVSVKAKSGELGILPGHIPLKAPLEISAARLKKGGKTQYIAVSGGNLEVRPDKVTIYAQAAERAEDIDVLRAKAAKERAERRLQSQQDDIDFKRAELALKRAMNRLSVAEMKGDRYWVFVKRV

Molecular cloning

Designations NFAST and CFAST stand for FAST(1-114) and FAST(115-125), respectively, and N-pFAST and C-pFAST stand for pFAST(1-114) and pFAST(115-125).

The plasmid pAG733, encoding ATP-FAST-1, was constructed by Gibson assembly from the plasmid pAG399 encoding pET28new-His-FAST. The fragment coding for NFAST was amplified by PCR using the primers ag1049/kanF. The fragment coding for CFAST was amplified using the primers ag1048/kanR. The insert coding for *B.*PS3 ε was amplified by PCR from the plasmid pAG729 using the primers ag1046/ag1047. The three fragments were then assembled by Gibson assembly.

The plasmid pAG734, encoding ATP-FAST-2, was constructed by Gibson assembly from the plasmid pAG400 encoding pET28new-His-cpFAST. The fragment coding for CFAST was amplified by PCR using the primers ag1050/kanF. The fragment coding for NFAST was amplified using the primers ag1051/kanR. The insert coding for the *B.*PS3 ε was amplified by PCR from the plasmid pAG729 using the primers ag1046/ag1047. The three fragments were then assembled by Gibson assembly.

The plasmid pAG735 and pAG736, encoding the ATP-FAST-3 and ATP-FAST-4, respectively, were constructed by Gibson assembly from the plasmid pAG729 encoding *B.*PS3 ε. The fragment coding for N-*B.*PS3 ε was amplified by PCR using the primers ag1058/kanF. The fragment coding for NFAST was amplified using the primers ag1052/kanR. The insert coding for FAST or cpFAST were amplified by PCR from the plasmid pAG399 or pAG400, respectively, using the primers ag1059/ag1060 or ag1061/1062, respectively. The three fragments were then assembled by Gibson assembly.

The plasmid pAG881, encoding ATP-pFAST-1, was constructed by Gibson assembly from the plasmid pAG641 encoding pET28new-His-pFAST. The fragment coding for the pET28new backbone was amplified by PCR using the primers ag579/kanF. The fragment coding for C-pFAST was amplified by PCR using the primers ag1259/kanR. The insert coding for N-pFAST was amplified using the primers ag601/1260. The insert coding for *B.*PS3 ε was amplified by PCR from the plasmid pAG729 using the primers ag1046/ag1047. The four fragments were then assembled by Gibson assembly.

The plasmid pAG882, encoding ATP-pFAST-2, was constructed by Gibson assembly from the plasmid pAG641 encoding pET28new-His-pFAST. The fragments coding for the pET28new backbone were amplified by PCR using the primers ag1262/kanF and 578/kanR. The fragment coding for N-pFAST was amplified by PCR using the primers ag1051/1192. The insert coding for *B.*PS3 ε was amplified by PCR from the plasmid pAG729 using the primers ag1193/ag1047. The four fragments were then assembled by Gibson assembly.

The plasmids pAG883 and pAG914, encoding CMV-ATP-FAST-1 and CMV-ATP-pFAST-1 respectively, were constructed by Gibson assembly from the plasmids pAG733 and pAG881. The fragments coding for the CMV backbone were amplified by PCR using the primers ag358/313 and ag848/314. The inserts coding for ATP-FAST-1 and ATP-pFAST-1 were amplified by PCR using the primers ag357/1020 and ag357/1045, respectively. The three fragments were then assembled by Gibson assembly.

The plasmids pAG884 and pAG915, encoding CMV-ER-ATP-FAST-1 and CMV-ER-ATP-pFAST-1 respectively, were constructed by Gibson assembly from the plasmids pAG733 and pAG881. The fragments coding for the CMV-ER backbone were amplified by PCR using the primers ag1306/313 and ag1358/314. The inserts coding for ATP-FAST-1 and ATP-pFAST-1 were amplified by PCR using the primers ag1359/1360. The three fragments were then assembled by Gibson assembly.

The plasmids pAG885, encoding CMV-NLS-ATP-FAST-1, was constructed by Gibson assembly from the plasmids pAG733 and pAG881. The fragment coding for NFAST was amplified by PCR using the primers ag313/1049. The fragment coding for CFAST was amplified by PCR using the primers ag314/1048.The insert coding for *B.*PS3 ε was amplified by PCR from the plasmid pAG729 using the primers ag1046/ag1047. The three fragments were then assembled by Gibson assembly.

The plasmids pAG886 and pAG917, encoding pDisplay-ATP-FAST-1 and pDisplay-ATP-pFAST-1 respectively, were constructed by Gibson assembly from the plasmids pAG733 and pAG881. The pDisplay backbone was amplified by PCR using the primers ag313/ag571 and ag314/ag572. The inserts coding for ATP-FAST-1 and ATP-pFAST-1 were amplified by PCR using the primers ag573/574. The three fragments were then assembled by Gibson assembly.

The plasmids pAG887 and pAG918, encoding pCMV(MinDis)-ATP-FAST-1 and pCMV(MinDis)-ATP-pFAST-1 respectively, were constructed by Gibson assembly from the plasmids pAG733 and pAG881. The pCMV(MinDis) backbone was amplified by PCR using primers ag571/ag313 and ag853/ag314. The inserts coding for ATP-FAST-1 and ATP-pFAST-1 were amplified by PCR using the primers ag574/1206. The three fragments were then assembled by Gibson assembly.

The plasmid pAG888, encoding CMV-mito-ATP-FAST-1, was constructed by Gibson assembly from the plasmid pAG733. The fragments coding for the CMV-mito backbone were amplified by PCR using primers ag927/ag313 and ag848/ag314. The insert coding for ATP-FAST-1 was amplified by PCR using the primers ag928/1020. The three fragments were then assembled by Gibson assembly.

The plasmid pAG916, encoding CMV-NLS-ATP-pFAST-1, was constructed by Gibson assembly from the plasmid pAG881. The fragments coding for the CMV-NLS backbone were amplified by PCR using primers ag358/ag313 and ag848/ag314. The insert coding for ATP-pFAST-1 was amplified by PCR using the primers ag357/1045. The three fragments were then assembled by Gibson assembly.

The plasmids pAG929 and pAG930, encoding CMV-MTS(COX4)-ATP-FAST-1 and CMV-MTS(COX4)-ATP-pFAST-1 respectively, were constructed by Gibson assembly from the plasmids pAG883 and pAG914. The fragment coding for the CMV-MTS(COX4) backbone was amplified by PCR using primers ag1412/ag313. The fragments coding for ATP-FAST-1 and ATP-pFAST-1 were amplified by PCR using the primers ag704/314. The two fragments were then assembled by Gibson assembly.

The plasmids pAG976 and pAG977, encoding CMV-2xMTS(COX4)-ATP-FAST-1 and CMV-2xMTS(COX4)-ATP-pFAST-1 respectively, were constructed by Gibson assembly from the plasmids pAG929 and pAG930. The fragment coding for the CMV-MTS(COX4) backbone was amplified by PCR using primers ag1493/ag313. The fragments coding for ATP-FAST-1 and ATP-pFAST-1 were amplified by PCR using the primers ag1492/314. The two fragments were then assembled by Gibson assembly.

The plasmids pAG1007 and pAG1020, encoding CMV-mCherry-ATP-pFAST-1 and CMV-mCherry-ATP-FAST-1 respectively, were constructed by Gibson assembly from the plasmids pAG914 and pAG883. The fragment coding for CMV-mCherry was amplified by PCR using primers ag1566/ag313. The fragments coding for ATP-pFAST-1 and ATP-FAST-1 were amplified by PCR using the primers ag336/314. The two fragments were then assembled by Gibson assembly.

The plasmids pAG1008 and pAG1021, encoding pET28new-mCherry-ATP-pFAST-1 and pET28new-mCherry-ATP-FAST-1 respectively, were constructed by Gibson assembly from the plasmids pAG881 and pAG733. The fragment coding for pET28new-mCherry was amplified by PCR using primers ag1566/kanF. The fragments coding for ATP-pFAST-1 and ATP-FAST-1 were amplified by PCR using the primers ag336/kanR. The two fragments were then assembled by Gibson assembly.

The plasmids pAG1091 and pAG1092, encoding pET28new-ATP-FAST-1-R112K/R126K and pET28new-ATP-pFAST-1-R122K/R126K respectively, were constructed by Gibson assembly from the plasmids pAG733 and pAG881. The fragment coding for the pET28new backbone was amplified by PCR using the primers ag579/kanF. The fragment coding for CFAST and C-pFAST were amplified by PCR using the primers ag1704/kanR. The inserts coding for NFAST-*B.*PS3 ε or N-pFAST-*B.*PS3 ε were amplified by PCR using the primers ag601/1703. The three fragments were then assembled by Gibson assembly.

The plasmids pAG1106 and pAG1107, encoding CMV-mCherry-ATP-FAST-1-R112K/R126K and CMV-mCherry-ATP-pFAST-1-R122K/R126K respectively, were constructed by Gibson assembly from the plasmids pAG1091 and pAG1092. The fragment coding for the CMV backbone was amplified by PCR using the primers ag848/314. The fragment coding for CMV-mCherry was amplified by PCR using primers ag1566/ag313. The fragments coding for ATP-FAST-1-R112K/R126K and ATP-pFAST-1-R112K/R126K were amplified by PCR using the primers ag336/1020 and ag336/1045, respectively. The three fragments were then assembled by Gibson assembly.

Plasmid	**From**	**Primers**
pAG399	pAG104 + pET28new	ag578, 579, 580, 581, 601, 602
pAG400	pAG120 + pET28new	ag578, 579, 580, 581, 603, 604
pAG729	synthetic gene + pET28new	ag578, 579, 1033, 1034
pAG733	pAG729 + pAG399	ag1046, 1047, 1048, 1049, kanF, kanR
pAG734	pAG729 + pAG400	ag1046, 1047, 1050, 1051, kanF, kanR
pAG735	pAG729 + pAG399	ag1052, 1058, 1059, 1060, kanF, kanR
pAG736	pAG729 + pAG400	ag1052, 1058, 1061, 1062, kanF, kanR
pAG881	pAG641 + pAG729	ag579, 601, 1046, 1047, 1259, 1260, kanF, kanR
pAG882	pAG641 + pAG734	ag578, 1047, 1051, 1192, 1193, 1262, kanF, kanR
pAG883	pAG733	ag313, 314, 357, 358, 848, 1020
pAG884	pAG733	ag313, 314, 1306, 1358, 1359, 1360
pAG885	pAG733	ag313, 314, 1046, 1047, 1048, 1049
pAG886	pAG733	ag313, 314, 571, 572, 573, 574
pAG887	pAG733	ag313, 314, 571, 574, 1064, 1206
pAG888	pAG733	ag313, 314, 848, 927, 928, 1020
pAG914	pAG881	ag313, 314, 357, 358, 848, 1045
pAG915	pAG881	ag313, 314, 1306, 1358, 1359, 1360
pAG916	pAG881	ag313, 314, 357, 574, 848, 1045
pAG917	pAG881	ag313, 314, 571, 572, 573, 574
pAG918	pAG881	ag313, 314, 571, 574, 1064, 1206
pAG929	pAG883	ag313, 314, 704, 1412
pAG930	pAG914	ag313, 314, 704, 1412
pAG976	pAG929	ag313, 314, 1492, 1493
pAG977	pAG930	ag313, 314, 1492, 1493
pAG1007	pAG158 + pAG914	ag313, 314, 336, 1566
pAG1008	pAG158 + pAG881	ag336, 1566, kanF, kanR
pAG1020	pAG883	ag313, 314, 336, 1566
pAG1021	pAG733	ag336, 1566, kanF, kanR
pAG1091	pAG733	ag579, 601, 1703, 1704, kanF, kanR
pAG1092	pAG881	ag579, 601, 1703, 1704, kanF, kanR
pAG1106	pAG1091	ag313, 314, 336, 848, 1020, 1566
pAG1107	pAG1092	ag313, 314, 336, 848, 1045, 1566

Primer	**Sequence**
kanf	gcatcaaccaaaccgttattcattcgtg
kanr	cacgaatgaataacggtttggttgatgc
ag231	gaaataagcttttgttcggatccggaaagggctttcttcatgtg
ag313	ctcaccttgctcctgccgagaaagtatcca
ag314	tggatactttctcggcaggagcaaggtgag
ag336	gcagcggcggagggggatccgagcatgttgcctttggcag
ag357	ccggactcagatctgccaccatggagcatgttgcctttggcag
ag358	ggtggcagatctgagtccggtag
ag571	gtcgacgaacaaaaactcatctcag
ag572	agatctggccggctgggcc
ag573	cagccggccagatctatggagcatgttgcc
ag574	gtttttgttcgtcgaccacccgtttcacaaag
ag578	taatgactcgagcaccaccaccacc
ag579	catgctagccatatggctgccg
ag580	gcctagagcaagacgtttcccgttgaatatg
ag581	attcaacgggaaacgtcttgctctaggc
ag601	ggcagccatatggctagcatggagcatgttgcctttgg
ag602	ggtggtggtgctcgagtcattacacccgtttcacaaagaccc
ag603	ggcagccatatggctagcatgggtgacagctattgggtc
ag604	ggtggtggtgctcgagtcattaggaaagggctttcttcatgtg
ag704	gagcatgttgcctttggc
ag848	ggatccgaacaaaagcttatttctgaagag
ag927	ggtggcagatctcaacgaatggatcttggc
ag928	gccaagatccattcgttgagatctgccaccatggagcatgttgcctttggc
ag1020	ataagcttttgttcggatcccacccgtttcacaaagacccaatagc
ag1033	ggcagccatatggctagcatgaagacaatacacgtttccgtagtc
ag1034	ggtggtggtgctcgagtcattacttcatttctgcaacgctgagtc
ag1045	ataagcttttgttcggatcccacccgtttcacaaagacccaatatc
ag1046	aagacaatacacgtttccgtagtcac
ag1047	cttcatttctgcaacgctgagtc
ag1048	ctcagcgttgcagaaatgaagggtgacagctattgggtctttg
ag1049	ctacggaaacgtgtattgtcttggaaagggctttcttcatgtgc
ag1050	ctacggaaacgtgtattgtcttcacccgtttcacaaagaccc
ag1051	ctcagcgttgcagaaatgaaggagcatgttgcctttggcag
ag1052	atagactttaaaagagctgaactcgc
ag1058	ggactgcaaccttcgttcc
ag1059	cggaacgaaggttgcagtccacaagggagcatgttgcctttggc
ag1060	gttcagctcttttaaagtctataccgagcacccgtttcacaaagaccc
ag1061	cggaacgaaggttgcagtccacaaggggtgacagctattgggtctttg
ag1062	gttcagctcttttaaagtctataccgagggaaagggctttcttcatgtgc
ag1064	agatctgtcaccagtggaacctg
ag1192	ggtggtggtgctcgagtcattaggaaagggctttcttcaagtgc
ag1193	tattgggtctttgtgaaacgggtg
ag1206	gttccactggtgacagatctatggagcatgttgcctttgg

ag1259	cagcgttgcagaaatgaagggtgacagatattgggtctttgtg
ag1260	cggaaacgtgtattgtcttggaaagggctttcttcaagtgc
ag1262	gtttcacaaagacccaatatctgtcacccatgctagccatatggctgccg
ag1306	cagcaggcccagcagcagggggacgggcagcagcatggtggcagatctgagtcc
ag1358	aaggacgagctgggatcc
ag1359	ctgctgctgggcctgctgggcgccgccgccgacgagcatgttgcctttggcag
ag1360	agaaataagcttttgttcggatcccagctcgtccttcacccgtttcacaaagaccc
ag1412	ggtggcgaattcggatctg
ag1492	ttttcaaacccgcaacgcggacgctctgttccagccggtaccttctgagatctgagcatgttgcctttg
ag1493	gcgttgcgggtttgaaaaaccttatactctgccgcaggctgagcagcaggtaccggctgc
ag1566	ggatccccctccgccgctgccgcctcctccggacttgtacagctcgtccatgcc
ag1703	caatgcgagttcagctcttttaaagtc
ag1704	ctttaaaagagctgaactcgcattgaaaaaggctatgaataagctcagcgttgcagaaatgaag

V.6. References

1. Gourine, A. V. *et al.* Astrocytes control breathing through pH-dependent release of ATP. *Science (80-.).* **329**, 571–575 (2010).
2. Shigetomi, E., Kracun, S., Sofroniew, M. V. & Khakh, B. S. A genetically targeted optical sensor to monitor calcium signals in astrocyte processes. *Nat. Neurosci.* **13**, 759–766 (2010).
3. Kaskova, Z. M., Tsarkova, A. S. & Yampolsky, I. V. 1001 lights: Luciferins, luciferases, their mechanisms of action and applications in chemical analysis, biology and medicine. *Chem. Soc. Rev.* **45**, 6048–6077 (2016).
4. Morciano, G. *et al.* Use of luciferase probes to measure ATP in living cells and animals. *Nat. Protoc.* **12**, 1542–1562 (2017).
5. Berg, J., Hung, Y. P. & Yellen, G. A genetically encoded fluorescent reporter of ATP:ADP ratio. *Nat. Methods* **6**, 161–166 (2009).
6. Tantama, M., Martínez-François, J. R., Mongeon, R. & Yellen, G. Imaging energy status in live cells with a fluorescent biosensor of the intracellular ATP-to-ADP ratio. *Nat. Commun.* **4**, (2013).
7. Yagi, H. *et al.* Structures of the thermophilic F1-ATPase ε subunit suggesting ATP-regulated arm motion of its C-terminal domain in F1. *Proc. Natl. Acad. Sci. U. S. A.* **104**, 11233–11238 (2007).
8. Kato-Yamada, Y. Isolated ε subunit of Bacillus subtilis F1-ATPase binds ATP. *FEBS Lett.* **579**, 6875–6878 (2005).
9. Kato, S., Yoshida, M. & Kato-Yamada, Y. Role of the ε subunit of thermophilic F1-ATPase as a sensor for ATP. *J. Biol. Chem.* **282**, 37618–37623 (2007).
10. Imamura, H. *et al.* Visualization of ATP levels inside single living cells with fluorescence resonance energy transfer-based genetically encoded indicators. *Proc. Natl. Acad. Sci. U. S. A.* **106**, 15651–15656 (2009).
11. Tsuyama, T. *et al.* In vivo fluorescent adenosine 5′-triphosphate (ATP) imaging of Drosophila melanogaster and Caenorhabditis elegans by using a genetically encoded fluorescent ATP Biosensor optimized for low temperatures. *Anal. Chem.* **85**, 7889–7896 (2013).
12. Vishnu, N. *et al.* ATP increases within the lumen of the endoplasmic reticulum upon intracellular Ca2+ release. *Mol. Biol. Cell* **25**, 368–379 (2014).
13. Conley, J. M., Radhakrishnan, S., Valentino, S. A. & Tantama, M. Imaging extracellular ATP with a genetically-encoded, ratiometric fluorescent sensor. *PLoS One* **12**, 1–24 (2017).
14. Yaginuma, H. *et al.* Diversity in ATP concentrations in a single bacterial cell population revealed by quantitative single-cell imaging. *Sci. Rep.* **4**, (2014).
15. Arai, S. *et al.* RGB-color intensiometric indicators visualize spatiotemporal dynamics of ATP in single cells Satoshi. *Angew. Chemie - Int. Ed.* (2018). doi:10.1002/ange.201901699
16. Lobas, M. A. *et al.* A genetically encoded single-wavelength sensor for imaging cytosolic and cell surface ATP. *Nat. Commun.* **10**, (2019).
17. Depaoli, M. R. *et al.* Real-Time Imaging of Mitochondrial ATP Dynamics Reveals the Metabolic Setting of Single Cells. *Cell Rep.* **25**, 501-512.e3 (2018).
18. Tebo, A. G. *et al.* Circularly Permuted Fluorogenic Proteins for the Design of Modular Biosensors. *ACS Chem. Biol.* **13**, 2392–2397 (2018).
19. Li, C. *et al.* Dynamic multicolor protein labeling in living cells. *Chem. Sci.* **8**, 5598–5605 (2017).
20. Benaissa, H. *et al.* An engineered multifunctional protein tag for advanced fluorescence imaging. *bioRxiv* 2021.01.29.428635 (2021).
21. Yu, Q. *et al.* Semisynthetic sensor proteins enable metabolic assays at the point of care. *Science (80-.).* **361**, 1122–1126 (2018).
22. Yu, Q. *et al.* A biosensor for measuring NAD+ levels at the point of care. *Nat. Metab.* **1**, 1219–1225 (2019).

23. Li, C. *et al.* Fluorogenic Probing of Membrane Protein Trafficking. *Bioconjug. Chem.* **29**, 1823–1828 (2018).
24. Li, C. *et al.* A Far-Red Emitting Fluorescent Chemogenetic Reporter for In Vivo Molecular Imaging. *Angew. Chemie - Int. Ed.* **59**, 17917–17923 (2020).
25. Liu, W. *et al.* Genetically encoded single circularly permuted fluorescent protein-based intensity indicators. *J. Phys. D. Appl. Phys.* **53**, (2020).
26. Plamont, M.-A. *et al.* Small fluorescence-activating and absorption-shifting tag for tunable protein imaging in vivo. *Proc. Natl. Acad. Sci.* **113**, 497–502 (2016).

Chapter VI

Identification and optimization of new cpFAST and split FAST reporters.

VI.1. Introduction

The design of biosensing tools relying on genetically encoded or chemogenetic reporters, including the developments described in chapters III to V of this manuscript, have underlined the crucial importance of optimizing conformational sensitivity of the reporter. Among strategies employed to improve coupling to the sensing module, circular permutation of the reporter has proven useful at enhancing optical properties change upon signal sensing.

The observation that, despite their rigid β-barrel structure, the green fluorescent protein GFP and its cyan and yellow variants CFP and YFP remained fluorescent upon circular permutation at position 144-145 was equally surprising and promising.[1] In fact, connecting the native termini of a fluorescent protein to create new ones at a site close to the chromophore, has allowed the remarkable generation of the Ca^{2+} sensor GCaMP and its subsequent improved versions by insertion of a circularly permuted GFP between the Ca^{2+}-dependent interacting pair calmodulin/M13.[2–4] The different parameters influencing fluorescence change upon signal detection, including a change in the extinction coefficient, the quantum yield or the equilibrium between the deprotonated and protonated state of the chromophore, have been further described by the systematic study of analogous biosensors.[5] In addition to high sensitivity and fast kinetics, insertion of a cpFP into a sensing domain also displays the advantage of relying on a properly folded reporter that conveniently dismisses any solubility concern from the reporter's side. Together with the development and improvement of screening techniques for the optimization of linkers connecting the reporter and the sensing units, these features have made the use of circularly permuted fluorescent proteins a common strategy to generate a wide range of intensiometric sensors.[6]

Circular permutation of chemogenetic reporters have also allowed the generation of innovative biosensing strategies, that were introduced in chapter II of this manuscript. In the case of hybrid biosensors, modifying the genetically encoded part by creating new termini enabled to modulate fluorescence properties by altering the binding pocket of the small-molecule fluorophore. Enzymatic activity could for example be visualized by the infrared fluorogenic protease reporter iProtease, based on a circularly permuted infrared fluorescent protein IFP generated by connecting its native termini with a cleavage sequence.[7] Binding to biliverdin was thus hampered by the displacement of the reactive cysteine, which was then restored after protease cleavage and reconstitution of a functional fluorophore binding site. A different approach necessitated the identification of viable circular permutation of the self-labelling HaloTag, in order to bring environment sensitive fluorophores closer to the sensing domain upon insertion of the hybrid reporter. Thus, coupling cpHaloTag bound to JF dyes with either a Ca^{2+} or a voltage-sensitive protein domain yielded HaloCaMP and HASASP, respectively.[8] These sensors display high sensitivity, good dynamic ranges, and benefit from an interesting modularity from their hybrid nature that was notably exploited to red-shift the emission by changing the fluorophore ligand.

The identification and characterization of a viable circular permutation site in the photoactive yellow protein PYP at position 114-115 was a very encouraging finding for the development of a circularly permuted FAST.[9] Indeed, similar to its parent protein, FAST tolerated circular permutation at the same site, and despite being relatively distant from the fluorogen binding cavity, this position proved to confer high conformational sensitivity to the reporter. The dissociation constant of its cognate fluorogen could thus be modulated by insertion of cpFAST between the calmodulin/M13 protein pair, yielding a Ca^{2+} biosensor that displayed a 2- to 3-fold fluorescence increase upon Ca^{2+} binding, due to the restoration of a proper conformation for fluorogen binding.[10]

Engineering fluorescent reporters has also enabled the development of innovative detection tools to visualize intermolecular processes, notably the widely studied protein interactome. Protein-protein interactions (PPIs) are in fact dynamic processes involved in a number of metabolic and signaling pathways. A common method to visualize PPIs is based on the reversible evolution of FRET efficiency between two fluorescent proteins fused to interacting partners.[11] Relying on the dependence of FRET efficiency on the distance and orientation between the donor and acceptor fluorescent proteins, structural information and control over expression levels are required to fully benefit from this widely used strategy, that can consequently be difficult to implement and quantify. Further engineering of fluorescent reporters enabled the development of the bimolecular fluorescence complementation (BiFC) technique, in which interacting partners are fused to fragments of a split fluorescent protein, that is subsequently able to properly fold thus fluoresce upon interaction. Splitting GFP and its variants into a large and a small fragment (the latter being composed of the last strand β11 of the barrel) has indeed found a number of applications for imaging biological processes.[12,13] Despite initial limitations in terms of solubility and self-assembly, much progress has been made in these regards using superfolder fluorescent proteins, that even enabled the recent development of a tripartite split GFP reporter.[14] Nevertheless, the use of BiFC is not applicable to the detection of rapid and reversible processes, as formation of the chromophore is irreversible and induces a maturation lag time.

In order to overcome these limitations, split hybrid reporters are very promising candidates, and examples of their applications have also been described in chapter II. The identification of three spectrally distinct near-infrared FPs took advantage of the pre-formed endogenous chromophore biliverdin and enabled engineering of irreversible miSplit systems for multiplexed imaging of simultaneous processes.[15] The monomeric infrared IFP1.4, also based on a bacterial phytochrome scaffold, achieved highly sensitive and reversible detection of PPIs,[16] and a similar strategy was followed to develop a green PPI reporter based on binding of the endogenous bilirubin chromophore to UnaG.[17] Moreover, the generation of a split FAP system based on bacterial lipocalin, named DiB-split, was a promising proof-of-concept demonstrating the potential tunability provided by chemogenetic reporters binding synthetic fluorophores.[18] Finally, our group recently demonstrated that FAST tolerates splitting at the previously identified cp position 114-115, yielding a large NFAST fragment and an 11-residues small peptide CFAST fragment.[19] Various cellular processes could be visualized by fusing splitFAST(114-115) fragments to interacting protein partners. The elegant application of the splitting strategy to the spectrally orthogonal variants greenFAST and redFAST, sharing a common CFAST fragment, has notably allowed two-color imaging of consecutive PPIs sharing a common interaction partner.[20] Split chemogenetic reporters are thus considered a valuable addition to the biosensing toolbox, showing high modularity, promising kinetic properties as well as wide applicability to various contexts.

Encouraged by the exciting opportunities offered by the engineering of new hybrid reporters with various properties, we investigated application of the circular permutation strategy to identify new viable cpFAST variants. Furthermore, based on the observation that positions for viable circular permutation and split sites usually coincide, we also considered engineering a new splitFAST system with tunable features, combining the modularity of a hybrid reporter, together with the various properties displayed by the growing series of FAST variants. The identification of additional viable circular permutation and split positions was envisioned to be useful in the development of FAST-based biosensors, and to provide complementary systems for the design of multiplexed imaging experiments entirely relying on chemogenetic fluorescent reporters.[1]

---

[1] A Master's project has been performed in the course of this study by Aurélien Brion, who helped performing the experiments and data analysis for the identification and characterization of ^{RspA}gFAST and its split version.

VI.2. Development and characterization of a new cpFAST

VI.2.1. Evaluation of seven positions for circular permutation of FAST

The systematic and comprehensive study of all possible circularly permuted variants of a protein, although feasible as previously demonstrated on DHFR,[21] can be tedious and time-consuming. In the aim of minimizing the trial-and-error phase, and relying on rational design, we used a prediction tool and applied the crystal structure of the FAST parent protein PYP (PDB 1NWZ) to the web server CPred.[22] The absence of a FAST crystal structure prevented direct prediction on our protein of interest. However, results from PYP analysis were considered transposable to FAST, thanks to the high sequence homology and the presumed common structural features between the two proteins. Based on the sequence, the secondary structures and several structure-derived residues properties, the CPred server provided a probability score for each position, allowing to identify several potential viable cleavage regions. After rational evaluation of the suggested regions, seven positions were selected for our study: cpFAST(24-25), cpFAST(35-36), cpFAST(59-60), cpFAST(72-73), cpFAST(89-90), cpFAST(98-99) and cpFAST(102-103) (Figure VI-1).

First, the different cpFAST versions were generated by inserting a *Tobacco Etch Virus* (TEV) protease cleavage sequence between FAST native termini. This sequence constituted a relatively long and flexible linker, enabling to evaluate the viability of the cpFAST version. The DNA sequences encoding the seven cpFAST(X-Y)tev versions were generated from the sequence encoding a FAST tandem connected with a TEV cleavage site. The resulting constructs were recombinantly expressed in *E. coli*. The expression level of each cpFAST version was evaluated by SDS-PAGE: protein overexpression was observable after induction with IPTG for most circular permutants, except for cpFAST(35-36)tev and cpFAST(102-103)tev. Despite some efforts to optimize induction parameters (in terms of time and temperature), they were not expressed in any conditions, and this observation was confirmed in higher volumes of bacterial culture. These circular permutations were then considered non-viable, supposedly due their low stability, and further characterization was consequently performed on the other five expressed and purified cpFAST versions.

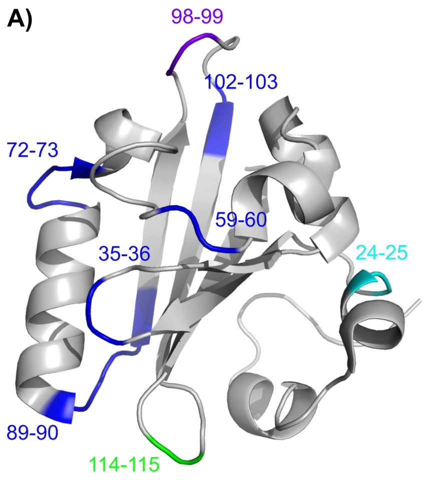

B)

cpFAST termini	expression in E. Coli	fluorogen binding
24-25	✓	✓
35-36	✗	-
59-60	✓	✗
72-73	✓	✗
89-90	✓	✗
98-99	✓	✓
102-103	✗	-
114-115	✓	✓

Figure VI-1. Screening circular permutations of FAST. A) Possible positions for circular permutation identified with CPred are represented on the crystal structure of PYP (PDB = 1NWZ), the parent protein of FAST. **B)** Properties of the different circular permutations of FAST.

We next evaluated the ability of the five circular permutations to bind HMBR fluorogen and stabilize its fluorescent state: no significant fluorescence intensity was observed from cpFAST(59-60)tev, cpFAST(72-73)tev and cpFAST(89-90)tev in presence of HMBR up to 16 µM. Circular permutation of FAST at these positions seemed to significantly affect the tag function, and these cpFAST versions were consequently excluded from further study. HMBR titration with cpFAST(24-25)tev and cpFAST(98-99)tev led to measurable fluorescence intensities at reasonable fluorogen concentrations (Figure VI-2). cpFAST(24-25)tev displayed an important affinity loss for the fluorogen compared to FAST ($K_{\mathrm{D,HMBR}}$ = 18 ± 1.6 µM). Surprisingly, the fluorogen affinity was substantially less affected by circular permutation at position 98-99 ($K_{\mathrm{D,HMBR}}$ = 1.1 ± 0.1 µM), although this cleavage site was located in the loop engineered for creating FAST and was directly involved in the fluorogen binding. Nevertheless, tertiary structures obtained upon circular permutation at positions 24-25 and 98-99 appeared to yield functional fluorogen-binding fluorescent tags.

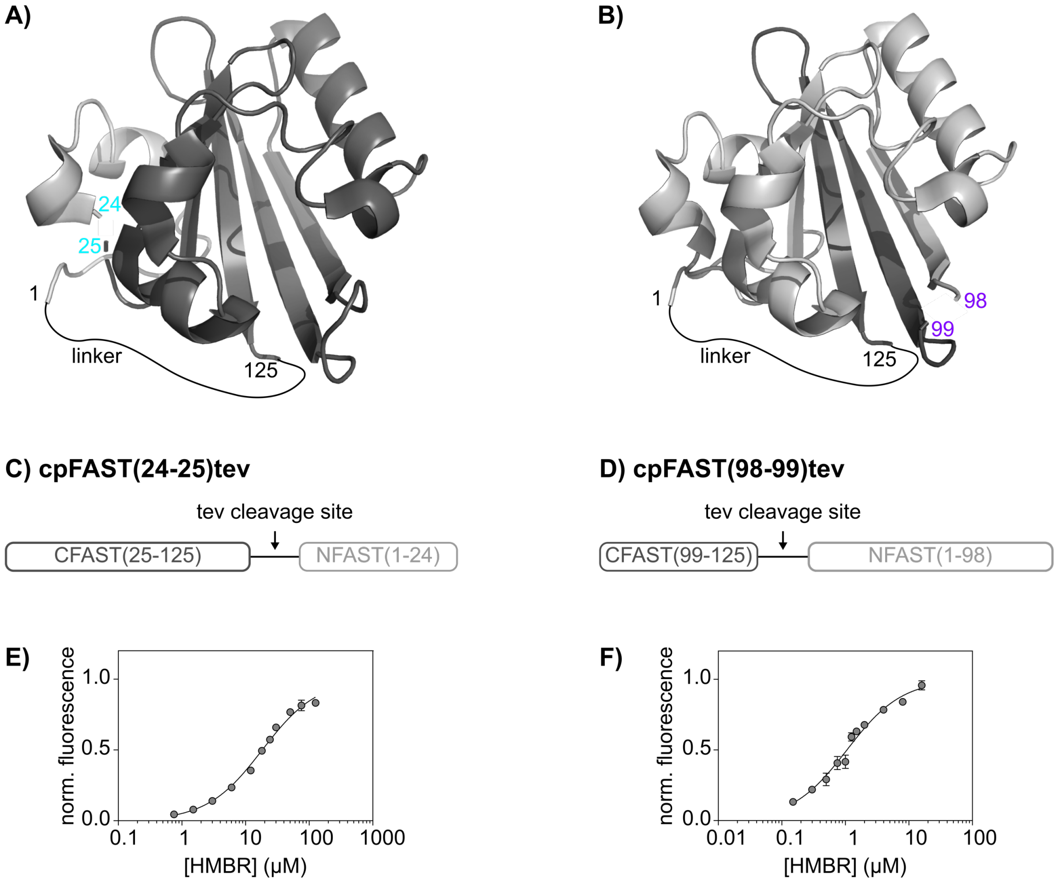

Figure VI-2. Identification of two viable circular permutation positions. A & B) Representation of the 3D structure of cpFAST(24-25) and cpFAST(98-99), respectively, where the N-terminal fragment (light grey) and the C-terminal fragment (dark grey) are connected by a linker between the native FAST termini. **C & D)** Schematic representation of cpFAST(24-25)tev and cpFAST(98-99)tev, respectively. **E & F)** HMBR titration curves of cpFAST(24-25)tev and cpFAST(98-99)tev, respectively, in pH 7.4 HEPES buffer (50 mM) containing NaCl (150 mM). The least-squares fit (line) gave the thermodynamic dissociation constant $K_{D,HMBR}$ provided in Table VI-1. The sensor concentration was fixed at 0.1 µM.

Table VI-1. For each reporter is given the dissociation constant of HMBR ($K_{D,HMBR}$).

	$K_{D,HMBR}$ (µM)
FAST	0.13 ± 0.01[23]
cpFAST(24-25)tev	18 ± 1.6
cpFAST(98-99)tev	1.1 ± 0.1

VI.2.2. Characterization of promising candidates cpFAST(25-24) and cpFAST(99-98)

The influence of the linker inserted between the native FAST termini was then studied for the two most promising candidates, cpFAST(24-25) and cpFAST(98-99). The TEV sequence was consequently replaced by flexible GGS linkers of varying size from 11 to 3 residues, yielding cpFAST(X-Y)Z (Z = 5 to 2). A version without any linker cpFAST(X-Y)1, thus directly connecting the terminal residues of FAST, was also studied for both circularly permuted tags. HMBR titration confirmed that insertion of varying linkers yielded functional tags (Figure VI-3). Interestingly, the effect of the linker length on the dissociation constants significantly differed between the two circular permutations.

Varying the connecting sequence in cpFAST(24-25) did not seem to affect the affinity of the tag for HMBR. Indeed, K_D values revolved around 10 µM for the five different linker lengths (Table VI-2). NFAST and CFAST fragments seemed to only weakly interact upon permutation at this position, yielding a less favourable binding of HMBR as they did not provide a fully folded functional tag. Low correlation between linker size and HMBR binding properties, supported by the observation of a poorly structured PYP(1-24) fragment, suggested that NFAST(1-24) was weakly involved in fluorogen binding in the context of cpFAST(24-25). However, NFAST(1-24) appeared important for the structural integrity of the tag, as circular permutation at this position yielded a 100-fold loss of affinity for HMBR compared to native FAST, and a 2- to 50-fold affinity loss compared to cpFAST(114-115) at equal linker size. The measured fluorescence quantum yield of cpFAST(24-25) was lower than FAST, yet sufficient to observe a reliable fluorescent signal in the presence of the fluorogen. These different observations were in agreement with the properties of the recently described nanoFAST,[24] a FAST variant truncated from residue 1 to 27, in which the binding pocket is suggested to be enlarged in both its apo- and bound states. Consequently, it appeared consistent that fluorogen binding only relied on the binding pocket conformation allowed by the virtually "truncated" fragment CFAST(25-125), thus altering the fluorescent properties of the fluorogen-bound tag.

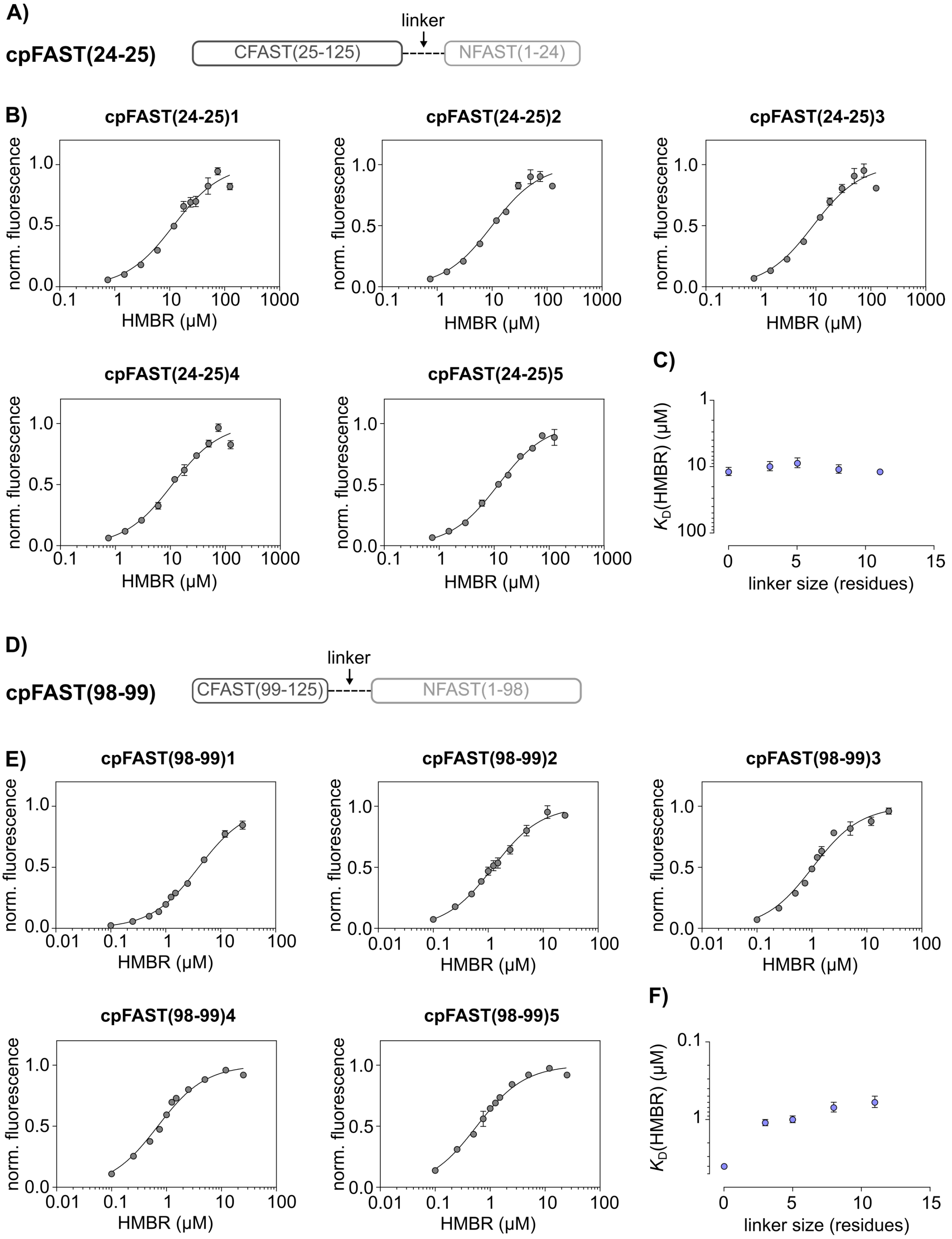

Figure VI-3. Influence of the linker in cpFAST(24-25) and cpFAST(98-99). A & D) Schematic representation of cpFAST(24-25)Z and cpFAST(98-99)Z, respectively**. B & E)** HMBR titration curves of cpFAST(24-25)Z and cpFAST(98-99)Z, respectively, in pH 7.4 HEPES buffer (50 mM) containing NaCl (150 mM). The least-squares fit (line) gave the thermodynamic dissociation constant $K_{D,HMBR}$ provided in Table VI-2. The sensor concentration was fixed at 0.1 μM. **C & F)** Evolution of HMBR dissociation constants depending on the linker size.

Table VI-2. Influence of the linker in cpFAST(24-25) and cpFAST(98-99). For each reporter is given the dissociation constant of HMBR ($K_{D,HMBR}$) and the fluorescence quantum yield, ϕ.

	cpFAST(114-115)[25]		**cpFAST(24-25)**		**cpFAST(98-99)**	
	$K_{D,HMBR}$ (μM)	**Φ**	**$K_{D,HMBR}$ (μM)**	**Φ**	**$K_{D,HMBR}$ (μM)**	**Φ**
0	5.1 ± 0.70	~ 0.2	12 ± 1.7	0.15	4.0 ± 0.2	0.20
3	0.99 ± 0.11	~ 0.2	10 ± 1.6	0.19	1.2 ± 0.1	0.22
5	0.65 ± 0.04	~ 0.2	8.9 ± 1.5	0.18	1.0 ± 0.1	0.24
8	0.30 ± 0.04	0.19	11 ± 1.6	0.18	0.7 ± 0.1	0.22
11	0.22 ± 0.03	0.28	12 ± 0.8	0.21	0.6 ± 0.1	0.20

A different tendency was observed for cpFAST(98-99). Firstly, this circularly permuted version showed reasonable affinity for HMBR, that was dependent on the size of the linker connecting its native termini (Table VI-2). Indeed, the dissociation constant increased with decreasing linker length (from $K_{D,HMBR}$ = 0.6 ± 0.1 μM with an 11-residues linker, to $K_{D,HMBR}$ = 4.0 ± 0.2 μM without linker). This indicated that fluorogen binding to cpFAST(98-99) was dependent on the interaction between the fragments NFAST and CFAST. Indeed, reconstitution of this circularly permuted version appeared more efficient with longer flexible linkers, while being impeded by shorter linkers, likely from conformational strain. The inferred high affinity between fragments was supported by the highly structured nature of CFAST(99-125), that belongs to the (Asn89-Arg124) β-sheet motif in the native tag. Noteworthy, reasonable fluorescence quantum yields were measured for all versions of cpFAST(98-99), that were independent on the linker length. The absence of correlation between fluorogen affinity and quantum yield was an interesting feature, as it suggested that once complexed, the fluorogen interactions with the tag binding cavity were to some extent able to favor an optimized binding conformation.

cpFAST(98-99) behaviour was similar to the previously characterized cpFAST(114-115), and was thus considered as a promising reporter, notably for the design of biosensors. Indeed, when fused to a protein sensing domain, cpFAST(98-99) and cpFAST(114-115) provided biosensors with comparable properties, as described in the preceding chapter III of this manuscript about the design of a FAST-based glutamate sensor. Consequently, these encouraging results incited us to further explore the biosensing possibilities provided by the identification of a new cleavage site in the FAST protein tag.

VI.3. Identification and optimization of a new splitFAST for biosensing of protein-protein interactions.

VI.3.1. Topological studies of the proof-of-concept FKBP-FRB system

The identification and characterization of a new circularly permuted FAST at position 98-99, showing a similar behaviour as cpFAST(114-115) and promising properties for biosensing applications (see chapter III of this manuscript), led us to consider this position as a potential splitting site. Indeed, in a similar manner as the recently described splitFAST(114-115), the fragments NFAST(1-98) and CFAST(99-125) were expected to allow the reconstitution of a functional reporter when brought in close proximity. As a proof-of-concept to demonstrate this ability, we selected the well-described protein pair formed by the FK506-binding protein (FKBP) and the mammalian FKBP-rapamycin-binding domain (FRB), that interact in a relatively fast and reversible manner upon addition of the exogenous small molecule rapamycin.

In order to evaluate splitFAST(98-99) association by flow cytometry, HEK293 cells were co-transfected with two bicistronic plasmids. These consisted in FKBP or FRB fused to either reporter fragments, and separated by an internal ribosome entry site (IRES) from a gene encoding either iRFP670 or mTurquoise2 (mT2) as transfection reporters (Figure VI-4). This strategy allowed to selectively analyze cells that were efficiently transfected by both plasmids, without affecting FKBP-FRB interaction. Titration of the fluorogen HMBR was performed in the presence of 500 nM of rapamycin (thus inducing the protein-protein interaction) or in the absence of the dimerizer, by measuring the mean fluorescence intensity of the co-transfected cell population. Several parameters could then be evaluated at several fluorogen concentrations: the relative brightness of our systems compared to the previously characterized splitFAST(114-115), the self-complementation yielding unspecific fluorescent signal, and the dynamic range (i.e. the fluorescence fold increase upon interaction).

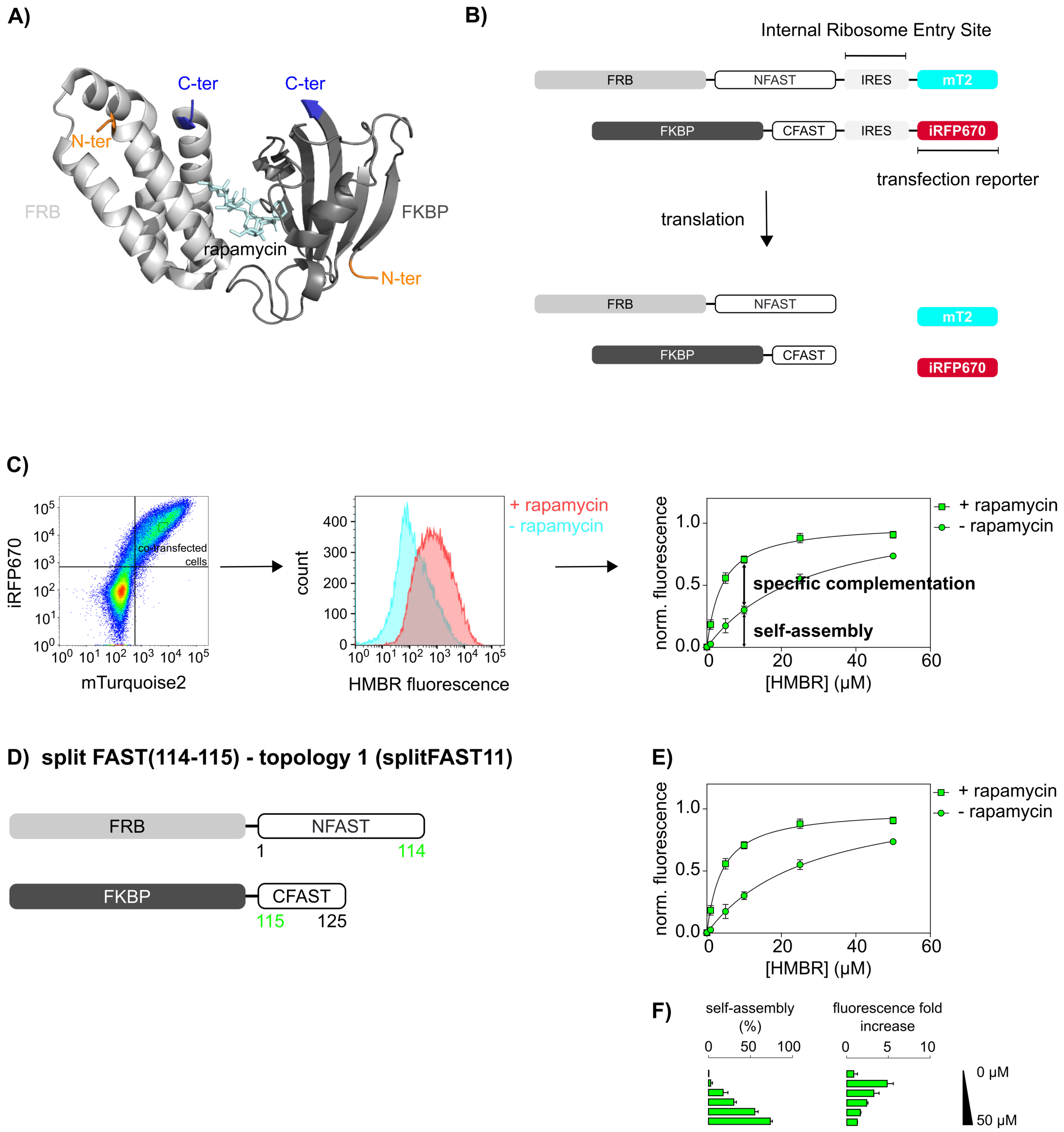

Figure VI-4. Workflow of the evaluation of split systems as PPI reporters using flow cytometry. A) Crystal structure of the heterodimer formed by FK506-binding protein FKBP (dark grey) and the FKBP-rapamycin-binding domain FRB (light grey) bound to rapamycin (light blue). **B)** Schematic representation of bicistronic plasmids encoding both interacting partners with mTurquoise2 and iRFP670 as transfection reporters. **C)** Co-transfected cells were selected by using the signal of iRFP670 and mTurquoise2 transfection reporters, and the mean fluorescence of each condition of HMBR concentration was then plotted and fitted with a one-site specific binding model. **D)** Schematic representation of split FAST(114-115) fused with FKBP-FRB in topology 1. **E)** Normalized average fluorescence of about 20,000 HEK293T cells co-expressing FKBP and FRB, fused to either fragment of the split reporters treated without (circle) or with (square) 500 nM of rapamycin, and with 0, 1, 5, 10, 25 or 50 μM of HMBR. Data represent the mean ± sem (n = 3). **F)** Dependence of the self-assembly and the association dynamic range (i.e. interaction-specific fluorescence fold increase) on the concentration of HMBR (from analysis shown in (E)).

The different biosensors development described in the preceding chapters of this manuscript underlined the importance of a system's topology for the proper interaction of FAST fragments. We consequently initiated the characterization of splitFAST(98-99) by the topological study of FKBP-FRB fusion to our reporter system. Observation of the crystal structure of the protein heterodimer (PDB 6M4U) indicated that while both FRB termini were located in close proximity, FKBP termini were situated on opposite sides of the protein. We consequently assumed that fusion of a FAST fragment to the spatially separated N-ter of FKBP would probably hinder the reporter reconstitution.

Four topologies were thus considered (Figure VI-5): fusing either FAST fragments at the C-ter of both interaction partners yielded the splitFAST(98-99)-1 and splitFAST(98-99)-3 systems (FRB-NFAST/FKBP-CFAST and FRB-CFAST/FKBP-NFAST, respectively), and fusing each FAST fragments to FRB N-ter and FKBP C-ter yielded the splitFAST(98-99)-2 and splitFAST(98-99)-4 systems (CFAST-FRB/FKBP-NFAST and NFAST-FRB/FKBP-CFAST, respectively). Evaluation of the four fusion pairs by flow cytometry indeed indicated a strong dependence on the topology. splitFAST(98-99)-2 was discarded as it showed very low fluorescence levels, that we attributed to a wrong orientation of the FAST fragments, hampering proper complementation and thus fluorogen binding. Despite a slightly higher fluorescence intensity, splitFAST(98-99)-3 displayed very high self-assembly and a low dynamic range, and was consequently discarded as well.

Although 2.1 to 2.7-fold less bright than splitFAST(114-115), splitFAST(98-99)-1 and splitFAST(98-99)-4 both showed reasonable fluorescence intensities. In particular, splitFAST(98-99)-4 was identified as a promising system in terms of fluorescence level and increase upon addition of rapamycin. Moreover, it displayed the highest affinity for the fluorogen upon FKBP-FRB interaction ($K_{D,HMBR+rap}$ = 7.5 ± 0.7 μM), providing an encouraging 2.9-fold fluorescence increase at [HMBR] = 5 μM.

Table VI-3. Characterization of splitFAST(98-99) topologies. For each split reporter is given the apparent dissociation constant in absence of rapamycin ($K_{D,HMBR-rap}$), in presence of 500 nM of rapamycin ($K_{D,HMBR+rap}$), and the dynamic range calculated as the ratio of the fluorescence intensities at 5 μM HMBR. The relative brightness compared to split FAST(114-115) at equivalent co-expression level is also given.

split	$K_{D,HMBR+rap}$ (μM)	$K_{D,HMBR-rap}$ (μM)	Dynamic range (at [HMBR] = 5 μM)	Relative brightness (to splitFAST11)
FAST(114-115)	4.1 ± 0.3	28 ± 3.6	3.2	1
FAST(98-99) – top. 1	17 ± 1.0	31 ± 3.4	1.6	0.37
FAST(98-99) – top. 2	11 ± 2.9	~ 30	0.2	0.04
FAST(98-99) – top. 3	11 ± 2.2	20 ± 3.9	1.5	0.16
FAST(98-99) – top. 4	7.5 ± 0.7	31 ± 4.3	2.9	0.47

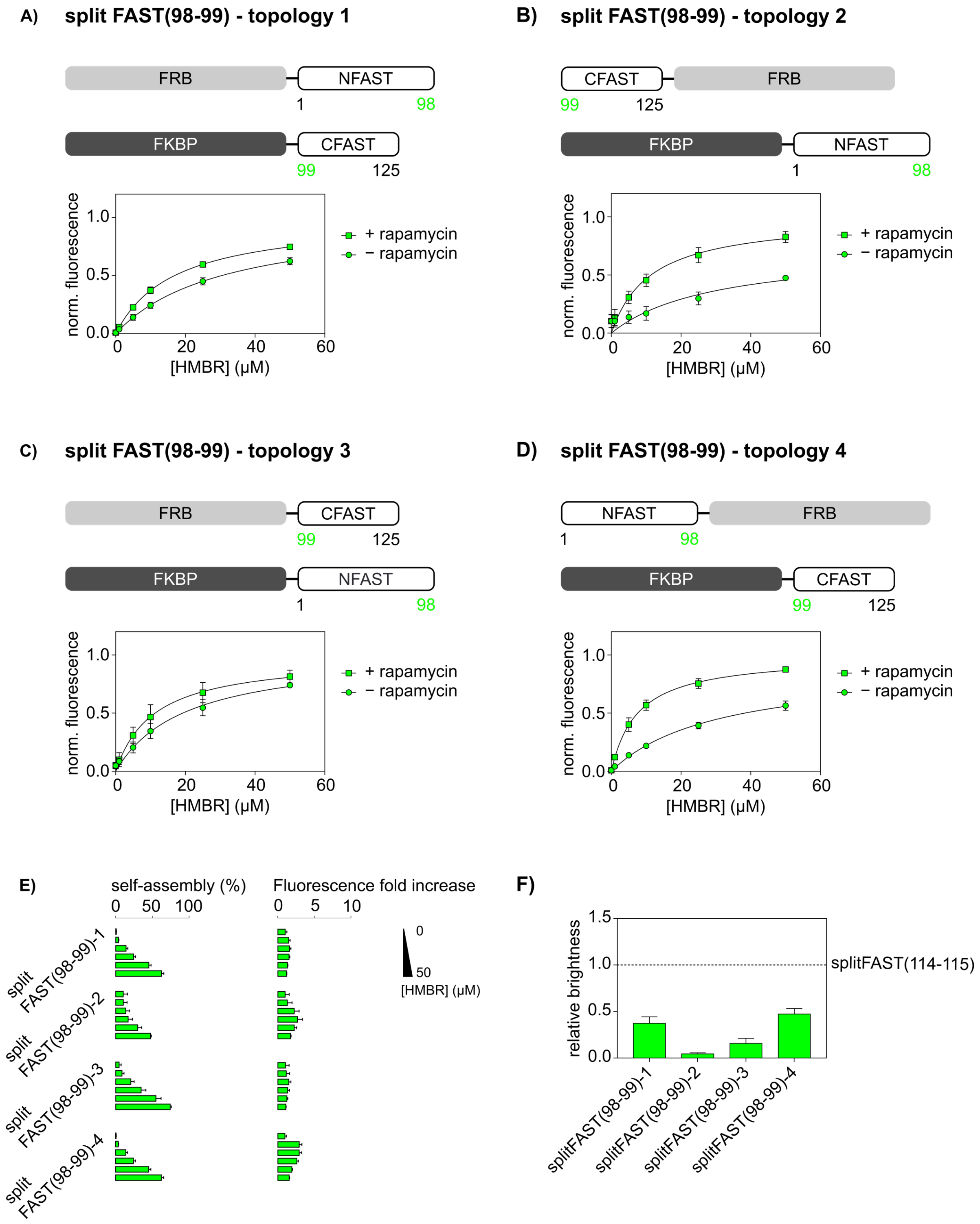

Figure VI-5. Characterization of splitFAST(98-99) topologies. A-D) Normalized average fluorescence of about 20,000 HEK293T cells co-expressing FKBP-FRB fused to either fragment of splitFAST(98-99) in topology 1, 2, 3 and 4 respectively, treated without (circle) or with (square) 500 nM of rapamycin, and with 1, 5, 10, 25 or 50 μM of HMBR. mTurquoise2 and iRFP670 were used as transfection reporters. Data represent the mean ± sem (n = 3). The least-squares fit (line) gave the thermodynamic dissociation constant $K_{\mathrm{D,HMBR+rap}}$ and $K_{\mathrm{D,HMBR-rap}}$ provided in Table VI-3. **E)** Dependence of the self-assembly and the association dynamic range (i.e. interaction-specific fluorescence fold increase) on the concentration of HMBR (from analysis shown in (A-D)). **F)** Normalized fluorescence of the different split reporters from cells with similar levels of mTurquoise2 and iRFP670 for direct comparison. Data represent the mean ± sem (n = 3).

VI.3.2. Effect of splitting FAST variants at position (98-99)

Split greenFAST(98-99)

The promising properties of splitFAST(98-99) nevertheless left room for improvement: thus, we decided to explore the effect of splitting different FAST variants at this position. A combination of directed evolution and rational design notably yielded the orthogonal variants greenFAST (G21E, P68T, G77R) and redFAST (F28L, E46Q, R52A, E81V, S99N) displaying selective binding for the green fluorogen HMBR and the red fluorogen HBR-3,5-DOM, respectively. Splitting greenFAST and redFAST at position 114-115 both provided reversible systems with similar kinetics and slightly improved dynamic range compared to the initially described splitFAST(114-115).[20] In our case, the mutation S99N in redFAST located at the envisioned split site was expected to potentially compromise the spectral orthogonality of the variant. Only the greenFAST variant was consequently split at position 98-99, and the FKBP-FRB protein pair was flanked with either resulting fragments. This system was applied to both previously identified topologies, and the resulting split greenFAST(98-99)-1 (FRB-greenNFAST/FKBP-CFAST) and split greenFAST(98-99)-4 (greenNFAST-FRB/FKBP-CFAST) were evaluated by flow cytometry (Figure VI-6).

While split greenFAST(98-99)-1 showed similar brightness as splitFAST(98-99)-1 and modest improvement in terms of fluorogen affinities and dynamic range, split greenFAST(98-99)-4 proved to be the most favourable system for this variant as well. In fact, in addition to promising fluorescence intensity level, a substantially decreased self-assembly provided an 8.8-fold fluorescence increase at [HMBR] = 5 μM. Moreover, the very low fluorogen affinity measured from the unspecific interaction between reporter fragments ($K_{\mathrm{D,HMBR-rap}}$ = 220 ± 73 μM) was expected to allow the use of high HMBR concentrations (10-25 μM), thus improving the apparent fluorescence intensity of the system without compromising its dynamic range.

Split ^{RspA}FAST(98-99)

The characterization of six different FAST orthologs, followed by the evaluation of their split versions at position 114-115, resulted in the identification of a bright, reversible and highly specific reporter system for the visualization of protein-protein interactions (Rakotoarison & Tebo et al., manuscript in preparation). Indeed, split ^{RspA}FAST(114-115) showed very low self-assembly and high affinity for the fluorogen upon rapamycin induced FKBP-FRB association, thus yielding a system with very high dynamic range. Both properties were desirable in order to further improve our splitFAST(98-99) system: consequently we attempted to split ^{RspA}FAST at position 98-99 and evaluated the resulting reporter in the context of FKBP-FRB interaction by flow cytometry. Fusion of the fragments ^{RspA}NFAST(1-98) and ^{RspA}CFAST(99-125) to FRB and FKBP, respectively, thus yielded split ^{RspA}FAST(98-99)-1 (FRB-^{RspA}NFAST/FKBP-^{RspA}CFAST) and split ^{RspA}FAST(98-99)-4 (^{RspA}NFAST-FRB/FKBP-^{RspA}CFAST).

Results were consistent with previous observations: splitting ^{RspA}FAST at position 98-99 provided improved dynamic range compared to splitFAST(98-99), and split ^{RspA}FAST(98-99)-4 displayed the most promising features. Indeed, self-assembly of this system in both topologies was very low; yet split ^{RspA}FAST(98-99)-4 in presence of rapamycin showed the highest affinity for HMBR encountered in the course of this study ($K_{D,HMBR+rap}$ = 3.0 ± 0.3 µM). Surprisingly, the brightness of split ^{RspA}FAST(98-99) suffered a 5-fold loss compared to splitFAST(114-115), suggesting that ^{RspA}FAST is more sensitive than FAST to cleavage close to the fluorogen binding loop. Nevertheless, the consistently high fluorescence fold increase observed from [HMBR] = 1 to 50 µM was expected to allow the use of high fluorogen concentrations in this case as well, thus providing reasonable intensities for applications in fluorescence microscopy.

Table VI-4. Characterization of split greenFAST(98-99) and split ^{RspA}FAST(98-99). For each split reporter is given the dissociation constant in absence ($K_{D,HMBR-rap}$) and in presence of 500 nM of rapamycin ($K_{D,HMBR+rap}$), and the dynamic range calculated as the ratio of the fluorescence intensities at 5 µM HMBR. The relative brightness compared to split FAST(114-115) at equivalent co-expression level is also given.

split	$K_{D,HMBR+rap}$ (µM)	$K_{D,HMBR-rap}$ (µM)	Dynamic range (at [HMBR] = 5 µM)	Relative brightness (to splitFAST11)
FAST(114-115)	4.1 ± 0.3	28 ± 3.6	3.2	1
greenFAST(98-99) – top. 1	16 ± 0.7	44 ± 7.6	2.5	0.37
greenFAST(98-99) – top. 4	12 ± 0.8	220 ± 73	8.8	0.57
^{RspA}FAST(98-99) – top. 1	13 ± 1.4	nd	7.8	0.21
^{RspA}FAST(98-99) – top. 4	3.0 ± 0.3	nd	17	0.20

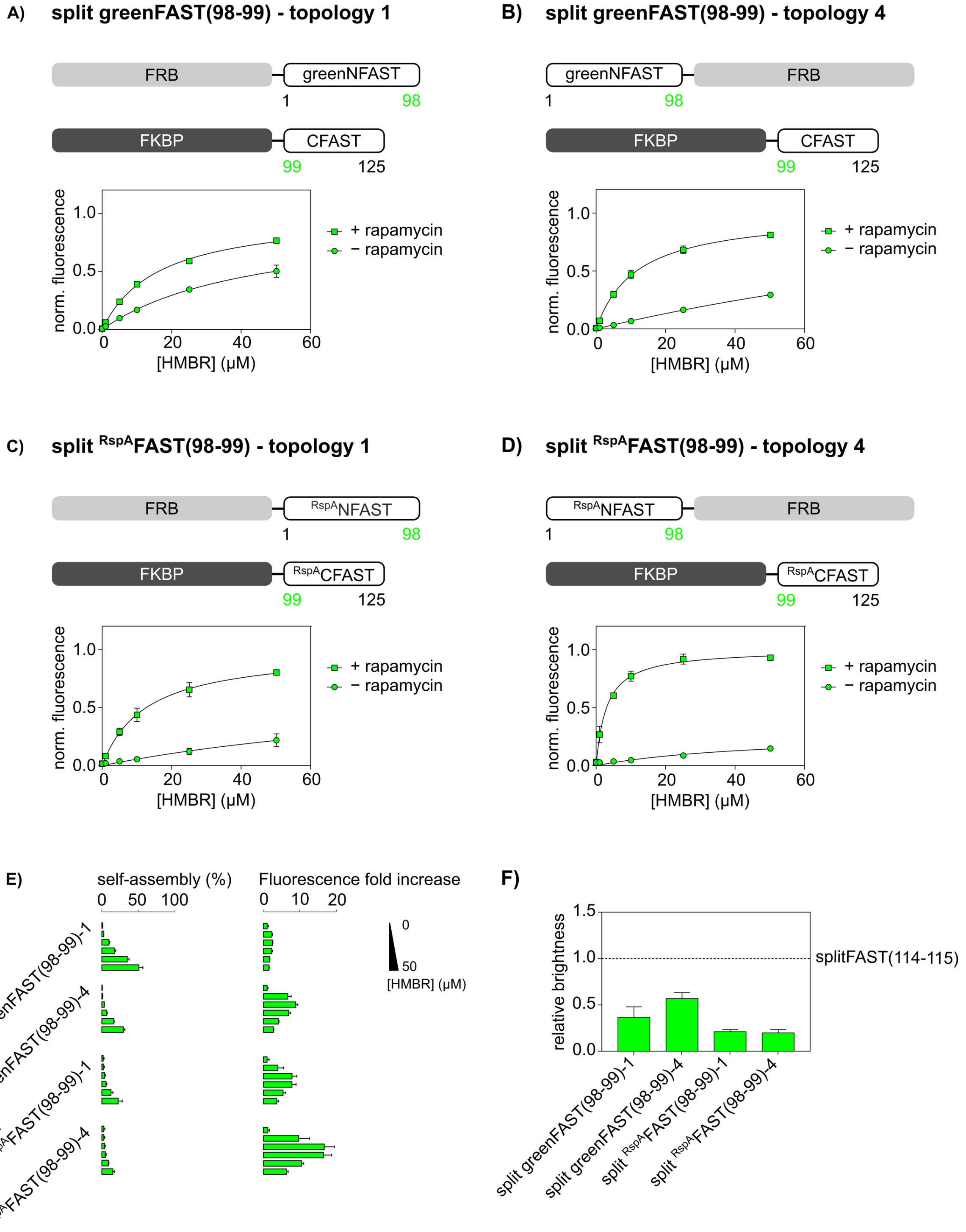

Figure VI-6. Characterization of split greenFAST(98-99) and split $^{\mathrm{RspA}}$FAST(98-99). A-D) Normalized average fluorescence of about 20,000 HEK293T cells co-expressing FKBP-FRB fused to either fragment of split greenFAST(98-99) and split $^{\mathrm{RspA}}$FAST(98-99) in topology 1 and 4, respectively, treated without (circle) or with (square) 500 nM of rapamycin, and with 1, 5, 10, 25 or 50 µM of HMBR. mTurquoise2 and iRFP670 were used as transfection reporters. Data represent the mean ± sem (n = 3). The least-squares fit (line) gave the thermodynamic dissociation constant $K_{\mathrm{D,HMBR+rap}}$ and $K_{\mathrm{D,HMBR-rap}}$ provided in Table VI-4. **E)** Dependence of the self-assembly and the association dynamic range (i.e. interaction-specific fluorescence fold increase) on the concentration of HMBR (from analysis shown in (A-D)). **F)** Normalized fluorescence of the different split reporters from cells with similar levels of mTurquoise2 and iRFP670 for direct comparison. Data represent the mean ± sem (n = 3).

VI.3.3. Design of an optimized and semi-orthogonal splitFAST(98-99)

Optimization of a selective reporter by combining RspA and greenFAST

Splitting greenFAST and ^{RspA}FAST variants at position 98-99 was possible and beneficial in both cases. While split ^{RspA}FAST(98-99) showed the most improvements in terms of dynamic range and decreased self-assembly, greenFAST also featured interesting properties regarding brightness and fluorogen selectivity. We indeed considered optimizing a split system that would retain spectral orthogonality with redFAST(114-115), that would then be suitable for multicolour imaging by fluorescence microscopy. Consequently, we decided to introduce within ^{RspA}FAST the three mutations (G21E, P68T and G77R) that confer greenFAST with selectivity for the green-emitting HMBR over the red-emitting HBR-3,5-DOM (Figure VI-7). Bacterial recombinant expression of the resulting mutant ^{RspA}gFAST, followed by affinity chromatography purification, enabled *in vitro* characterization. Satisfyingly, titration of HMBR and HBR-3,5-DOM with ^{RspA}gFAST resulted in reasonable brightness upon binding of both fluorogens, and a much lower dissociation constant was measured with HMBR than HBR-3,5-DOM ($K_{D,HMBR}$ = 16 ± 1.9 nM and $K_{D,HBR\text{-}3,5\text{-}DOM}$ = 1.2 ± 0.1 µM), indicating a conserved selectivity (Table VI-5).

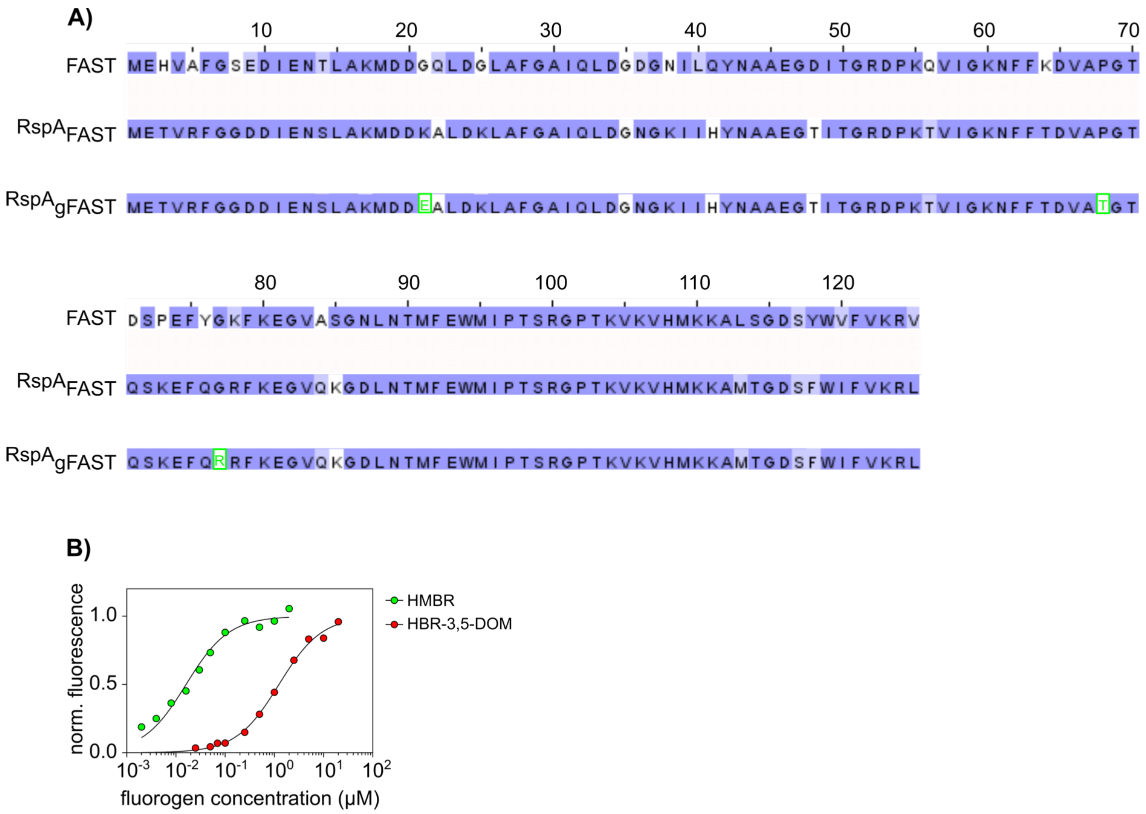

Figure VI-7. Characterization of gFAST. A) Comparison of residue sequences of FAST, ^{RspA}FAST and ^{RspA}gFAST. **B)** Titration curves of HMBR and HBR-3,5-DOM with ^{RspA}gFAST in pH 7.4 HEPES buffer (50 mM) containing NaCl (150 mM). The least-squares fit (line) gave the thermodynamic dissociation constants $K_{D,HMBR}$ and $K_{D,HBR\text{-}3,5\text{-}DOM}$ provided in Table VI-5. The sensor concentration was fixed at 10 nM for HMBR titration and 0.1 µM for HBR-3,5-DOM titration.

Table VI-5. Characterization of ^{RspA}gFAST. Dissociation constants of HMBR and HBR-3,5-DOM for ^{RspA}gFAST ($K_{D,HMBR}$ and $K_{D,HBR-3,5DOM}$).

protein	$K_{D,HMBR}$ (nM)	$K_{D,HBR-3,5DOM}$ (μM)
^{RspA}gFAST	16 ± 1.9	1.2 ± 0.1

The functionality and selectivity of ^{RspA}gFAST consequently encouraged us to evaluate its performances as a protein-protein interaction reporter upon splitting. In order to assess the effect of FAST mutations first, split ^{RspA}gFAST(114-115) in topology 1 (FRB-^{RspA}gNFAST/FKBP-^{RspA}CFAST) was first generated and compared to split ^{RspA}FAST(114-115)-1. The green mutations being located in the N-ter fragment of the reporter, both systems shared the same C-terminal fragment ^{RspA}CFAST. Interestingly, split ^{RspA}FAST(114-115)-1 and split ^{RspA}gFAST(114-115)-1 displayed comparable brightness and high affinity for the fluorogen upon specific complementation ($K_{D,HMBR+rap}$ = 1.6 ± 0.1 μM and 1.2 ± 0.1 μM, respectively) (Figure VI-8). However, split ^{RspA}gFAST(114-115) showed a dramatically decreased dynamic range at [HMBR] = 5 μM. Introduction of greenFAST mutations indeed appeared to substantially increase the affinity between the reporter fragments, thus yielding an increased fluorescent signal from their unspecific interaction. This result was in agreement with preliminary observations of the on-going ortholog FAST studies, presuming that self-assembly is mostly influenced by the NFAST fragment sequence.

Results of the subsequent evaluation of split ^{RspA}gFAST(98-99) in both topologies 1 and 4 (FRB-^{RspA}gNFAST/FKBP-^{RspA}CFAST and ^{RspA}gNFAST-FRB/FKBP-^{RspA}CFAST) were consistent with previous observations from the variants greenFAST and ^{RspA}FAST. Indeed, insertion of the green mutations in split ^{RspA}FAST enabled to maintain high fluorogen affinity upon complementation, and despite the expected increased self-assembly, this system displayed a high dynamic range in both topologies (especially split ^{RspA}gFAST(98-99)-4, showing a 18-fold fluorescence increase upon rapamycin addition at [HMBR] = 5 μM). Furthermore, splitting of the combined variant ^{RspA}gFAST allowed to achieve satisfying brightness levels, that should enable fluorescence microscopy imaging of protein-protein interactions with a reliable intensity and dynamic range at high fluorogen concentrations.

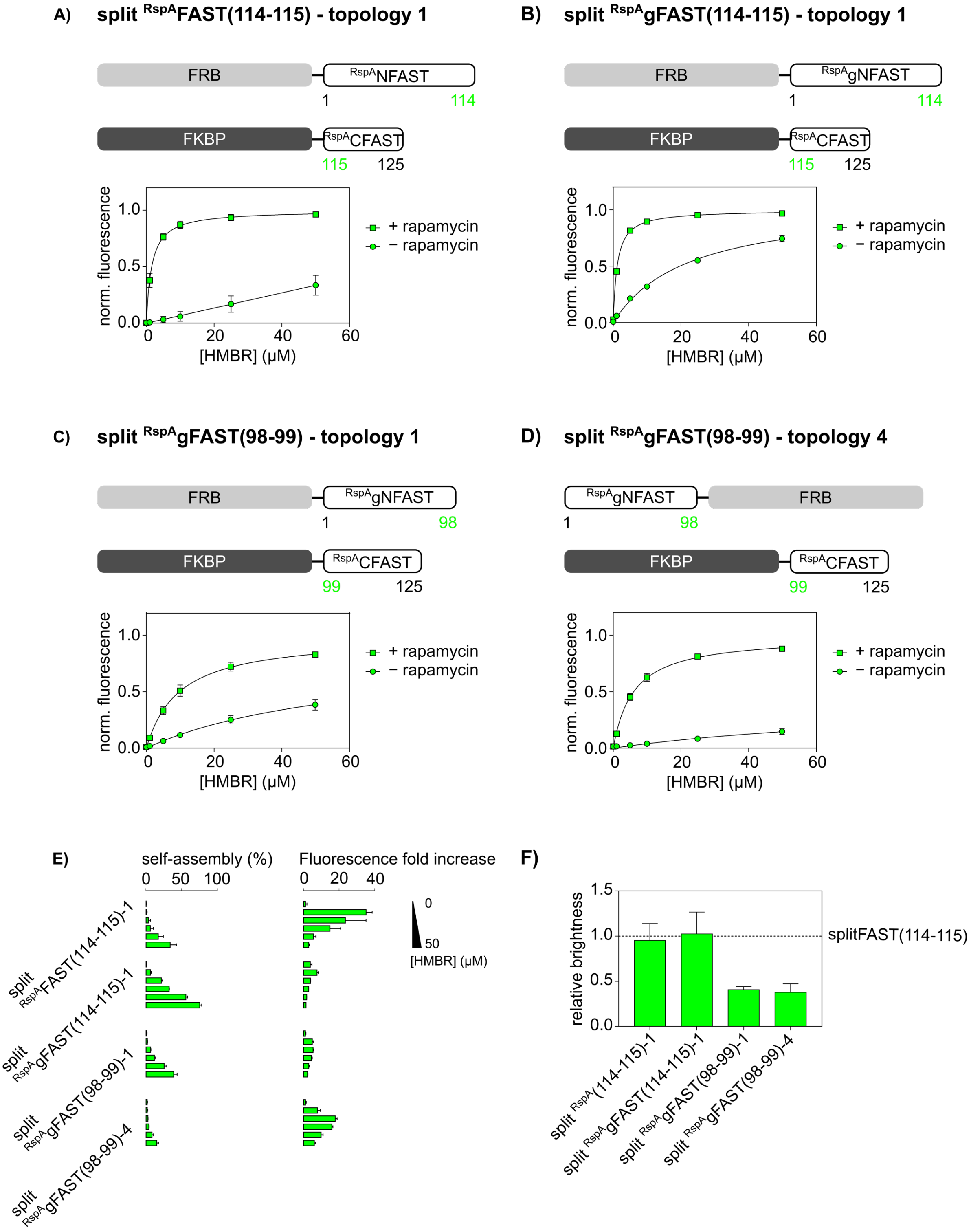

Figure VI-8. Characterization of split ^{RspA}gFAST. A-D) Normalized average fluorescence of about 20,000 HEK293T cells co-expressing FKBP-FRB fused to split ^{RspA}FAST(114-115) and (98-99) in topology 1, or split ^{RspA}gFAST(98-99) in topology 1 and 4, respectively, treated without (circle) or with (square) 500 nM of rapamycin, and with 1, 5, 10, 25 or 50 µM of HMBR. mTurquoise 2 and IRP670 were used as transfection reporters. Data represent the mean ± sem (n = 3). The least-squares fit (line) gave the thermodynamic dissociation constants $K_{D,HMBR+rap}$ and $K_{D,HMBR-rap}$ provided in Table VI-6. **E)** Dependence of the self-assembly and the association dynamic range (i.e. interaction-specific fluorescence fold increase) on the concentration of HMBR (from analysis shown in (A-D)). **F)** Normalized fluorescence of the different split reporters from cells with similar levels of mTurquoise2 and iRFP670 for direct comparison. Data represent the mean ± sem (n = 3).

Table VI-6. Characterization of split $^{\text{RspA}}$gFAST. For each split reporter is given the dissociation constant in absence of rapamycin ($K_{\text{D,HMBR-rap}}$), in presence of 500 nM of rapamycin ($K_{\text{D,HMBR+rap}}$), and the dynamic range calculated as the ratio of the fluorescence intensities at 5 µM HMBR. The relative brightness compared to split FAST(114-115) at equivalent co-expression level is also given.

split	$K_{\text{D,+rap}}$(HMBR) (µM)	$K_{\text{D,HMBR-rap}}$ (µM)	Dynamic range (at [HMBR] = 5 µM)	Relative brightness (to splitFAST11)
FAST(114-115)	4.1 ± 0.3	28 ± 3.6	3.2	1
$^{\text{RspA}}$FAST(114-115) – top. 1	1.6 ± 0.1	nd	23	0.95
$^{\text{RspA}}$gFAST(114-115) – top. 1	1.2 ± 0.1	22 ± 1.7	3.8	1.0
$^{\text{RspA}}$gFAST(98-99) – top. 1	9.7 ± 0.8	62 ± 16	5.3	0.41
$^{\text{RspA}}$gFAST(98-99) – top. 4	6.0 ± 0.4	~ 100	18	0.38

Preliminary use of new split FAST reporters in fluorescence microscopy

Preliminary observations from a single fluorescence microscopy experiment confirmed the behaviour of each splitFAST system upon association of the interacting proteins FKBP-FRB. Indeed, upon addition of 500 nM rapamycin, the fluorescence increase from HMBR was consistent with the tendencies observed from flow cytometry experiments (Figure VI-9). First, the improved dynamic range of split $^{\text{RspA}}$FAST(114-115) compared to split FAST(114-115) in topology 1 was confirmed, showing a median 5.9-fold compared to a 2.8-fold fluorescence increase upon association, respectively, in the presence of 10 µM HMBR. Moreover, despite a significantly lower fluorescence intensity, splitting $^{\text{RspA}}$FAST at position 98-99 allowed the observation of a median 8.5-fold fluorescence increase in the same topology, that was even improved up to a 9.7-fold increase when switching the split system to topology 4. Although moderately fluorescent, these two systems are thus characterized by a very low background signal, that could for instance be envisioned as suitable split reporters for visualizing interacting proteins with high expression levels. Finally, a satisfying compromise could be obtained from split $^{\text{RspA}}$gFAST(98-99) in topology 4, showing a median 12.3-fold fluorescence increase upon FKBP-FRB association with reasonable fluorescence intensity. This improved brightness from the introduction of the greenFAST mutations in $^{\text{RspA}}$FAST was previously observed in flow cytometry experiments, and conferred split $^{\text{RspA}}$gFAST(98-99) promising properties as an additional reporter of protein-protein interactions. These results nevertheless need to be confirmed by further association experiments, as well as complementary studies of the reversibility of this system upon dissociation.

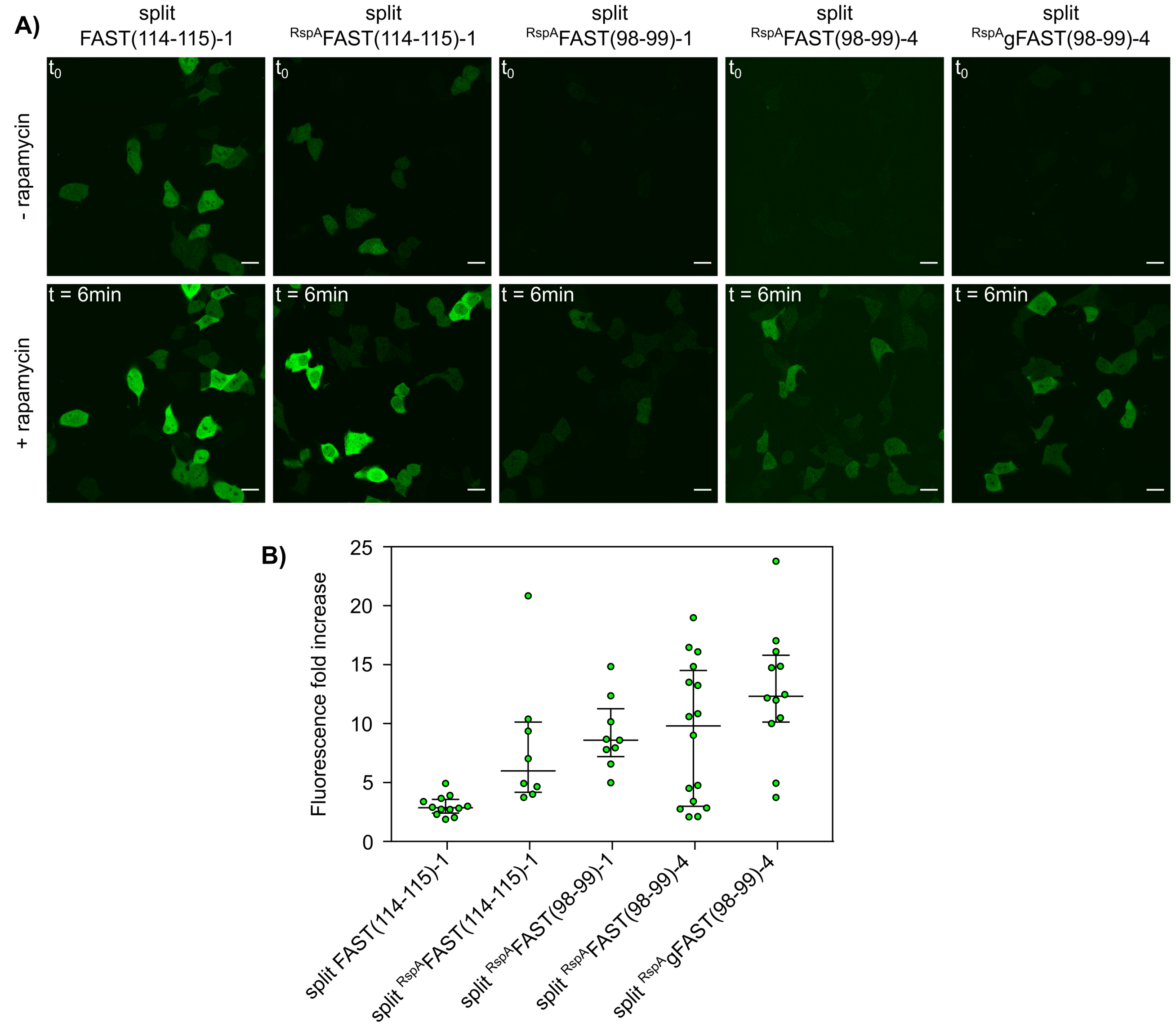

Figure VI-9. A) Confocal micrographs from a single-experiment of HEK293T cells co-expressing the FKBP/FRB system fused to either splitFAST(114-115)-1, split^{RspA}FAST(114-115)-1, split^{RspA}FAST(98-99)-1, split^{RspA}FAST(98-99)-4, split^{RspA}gFAST(98-99)-4, labeled with 10 µM HMBR, and imaged before and after addition of 500 nM of rapamycin. **B)** Fluorescence fold increase upon FRB–FKBP association for each reporter system. Lines indicate the medians, the 25th and 75th percentiles as calculated by Prism 7. SplitFAST(114-115)-1: *n* = 13 cells, split^{RspA}FAST(114-115)-1: *n* = 11 cells, split^{RspA}FAST(98-99)-1: *n* = 10 cells, split^{RspA}FAST(98-99)-4: *n* = 16 cells, split^{RspA}gFAST(98-99)-4: *n* = 12 cells from a single experiment. Scale bars, 20 µm.

Towards a semi-orthogonal system: $^{\text{RspA}}$greenFAST(98-99) vs redFAST(114-115)

The previously described splitting of the variants greenFAST and redFAST at position 114-115 allowed the generation of a spectrally orthogonal system able to probe sequential protein-protein interactions sharing a common interaction partner. They indeed shared a common fragment CFAST(115-125) and this feature could give rise to uncertainty in terms of complementation specificity for visualization of two co-localized and simultaneous protein-protein interactions. The identification of a new cleavage site at position 98-99, and its application to the optimized HMBR-selective FAST variant $^{\text{RspA}}$gFAST, foreshadowed the possible development of a split reporter pair with spectral and complementation orthogonality.

In order to determine whether the combination of two different FAST orthologs and two different split sites provided complementation orthogonality, we measured the signal intensity obtained from pairing either NFAST(1-114) or $^{\text{RspA}}$NFAST(1-98) to CFAST(115-125) or $^{\text{RspA}}$CFAST(99-125) in topology 1 at [HMBR] = 5 and 25 µM (Figure VI-10). Results from splitFAST(114-115) and split $^{\text{RspA}}$FAST(98-99) were consistent with previous observations in terms of brightness, dynamic range and self-assembly. As expected from the missing sequence of residues from Ser99 to Ser114, coupling $^{\text{RspA}}$NFAST(1-98) to CFAST(115-125) did not yield any fluorescent signal. Yet, substantial fluorescence and self-assembly arose from coupling NFAST(1-114) to $^{\text{RspA}}$CFAST(99-125). Indeed, the extra sequence $^{\text{RspA}}$FAST(99-114) did not seem to hamper interaction of the $^{\text{RspA}}$C-fragment with NFAST(1-114). On the contrary, the significant signal observed from unspecific reporter complementation suggested a substantial affinity between the two fragments. These results were also consistent with conclusions from the on-going split ortholog FAST studies (Rakotoarison & Tebo et al. in preparation), that yielded a high-affinity split system based on the strong interaction between NFAST(1-114) and $^{\text{RspA}}$CFAST(115-125).

In addition to the complementation semi-orthogonality, we next verified that the split redFAST(114-115) and split $^{\text{RspA}}$gFAST(98-99) reporter pair retained spectral orthogonality. To that aim, we measured the fluorescent signal from either HMBR or HBR-3,5DOM ([fluorogen] = 5 µM), in the presence or in the absence of the rapamycin-induced specific interaction of FRB fused to redNFAST(1-114), with FKBP fused to $^{\text{RspA}}$gNFAST(1-98) with CFAST(115-125) and $^{\text{RspA}}$CFAST(99-125). Complementation of the variants split redFAST(114-115) and split $^{\text{RspA}}$gFAST(98-99) indeed provided a spectrally orthogonal system, selectively binding HBR-3,5-DOM and HMBR, respectively. Coupling of $^{\text{RspA}}$gNFAST(1-98) to CFAST(115-125) yielded no fluorescence from either fluorogen, consistently with the missing residue sequence of the interacting reporter. Finally, we observed a strong and selective fluorescent signal from HBR-3,5-DOM upon interaction of redNFAST(1-114) with $^{\text{RspA}}$CFAST(99-125), attesting a substantial affinity between the two fragments.

Complete titration of HBR-3,5-DOM with FRB fused to redNFAST(1-114) interacting with FKBP fused to either CFAST(115-125) or ^{RspA}CFAST(99-125), in the presence and in the absence of rapamycin, allowed to confirm the aforementioned conclusions. Despite higher self-assembly observed from redNFAST(1-114)-^{RspA}CFAST(99-125), the concomitant affinity increase for HBR-3,5-DOM upon specific interaction allowed this combined system to provide a satisfying dynamic range (a 3.6-fold fluorescence increase was observed at [HBR-3,5-DOM] = 5 µM). It was thus expected to be a suitable split reporter as well for the visualization of protein-protein interactions

Table VI-7. Evaluation of the topological orthogonality. For each split reporter is given the dissociation constant in absence of rapamycin ($K_{\mathrm{D,HBR\text{-}3,5\text{-}DOM\text{-}rap}}$), in presence of 500 nM of rapamycin ($K_{\mathrm{D,HBR\text{-}3,5\text{-}DOM+rap}}$), and the dynamic range calculated as the ratio of the fluorescence intensities at 5 µM HBR-3,5-DOM.

split	$K_{\mathrm{D,HBR\text{-}3,5\text{-}DOM+rap}}$ (µM)	$K_{\mathrm{D,HBR\text{-}3,5\text{-}DOM–rap}}$ (µM)	Dynamic range (at [HBR-3,5-DOM] = 5 µM)
redFAST(114-115) top. 1	13 ± 4.6	77 ± 37	4.0
redNFAST(1-114) + ^{RspA}CFAST(99-125) top. 1	9.1 ± 1.1	38 ± 5.9	3.6

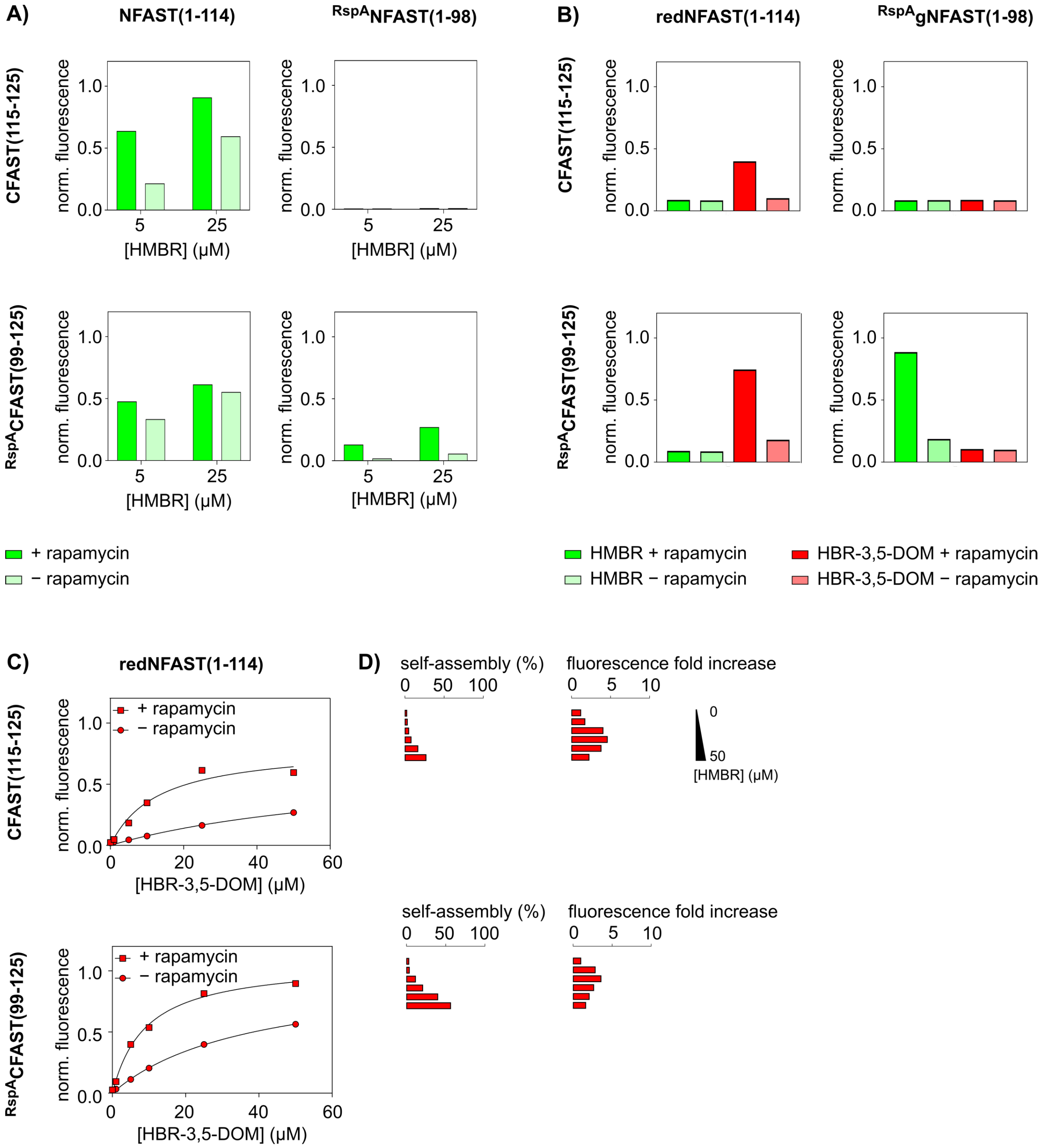

Figure VI-10. Orthogonality evaluation. A) Normalized average fluorescence of about 20,000 HEK293T cells co-expressing FRB fused to NFAST(1-114) or $^{\text{RspA}}$NFAST(1-98), and FKBP fused to CFAST(115-125) or $^{\text{RspA}}$CFAST(99-125) in topology 1, treated without (light green) or with (green) 500 nM rapamycin, and with 5, or 25 µM HMBR. **B)** Normalized average fluorescence of about 20,000 HEK293T cells co-expressing FRB fused to redNFAST(1-114) or $^{\text{RspA}}$gNFAST(1-98), and FKBP fused to CFAST(115-125) or $^{\text{RspA}}$CFAST(99-125) in topology 1, treated without (light) or with (bright) 500 nM rapamycin, and with 5 µM HMBR (green) or HBR-3,5-DOM (red). **C)** Normalized average fluorescence of about 20,000 HEK293T cells co-expressing FRB fused to redNFAST and FKBP fused to either CFAST(115-125) or $^{\text{RspA}}$CFAST(99-125), treated without (circle) or with (square) 500 nM of rapamycin, and with 0, 1, 5, 10, 25 or 50 µM of HBR-3,5-DOM. mTurquoise2 and iRFP670 were used as transfection reporters. Data represent the results from a single experiment. The least-squares fit (line) gave the thermodynamic dissociation constants $K_{\text{D,HBR-3,5-DOM+rap}}$ and $K_{\text{D,HBR-3,5-DOM-rap}}$ provided in Table VI-7. **D)** Dependence of the self-assembly and the association dynamic range (i.e. interaction-specific fluorescence fold increase) on the concentration of HMBR (from analysis shown in (C)).

VI.4. Discussion

Two new circularly permuted versions of FAST, cpFAST(24-25) and cpFAST(98-99), were identified and characterized as potential reporters for the rational design of biosensors, and their different properties could be exploited to address desirable biosensing features. On the one hand, cpFAST(24-25) showed a dramatic affinity loss for its cognate fluorogen, from an altered 3D structure of the tag failing to properly reconstitute. These observations were consistent with the recently described nanoFAST, a truncated version of the protein tag. In fact, truncation of the reporter N-terminal fragment yielded a modification of its binding cavity, thus compromising proper binding of HBR derivatives HMBR and HBR-3,5-DOM. cpFAST(24-25) could nevertheless be considered as a reporter in the design of biosensors. Indeed, we could imagine that coupling to a sensing module could yield a sensor with high dynamic range, supposing that interactions between the low-affinity fragments could be forced by conformational strain from the sensing domain, while providing low background. On the other hand, cpFAST(98-99) showed properties comparable to the previously reported cpFAST(114-115): it efficiently reconstituted into a functional tag with high affinity for the fluorogen when interaction between the protein fragments was allowed by a sufficient linker length and flexibility. It was consequently expected to behave similarly when inserted in biosensors, and a promising example was described in chapter III of this manuscript, in which a glutamate sensor was generated by inserting the sensing domain GltI in cpFAST(98-99).

The fruitful study of FAST circular permutations encouraged us to further investigate engineering of FAST for diverse biosensing opportunities. Splitting of FAST at position 98-99 combined with topological studies enabled to identify a new splitFAST version with lower brightness than the recently described splitFAST(114-115), but a promising higher dynamic range. The subsequent splitting of greenFAST and ^{RspA}FAST variants yielded several split reporters with improved properties, that were suitable for the visualization of protein-protein interactions. It should nevertheless be noted that the performances of each FKBP-FRB probing system was highly dependent on its topology. This parameter should consequently be kept in mind and carefully investigated when expanding the use of splitFAST(98-99) to other interacting protein partners.

This project also yielded the generation of a FAST mutant, ^{RspA}gFAST, by insertion of the green mutations G21E, P68T and G77R into ^{RspA}FAST. This selective reporter for HMBR would now require further biophysical characterization, and its full-length version is also expected to be a suitable reporter for fluorescence microscopy. Engineering and splitting this optimized variant ^{RspA}gFAST at the position 98-99 thus allowed to generate a new split reporter with high selectivity for HMBR, high dynamic range, low self-assembly and reasonable brightness. Moreover, combination of split ^{RspA}gFAST(98-99) and split redFAST(114-115) yielded a semi-orthogonal system, showing spectral orthogonality from selective binding to HMBR and HBR-3,5-DOM respectively, and complementation semi-orthogonality (Figure VI-11). Properties of this semi-orthogonal reporter pair will require confirmation as results presented in the last paragraph of this chapter originate from single experiments. Furthermore, preliminary results from ongoing flow cytometry experiments demonstrated the reversibility of the system, by evaluation of the rapamycin-induced dissociation of the FKBP-F36M homodimer. Observation by fluorescence microscopy of the association and dissociation of interacting protein partners fused to split ^{RspA}gFAST(98-99) is also currently being confirmed. Application of the split redFAST(114-115) / split ^{RspA}gFAST(98-99) reporter pair should be validated in fluorescence microscopy, for instance for the visualization of a protein-protein interaction cascade with several common interacting partners.

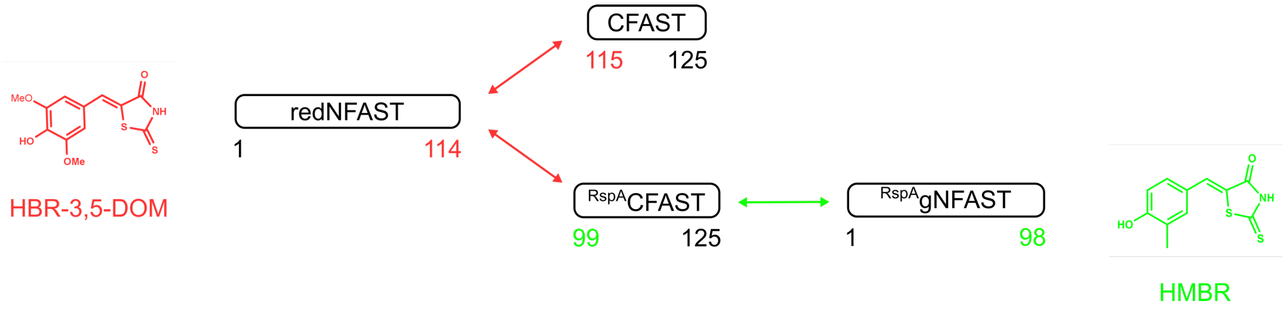

Figure VI-11. Schematic representation of the developed systems relying on two split fluorescent reporters showing spectral orthogonality and complementation semi-orthogonality.

In the aim of reliably visualizing co-localized and simultaneous protein-protein interactions, a reporter pair showing both spectral and complementation orthogonality remains desirable. This would notably require engineering of a rigid ^{RspA}CFAST(99-125) fragment, that would preclude its interaction with redNFAST(1-114). Further characterization of the different C-terminal fragments, notably by circular dichroism, followed by screening and optimization is expected to provide a fully orthogonal system. Finally, the identification of a second FAST cleavage site at position 98-99 represents an interesting step towards engineering of a tripartite splitFAST reporter, relying on the complementation of FAST(1-98), FAST(99-114) and FAST(115-125) fragments. These prospective reporter design opportunities thus open a wide range of new perspectives for chemogenetic biosensing applications.

VI.5. Material & methods

General

Synthetic oligonucleotides used for cloning were purchased from Integrated DNA Technology. PCR reactions were performed with Q5 polymerase (New England Biolabs) in the buffer provided. PCR products were purified using QIAquick PCR purification kit (Qiagen). Isothermal assemblies (Gibson assembly) were performed using homemade mix prepared according to previously described protocols (modified from the original described protocol).[26] Gibson products were purified using MinElute PCR purification kit (Qiagen). Gibson products were transformed in DH10 E. coli. Small-scale isolation of plasmid DNA was done using QIAprep miniprep kit (Qiagen) from 3 mL of overnight culture supplemented with appropriate antibiotics. Large-scale isolation of plasmid DNA was done using the QIAprep maxiprep kit (Qiagen) from 150 mL of overnight culture supplemented with appropriate antibiotics. All plasmid sequences were confirmed by Sanger sequencing with appropriate sequencing primers (GATC Biotech). The preparation of HMBR and HBR-3,5DOM was previously described.[23,27]

Protein expression and purification

Expression vectors of the glutamate biosensors with an N-terminal His-tag under the control of a T7 promoter were transformed in Rosetta(DE3)pLysS *Escherichia coli* competent cells. Bacterial cells were grown at 37 °C in Lysogeny Broth (LB) supplemented with chloramphenicol (34 µg/mL) and kanamycin (50 µg/mL) until OD_{600nm} = 0.6. Subsequent production and purification steps have been described in chapter III of this manuscript. The buffer was afterwards exchanged with HEPES buffer (HEPES 50 mM, $MgCl_2$ 75 mM pH 8) using PD-10 or PD-MidiTrap G-25 desalting columns (GE Healthcare). Purity of the proteins was evaluated using SDS-PAGE electrophoresis stained with Coomassie blue. The buffer was afterwards exchanged with HEPES buffer (HEPES 50 mM, NaCl 150 mM pH 8) using PD-10 or PD-MidiTrap G-25 desalting columns (GE Healthcare). Purity of the proteins was evaluated using SDS-PAGE electrophoresis stained with Coomassie blue.

Thermodynamic analysis

Determination of the thermodynamic constants by titration experiments were performed with a Spark 10M plate reader (Tecan) in HEPES buffer (HEPES 50 mM, NaCl 150 mM, pH 7.4). Normalized fluorescence intensity was plotted as a function of fluorogen concentration and fitted in GraphPad Prism 7 to a one-site specific binding model.

Mammalian cell culture

HEK 293T cells (ATCC CRL-3216) were cultured in Dulbecco's modified Eagle's medium (DMEM) supplemented with phenol red, Glutamax I, and 10% (vol/vol) fetal calf serum, at 37 °C in a 5% CO2 atmosphere.

Cell cytometry

Flow cytometry analysis were performed in 96-well plates on MACSQuant® Analyser equipped with three lasers (405 nm, 488 nm and 635 nm) and eight filters and channels. Transfected cells were pelleted by centrifugation, washed with PBS-BSA (1mg/ml) and treated with 0, 1, 5, 10, 25, 50 mM of fluorogen and ± 500 nM of rapamycin (final volume of the cell suspension 200 mL). Cells expressing only mTurquoise2, IRF670 and FAST were used to adjust PMT voltage and compensation. Data were analyzed using FlowJo_v10.7.1.

Fluorescence microscopy

Confocal micrographs of mammalian cells were acquired on a Leica TCS SP5 confocal laser scanning microscope equipped with a 63×/ 1.4 NA oil immersion objective. Live cells were washed twice with DPBS (Dulbecco’s Phosphate-Buffered Saline), immediately prior to imaging. DMEM media (without serum and phenol red) containing the fluorogens at the indicated concentration was added to the cells. The cells were imaged directly without washing. Leica LAS AF software was used to collect the data. The images were analyzed with Fiji (Image J).

Sequences

Protein sequence of FAST:
EHVAFGSEDIENTLAKMDDGQLDGLAFGAIQLDGDGNILQYNAAEGDITGRDPKQVIGKNFFKDVA
PGTDSPEFYGKFKEGVASGNLNTMFEWMIPTSRGPTKVKVHMKKALSGDSYWVFVKRV

Protein sequence of ^{RspA}FAST:
ETVRFGGDDIENSLAKMDDKALDKLAFGAIQLDGNGKIIHYNAAEGTITGRDPKTVIGKNFFTDVAP
GTQSKEFQGRFKEGVQKGDLNTMFEWMIPTSRGPTKVKIHMKKAMTGDSFWIFVKRL

Protein sequence of greenFAST:
EHVAFGSEDIENTLAKMDDEQLDGLAFGAIQLDGDGNILQYNAAEGDITGRDPKQVIGKNFFKDVA
TGTDSPEFYRKFKEGVASGNLNTMFEWMIPTSRGPTKVKVHMKKALSGDSYWVFVKRV

Protein sequence of ^{RspA}gFAST:
ETVRFGGDDIENSLAKMDDEALDKLAFGAIQLDGNGKIIHYNAAEGTITGRDPKTVIGKNFFTDVAT
GTQSKEFQRRFKEGVQKGDLNTMFEWMIPTSRGPTKVKVHMKKAMTGDSFWIFVKRL

Protein sequence of cpFAST(24-25):
GLAFGAIQLDGDGNILQYNAAEGDITGRDPKQVIGKNFFKDVAPGTDSPEFYGKFKEGVASGNLNT
MFEWMIPTSRGPTKVKIHMKKALSGDSYWVFVKRV**linker**EHVAFGSEDIENTLAKMDDGQLD

Protein sequence of cpFAST(35-36):
GDGNILQYNAAEGDITGRDPKQVIGKNFFKDVAPGTDSPEFYGKFKEGVASGNLNTMFEWMIPTSRGPTKVKIHMKKALSGDSYWVFVKRV**linker**EHVAFGSEDIENTLAKMDDGQLDGLAFGAIQLDG

Protein sequence of cpFAST(59-60):
GKNFFKDVAPGTDSPEFYGKFKEGVASGNLNTMFEWMIPTSRGPTKVKIHMKKALSGDSYWVFVKRV**linker**EHVAFGSEDIENTLAKMDDGQLDGLAFGAIQLDGDGNILQYNAAEGDITGRDPKQVIG

Protein sequence of cpFAST(72-73):
PEFYGKFKEGVASGNLNTMFEWMIPTSRGPTKVKIHMKKALSGDSYWVFVKRV**linker**EHVAFGSEDIENTLAKMDDGQLDGLAFGAIQLDGDGNILQYNAAEGDITGRDPKQVIGKNFFKDVAPGTDS

Protein sequence of cpFAST(89-90):
TMFEWMIPTSRGPTKVKIHMKKALSGDSYWVFVKRV**linker**EHVAFGSEDIENTLAKMDDGQLDGLAFGAIQLDGDGNILQYNAAEGDITGRDPKQVIGKNFFKDVAPGTDSPEFYGKFKEGVASGNLN

Protein sequence of cpFAST(98-99):
SRGPTKVKIHMKKALSGDSYWVFVKRV**linker**EHVAFGSEDIENTLAKMDDGQLDGLAFGAIQLDGDGNILQYNAAEGDITGRDPKQVIGKNFFKDVAPGTDSPEFYGKFKEGVASGNLNTMFEWMIPT

Protein sequence of cpFAST(103-104):
TKVKIHMKKALSGDSYWVFVKRV**linker**EHVAFGSEDIENTLAKMDDGQLDGLAFGAIQLDGDGNILQYNAAEGDITGRDPKQVIGKNFFKDVAPGTDSPEFYGKFKEGVASGNLNTMFEWMIPTSRGP

Protein sequence of cpFAST(114-115):
GDSYWVFVKRV**linker**EHVAFGSEDIENTLAKMDDGQLDGLAFGAIQLDGDGNILQYNAAEGDITGRDPKQVIGKNFFKDVAPGTDSPEFYGKFKEGVASGNLNTMFEWMIPTSRGPTKVKVHMKKALS

Linkers sequence:

TEV : ENLYFQGGSGG
Linker 5 : GGSGGSGGSGG
Linker 4 : GGSGGSGG
Linker 3 : GGSGG
Linker 2 : GGS
Linker1 : -

Molecular cloning

The plasmid pAG398, encoding CMV-FAST(V107I)-Tev-FAST(V107I)-myc, was constructed by Gibson assembly from the plasmid pAG328 encoding CMV-td-iFAST-myc. The original plasmid was amplified by PCR using the primer ag576, containing the sequence coding for the Tev linker to be inserted. The fragment coding for Tev-FAST(V107)I-2 was amplified using primers ag576/ag314. The fragment coding for FAST(V107)I-1 was amplified using primers ag597/ag313. The two fragments were then assembled by Gibson assembly.

The plasmid pAG404, encoding pET28new-His-CFAST(25-125)-Tev-NFAST(1-24), was constructed by Gibson assembly from the plasmid pAG398 encoding CMV-FAST(V107I)-Tev-FAST(V107I)-myc. The sequence coding for FAST(25-125)-Tev-FAST(1-24) was amplified by PCR from the plasmid pAG398 using primers ag645/ag646. The pET26new backbone was amplified in two fragments using primers ag578/kanR and 579/kanF. The three fragments were then assembled by Gibson assembly.

Similarly, the plasmids pAG405-410 were constructed by Gibson assembly from the plasmid pAG398 encoding CMV-FAST(V107I)-Tev-FAST(V107I)-myc. The sequence coding for FAST(XX-125)-Tev-FAST(1-XX) were amplified by PCR from the plasmid pAG398 using primers ag584/ag585, ag586/ag587, ag588/ag589, ag590/ag591, ag592/ag593 and ag594/595. The three fragments were then assembled by Gibson assembly.

The plasmid pAG473, encoding pET28new-His-CFAST(25-125)-GGSGGSGGSGG-NFAST(1-24), was constructed by Gibson assembly from the plasmid pAG404. The original plasmid was amplified by PCR using the primer ag686, containing the sequence coding for the GGS linker to be inserted. The fragment coding for NFAST(1-24) was amplified using primers ag686/kanR. The fragment coding for CFAST(25-125) was amplified using primers ag682/kanF. The two fragments were then assembled by Gibson assembly.

Similarly, the plasmids pAG475, pAG478, pAG480 and pAG482 were constructed by Gibson assembly from the plasmid pAG404. The original plasmid was amplified by PCR using the primer ag685, ag684, ag683 and ag682 respectively, containing the sequence coding for the GGS linker to be inserted. The fragment coding for NFAST(1-24) was amplified using primers ag686/kanR, ag684/kanR, ag683/kanR and ag691/kanR respectively. The fragment coding for CFAST(25-125) was amplified using primers ag682/kanF. The two fragments were then assembled by Gibson assembly.

The plasmid pAG474, encoding pET28new-His-CFAST(99-125)-GGSGGSGGSGG-NFAST(1-98), was constructed by Gibson assembly from the plasmid pAG409. The original plasmid was amplified by PCR using the primer ag686, containing the sequence coding for the GGS linker to be inserted. The fragment coding for NFAST(1-98) was amplified using primers ag686/kanR. The fragment coding for CFAST(99-125) was amplified using primers ag682/kanF. The two fragments were then assembled by Gibson assembly.

Similarly, the plasmids pAG476, pAG479, pAG481 and pAG483 were constructed by Gibson assembly from the plasmid pAG409. The original plasmid was amplified by PCR using the primer ag685, ag684, ag683 and ag682 respectively, containing the sequence coding for the GGS linker to be inserted. The fragment coding for NFAST(1-98) was amplified using primers ag686/kanR, ag684/kanR, ag683/kanR and ag691/kanR respectively. The fragment coding for CFAST(99-125) was amplified using primers ag682/kanF. The two fragments were then assembled by Gibson assembly.

The plasmid pAG800, encoding CMV-FRB-NFAST(1-98)-IRES-mT2, was constructed by Gibson assembly from the plasmid pAG570 encoding CMV-FRB-NFAST(1-114)-IRES-mT2. The fragment coding for FRB-NFAST(1-98) was amplified by PCR using the primers ag313/1150. The fragment coding for IRES-mT2 was amplified by PCR using the primers ag314/694. The two fragments were then assembled by Gibson assembly.

The plasmid pAG801, encoding CMV-FRB-greenNFAST(1-98)-IRES-mT2, was constructed by Gibson assembly from the plasmid pAG570 encoding CMV-FRB-NFAST(1-114)-IRES-mT2. The fragment coding for FRB was amplified by PCR using the primers ag313/374. The fragment coding for IRES-mT2 was amplified by PCR using the primers ag314/694. The insert coding for greenNFAST(1-98) was amplified by PCR from the plasmid pAG464 encoding pET28a-His-TEV-greenNFAST(1-114), using the primers ag175/1150. The three fragments were then assembled by Gibson assembly.

The plasmid pAG802, encoding CMV-FKBP-CFAST(99-125)-IRES-iRFP670, was constructed by Gibson assembly from the plasmid pAG577 encoding CMV-FKBP-CFAST11-IRES-iRFP670. The fragment coding for FKBP was amplified by PCR using the primers ag313/1237. The fragment coding for CFAST(99-125)-IRES-iRFP670 was amplified by PCR using the primers ag314/1236. The two fragments were then assembled by Gibson assembly.

The plasmids pAG903 and pAG904, encoding CMV-CFAST(99-125)-FRB-IRES-iRFP670 and CMV-$^{\mathrm{RspA}}$CFAST(99-125)-FRB-IRES-iRFP670 respectively, were constructed by Gibson assembly from the plasmid pAG802. The CMV backbone was amplified by PCR using the primers ag313/358. The fragment coding for IRES-iRFP670 was amplified by PCR using the primers ag314/694. The inserts coding for CFAST(99-125)-FRB or $^{\mathrm{Rspa}}$CFAST(99-125)-FRB were amplified by PCR from the plasmid pAG142 encoding CMV-CFAST(66-125)-linker-FRB-myc using the primers ag699/1386, or originated from a synthetic gene, respectively. The three fragments were then assembled by Gibson assembly.

The plasmids pAG905 and pAG906, encoding CMV-FKBP-NFAST(1-98)-IRES-mT2 and CMV-FKBP-greenNFAST(1-98)-IRES-mT2 respectively, were constructed by Gibson assembly from the plasmid pAG802. The fragment coding for FKBP was amplified by PCR using the primers ag313/1040. The fragment coding for NFAST(1-98)-IRES-mT2 or greenNFAST(1-98)-IRES-mT2 were amplified by PCR from the plasmids pAG800 or pAG801, respectively, using the primers ag314/1042. The two fragments were then assembled by Gibson assembly

The plasmid pAG907, encoding CMV-FKBP-$^{\mathrm{RspA}}$NFAST(1-98)-IRES-mT2, was constructed by Gibson assembly from the plasmid pAG802. The fragment coding for FKBP was amplified by PCR using the primers ag313/1040. The fragment coding for IRES-mT2 was amplified by PCR from the plasmid pAG800 using the primers ag314/694. The insert coding for $^{\mathrm{Rspa}}$NFAST(1-98) was amplified by PCR from the plasmid pAG573 encoding CMV-FRB-$^{\mathrm{RspA}}$NFAST(1-114)-IRES-mT2 using the primers ag1042/1385. The three fragments were then assembled by Gibson assembly.

The plasmids pAG908 and pAG909, encoding pET28new-His-O3greenFAST and pET28new-His-O3redFAST respectively, by inserting the sequence coding for the FAST mutant (synthetic gene) between *Nhe* I and *Xho* I restriction in a pET28a plasmid.

The plasmid pAG934, encoding CMV-FRB-CFAST(99-125)-IRES-iRFP670, was constructed by Gibson assembly from the plasmid pAG903. The fragment coding for CFAST(99-125)-IRES-iRFP670 was amplified by PCR using the primers ag1416/314. The fragment coding for FRB was amplified from pAG490 encoding FRB-NFAST-IRES-mT2 using the primers ag313/374. The two fragments were then assembled by Gibson assembly.

The plasmid pAG935, encoding CMV-NFAST(1-98)-FRB-IRES-mT2, was constructed by Gibson assembly from the plasmid pAG104 encoding CMV-FAST. The fragment coding for NFAST(1-98) was amplified by PCR using the primers ag313/1417. The fragment coding for FRB was amplified by PCR from the plasmid pAG903 using the primers ag1063/699. The fragment coding for IRES-mT2 was amplified by PCR from the plasmid pAG907 using the primers ag694/314. The three fragments were then assembled by Gibson assembly.

The plasmid pAG972, encoding CMV-greenNFAST(1-98)-FRB-IRES-mT2, was constructed by Gibson assembly from the plasmid pAG364 encoding CMV-greenFAST. The fragment coding for greenNFAST(1-98) was amplified by PCR using the primers ag313/1417. The fragment coding for FRB-IRES-mT2 was amplified by PCR from the plasmid pAG935 using the primers ag1063/314. The two fragments were then assembled by Gibson assembly.

The plasmid pAG973, encoding CMV-^{RspA}gNFAST(1-98)-FRB-IRES-mT2, was constructed by Gibson assembly from the plasmid pAG935. The CMV backbone was amplified by PCR using the primers ag313/358. The fragment coding for FRB-IRES-mT2 was amplified by PCR using the primers ag1063/314. The fragment coding for ^{RspA}gNFAST(1-98) was amplified by PCR from the plasmid pAG908 using the primers ag1357/1472. The three fragments were then assembled by Gibson assembly.

The plasmid pAG974 encoding CMV-FKBP-^{RspA}CFAST(99-125)-IRES-iRFP670 was constructed by Gibson assembly from the plasmid pAG802. The fragment coding for FKBP was amplified by PCR using the primers ag313/374. The fragment coding for IRES-iRFP670 was amplified by PCR from the plasmid pAG934, using the primers ag694/314. The insert coding for ^{RspA}CFAST(99-125) was amplified by PCR from the plasmid pAG908 using the primers ag1473/1474. The three fragments were then assembled by Gibson assembly.

The plasmid pAG975, encoding CMV-FRB-^{RspA}gNFAST(1-98)-IRES-mT2 was constructed by Gibson assembly from the plasmid pAG801. The fragment coding for FRB was amplified by PCR using the primers ag313/374. The fragment coding for IRES-mT2 was amplified by PCR using the primers ag694/314. The insert coding for ^{RspA}gNFAST(1-98) was amplified by PCR from the plasmid pAG908 using the primers ag766/1475. The three fragments were then assembled by Gibson assembly.

The plasmid pAG1009, encoding CMV-FRB-^{RspA}NFAST(1-98)-IRES-mT2, was constructed by Gibson assembly from the plasmid pAG907. The fragment coding for ^{RspA}NFAST(1-98)-IRES-mT2 was amplified by PCR using the primers ag314/766. The fragment coding for FRB was amplified by PCR from the plasmid pAG934 using the primers ag313/374. The two fragments were then assembled by Gibson assembly.

The plasmid pAG1010, encoding CMV-FRB-redNFAST(1-114)-IRES-mT2, was constructed by Gibson assembly from the plasmid pAG907. The fragment coding for IRES-mT2 was amplified by PCR using the primers ag314/694. The fragment coding for FRB-redNFAST(1-114) was amplified by PCR from the plasmid pAG461 encoding CMV-FRB-redNFAST(1-114) using the primers ag313/374. The two fragments were then assembled by Gibson assembly.

The plasmid pAG1093, encoding CMV-FRV-^{RspA}gNFAST(1-114)-IRES-mT2, was constructed by Gibson assembly from the plasmid pAG975. The fragment coding for FRB was amplified by PCR using the primers ag313/374. The fragment coding for IRES-mT2 was amplified by PCR using the primers ag694/314. The insert coding for ^{RspA}gNFAST(1-114) was amplified by PCR from the plasmid pAG908 using the primers ag766/769. The three fragments were then assembled by Gibson assembly.

The plasmid pAG1095, encoding CMV-^{RspA}NFAST(1-98)-FRB-IRES-mT2, was constructed by Gibson assembly from the plasmid pAG973. The CMV backbone was amplified by PCR using the primers ag313/358. The fragment coding for FRB-IRES-mT2 was amplified by PCR using the primers ag413/314. The fragment coding for ^{RspA}NFAST(1-98) was amplified by PCR from the plasmid pAG1009 using the primers ag1354/1472. The three fragments were then assembled by Gibson assembly.

Plasmid	**From**	**Primers**
pAG398	pAG328	ag313, 314, 576, 597
pAG404	pAG398	ag645, 646, 578, 579, 580, 581
pAG405	pAG398	ag584, 585, 578, 579, 580, 581
pAG406	pAG398	ag586, 587, 578, 579, 580, 581
pAG407	pAG398	ag588, 589, 578, 579, 580, 581
pAG408	pAG398	ag590, 591, 578, 579, 580, 581
pAG409	pAG398	ag592, 593, 578, 579, 580, 581
pAG410	pAG398	ag594, 595, 578, 579, 580, 581
pAG473	pAG404	ag682, 686, kanF, kanR
pAG474	pAG404	ag682, 686, kanF, kanR
pAG475	pAG404	ag682, 685, kanF, kanR
pAG476	pAG404	ag682, 685, kanF, kanR
pAG478	pAG404	ag682, 684, kanF, kanR
pAG479	pAG409	ag682, 684, kanF, kanR
pAG480	pAG409	ag682, 683, kanF, kanR
pAG481	pAG409	ag682, 683, kanF, kanR
pAG482	pAG409	ag682, 691, kanF, kanR
pAG483	pAG409	ag682, 691, kanF, kanR
pAG800	pAG570	ag313, 314, 694, 1150
pAG801	pAG571	ag175, 313, 314, 374, 694, 1150
pAG802	pAG577	ag313, 314, 1236, 1237
pAG903	pAG142 + pAG802	ag313, 314, 358, 694, 699, 1386
pAG904	pAG802 + synthetic gene	ag313, 314, 358, 694
pAG905	pAG800	ag313, 314, 1040, 1042
pAG906	pAG801	ag313, 314, 1040, 1042
pAG907	pAG800	ag313, 314, 694, 1040, 1042, 1385
pAG908	pET28new + synthetic gene	NheI/XhoI
pAG909	pET28new + synthetic gene	NheI/XhoI
pAG934	pAG490 + pAG903	ag313, 314, 374, 1416
pAG935	pAG104 + pAG903 + pAG907	ag313, 314, 694, 699, 1063, 1417
pAG972	pAG364 + pAG935	ag313, 314, 1063, 1417
pAG973	pAG908 + pAG935	ag313, 314, 358, 1063, 1354, 1472
pAG974	pAG802 + pAG908 + pAG934	ag313, 314, 374, 694, 1473, 1474
pAG975	pAG801 + pAG908	ag313, 314, 374, 694, 766, 1475
pAG1009	pAG903 + pAG907	ag313, 314, 374, 766
pAG1010	pAG800 + pAG461	ag313, 314, 694, 1423
pAG1093	pAG975 + pAG908	ag313, 314, 374, 694, 766, 769
pAG1095	pAG973 + pAG1009	ag313, 314, 358, 413, 1354, 1472

Primer	Sequence
kanf	gcatcaaccaaaccgttattcattcgtg
kanr	cacgaatgaataacggtttggttgatgc
ag175	gcagcggcggagggggatccatggagcatgttgcctttggc
ag313	ctcaccttgctcctgccgagaaagtatcca
ag314	tggatactttctcggcaggagcaaggtgag
ag358	ggtggcagatctgagtccggtag
ag374	ggatccccctccgccgctgccgcctcctccgga
ag413	tccggaggaggcggc
ag576	aacctgtattttcagggcggctccggcggcgaacacgttgcctttggctctgagg
ag578	taatgactcgagcaccaccaccacc
ag579	catgctagccatatggctgccg
ag580	gcctagagcaagacgtttcccgttgaatatg
ag581	attcaacgggaaacgtcttgctctaggc
ag584	ggcagccatatggctagcatggacggtaatattctccagtacaatgcag
ag585	ggtggtggtgctcgagtcattagccgtcaagctgtatggc
ag586	ggcagccatatggctagcatgaagaatttcttcaaagatgttgctcccg
ag587	ggtggtggtgctcgagtcattagccaataacctgttttggatcgc
ag588	ggcagccatatggctagcatgcctgagttttacgggaagttcaaagag
ag589	ggtggtggtgctcgagtcattaagagtcagtcccgggtg
ag590	ggcagccatatggctagcatgactatgttcgaatggatgataccgacaag
ag591	ggtggtggtgctcgagtcattaattaagattgccagatgccaccc
ag592	ggcagccatatggctagcatgagcagaggcccaaccaag
ag593	ggtggtggtgctcgagtcattaagtaggaatcatccattcaaacattgtattaagattgc
ag594	ggcagccatatggctagcatgaccaaggtaaaaattcatatgaagaaagctctgtc
ag595	ggtggtggtgctcgagtcattatggtcctctactagtaggaatcatccattc
ag597	ggagccgccctgaaaatacaggttttcgactctcttcacaaacaccc
ag645	ggcagccatatggctagcatgggcttggcattcggggccattc
ag646	ggtggtggtgctcgagtcattaatccagctgaccgtcatccattttgg
ag682	gactctcttcacaaacacccaataag
ag683	gggtgtttgtgaagagagtcggcggctccgaacacgttgcctttggc
ag684	gggtgtttgtgaagagagtcggcggctccggcggcgaacacgttgcctttggc
ag685	gggtgtttgtgaagagagtcggcggctccggcggctccggcggcgaacacgttgcctttggc
ag686	gggtgtttgtgaagagagtcggcggctccggcggctccggcggctccggcggcgaacacgttgcctttggc
ag691	gggtgtttgtgaagagagtcgaacacgttgcctttggctc
ag694	taactcgaggactacaaggacgacg
ag699	cgtcgtccttgtagtcctcgagttacaagtcctcttcagaaataagcttttgttc
ag766	gcagcggcggagggggatccatggagaccgtgagattcggcg
ag769	cgtcgtccttgtagtcctcgagttaggtcatggccttcttcatgtgcac
ag1040	ccgctgccgcctcctccggattcttccagttttagaagctcc
ag1042	gagcttctaaaactggaagaatccggaggaggcggcag
ag1063	tccggaggaggcggcag
ag1150	cgtcgtccttgtagtcctcgagttatgtcggtatcatccattcgaac
ag1236	caaggtcaaggtgcacatgaagaaagccctttccggtgacagctattgggtctttg
ag1237	tcatgtgcaccttgaccttggttggtcccctgctggatccccctccgccgc
ag1354	ccggactcagatctgccaccatggagaccgtgagattcggcgg

ag1385	ccttgtagtcctcgagttaggtggggatcatccactcg
ag1386	ctcagatctgccaccatgagcaggggaccaaccaag
ag1416	cagcggcggagggggatccagcaggggaccaaccaag
ag1417	cgctgccgcctcctccggatgtcggtatcatccattcgaacatg
ag1423	cttgtagtcctcgagttaggaaagggctttcttcatgtgc
ag1472	gctgccgcctcctccggaggtggggatcatccactcg
ag1473	agcggcggagggggatccagcagaggccccaccaag
ag1474	gtccttgtagtcctcgagttacagtctcttcacgaagatccagaagc
ag1475	cttgtagtcctcgaggttaggtggggatcatccactcg

VI.6. References

1. Baird, G. S., Zacharias, D. A. & Tsien, R. Y. Circular permutation and receptor insertion within green fluorescent proteins. *Proc. Natl. Acad. Sci. U. S. A.* **96**, 11241–11246 (1999).
2. Nakai, J., Ohkura, M. & Imoto, K. A high signal-to-noise Ca(2+) probe composed of a single green fluorescent protein. *Nat. Biotechnol.* **19**, 137–141 (2001).
3. Tian, L. *et al.* Imaging neural activity in worms, flies and mice with improved GCaMP calcium indicators. *Nat. Methods* **6**, 875–881 (2009).
4. Chen, T.-W. *et al.* Ultrasensitive fluorescent proteins for imaging neuronal activity. *Nature* **499**, 295–300 (2013).
5. Molina, R. S. *et al.* Understanding the Fluorescence Change in Red Genetically Encoded Calcium Ion Indicators. *Biophys. J.* **116**, 1873–1886 (2019).
6. Liu, W. *et al.* Genetically encoded single circularly permuted fluorescent protein-based intensity indicators. *J. Phys. D. Appl. Phys.* **53**, (2020).
7. To, T. L. *et al.* Rationally designed fluorogenic protease reporter visualizes spatiotemporal dynamics of apoptosis in vivo. *Proc. Natl. Acad. Sci. U. S. A.* **112**, 3338–3343 (2015).
8. Deo, C. *et al.* The HaloTag as a general scaffold for far-red tunable chemigenetic indicators. *Nat. Chem. Biol.* **17**, 718–723 (2021).
9. Kumar, A., Burns, D. C., Al-Abdul-Wahid, M. S. & Woolley, G. A. A circularly permuted photoactive yellow protein as a scaffold for photoswitch design. *Biochemistry* **52**, (2013).
10. Tebo, A. G. *et al.* Circularly Permuted Fluorogenic Proteins for the Design of Modular Biosensors. *ACS Chem. Biol.* **13**, 2392–2397 (2018).
11. Wiens, M. D. & Campbell, R. E. Surveying the landscape of optogenetic methods for detection of protein-protein interactions. *Wiley Interdiscip. Rev.: Syst. Biol. Med.* **10**, (2018).
12. Cabantous, S., Terwilliger, T. C. & Waldo, G. S. Protein tagging and detection with engineered self-assembling fragments of green fluorescent protein. *Nat. Biotechnol.* **23**, 102–107 (2005).
13. Pedelacq, J. D. & Cabantous, S. Development and applications of superfolder and split fluorescent protein detection systems in biology. *Int. J. Mol. Sci.* **20**, (2019).
14. Cabantous, S. *et al.* A new protein-protein interaction sensor based on tripartite split-GFP association. *Sci. Rep.* **3**, 2854 (2013).
15. Shcherbakova, D. M. *et al.* Bright monomeric near-infrared fluorescent proteins as tags and biosensors for multiscale imaging. *Nat. Commun.* **7**, 12405 (2016).
16. Tchekanda, E., Sivanesan, D. & Michnick, S. W. An infrared reporter to detect spatiotemporal dynamics of protein-protein interactions. *Nat. Methods* **11**, 641–644 (2014).
17. To, T. L., Zhang, Q. & Shu, X. Structure-guided design of a reversible fluorogenic reporter of protein-protein interactions. *Protein Sci.* **25**, 748–753 (2016).
18. Bozhanova, N. G., Gavrikov, A. S., Mishin, A. S. & Meiler, J. DiB-splits: nature-guided design of a novel fluorescent labeling split system. *Sci. Rep.* **10**, 1–11 (2020).
19. Tebo, A. G. & Gautier, A. A split fluorescent reporter with rapid and reversible complementation. *Nat. Commun.* **10**, 2822 (2019).
20. Tebo, A. G. *et al.* Orthogonal fluorescent chemogenetic reporters for multicolor imaging. *Nat. Chem. Biol.* **17**, 30–38 (2021).
21. Iwakura, M., Nakamura, T., Yamane, C. & Maki, K. Systematic circular permutation of an entire protein reveals essential folding elements. *Nat. Struct. Biol.* **7**, 580–585 (2000).
22. Lo, W. C. *et al.* CPred: A web server for predicting viable circular permutations in proteins. *Nucleic Acids Res.* **40**, 232–237 (2012).
23. Plamont, M.-A. *et al.* Small fluorescence-activating and absorption-shifting tag for tunable protein imaging in vivo. *Proc. Natl. Acad. Sci.* **113**, 497–502 (2016).
24. Mineev, K. S. *et al.* NanoFAST: Structure-based design of a small fluorogen-activating protein with only 98 amino acids. *Chem. Sci.* **12**, 6719–6725 (2021).
25. Tebo, A. G. *et al.* Circularly Permuted Fluorogenic Proteins for the Design of Modular Biosensors. *ACS Chem. Biol.* **13**, 2392–2397 (2018).
26. Gibson, D. G. *et al.* Enzymatic assembly of DNA molecules up to several hundred kilobases. *Nat. Methods* **6**, 343–5 (2009).
27. Li, C. *et al.* Dynamic multicolor protein labeling in living cells. *Chem. Sci.* **8**, 5598–5605 (2017).

Chapter VII

General discussion

VII.1. Generalization of biosensors design based on FAST and its variants

Throughout the development of various chemogenetic biosensors based on FAST for the detection of biologically relevant analytes, we have confirmed the hypothesis of a possible allosteric coupling between our fluorogenic reporter and a recognition module undergoing a conformational change upon analyte binding. The exploration of different conception strategies to identify a general design of FAST-based biosensors yielded to large differences of behaviour between the tested systems, depending on various parameters.

First, intrinsic properties of the sensing domain appeared to highly determine the significance of the allosteric coupling observed from the corresponding biosensor. This parameter was expected to be a key factor towards the generalization of FAST-based sensors relying on a single-protein sensing domain (contrary to FAST-based Ca^{2+} sensors, in which the sensing module was composed of domains from two interacting proteins calmodulin/M13).[1,2] Although convenient in terms of design, this constraint required the identification of proteins showing a large structural change between their analyte-bound and -free forms.

Subsequent study of the connectivity between protein domains also highlighted the importance of topological screening: indeed, changing the topological variant of FAST or the insertion strategy between the sensing and the reporter domain, have demonstrated to significantly influence the resulting allosteric modulation. Although involving substantial preliminary studies in the biosensor development process, this step has proven essential to identify functional topological variants. It also turned out to be useful in the identification of various sensors based on the same components with different thermodynamic and optical properties (this was notably demonstrated in the design of ATP-FASTs, described in chapter V). The most promising topology of our three FAST-based biosensors for the detection of glutamate, K^+ ions and ATP, all consisted in the insertion of the native analyte-binding protein into FAST or cpFAST. This was an encouraging observation towards the aim of generalizing our design of chemogenetic sensors, as it does not require engineering of the sensing domain to identify an insertion site for the reporter.

Interestingly, insertion of the ATP sensing domain *B.* PS3 ε into FAST or cpFAST directly yielded ATP biosensors with suitable selectivity and dynamic range, without the need for any further protein engineering. Benefitting from a significant negative allosteric modulation, this system allowed us to fully explore the opportunities offered by the design of chemogenetic sensors based on FAST, notably in terms of modularity. This characterization will be presented in a research article entitled “Allosteric fluorogenic protein sensors for the detection of biological analytes” (Broch F., El Hajji L., Pietrancosta N. and Gautier A., manuscript in preparation). It was envisioned that extending our study of the different tunable factors, by inserting different FAST variants or evaluate the fluorescence response from other fluorogens, would provide a palette of ATP-FASTs with modular optical and thermodynamic properties.

However, development of both Glu-FAST and K^+-FAST yielded systems with moderate dynamic range, that could barely be improved despite a number of optimization strategies. Similar parameters were identified to influence the performance of single-FP sensors and our chemogenetic biosensors. The position of the reporter's termini relative to the chromophore (or its binding site), often requiring the circular permutation of the fluorescent protein (or protein tag), is obviously crucial to modulate the fluorescent signal upon analyte-binding to a coupled sensing domain. In addition to the identification of a suitable insertion position, addition and optimization of linkers at the connecting sites is usually necessary to improve the fluorescence dynamic range.[3] Although often time- and effort-intensive, rational or random mutagenesis of linkers followed by high-throughput screening has proven very useful in the design of intensiometric fluorescent protein sensors, and is a relatively common and optimized process.[4]

Significantly less examples from the optimization of hybrid systems have been reported, as the addition of a synthetic compound involves a number of additional considerations to take into account for screening. A library of RNA aptamer biosensors for theophylline could for instance be amplified using PCR droplets, that were subsequently evaluated and sorted upon analyte-dependent fluorescence activation using a microfluidic device. This process interestingly combined several rounds of positive and negative selection to identify systems with high affinity and dynamic range.[5] Microfluidics have also been reported to allow cell sorting based on the fluorescence signal from a genetically encoded biosensor.[6,7] However, analogous screening of hybrid systems for biosensing with a protein recognition module would require further optimization. More commonly used screening methods require either purification prior to evaluation in microwell-plates.[8] Screening of surface-displayed hybrid biosensors also appears possible, after preliminary characterizations to identify suitable experimental conditions.

The necessity for efficient membrane-targeting for improved design and applications of our FAST-based sensors indeed represents a substantial issue. Genetically encoded or chemogenetic biosensors are in fact complex protein chimeras that need to display high flexibility to undergo significant conformational change upon analyte binding, while their structural features need to provide sufficient stability and solubility for proper expression. Completion of the secretion pathway to the plasma membrane can be particularly challenging: for instance, optimization of iATPSnFR required the replacement of eGFP to the superfolding sfGFP to be correctly exported to the membrane of mammalian cells.[9] In our case, the apparent improved solubility of our mCherry-ATP-FAST biosensors overexpressed in bacteria represents a promising perspective for improved trafficking in mammalian cells. Nevertheless, in the event of unsuccessful membrane-expression of the FAST-based sensors fused to mCherry, other targeting strategies may be envisioned. Recent examples of exogenous targeting of fluorescent biosensors to the membrane of neurons were reported by fusion of the BoNT/C-Hc, a non-toxic subunit of *Clostridium botulinum* neurotoxin that binds a neuron-specific ganglioside[10]: this strategy allowed the visualization of action potential (AP) evoked glutamate[8] and ATP[11] release. Analogous systems would thus need to be identified for the envisioned applications of extracellular biosensing with FAST-based sensors, such as visualization of neurotransmission or purinergic signalling.

Finally, further structural studies either based on X-ray crystallography or computational modelling, would tremendously improve our understanding of the general design of chemogenetic biosensors based on the reporter FAST. In fact, in addition to the undeniable contribution of high-throughput screening, rational design provided many insights for the development of FAST reporter variants and would be greatly facilitated by additional structural information. Indeed, identification of an optimized reporter module with improved solubility, decreased unspecific reconstitution (thus lower affinity between fragments) and suitable optical properties would provide an invaluable breakthrough towards our aim to generalize the design of such biosensors.

VII.2. Engineering reporter modules based on FAST for new imaging and biosensing opportunities

The parallel study aiming at exploring topological variants of FAST notably allowed the identification and optimization of the new chemogenetic reporter cpFAST(98-99) and several versions of splitFAST(98-99). Their use for biosensing applications were already demonstrated: insertion of the GltI sensing domain into cpFAST(98-99) allowed the generation of a glutamate biosensor described in chapter III, showing properties similar to Glu-FAST-2 based on cpFAST(114-115). The well-characterized interaction between FKBP and FRB could then be probed by splitFAST(98-99), that was subsequently improved with the variants split ^{RspA}FAST(98-99) and split ^{RspA}gFAST(98-99) showing high dynamic range and low background fluorescence.

This exploration led to similar considerations as our biosensors study, in terms of structural information for rational design. Any site-directed mutagenesis performed in this project, as well as the preliminary computer-based predictions of viable circular permutation positions, were indeed relying on the crystal structure of PYP, the parent protein of FAST. The exact structure of the tag in its ligand-bound and -free conformation would thus provide valuable insights in the aim of expanding the family of FAST reporters. In addition, fragmentation of the reporter appears to have a variable influence depending on the FAST variants. In particular, the unexpected loss of brightness from split $^{\text{RspA}}$FAST(98-99) compared to splitFAST(98-99), might raise the need for further screening of a more suitable splitting position among residues surrounding the initial fragmentation site.

Identification of a new position for the expansion of the reporter toolbox based on FAST represents a promising step towards new biosensing opportunities. Indeed, in addition to the characterization of splitFAST(98-99), we observed a possible complementation between fragments from different topological and mutational variants of FAST: for instance, the fragment $^{\text{RspA}}$CFAST(99-125) appears to interact with NFAST(1-114) with higher affinity than CFAST(115-125). The growing family of FAST mutational and topological variants thus represents a valuable source of possibilities to design cross-coupled split reporters with tunable optical properties and affinities.

Finally, the demonstration that FAST tolerated circular permutation and splitting at several spatially separated positions has set the ground work for the development of a tripartite split chemogenetic reporter. The interaction between the large N-terminal fragment and two C-terminal β-sheets is currently being studied and optimized in our group, and shows a promising potential to yield a split reporter with very low background signal. Such tripartite system would notably be useful for the visualization of ternary interactions, including ternary protein complexes, contact sites between different cellular organelles, or even interactions between different cell populations. These developments fall within the growing *palette* of innovative reporters for fluorescence microscopy, that include the engineering of tools based on fluorescent proteins,[12,13] and will be elegantly complemented with highly tunable chemogenetic reporters.

VII. References

1. Tebo, A. G. *et al.* Circularly Permuted Fluorogenic Proteins for the Design of Modular Biosensors. *ACS Chem. Biol.* **13**, 2392–2397 (2018).
2. Tebo, A. G. & Gautier, A. A split fluorescent reporter with rapid and reversible complementation. *Nat. Commun.* **10**, 2822 (2019).
3. Nasu, Y., Shen, Y., Kramer, L. & Campbell, R. E. Structure- and mechanism-guided design of single fluorescent protein-based biosensors. *Nat. Chem. Biol.* **17**, 509–518 (2021).
4. Gräwe, A. & Stein, V. Linker Engineering in the Context of Synthetic Protein Switches and Sensors. *Trends Biotechnol.* **39**, 731–744 (2021).
5. Autour, A., Bouhedda, F., Cubi, R. & Ryckelynck, M. Optimization of fluorogenic RNA-based biosensors using droplet-based microfluidic ultrahigh-throughput screening. *Methods* **161**, 46–53 (2019).
6. Ma, H., Gibson, E. A., Dittmer, P. J., Jimenez, R. & Palmer, A. E. High-throughput examination of fluorescence resonance energy transfer-detected metal-ion response in mammalian cells. *J. Am. Chem. Soc.* **134**, 2488–2491 (2012).
7. Fiedler, B. L. *et al.* Droplet Microfluidic Flow Cytometer for Sorting on Transient Cellular Responses of Genetically-Encoded Sensors. *Anal. Chem.* **89**, 711–719 (2017).
8. Takikawa, K. *et al.* High-throughput development of a hybrid-type fluorescent glutamate sensor for analysis of synaptic transmission. *Angew. Chem. Int. Ed.* **53**, 13439–13443 (2014).
9. Lobas, M. A. *et al.* A genetically encoded single-wavelength sensor for imaging cytosolic and cell surface ATP. *Nat. Commun.* **10**, (2019).
10. Tsukamoto, K. *et al.* Binding of Clostridium botulinum type C and D neurotoxins to ganglioside and phospholipid: Novel insights into the receptor for clostridial neurotoxins. *J. Biol. Chem.* **280**, 35164–35171 (2005).
11. Kitajima, N. *et al.* Real-time in vivo imaging of extracellular atp in the brain with a hybrid-type fluorescent sensor. *Elife* **9**, 1–18 (2020).
12. Cabantous, S. *et al.* A new protein-protein interaction sensor based on tripartite split-GFP association. *Sci. Rep.* **3**, 2854 (2013).
13. Pedelacq, J. D. & Cabantous, S. Development and applications of superfolder and split fluorescent protein detection systems in biology. *Int. J. Mol. Sci.* **20**, (2019).

Résumé en français

1. Introduction : principe de FAST, un rapporteur chémogénétique fluorogénique

Parmi les exemples de reporters chémogénétiques récemment développés et décrits dans le chapitre II de ce mansuscrit, notre groupe a développé en 2016 le Fluorescence Activating and absorption-Shifting Tag FAST, une étiquette protéique (14 kDa) conçue à partir de la protéine jaune photoactive (Photoactive Yellow Protein, PYP). L'évolution dirigée sur la boucle 94-101 de ce photorécepteur issu de *Halorhodospira halophila* a en effet permis d'obtenir un variant qui lie de manière non-covalente des dérivés d'hydroxybenzylidène-rhodanine (HBR). Associé à la mutation du résidu cystéine réactif C69 en glycine, le variant obtenu se lie aux dérivés HBR de manière hautement dynamique et entièrement réversible. Les dérivés HBR sont de petites molécules fluorogéniques dont l'absorption est décalée vers le rouge et la fluorescence est activée lors de leur déprotonation et de leur immobilisation dans la cavité de liaison de FAST. Ces fluorogènes synthétiques peuvent être fonctionnalisés, offrant ainsi une grande diversité de propriétés biophysiques, permettant notamment aux complexes FAST:fluorogène de couvrir une large gamme spectrale, compatible avec l'imagerie multicouleur. De plus, les cinétiques rapides de complexation ainsi que la possibilité de marquer FAST de manière stochastique en contrôlant la concentration de fluorogène, font de ce tag un marqueur approprié pour la microscopie de super-résolution.

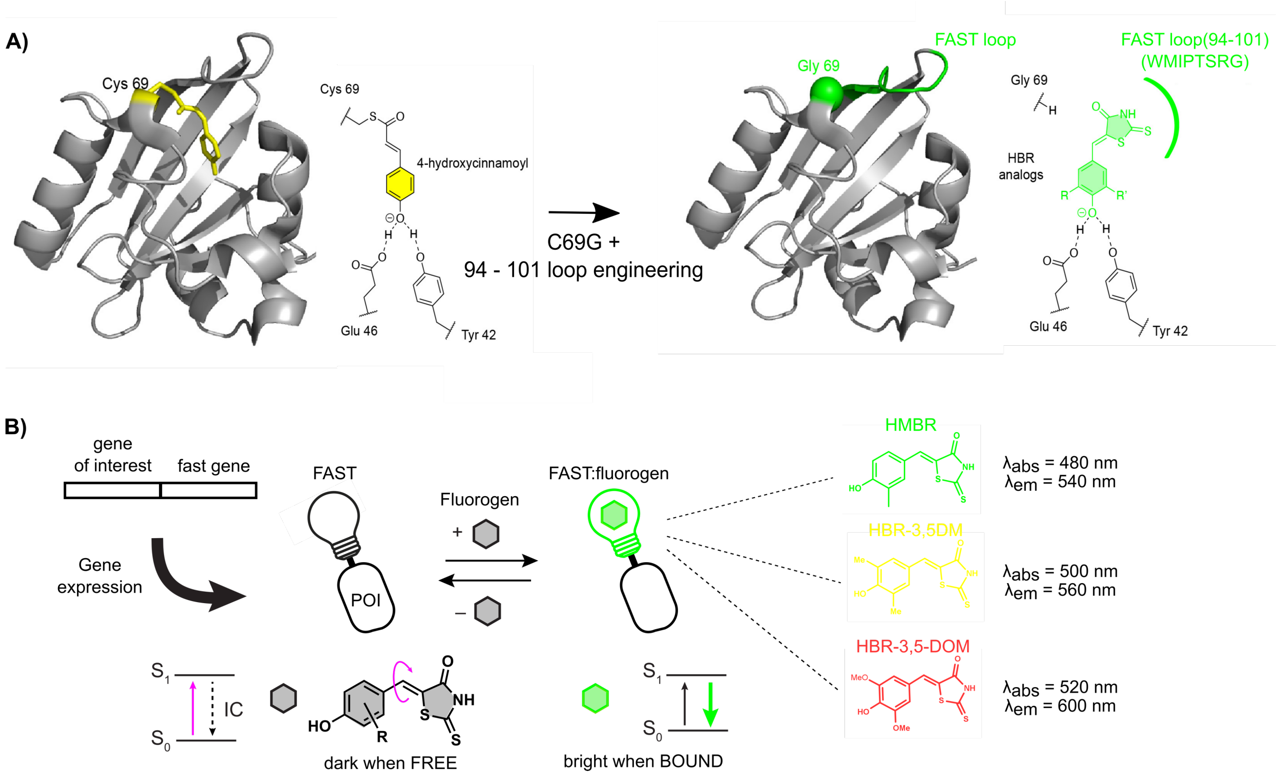

Figure 1. Principe du tag protéique chémogénétique FAST. **A)** FAST a été évolué à partir de PYP en introduisant la mutation C69G et la boucle 94-101 générée par évolution dirigée. **B)** FAST lie de manière sélective, non-covalente et réversible les dérivés de HBR, dont HMBR (vert), HBR-3,5-DM (jaune) et HBR-3,5-DOM (rouge).

En plus de son repliement rapide et de sa grande modularité, FAST présente plusieurs avantages en termes d'application en imagerie. En effet, la complexation du fluorogène permet une activation instantanée de la fluorescence, qui est par conséquent indépendante de la présence d'oxygène et ne nécessite aucun temps de maturation. Outre le marquage de protéines dans diverses localisations cellulaires et l'imagerie in vivo (notamment chez le poisson zèbre), ces propriétés avantageuses ont repoussé les frontières de l'imagerie par fluorescence dans de multiples contextes, notamment en milieu anaérobique. L'ingénierie initiale de FAST a été suivie du développement de plusieurs variants de FAST, élargissant les propriétés spectrales et les possibilités d'imagerie offertes par ce rapporteur hybride. Les variants iFAST et td-iFAST ont permis d'obtenir des rapporteurs avec une plus grande brillance grâce à la mutation V107I ; puis la combinaison de l'ingénierie moléculaire et de l'évolution dirigée ont conduit à l'optimisation de frFAST émettant dans rouge lointain (λ_{em} = 670 nm). Ces propriétés d'absorption/émission ont permis l'imagerie multicouleur en organisme multicellulaire. Le système orthogonal comprenant greenFAST et redFAST, liant sélectivement le fluorogène vert HMBR et le fluorogène rouge HBR-3,5-DOM, respectivement, a été décrit la même année. Enfin, la stratégie la plus récente d'ingénierie de FAST par évolution dirigée et conception rationnelle a permis d'identifier le tag polyvalent pFAST, qui se lie à une large gamme de fluorogènes couvrant l'ensemble du spectre visible, avec une brillance et une affinité améliorées. Ce tag chémogénétique est adapté à une multitude de protocoles d'imagerie dans des cellules mammifères vivantes et fixées, des neurones en culture, ainsi qu'en organisme multicellulaire en microscopie confocale et de super-résolution.

L'exploration de nouveau variants de FAST afin d'étendre ses propriétés optiques a mené à la génération de plusieurs versions orthologues de FAST (Rakotoarison & Tebo et al., manuscrit en préparation). À cette fin, la boucle 94-101 a été remplacée par la séquence mutée WMIPTSRG dans six orthologues de PYP présentant une homologie de séquence de 70-78% avec le prototype initial provenant de *Halorhodospira halophila* (Hha). Ces versions orthologues sont capables de lier les fluorogènes de FAST avec une brillance et une affinité similaires ou supérieures à celles de ^{Hha}FAST, et sont donc des candidats prometteurs pour des applications d'imagerie et de biodétection.

Dans le but de concevoir un domaine rapporteur pour des outils de biodétection, des variants topologiques de FAST ont également été conçus. Une version permutée circulairement de FAST a été développée en reliant ses extrémités et en en créant de nouvelles à la position 114-115. Le couplage de cpFAST(114-115) à la paire protéique calmoduline/M13 interagissant en présence de Ca^{2+} a notamment permis de générer un capteur intramoléculaire de Ca^{2+}. La caractérisation et l'optimisation de splitFAST(114-115) en tant que rapporteur d'interactions protéine-protéine a également permis d'obtenir une version intermoléculaire de cet indicateur. Divers processus cellulaires ont également pu être visualisés avec splitFAST, et il a été démontré que d'autres systèmes rapporteurs fonctionnels peuvent être obtenus par le fractionnement d'autres variants de FAST. L'interaction induite par la rapamycine entre FKBP et FRB a notamment été visualisée par fusion avec l'un ou l'autre des fragments frFAST, et la stratégie de fractionnement peut également être appliquée au système orthogonal constitué par greenFAST et redFAST. Ces diverses applications ont montré la polyvalence du système chémogénétique FAST et les diverses possibilités de biodétection offertes par un tel rapporteur dans le contexte de la conception de biocapteurs.

2. Objectifs de la thèse

Encouragés par l'utilité démontrée de FAST en tant que rapporteur chémogénétique fluorescent dans divers contextes, et par les possibilités d'imagerie offertes par ses propriétés uniques, mon projet de doctorat avait pour objectif de généraliser et optimiser l'utilisation de FAST et de ses variants pour des applications de biodétection.

La conception d'un biocapteur intramoléculaire de Ca^{2+} basé sur FAST a montré que la liaison du fluorogène au domaine rapporteur, donc la fluorescence, peut être conditionnée par la complexation d’un analyte par l'unité de détection. Nous avons supposé que ce principe pouvait être généralisé afin de concevoir des biocapteurs à partir de n'importe quel domaine de reconnaissance donné, à la condition que ce dernier subisse un changement conformationnel suffisant lors de sa liaison avec un analyte. Cette hypothèse repose sur un couplage allostérique supposé entre notre rapporteur hybride et un domaine protéique de détection. En effet, un biocapteur fluorogénique est capable de lier à la fois un fluorogène et un analyte d'intérêt, et la complexation de l’un influence celle de l’autre.

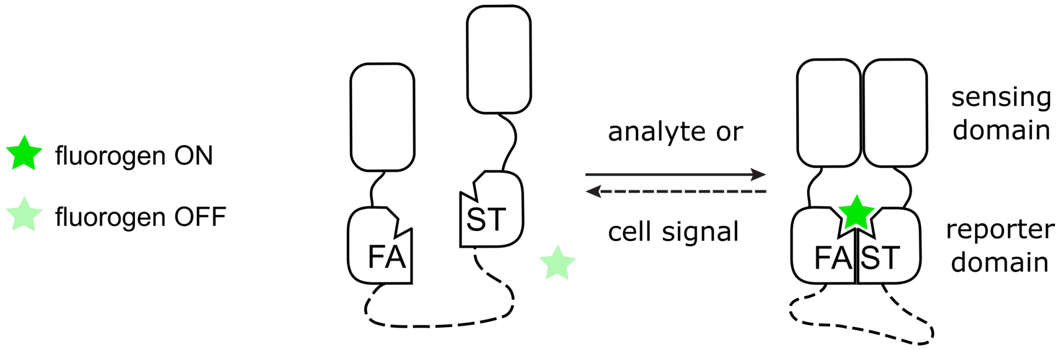

Figure 2. Conception de biocapteurs basés sur le rapporteur FAST. FAST ou l’un de ses variants est couplé à un domaine de détection, qui conditionne la liaison du fluorogène au domaine rapporteur en fonction de la présence ou non de l’analyte ou du signal d’intérêt.

Nous avons donc émis l'hypothèse que l'ingénierie de biocapteurs basés sur FAST permettrait la visualisation et la quantification de différents types d'analytes, tels que le cation métallique K^{+}, ou des biomolécules telles que le glutamate et l'adénosine-5'-triphosphate (ATP). A partir de domaines de reconnaissance précédemment identifiés et caractérisés, nous avons concentré nos efforts sur l'ingénierie des protéines afin d'optimiser le couplage allostérique, générant ainsi des biocapteurs avec une gamme dynamique élevée.

Un second objectif consistait à explorer les variants topologiques de FAST afin d’identifier de nouveaux rapporteurs fluorogéniques chémogénétiques utiles aux applications de biodétection. En effet, nous avons suggéré que l'identification d'une nouvelle position viable de permutation circulaire et de fragmentation de FAST représenterait une étape importante pour l'imagerie multiplexée avec divers rapporteurs chémogénétiques. Profitant de la large palette de propriétés offertes par les différents variants de FAST, nous espérions développer et optimiser des modules rapporteurs aux propriétés optiques et thermodynamiques complémentaires. Cet objectif s'inscrit dans le cadre des développements récents et croissants d'outils de biodétection hybrides, qui bénéficient grandement de l'optimisation des rapporteurs chémogénétiques et tirent parti de leurs caractéristiques uniques pour repousser les limites de la biodétection par fluorescence.

3. Développement de biosenseurs basés sur FAST

3.1. Développement d'un senseur pour le glutamate, Glu-FAST

Le développement d'un biocapteur de glutamate basé sur le couplage entre FAST et le module de détection GltI a illustré la possibilité de moduler la liaison du fluorogène au domaine rapporteur par la complexation de l'analyte au domaine de détection. La première étape de notre étude a démontré l'importance d'un criblage préliminaire des différentes topologies possibles qui influencent de manière significative la capacité des biocapteurs générés à détecter le glutamate. L'insertion de GltI entre les fragments de cpFAST(114-115) a permis d'obtenir Glu-FAST-2, un biocapteur présentant un couplage coopératif positif entre la liaison du glutamate et du fluorogène. Glu-FAST-2 lie le glutamate avec une haute affinité ($K_{D,glu}$ = 8.7 ± 0.8 µM) et une augmentation modérée de la fluorescence de lors de l'ajout de l'analyte (1.8 fois).

Différentes stratégies ont été envisagées afin d'améliorer la gamme dynamique de Glu-FAST-2. Malgré une tentative infructueuse de remplacer FAST par l'une de ses versions orthologues, nous avons souhaité optimiser le domaine rapporteur afin de progresser vers l'objectif de généralisation de biocapteurs fluorogéniques conçus à partir de FAST. L'effet des délétions de résidus aux extrémités des fragments de FAST a été évalué, basé sur l'amélioration précédemment décrite des propriétés de cpFAST et splitFAST grâce à l'utilisation de CFAST10 (115-124) au lieu de CFAST11 (115-125). Tandis que la délétion analogue du résidu 125 ne s'est pas avérée utile dans le contexte de Glu-FAST-2, probablement en raison de la connectivité différente entre les domaines de détection et le domaine rapporteur, la gamme dynamique de notre capteur de glutamate a été améliorée par la délétion du résidu Gly115.

Les développements précédents de capteurs ratiométriques et intensiométriques basés sur GltI ont mis en évidence la nécessité d'optimiser les régions de connexion interdomaines, soit par la délétion de résidus flexibles aux extrémités du domaine de détection, soit par l'ajout et le criblage de connecteurs rigides. Dans le cas de Glu-FAST-2, nous avons supposé que l'insertion de connecteurs flexibles pouvait améliorer la constante de coopérativité α en diminuant la valeur de $K_{D,HMBR/glu}$, en supposant qu'elle permettrait une meilleure complémentation du domaine rapporteur lors de la liaison de l'analyte au capteur. Cependant, l'accessibilité accrue des fragments de FAST n'a pas permis d'augmenter l'affinité du rapporteur pour le fluorogène dans la conformation fermée du biocapteur : au contraire, un signal non-spécifique plus important a été observé, favorisé par l'auto-assemblage de cpFAST. Des résultats imprévisibles et peu concluants ont également été obtenus de la tentative d'ajouter une contrainte conformationnelle au niveau de sites de connexion, en supprimant jusqu'à dix résidus aux terminis du domaine de détection GltI. Néanmoins, une version optimisée du biocapteur de glutamate Glu-FAST-2.1 a été obtenue par l'insertion de deux prolines entre GltI et NFAST, combinée à la troncation de Gly115 dans le fragment CFAST.

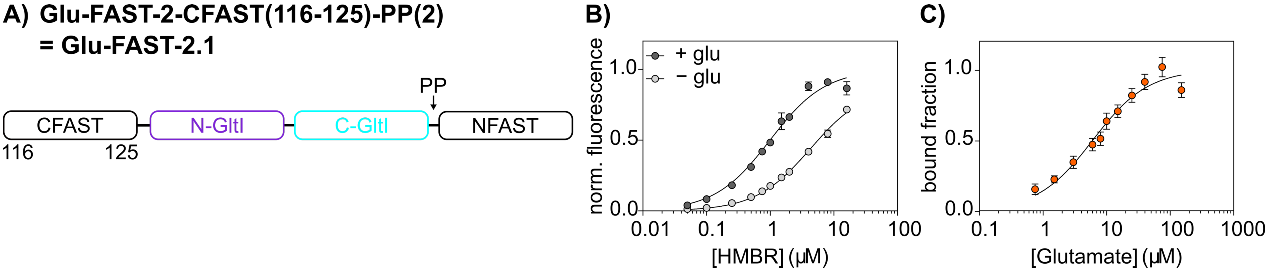

Figure 3. Biocapteur de glutamate basé sur FAST. La topologie du senseur Glu-FAST-2 a été optimisée par la troncation du résidu C-terminal de CFAST, Gly115, et l'insertion d'un connecteur proline entre le domaine de détection GltI et NFAST. Le senseur optimisé Glu-FAST-2.1 possède une constante de coopérativité α = 4.3 et une intensité de fluorescence 2.5 fois plus élevée en présence qu'en absence de glutamate.

Une amélioration significative de la constante de coopérativité (de α = 2.2 dans le cas de Glu-FAST-2 à α = 4,3 dans le cas de Glu-FAST-2.1) a été nécessaire pour obtenir une amélioration modérée de la gamme dynamique (l'augmentation de la fluorescence ayant été améliorée de 1.8 à 2.5). Ces résultats suggèrent un couplage allostérique modéré entre cpFAST et GltI. Le repliement du rapporteur dans la conformation liée à l'analyte a fourni des constantes de dissociation du fluorogène raisonnables. L'amélioration de α repose donc principalement sur l'entrave à la reconstitution de cpFAST dans la conformation ouverte du capteur. Une optimisation plus poussée des connecteurs serait ainsi nécessaire pour améliorer de manière plus probante les propriétés du biocapteur Glu-FAST-2.

Les difficultés d'expression à la membrane cellulaire Glu-FAST-2 et Glu-FAST-2.1 semblent être la principale limite de notre approche. De tels biocapteurs avec des affinités dans la gamme des micromolaires pour le glutamate étaient en effet principalement envisagés pour des applications extracellulaires telles que l'imagerie de la signalisation glutamatergique. Des problèmes de conformation ou d'agrégation semblent empêcher l'export de nos biocapteurs par voie de sécrétion. Néanmoins, le couplage d'un variant de FAST avec un repliement et une solubilité améliorés (par exemple pFAST) à l'unité de détection GltI pourrait éventuellement faciliter l'expression correcte des Glu-FAST à la membrane. De plus, l'insertion du rapporteur dans le module de détection (au lieu d'encadrer ce dernier des fragments de FAST) pourrait prévenir l'exposition de surfaces hydrophobes entraînant un mauvais repliement du domaine rapporteur.

3.2. Développement d'un senseur pour l'ion potassium K^+, K^+-FAST

Le développement d'un capteur chémogénétique pour l'ion potassium K^+ basé sur FAST a ensuite été envisagé, afin d'étendre la gamme de biocapteurs pour cet analyte qui n'a que récemment été étendue aux indicateurs génétiquement encodés, suite à la caractérisation de la protéine Kbp capable de lier K^+ avec une grande sélectivité. Une étude topologique préliminaire s'est également avérée très utile dans le cadre de ce développement pour identifier la connectivité la plus prometteuse entre le rapporteur et le module de détection. L'insertion de Kbp dans cpFAST(114-115) a montré un couplage coopératif positif encourageant ($\alpha = 2.3$) : cette topologie étant similaire à Glu-FAST-2 identifiée dans le chapitre II, elle présentait donc des avantages pour la conception de biocapteurs. La fusion des fragments de FAST aux extrémités d'un domaine de détection de protéine est en effet propice à la conception généralisée d'outils pour la détection d'analyte avec un rapporteur hybride. Néanmoins, l'optimisation de K^+-FAST-2 a été nécessaire afin d'adapter ce biocapteur à des applications de visualisation en cellules, notamment en termes d'affinité et de gamme dynamique.

Le repliement de FAST ne semblait pas affecté de façon significative par le changement de conformation subi par Kbp entre la forme apo et la forme liée à K^+. Une affinité très élevée entre le domaine rapporteur et le fluorogène a en effet été observée dans les deux conformations ($K_{D,HMBR} = 0.44 \pm 0.02$ µM et $K_{D,HMBR/K^+} = 0.19 \pm 0.01$ µM). L'affinité de K^+-FAST-2 pour K^+ était également étonnamment élevée, approchant de la constante de dissociation entre K^+ et Kbp ($K_{D,K+} = 0.14 \pm 0.02$ mM), ce qui indique que le domaine de détection n'a pas été affecté par la fusion avec le rapporteur FAST. Kbp semble également conserver une grande sélectivité pour K$^+$ par rapport à Na$^+$: ainsi la titration par K$^+$-FAST-2 a permis de déterminer une affinité 350 fois plus faible pour Na$^+$ (K_{D,Na^+} ~ 50 mM).

L'affinité de notre capteur de K$^+$ basé sur FAST a été ajustée par l'ingénierie protéique du domaine de détection Kbp. En effet, l'insertion d'un connecteur de 15 résidus $(GGGGS)_3$ entre les domaines BON et Lys a considérablement diminué l'affinité du capteur K$^+$-FAST-5 (K_{D,K^+} = 1.1 ± 0.3 mM). Une augmentation de la fluorescence de 1.9 a ainsi été mesurée lors de l'ajout de K$^+$ à concentration saturante. La conservation d'une très haute sélectivité pour K$^+$ par rapport à Na$^+$ a également permis de ne détecter aucune réponse de K$^+$-FAST-5 lors de l'ajout de Na$^+$ jusqu'à une concentration de 350 mM, une propriété cruciale pour que l'utilisation du biocapteur soit possible en conditions biologiques. Nous avons supposé que la gamme dynamique de K$^+$-FAST-5 pouvait être améliorée par l'optimisation du couplage allostérique entre FAST et Kbp. Compte tenu du comportement similaire de Glu-FAST-2 et de K$^+$-FAST-5, l'optimisation de notre système de détection de K$^+$ était largement inspirée des conclusions tirées précédemment lors du développement du biocapteur de glutamate basé sur FAST. L'augmentation de la rigidité du système par le remplacement de deux glycines par deux prolines aux sites de connection interdomaines n'a pas été concluante. Toutefois la suppression du résidu Gly115 dans le fragment CFAST a semblé diminuer l'affinité entre les fragments FAST, permettant d'obtenir une augmentation de la fluorescence de 2.2 lors de l'ajout de K$^+$. La gamme dynamique et les constantes de coopérativité modestes obtenues avec nos capteurs hybrides de K$^+$, malgré un changement structurel significatif de Kbp lors de la liaison de K$^+$, ont suggéré une nouvelle fois la nécessité d'optimiser les régions de connexion entre le module de détection et le module rapporteur. Une ingénierie plus poussée des fragments du domaine rapporteur avec un auto-assemblage plus faible pourrait également améliorer les propriétés de notre capteur ; néanmoins, le criblage des connecteurs semble être nécessaire, en plus des stratégies de conception rationnelle.

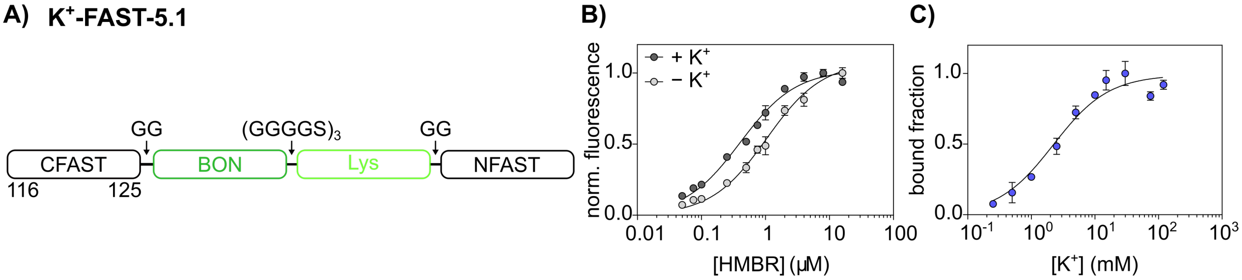

Figure 4. Biocapteurs de K$^+$ basé sur FAST. La topologie du senseur K$^+$-FAST-2 a été optimisée par la troncation du résidu C-terminal de CFAST, Gly115, et l'insertion d'un long connecteur flexible dans le domaine de détection Kbp. Le senseur optimisé K$^+$-FAST-5.1 possède une constante de coopérativité α = 2.5 et une intensité de fluorescence 2.2 fois plus élevée en présence qu'en absence de K$^+$.

Des cellules HEK293T exprimant K^+-FAST-5 ont montré un niveau d'expression correcte dans le cytosol, bien que les biocapteurs soient totalement saturés par la très haute concentration intracellulaire de K^+. De nouvelles étapes d'ingénierie protéique du module de détection Kbp, notamment par mutagenèse rationnelle (qui s'est avérée fructueuse dans l'optimisation des GEPIIs), pourrait être envisagée pour générer un indicateur de K^+ basé sur FAST adapté aux applications intracellulaires. Malheureusement, l'observation de cellules transfectées avec des capteurs de K^+ ciblés à la membrane a mené à des conclusions similaires à celles obtenues avec les capteurs de glutamate basés sur FAST décrits dans le chapitre III. En effet, un signal fluorescent provenant uniquement du réticulum endoplasmique a également indiqué un mauvais repliement du capteur dans ce cas, soutenant l'hypothèse d'un phénomène d'agrégation liée aux fragments de FAST. Le passage à une topologie résultant de l'insertion de cpFAST dans le module de détection pourrait améliorer la sécrétion ; néanmoins, la ré-ingénierie du capteur serait alors nécessaire.

Ce chapitre a confirmé l'hypothèse selon laquelle FAST peut être couplé de manière allostérique à des modules de détection pour générer différents types d'analytes, notamment des petites molécules et des ions métalliques.

3.3. Développement d’un senseur pour l’ATP, ATP-FAST

L'ATP est une biomolécule omniprésente, impliquée dans une grande variété de processus biologiques : la détection de l'ATP est donc considérée comme une composante cruciale à l’étude de systèmes biologiques. Bien que plusieurs biocapteurs synthétiques ou génétiquement encodés pour l'ATP aient été développés, aucune détection de l'ATP basée sur un système chémogénétique n'a encore été décrite, à notre connaissance.

Au cours de ce projet visant à concevoir un capteur d'ATP basé sur le rapporteur chémogénétique FAST, nous avons identifié ATP-FAST-1, un biocapteur aux propriétés très prometteuses, qui a révélé un important couplage allostérique entre le domaine rapporteur et le module de détection de l’ATP. Cette importante dépendance interdomaine a permis de tirer pleinement parti de la nature hybride du module rapporteur. En effet, nous avons pu générer un biocapteur hautement modulable, en ajustant différents paramètres. D'une part, les propriétés optiques de notre capteur d'ATP basé sur FAST ont pu être modulées par la nature du fluorogène. D'autre part, les propriétés thermodynamiques ont pu être contrôlées par un certain nombre de paramètres, tels que les propriétés de complexation du fluorogène, l'ingénierie protéique du domaine de détection, ainsi que la modification du domaine rapporteur. Cette étude a permis de montrer qu’il est possible de modifier les propriétés spectrales de notre biocapteur en changeant de fluorogène entre HMBR (qui fluoresce en vert), HBR-3,5-DM (jaune) et HBR-3,5-DOM (rouge). Les caractéristiques du capteur hybride ont également pu être modulées par le remplacement de FAST par son variant pFAST : une plus haute affinité pour les fluorogènes a ainsi permis la génération d’un système de détection avec une affinité pour l’ATP dans la gamme du millimolaire. Il serait alors intéressant d'explorer les multiples possibilités offertes par d'autres fluorogènes (tels que les fluorogènes imperméants ou les fluorophores couvrant l'ensemble du spectre visible liant pFAST), et différents variants de FAST (notamment frFAST), élargissant ainsi l'éventail d’application pour la biodétection de l'ATP.

Ce développement a une nouvelle fois démontré l'importance d’une étude topologique préliminaire. En effet, la connectivité entre les différents composants du biocapteur a été identifiée comme un paramètre influençant le comportement des capteurs de manière significative. La simple permutation entre les fragments de FAST autour du domaine de détection a notamment permis d'obtenir un biocapteur d'ATP de très haute affinité, ATP-FAST-2. La capacité de détecter de très faibles concentrations d'ATP dans la gamme du micromolaire permet d'envisager des applications de biodétection de l'ATP extracellulaire, notamment dans le contexte de la signalisation purinergique.

La génération de capteurs ratiométriques d'ATP basés sur FAST a également offert des perspectives prometteuses. En effet, la fusion N-terminale avec mCherry a semblé augmenter le rendement et la solubilité des biocapteurs obtenus par expression recombinante en bactéries *E. Coli* : ces propriétés améliorées pourraient s'avérer utiles en contexte cellulaire, notamment pour l'expression membranaire qui s'est révélée infructueuse jusqu'à présent. De plus, un signal FRET relativement faible a pu être observé provenant de mCherry lors de l'excitation du fluorogène HMBR lié à ATP-*p*FAST-1. Bien que ce transfert d'énergie puisse probablement être annihilé en introduisant un connecteur plus long et plus rigide entre mCherry et le rapporteur fluorescent, ce signal FRET pourrait être utile dans la perspective de générer des capteurs FRET basés sur FAST. La dépendance de l'efficacité du FRET vis-à-vis de l'ATP pourrait par exemple être améliorée en liant mCherry au fragment CFAST plutôt qu'au fragment NFAST, ce qui augmenterait l'effet des changements de conformation sur l'interaction entre les deux fluorophores. De plus, la conception d'autres biocapteurs innovants pourrait être envisagée à partir de ce transfert d'énergie entre HMBR et un fluorophore à proximité : le couplage d'un capteur basé sur FAST à un rapporteur bioluminescent pourrait en effet générer un capteur BRET avec une gamme dynamique élevée.

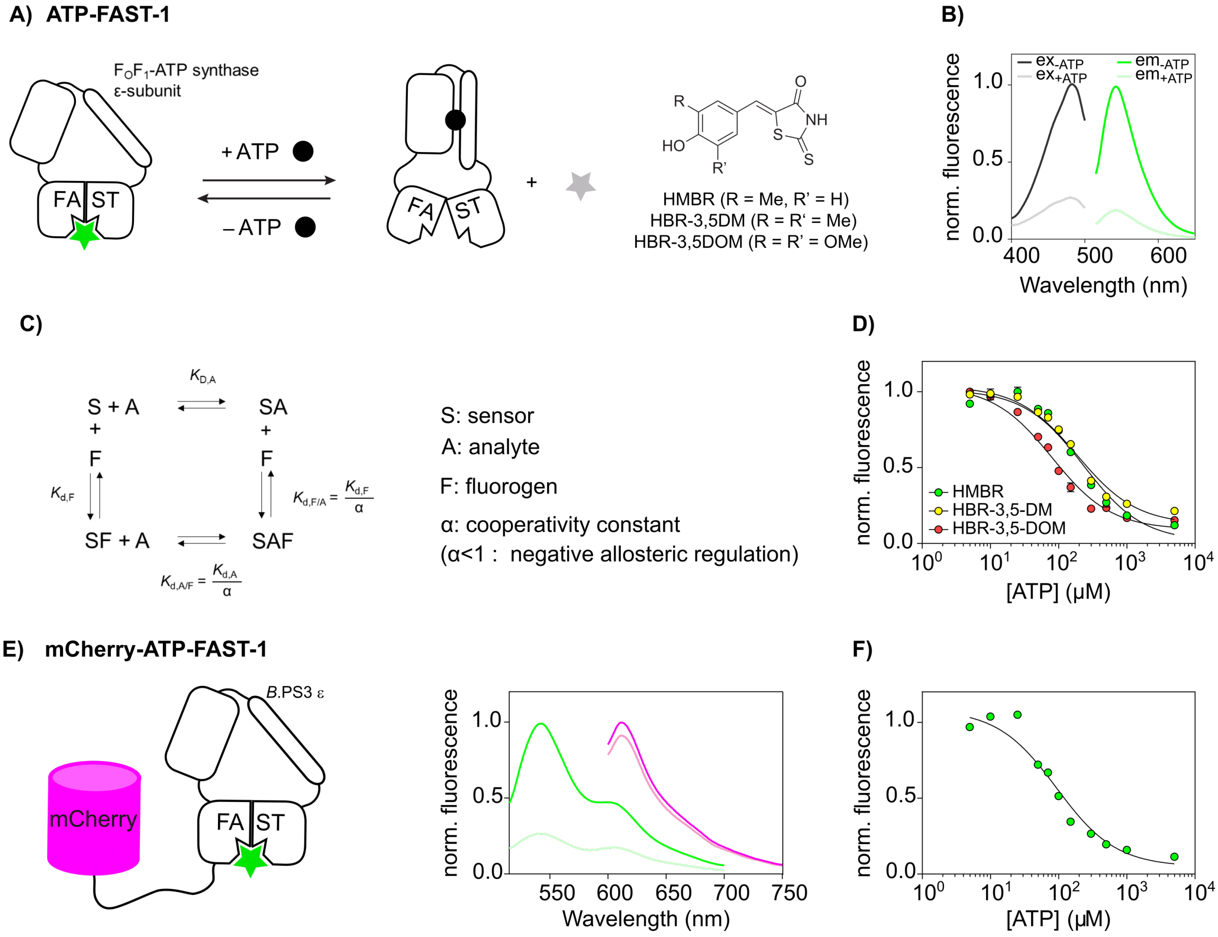

Figure 5. Conception d'un biocapteur d'ATP modulable basé sur FAST et ses variants. La grande coopérativité négative obtenue par le développement d'ATP-FAST-1 a permis d'explorer la modularité d'un biosenseur basé sur un domaine rapporteur chémogénétique. Le contrôle de différents paramètres tels que la nature et la concentration du fluorogène, ainsi que la possibilité d'utiliser différents variants de FAST comme domaine rapporteur, a permis d'obtenir un biocapteur aux propriétés optiques et thermodynamiques modulables. Une mesure ratiométrique de l'ATP a également été rendue possible par la fusion de la protéine fluorescente mCherry en N-terminus du biocapteur.

Néanmoins, le signal normalisé à une seule longueur d'onde d'ATP-FAST-1 présente une augmentation significative de la fluorescence lors de la déplétion de l'ATP, ainsi rendue indépendante de la concentration du biocapteur. Cette caractéristique, en plus de la grande adaptabilité de notre système aux diverses exigences expérimentales, est notamment intéressante pour la visualisation des variations de concentration d'ATP cellulaires, en échantillons biologiques et *in vivo*. mCherry-ATP-FAST-1 a déjà permis la quantification optique *in vitro* du glucose avec une gamme dynamique supérieure ou comparable à celle des tests existants basés sur un signal fluorescent, provenant directement d'un biocapteur de glucose. De plus, la possibilité de généraliser cette méthode de quantification à n'importe quel métabolite pouvant être consommé par une réaction enzymatique dépendante de l'ATP représente un avantage considérable de notre système. Ce principe pourrait ainsi être généralisé à une grande variété de tests, tels que le criblage de l'activité enzymatique de kinases, ou le développement de tests au « point d'intervention » pour la quantification de biomarqueurs.

3.4. Ingénierie de nouveaux variants du domaine rapporteur FAST

Deux nouvelles versions de FAST permutées circulairement, cpFAST(24-25) et cpFAST(98-99), ont été identifiées et caractérisées comme des rapporteurs potentiels pour la conception de systèmes de biodétection. D'une part, cpFAST(24-25) a montré une perte d'affinité spectaculaire pour le fluorogène, attribuée à l'altération de la structure tridimensionnelle ne permettant pas un repliement correct. Ces observations étaient cohérentes avec le nanoFAST récemment décrit, une version tronquée jusqu'au 27ème résidu de l'étiquette protéique. En effet, la troncation du fragment N-terminal du rapporteur semble entraîner une modification de sa cavité, compromettant ainsi la bonne complexation des dérivés de HBR. cpFAST(24-25) pourrait néanmoins être considéré comme un rapporteur dans la conception de biocapteurs. Un système avec une gamme dynamique élevée pourrait ainsi être obtenu par le couplage de cpFAST(24-25) à un domaine de détection, en supposant que l'interaction entre les fragments de faible affinité pourraient être forcée par la contrainte conformationnelle du domaine de détection.

D'autre part, la caractérisation de cpFAST(98-99) a montré des propriétés comparables à celles de cpFAST(114-115): il se reconstitue efficacement en un tag protéique fonctionnel, et lie le fluorogène HMBR avec une haute affinité lorsque l'interaction entre ses fragments est possible. Il a donc été suggéré que l'insertion d'un module de détection dans cpFAST(98-99) permettrait de générer des biocapteurs, et un exemple prometteur a été décrit dans le chapitre III de ce manuscrit, dans lequel un capteur de glutamate a en effet été conçu en insérant le domaine de détection GltI entre les fragments de ce variant topologique de FAST.

L'identification de permutations circulaires viables de FAST nous a encouragés à approfondir l'ingénierie de FAST comme rapporteur pour diverses applications de biodétection. Le fractionnement de FAST à la position 98-99, combiné à des études topologiques du système modèle d'interaction protéine-protéine FKBP-FRB, a permis d'identifier une nouvelle version de splitFAST avec une brillance plus faible que splitFAST(114-115) mais une gamme dynamique prometteuse. Le fractionnement des variants greenFAST et ^{RspA}FAST a ensuite permis d'obtenir plusieurs rapporteurs aux propriétés améliorées, plus adaptés à la visualisation des interactions protéine-protéine dans un contexte cellulaire. Il convient néanmoins de noter que les performances de chaque système de détection de l'interaction

FKBP-FRB dépendaient fortement de sa topologie. Ce paramètre doit donc être gardé à l'esprit et étudié avec soin lors de l'extension de l'utilisation de splitFAST(98-99) à d'autres partenaires d’interaction protéiques.

Un nouveau variant de FAST a également été développé au cours de ce projet, ^{RspA}gFAST, par insertion des mutations conférant à greenFAST la sélectivité pour HMBR (G21E, P68T et G77R) dans ^{RspA}FAST. Ce rapporteur sélectif pour HMBR, qui apparaît comme un rapporteur approprié pour la microscopie de fluorescence, devra faire l'objet d'une caractérisation biophysique plus approfondie. Un nouveau rapporteur a ainsi été obtenu par l’ingénierie et le fractionnement de ce variant optimisé ^{RspA}gFAST à la position 98-99, démontrant une haute sélectivité pour HMBR, une gamme dynamique élevée, un faible auto-assemblage et une brillance raisonnable. De plus, la combinaison de split ^{RspA}gFAST(98-99) et de split redFAST(114-115) est un système semi-orthogonal. Les deux systèmes ont en effet démontré une orthogonalité spectrale grâce à leur sélectivité pour HMBR et HBR-3,5-DOM, respectivement, et une semi-orthogonalité de complémentation. Les propriétés de cette paire de rapporteurs semi-orthogonaux devront être confirmées. Par ailleurs, les résultats préliminaires d’expériences de cytométrie en flux ont démontré la réversibilité du système, par l'évaluation de la dissociation de l'homodimère FKBP-F36M induite par la rapamycine. L'application de cette paire de rapporteurs split redFAST(114-115) / split ^{RspA}gFAST(98-99) doit être validée en microscopie de fluorescence, par exemple pour la visualisation d'interactions protéine-protéine consécutives avec plusieurs partenaires d'interaction communs.

Les possibilités de détection offertes par la conception de nouveaux rapporteurs fluorescents hybrides ouvrent donc un large éventail de nouvelles perspectives pour la visualisation de processus biologiques par des systèmes chémogénétiques.

RÉSUMÉ

La détection optique et la quantification de biomolécules dans des échantillons biologiques nécessitent des systèmes robustes et spécifiques. Les biocapteurs fluorescents génétiquement encodés sont des outils prometteurs car ils permettent généralement d'obtenir une grande sélectivité pour l'analyte sélectionné. Les biosenseurs sont généralement conçus en couplant un domaine de détection (par exemple un domaine de fixation d'un analyte ou un domaine de substrat enzymatique), capable de subir un important changement conformationnel dépendant d'un signal d'entrée, conjointement avec un module de signalisation fluorescent. Afin d'obtenir des biosenseurs avec un large spectre dynamique, nous proposons d'utiliser le fluorogen activating and absorption-shifting tag (FAST) comme module de signalisation. FAST est un marqueur fluorescent chemo-génétique inductible conçu à partir de la protéine jaune photoactive (photoactive yellow protein, PYP). Ses propriétés fluorescentes proviennent de la fixation réversible et sélective de chromophores fluorogènes. Des biosenseurs pour diverses biomolécules telles que le glutamate, l’ion potassium ou l'adénosine-5'-triphosphate (ATP) ont été générés en couplant des variants de FAST avec différents domaines de détection. Ces développements nous ont permis de coupler la reconnaissance de l'analyte à la fixation du fluorogène, et donc à un changement de fluorescence. Le caractère hybride du module rapporteur a également permis d'obtenir un biosenseur avec une grande modularité, à la fois en termes de propriétés thermodynamiques et optiques. Dans un second temps, diverses permutations circulaires de FAST ont été explorées, et un nouveau site de fragmentation de l’étiquette protéique a été identifié. Cette étude a permis le développement et l'optimisation de nouveaux rapporteurs fluorescents, pouvant être utilisés pour la conception de biosenseurs. De plus, la nouvelle version d'un système splitFAST a permis de visualiser des interactions protéine-protéine avec un très haut contraste.

MOTS CLÉS

Biocapteurs - Fluorescence - Fluorogénique - FAST

ABSTRACT

Optical detection and quantification of biomolecules in biological samples require robust and specific systems. In this aim, genetically encoded fluorescent biosensors are promising tools as they generally provide a high selectivity for the selected analyte. Biosensors are commonly designed by coupling a sensing domain (e.g. analyte-binding domain or enzyme substrate domain), able to undergo a large conformational change upon input signal, together with a fluorescent reporting module. In order to obtain biosensors with high dynamic range, we propose to use fluorogen activating and absorption-shifting tag (FAST) as reporting module. FAST is an inducible chemical-genetic fluorescent marker, that was previously engineered from the photoactive yellow protein (PYP) by directed evolution. Its fluorescent properties arise from the reversible and selective binding of fluorogenic chromophores. High contrast can be achieved as these so-called fluorogens are dark when free in solution. Biosensors for various analytes, such as glutamate, potassium ion or adenosine-5'-triphosphate (ATP), were generated by conformational coupling of FAST variants with various sensing domains. This design allowed us to condition fluorogen binding, thus fluorescence change, to analyte recognition. The hybrid nature of the reporter unit also provided a large modularity in terms of thermodynamic and optical properties of the biosensors. In a second part, we explored several circular permutations of FAST, and a new splitting site of the tag was identified. This study allowed the development and optimization of new fluorescent reporters, that can be useful in the design of biosensors. Moreover, the newly identified splitFAST system was demonstrated to provide very high imaging contrast for the visualization of protein-protein interactions.

KEYWORDS

Biosensors - Fluorescence - Fluorogenic - FAST